Effects of biocompatible ions and functional groups on the formation dynamics and crystallographic structures of biogenic minerals

生体適合性イオンおよび官能基が生体鉱物の形成ダイナミクスおよび結晶構造に与える影響

February 2015

Waseda University
Graduate School of
Creative Science and Engineering
Department of Earth Science, Resources and
Environmental Engineering
Research on Applied Mineralogy

Yuki SUGIURA

General Abstract

The phase transformation process from amorphous to crystalline phases in calcium carbonate and calcium phosphate systems were explored on the basis of cluster-base transformation and non-classical nucleation processes of biogenic mineralization. There were two principle concepts of investigation: the fine characterization of the physico-chemical properties of the intermediate phases during phase transformation in weakly-acidic to weakly-basic solutions and the effect of additives on the physico-chemical properties, including ionic charge and hydration, as well as on the dynamics of the mineral phase transformations. These crystal-growth studies resulted in the development of new concepts in non-classical nucleation and biomineralization.

In calcium carbonate systems, the effect of the charge of phosphate ions or phosphate functional group-containing molecules (single charge: $H_2PO_4^-$ or double charge: HPO_4^{2-} and $-PO_4^{2-}$) on the physico-chemical properties and formation dynamics of calcium carbonate minerals was investigated. During vaterite formation, a minute amount of $H_2PO_4^-$ (molar ratio of Ca^{2+} ions approximately 1/5000) acted as an accelerator; however, at higher concentrations, $H_2PO_4^-$ acted instead as a significant inhibitor. Furthermore, the presence of $H_2PO_4^-$ induced the formation of a low-stability phase of vaterite, called pseudo-vaterite, prior to actual vaterite formation. When vaterite formed in a solution containing a high amount of $H_2PO_4^-$, its stability was relatively low; the presence of $H_2PO_4^-$ affected the surface energies of the vaterite and the pseudo-vaterite. In $H_2PO_4^-$ free solution, the surface energies of vaterite and pseudo-vaterite were 20.3 and 30.2 mJ/m^2, respectively; however, in a 10 μM $H_2PO_4^-$ solution, the surface energies were 210.5 mJ/m^2 for vaterite and 105.4 mJ/m^2 for

pseudo-vaterite.

The inhibition of dissolution by $H_2PO_4^-$ was much higher for vaterite than for pseudo-vaterite. Thus, when vaterite spherulites dissolved in an $H_2PO_4^-$-containing solution, the pseudo-vaterite in the inner parts of the spherules dissolved prior to the outer vaterite. Thus, hollow vaterite spherulites were typically formed.

However, the opposite calcium carbonate mineralization behavior was observed in HPO_4^{2-}- or $-PO_4^{2-}$-containing solutions. A $-PO_4^{2-}$-containing molecule, flavin mononucleotide (FMN), affected calcium carbonate formation. In contrast to $H_2PO_4^-$, FMN enhanced vaterite formation by absorbing onto the calcite, which is in a stable phase, and relatively developing calcite formation. Thus, the charge on the phosphate groups was the dominant factor in the formation of calcium carbonate polymorphs.

In calcium phosphate systems, the effects of the hydration properties of carboxylic functional groups (-COOH) on calcium phosphate mineralization were studied. To investigate how insoluble -COOH affects calcium phosphate mineralization, a hybrid material of carboxylic thiol and gold nanoparticles (CGNs) was used as a source of immobilized -COOH groups.

When hydroxyapatite (HAP) formed in a weak basic solution, a small amount of CGNs (molar ratio of $CaPO_4$ approximately 1/1000) acted as a significant accelerator (maximum acceleration of 45%). The presence of the CGNs also altered the formation path of HAP, from amorphous calcium phosphate (ACP) via Ca-deficient octacalcium phosphate (OCP) to direct HAP formation from amorphous calcium phosphate. CGNs selectively affected the HPO_4-OH layer structure that only formed in OCP; thus, when OCP was generated in a CGN-containing solution, an OCP-deficient HPO_4-OH layer structure without a typical OCP peak at $2\theta = 4.7°$ was formed.

Acetic acid was used as a source of hydrated -COOH functional groups. When OCP formed in an acetic acid-containing solution, it was observed that the HAP-like layer and HPO_4-OH layer structure of the OCP was enhanced. This tendency was clearly different from the effect of immobilized -COOH.

The effects of additives on the intermediate transition phase of biogenic minerals formation are described. Small amounts of additive (molar ratio of Ca^{2+} ions 1/5000 to 1/1000) acted as an accelerator of mineral formation; however, as the amount of additive increased, the effect altered towards inhibition. The physico-chemical properties, charge and hydration, of the additives greatly affected the biogenic mineralization processes, dynamics, and polymorphism.

Contents

General Abstract

Division I: Calcium Carbonate Systems

Division II: Calcium Phosphate Systems

Chapter 1

General Introduction

Minerals formed via biomineralization are known as biogenic minerals.[1-14] Biomineralization includes biogenic mineralization brought about by biological organisms for sustenance, as well as mineralization occurring in or on biological entities.[1,2] Biomineralization is regard as a mineralization process that occurs in aqueous solutions at normal temperature and pressure in the presence of weakly acidic to weakly basic solutions.[15,16] Well-designed mineral crystals with a suitable form for biological organisms formed through biomineralization process. Components of biological hard tissues, such as shells, coral reefs, coccoliths, bones, and teeth are formed through biomineralization.[1,2,15,17-25] For example, the nacre shell exhibits a well-arranged accumulation of hexagonal plate-like aragonite crystals.[26-28] This structure demonstrates not only high mechanical strength with flexibility, which originating from its structure, but also beautiful interference colors.[28-30]

As described, the biomineralization process is mainly regarded as calcium carbonate and calcium phosphate mineralization processes in aqueous solutions.[15,16] The formation processes of calcium carbonate and calcium phosphate is far more complex and unique compared with that of other inorganic salt crystals. In the case of normal inorganic salt crystals in an aqueous solution, the salt crystals directly form through simple monomer molecules aggregation, and the radii of these salt crystals exceed the critical radius of the seed.[17,31-35] The formation process is described as the classical nucleation process.[31,32] However, although calcium carbonate and calcium phosphate crystals are described as inorganic crystals, their formation process is completely different from that of normal inorganic salt crystals; this process is called as non-classical crystallization process.[36] The physico-chemical properties of calcium carbonate and calcium phosphate that control the crystallization process are similar to those of large molecular mass materials, such as protein and virus crystallization. For example, step coefficient constant, β of hydroxyapatite (HAP) is calculated as 0.4×10^{-4} cm/s,[37] the edge free energy, γ of HAP is calculated $\gamma = 3.3k_BT$.[38] The values of β and γ are similar to large-molecule crystals and is completely different from that of simple salt crystals (γ of ammonium dihydrogen phosphate (ADP) was showed $\gamma = 0.8k_BT$).[37,38,39-41]

The overall description of the calcium carbonate and calcium phosphate minerals formation process is provided below. When calcium carbonate and calcium phosphate minerals formed in aqueous solutions, amorphous phases form as the initial phase.[42-45] These amorphous phases comprising relatively loose structures and water molecules[32-49] immediately transform into crystalline phases, particularly metastable phases.[50-55] In general, metastable phases show higher solubility and lower stability than stable phases.[56-59] The stable phases form through a phase transformation process that comprises different molecular structural stages, such as dissolution and precipitation, or a direct crystal-structure conversion process from metastable or amorphous phases.[36] However, the phase transformation from a amorphous phase to a metastable phase or crystalline phase, is still unclear.

The phase transformation from amorphous to crystalline phases is considered to be a cluster-based conversion.[60-65] The smallest units of amorphous and crystalline phases are the same. Cluster models postulate that tens of ions form a short-range symmetric structure.[60-69] In amorphous phases, clusters are randomly aggregated. The cluster-based structure is expected to transform to a regular structure via phase transformation. This hypothesis was proposed by Onuma and Ito[70] in 1998 from direct cluster observation in calcium phosphate systems. Gebauer et al.[71] presented a prenucleation cluster hypothesis in calcium carbonate systems. They also showed that polymorphs were determined during the cluster formation stages.[71,72] Sommerdijk and colleagues directly showed prenucleation cluster and phase transformation from amorphous to crystalline phases using cryogenic-transmission electron microscopy (cryo-TEM).[73-75] Gale and colleagues presented the phase transformation process and prenucleation cluster structure using an *ab initio* calculation method.[76-78]

Recently, several studies have reported on phase transformation from amorphous to crystalline phases.[60-77] However, some factors remain unclear in these reported models. In the cluster-based phase transformation, it is postulated that there is no dis-sequence during transformation between amorphous and crystalline phases. Thus, it is suggested that intermediate transition phases, whose physicochemical properties are essentially different from both amorphous and crystalline phases, are formed as local energy minimum phases during the phase transformation process. Clear identification of intermediate transition phases is expected to contribute toward the understanding of biogenic mineralization and crystal growth processes.

Furthermore, in biomineralization and bio-inspiration, the roles of additives, ions, and functional groups are also important for biogenic mineralization. Numerous studies have shown the role of additives in the formation of biogenic minerals.[79-93] The effect of additives on biogenic mineral formation can be categorized as static or dynamic effects.

In dynamic effects, additives not only inhibit or accelerate the formation dynamics of biogenic minerals but also alter their reaction pathway. For example, He et al.[94] showed that proteins rich in the carboxyl-functional group (–COOH) may accelerate HAP mineralization on glass templates. Tsuji et al.[95-97] showed that some types of –COOH-rich polypeptides not only accelerate HAP mineralization but also alter the phase transformation process. Katsifaras and Spanos[98] reported that PO_4 ions inhibit the vaterite and calcite conversion in high pH solutions. In addition, additives altered biogenic mineralization process at some stages and the phenomena induce metastable phases. For example, amorphous calcium carbonate (ACC) phases are often found in lobster shells. Thermodynamically, ACC cannot exist for a prolonged time in biological environments. However, some PO_4-containing molecules inhibit the crystallization of calcium carbonates, thus enabling ACC to exist in lobster-shell structures.[99-101]

Static effects of additives are described as morphological, crystal structure, and polymorph alteration of biogenic minerals formed via their mineralization process. For example, Mg^{2+} ions and some polypeptides altered calcium carbonate polymorphs from calcite to aragonite phases.[102-105] Some polymers and cation induced a mesoporous structure called *mesocrystal* structures of biogenic minerals, thus maintaining their overall morphologies.[36,106-109] The same type of carboxylic acids intercalated and altered the octacalcium phosphate (OCP) crystal structure.[108-114]

However, it has been reported that molecules containing the same functional groups can have completely different effects on the biogenic mineralization process. Markovic[113,114] investigated how various carboxylic acids affect OCP structural formation. For example, although succinic acid and citric acid significantly affect the OCP structure, azelaic acid and maleic acid, whose structures are very similar to succinic acid and citric acid, have no effect on OCP structures.

The aim of this thesis is investigating for characterization and dynamics measurement of intermediate transition phase during phase transformation from amorphous phases into crystalline phases and how difference physico-chemical properties, charges and hydration of the same ions or functional groups affect into biogenic mineralization. In this work, two main systems of biogenic minerals were investigated, i.e., the calcium carbonate and calcium phosphate systems. In calcium carbonate systems (*Division I*), the effect of PO_4 charge ($–HPO_4^{2–}$or $–PO_4^{3–}$) on calcium carbonate mineralization was investigated. In calcium phosphate systems (*Division II*), the effect of –COOH hydration (soluble –COOH molecules or immobilized –COOH molecules) on calcium phosphate mineralization was investigated.

In Chapter 2, it is described that the effects of inorganic $H_2PO_4^-$ ions on calcium carbonate nucleation dynamics and its polymorph formation in weak basic solutions. $H_2PO_4^-$ not only altered crystalline calcium carbonate phases from vaterite to calcite but also inhibited the transformation from amorphous calcium carbonate (ACC) phase to crystalline phases. These phenomena occurred when small amounts of $H_2PO_4^-$ ($H_2PO_4^-$/Ca molar ratio 1/1000) was containing. When vaterite spherulites formed in $H_2PO_4^-$-rich solutions, dissolution produced hollow structures.

In Chapter 3, the dissolution behavior of vaterite is discussed in $H_2PO_4^-$-containing solutions. In addition, it was also discussed how hollow structural vaterite formed in $H_2PO_4^-$-containing solutions. Crystallographic data suggest that the core of the vaterite spherulites consists of pseudo-vaterite with different physico-chemical properties than vaterite; this tendency is enhanced in $H_2PO_4^-$-containing solutions. Thus, under $H_2PO_4^-$-rich conditions, the structure of the core of vaterite appears to be hollow because the core dissolved prior to the outer part.

In Chapter 4, the surface energies of vaterite and pseudo-vaterite under various $H_2PO_4^-$ concentrations are discussed. With increasing $H_2PO_4^-$ concentration, the surface energies of vaterite and pseudo-vaterite increased. The increase in the ratio of vaterite was much higher than that of pseudo-vaterite. Thus, $H_2PO_4^-$ not only inhibits the formation of vaterite but also lowers the stability of vaterite. Furthermore, $H_2PO_4^-$ alters the ACC structure, which is an essential growth unit of vaterite.

In Chapter 5, the effect of ionic charge on calcium carbonate formation was discussed. The effect of PO_4 functional groups ($-PO_4$), mainly $-PO_4^{2-}$-containing molecules because inorganic PO_4^- is typically present as $H_2PO_4^-$ in weak basic solutions, and flavin mononucleotide (FMN) as $-PO_4^{2-}$ molecules on calcium carbonate nucleation was showed. In contrast to $H_2PO_4^-$, FMN inhibits calcite and favors vaterite formation.

In *Division II* (Chapter 6, 7 and 8), the investigation of the calcium phosphate system was described. For creating advanced biomaterials, it was mainly investigated that the physicochemical properties and dynamics of HAP and its precursor, octacalcium phosphate (OCP), with immobilized and soluble COOH.

In Chapter 6, the protocol for carboxyl-rich pseudo-simulated artificial proteins (CGNs: **C**arboxylic-functional-groups on **G**old **N**anoparticle**s**) and their effect on the HAP formation dynamics from the amorphous calcium phosphate (ACP) phase were described. A small amount of CGNs (about 1/1000) accelerates HAP formation to a maximum of 45%. In addition, the OCP structure in HAP was inhibited as the concentration of CGNs increased. Thus, CGNs favor the formation of HAP directly from ACP without the intermediate OCP phase.

In Chapter 7, the effect of CGNs on OCP formation in weak acidic conditions was investigated. When OCP forms in CGN-containing solutions, the HPO_4–OH layer structure, which is unique in the OCP to HAP process, HPO_4-OH layer deficient OCP formed prior to conventional OCP. In addition, the ACP to OCP phase transformation lasted longer. Thus, CGNs inhibit the HPO_4–OH layer structure and OCP structure during HAP formation. This process may accelerate HAP formation.

In Chapter 8, the effect of the carboxyl hydration rate on the OCP physicochemical properties was discussed. Acetic acid was used as the soluble COOH. Crystallographic studies showed that the HPO_4–OH layer structure of OCP was favored as the concentration of the soluble COOH increased. This tendency is clearly opposite to the effect of the insoluble COOH on OCP mineralization.

In Chapter 9, it is summary of the study and discussion for future work on biogenic minerals and its contribution to various academic fields.

References

(1) Mann, S. *Biomineralization Principles and Concepts in Bioinorganic Materials Chemistry*, Oxford University Press, U.K., **2001**.

(2) Weiner, S., Dove, P.M. *An Overview of Biomineralization Processes and the Problem of the Vital Effect.* P.M. Dove, J.J. DeYoreo, and S. Weiner (Eds.), *Biomineralization, Reviews in Mineralogy and Geochemistry Vol. 54.* pp. 1–30. Mineralogical Society of America, Chantilly Virginia, USA, **2003**.

(3) Kolinko, I., Lohbe, A., Borg, S., Raschdorf, O., Jogler, C., Tu, Q., Postal, M., Tompa, E., Plitzko, J.M., Brachmann, A., Wanner, G., Muller, R., Zhang, Y., Schuler, D. Biosynthesis of magnetic nanostructures in a foreign organism by transfer of bacterial magnetosome gene clusters. *Nat. Nanotech.*, **2014**, *9*, 193-197.

(4) Gorby, Y.A., Beveridge, T.J., Blakemore, R.P. Characterization of the bacterial magnetosome membrane. *J. Bacteriol.*, **1988**, *170*, 834-841.

(5) Delvigne, C., Opfergelt, S., Cardinal, D., Delvaux, B., Andre, L. Distinct silicon and germanium pathways in the soil-plant system: Evidence from banana and horsetail. *J. Geophys. Res.*, **2009**, *114*, doi:10.1029/2008JG000899.

(6) Wickramasinghe, D.B. and Rowell, D.L. The release of silicon from amorphous silica and rice straw in Sri Lankan soils. *Biol. Fertil. Soils.*, **2006**, *42*, 231-240.

(7) Simkiss, K. and Wilbur, K. *Biomineralization. Cell Biology and Mineral Deposition.* Academic Press, Inc., San Diego, **1989**.

(8) Zhao, J., Liu, Y., Sun, W.-B., Yang, X. First detection, characterization, and application of amorphous calcium phosphate in dentistry. *J. Dent. Res.*, **2012**, *7*, 316-322.

(9) Berkovitz, B.K.B., Boyde, A., Frank, R.M., Hohling, H.J., Moxham, B.J.,

Nalbandian, J., Tonge, C.H. *Handbook of Microscopic Anatomy, Volume V/6: Teeth.* Springer-Verlag, Berlin Heidelberg, **1989**.

(10) Johnston, C.W., Wyatt, M.A., Li, X., Ibrahim, A., Shuster, J., Gordon, S., Magarvey, N.A. Gold Biomineralization by a metallophore from a gold-associated microbe. *Nat. Chem. Biol.*, **2013**, *9*, 241-243.

(11) Young, J.R., Davies, S.A., Bown, P.R., Mann, S. Coccolith ultrastructure and biomineralization. *J. Struct. Biol.*, **1999**, *126*, 195-215.

(12) Simkiss, K., Wilbur, K. *Biomineralization. Cell Biology and Mineral Deposition.* Acad. Press Inc., San Diego, USA, **1989**.

(13) Wu, S., Yin, S., Cao, H., Lu, Y., Yin, J., Li, B. Glucosan controlled biomineralization of $SrCO_3$ complex nanostructures with superhydrophobicity and adsorption properties. *J. Mater. Chem.*, **2011**, *21*, 8734-8741.

(14) Brutchey, R.L., Morse, D.E. Silicatein and the Translation of its Molecular Mechanism of Biosilicification into Low Temperature Nanomaterials Synthesis. *Chem. Rev.*, **2008**, *108*, 4915-4934.

(15) Sunagawa, I. *Crystals Growth, Morphology and Perfection*, Cambridge University Press, U.K., **2005**.

(16) 佐藤清隆編　結晶成長のダイナミクス　6 巻: 溶液からの結晶成長　共立出版株式会社、**2002**.

(17) Gago-Duport, L., Briones, M.J.I., Rodriguez, J.B., Covelo, B. Amorphous calcium carbonate biomineralization in the earthworm’s calciferous gland: Pathways to the formation of crystalline phases. *J. Struct. Biol.*, **2008**, *162*, 422-435.

(18) Goffredo, S., Caroselli, E., Mezzo, F., Laiolo, L., Vergni, P., Pasquini, L., Levy, O., Zaccanti, F., Tribollet, A., Dubinsky, Z., Falini, G. The puzzling presence of calcite in

skeletons of modern solitary corals from the Mediterranean Sea. *Geochim. Cosmochim. Acta*, **2012**, *85*, 187-199.

(19) Kozawa, Y., Yokota, R., Chisaka, H., Yamamoto, H., Suzuki, K., Elsey, R.M. Evagination and Invagination of the Oral Epithelium during Tooth Development in Alligator Mississippiensis. *Int. Symp. Maxillofacial Oral Regen. Biol.*, **2005**, 170-171.

(20) Beniash, E., Metzler, R.A., Lam, R.S.K., Gilbert, P.U.P.A. Transient amorphous calcium phosphate in forming enamel. *J. Struct. Biol.*, **2009**, *166*, 133-143.

(21) Reeder, R.J., Tang, Y., Schmidt, M.P., Kubista, L.M., Cowan, D.F., Phillips, B.L. Characterization of Structure in Biogenic Amorphous Calcium Carbonate: Pair Distribution Function and Nuclear Magnetic Resonance Studies of Lobster Gastrolith. *Cryst. Growth Dec.*, **2013**, *13*, 1905-1914.

(22) Young, J.R. and Henriksen, K. *Biomineralization Within Vesicles: The Calcite of Coccoliths*. P.M. Dove, J.J. DeYoreo, and S. Weiner (Eds.), *Biomineralization, Reviews in Mineralogy and Geochemistry Vol. 54*. pp. 189–215. Mineralogical Society of America, Chantilly Virginia, USA., **2003**.

(23) Miake, Y., Shimoda, S., Fukae, M., Aoba, T. Epitaxial overgrowth of apatite crystals on the thin-ribbon precursor at early stages of porcine enamel mineralization. *Calcif. Tissue Int.*, **1993**, *53*, 257-261.

(24) Darwin, C. *The structure and distribution of coral reefs*. Smith, Elder and Co., London, **1842**.

(25) Crawford, S.A., Higgins, M.J., Mulvaney, P., Wetherbee, R. Nanostructure of the diatom frustule as revealed by atomic force and scanning electron microscopy. *J. Phycol.*, **2001**, *37*, 543-554.

(26) Zhang, G., Li, X. Uncovering Aragonite Nanoparticle Self-assembly in Nacre-A

Natural Armor. *Cryst. Growth Des.*, **2012**, *12*, 4306-4310.

(27) Yao, H.-B., Ge, J., Mao, L.-B., Yan, Y.-X., Yu, S.-H. 25th Anniversary Article: Artificial Carbonate Nanocrystals and Layered Structural Nanocomposites Inspired by Nacre: Synthesis, Fabrication and Applications. *Adv. Mater.*, **2014**, *26*, 136-188.

(28) Finnemore, A., Cunha, P., Shean, T., Vignolini, S., Guldin, S., Oyen, M., Steiner, U. Biomimetic layer-by-layer assembly of artificial nacre. Nat. Comm., 2012, 3, 966-970.

(29) Xu, G., Yao, N., Aksay, I.A., Groves, J.T., Biomimetic Synthesis of Macroscopic-Scale Calcium Carbonate Thin Films. Evidence for a Multistep Assembly Process. *J. Am. Chem. Soc.*, **1998**, *120*, 11977-11985.

(30) Zi, J., Dong, B., Zhan, T., Liu, X. *Photonic Structures for Coloration in the Biological World.* X.Y. Liu (Ed.), In *Bioinspiration.* pp. 275–330. Springer, USA, **2012**.

(31) Bennema, P. Analysis of crystal growth models for slightly supersaturated solutions. *J. Cryst. Growth*, **1967**, *1*, 278-286.

(32) Bennema P. Interpretation of the relation between the rate of crystal growth from solution and the relative supersaturation at low supersaturation. *J. Crystal Growth*, **1967**, *1*, 287-292.

(33) Ookawa, A. Chapter 1: Growth of complete crystal. Crystal growth. Syokabo Co., Japan, pp.2-28, **1977**. (in Japanese)

(34) Saito, Y. Chapter 5: Surface kinetics. Crystal growth. Syokabo Co., Japan. pp. 81-90, **2002**. (in Japanese)

(35) Chernov, A.A., Rashkovich, L.N. Spiral crystal growth with nonlinear dependence of step growth rate on supersaturation: the {110} faces of KH_2PO_4 crystals in aqueous solution. *J. Cryst. Growth*, **1987**, *84*, 389-393.

(36) Colfen, H., Antonietti, M. *Mesocrystals and Nonclassical Crystallization.* John

Wiley and Sons Ltd., England, **2008**.

(37) Onuma, K., Ito, A., Tateishi, T. Investigation of a growth unit of hydroxyapatite crystal from the measurements of step kinetics. *J. Cryst. Growth*, **1996**, *167*, 773-776.

(38) Onuma, K., Kanzaki, N., Ito, A., Tateishi, T. Growth Kinetics of the Hydroxyapatite (0001) Face Revealed by Phase Shift Interferometry and Atomic Force Microscopy. *J. Phys. Chem. B*, **1998**, *102*, 7833-7838.

(39) Malkin, A.I., Chernov, A.A., Alexeev, L.V. Growth of dipyramidal face of dislocation-free ADP crystals; free energy of steps. *J. Cryst. Growth*, **1989**, *97*, 765-769.

(40) Maiwa, K., Tsukamoto, K., Sunagawa, I. Activities of spiral growth hillocks on the (111) faces of barium crystals growing in an aqueous solution. *J. Cryst. Growth*, **1990**, *102*, 42-53.

(41) Sazaki, G., Kurihara, K., Miyashita, S., Komatsu, H., Nakada, T. *In situ* observation of the concentration distribution around a lysozyme crystal by two-beam interferometry. *J. Jpn. Asso. Cryst. Growth*, **1996**, *23*, 413-421. (in Japanese)

(42) Brecevic, L., Nielsen, A.E. Solubility of Amorphous Calcium Carbonate, *J. Cryst. Growth*, **1989**, *98*, 504-510.

(43) Addadi, L., Raz, S., Weiner, S. Taking Advantage of Disorder: Amorphous Calcium Carbonate and its Roles in Biomineralization, *Adv. Mater.*, **2003**, *15*, 959-970.

(44) Jiang, J., Gao, M.-R., Xu, T.-F., Yu, S.-H. *Amorphous Calcium Carbonate: Synthesis and Transformation.* X.Y. Liu (Ed.), In *Bioinspiration.* pp. 189–220. Springer, USA, **2012**.

(45) Eanes, E.D., Gillessen, I.H., Posner, A.S. Intermediate states in the precipitation of hydroxyapatite. *Nature*, **1965**, *208*, 365-367.

(46) Posner, A., Betts, F. Synthetic amorphous calcium phosphate and its relation to

bone mineral structure. *Acc. Chem. Res.* **1975**, *8*, 273-281.

(47) Christofferesen, J., Christofferesen, M.R., Kibalczyc, W. Apparent solubilities of two amorphous calcium phosphates and octacalcium phosphate in the temperature range 30-42°C. *J. Cryst. Growth*, **1990**, *105*, 349-354.

(48) Andersen, F.A., Brecevic, L. Infrared Spectra of Amorphous and Crystalline Calcium Carbonate. *Acta Chem. Scand.*, **1991**, *45*, 1018-1024.

(49) Nebel, H., Neumann, M., Mayer, C., Epple, M. On the Structure of Amorphous Calcium Carbonate-A Detailed Study by Solid State NMR Spectroscopy. *Inorg. Chem.*, **2008**, *47*, 7874-7879.

(50) Nelson, D.G.A., McLean, J.D. High-Resolution Electron Microscopy of Octacalcium Phosphate and its Hydrolysis Products. *Calcif. Tiss. Int.*, **1984**, *36*, 219-232.

(51) Rodriguez-Blanco, J.D., Shaw, S., Benning, L.G. The kinetics and mechanisms of amorphous calcium carbonate (ACC) crystallization to calcite, via vaterite, *Nanoscale*, **2010**, *3*, 265-271.

(52) Onuma, K., Oyane, A., Tsutsui, K., Tanaka, K., Treboux, G., Kanzaki, N., Ito, A. Precipitation Kinetics of Hydroxyapatite Revealed by the Continuous-Angle Laser Light Scattering Technique. *J. Phys. Chem. B*, **2000**, *104*, 10563-10568.

(53) Nonoyama, T., Kinoshita, T., Higuchi, M., Nagata, K., Tanaka, M., Sato, S., and Kato, K. Multistep Growth Mechanism of Calcium Phosphate in the Earliest Stage of Morphology-Controlled Biomineralization. *Langmuir*, **2011**, *27*, 7077–7083.

(54) Wang, C.G., Liao, J.W., Gou, B.D., Huang, J., Tang, R.K., Tao, J.H., Zhang, T.L., Wang, K. Crystallization at multiple sites inside particles of amorphous calcium phosphate. *Cryst. Growth Des.*, **2009**, *9*, 2620-2626.

(55) Greenwald, I. The effect of phosphate on the solubility of calcium carbonate and of bicarbonate on the solubility of calcium and magnesium phosphates. *J. Biol. Chem.*, **1945**, *161,* 697-704.

(56) Plummer, L.N., Busenberg, E. The solubilities of calcite, aragonite and vaterite in CO_2-H_2O solutions between 0 and 90°C, and an evaluation of the aqueous model for the system $CaCO_3$-CO_2-H_2O, *Geochim. Cosmochim. Acta*, **1982**, *46*, 1011-1040.

(57) Kraji, D., Brecevic, L. Dissolution kinetics and solubility of calcium carbonate monohydrate, *Colloid and Surf. A*, **1995**, *96*, 287-293.

(58) Sendroy, J.J., Hastings, A.B. Studies of the solubility of calcium salts. III. The solubility of calcium carbonates and tertiary calcium phosphate under various conditions. *J. Biol. Chem.*, **1927**, *71,* 797-846.

(59) Pan, H.-B., Darvell, B.W. Calcium phosphate solubility: the need for re-evaluation. *Cryst. Growth Des.*, **2009**, *9*, 639-645.

(60) Onuma, K., Oyane, A., Kokubo, T., Treboux, G., Kanzaki, N., Ito, A. Nucleation of Calcium Phosphate on 11-Mercaptoundecanoic Acid Self-assembled Monolayer in a Pseudophysiological Solution. *J. Phys. Chem. B*, **2000**, *104*, 11950-11956.

(61) Gower, L.B., Odom, D.J. Deposition of calcium carbonate films by a polymer-induced liquid-precursor (PILP) process. *J. Cryst. Growth*, **2000**, *210*, 719-734.

(62) Habraken, W.J.E.M., Tao, J.T., Brylka, L.J., Friedrich, H., Bertinetti, L., Schenk, S.A., Verch, A., Dmitrovic, V., Bomans, P.H.H., Frederik, P.M., Laven, J., van der Schoot, P., Aichmayer, B., deWith, G., DeYoreo, J.J., Sommerdijk, N.A.J.M. Ion-association complexes unite classical and non-classical theories for the biomimetic nucleation of calcium phosphate. *Nat. Comm.* **2013**, DOI: 10.1038/ncomms2490.

(63) Tribello, G.A., Bruneval, F., Liew, C.C., Parrinello, M. A Molecular Dynamics Study of the Early Stages of Calcium Carbonate Growth. *J. Phys. Chem. B*, **2009**, *113*, 11680-11687.

(64) Du, L.W., Bian, S., Gou, B.D., Jiang, Y., Huang, J., Gao, Y.X., Zhao, Y.D., Wen, W., Zhang, T.L., Wang, K. Structure of Clusters and Formation of Amorphous Calcium Phosphate and Hydroxyapatite: From the Perspective of Coordination Chemistry. *Cryst. Growth Des.*, **2013**, *13*, 3103–3109.

(65) Sugiura, Y., Onuma, K., Kimura, Y., Miura, H., Tsukamoto, K. Morphological Evolution of Precipitates during Transformation of Amorphous Calcium Phosphate into Octacalcium Phosphate in relation to Role of Intermediate Phase. *J. Cryst. Growth*, **2011**, *332*, 58–67.

(66) Kanzaki, N., Treboux, G., Onuma, K., Tsutsumi, S., Ito, A. Calcium Phosphate Clusters, *Biomater.*, **2001**, *22*, 2921-2929.

(67) Treboux, G., Layrolle, P., Kanzaki, N., Onuma, K., Ito, A. Symmetry of Posner's Cluster, *J. Am. Chem. Soc.*, **2000**, *122*, 8323-8324.

(68) Treboux, G., Kanzaki, N., Onuma, K., Ito, A. Energy-preeminent isomer of the $Ca_3(PO_4)_2$ cluster. *J. Phys. Chem. A*, **1999**, *103*, 8118-8120.

(69) Yin, X., Stott, M.J. Biological calcium phosphates and Posner's cluster, *J. Chem. Phys.*, **2003**, *118*, 3717-3723.

(70) Onuma, K., Ito, A. Cluster Growth Model for Hydroxyapatite. *Chem. Mater.*, **1998**, *10*, 3346–3351.

(71) Gebauer, D., Völkel, A., Colfen, H. Stable Prenucleation Calcium Carbonate Clusters, *Science*, **2008**, *322*, 1819-1822.

(72) Gebauer, D., Gunawidjaja, P.N., PeterKo, J.Y., Bacsik, Z., Aziz, B., Liu, L., Hu, Y.,

Bergstrom, L., Tai, C.W., Sham, T.K., Eden, M., Hedin, N. Proto-Calcite and Proto-Vaterite in Amorphous Calcium Carbonates, *Angew. Chem. Int. Ed.*, **2010**, *49*, 8889-8891.

(73) Pouget, E.M., Bomans, P.H.H., Goos, J.A.C.M., Frederik, P.M., deWith, G., Sommerdijk, N.A.J.M. The Initial Stages of Template-Controlled $CaCO_3$ Formation Revealed by Cryo-TEM, *Science*, **2009**, *323*, 1455-1458.

(74) Pouget, E.M., Bomans, P.H.H., Dey, A., Frederik, P.M., deWith, G., Sommerdijk, N.A.J.M. The development of morphology and structure in hexagonal vaterite, *J. Am. Chem. Soc.*, **2010**, *132*, 11560-11565.

(75) Dey, A., Bomans, P.H.H., Muller, F.A., Will, J., Frederick, P.M., deWith, G., and Sommerdijk, N.A.J.M. The Role of Prenucleation Clusters in Surface-Induced Calcium Phosphate Crystallization. *Nat. Mater.*, **2010**, *9*, 1010–1014.

(76) Raiteri, P., Gale, J.D. Water Is the Key to Nonclassical Nucleation of Amorphous Calcium Carbonate, *J. Am. Chem. Soc.*, **2010**, *132*, 17623-17634.

(77) Demichelis, R., Raiteri, P., Gale, J.D., Dovesi, R. A new structural model for disorder in vaterite from first-principles calculations. *CrystEngComm*, **2012**, *14*, 44-47.

(78) Demichelis, R., Raiteri, P., Gale, J.D., Quigley, D., Gebauer, D. Stable prenucleation mineral clusters are liquid-like ionic polymers. *Nat. Comm.*, **2011**, DOI: 10.1038/ncomms1604.

(79) Sohnel, O., Mullen, J.W. Precipitation of Calcium Carbonate, *J. Cryst. Growth*, **1982**, *60*, 239-250.

(80) Wang, S.-S., Picker, A., Colfen, H., Xu, A.-W. Heterostructured Calcium Carbonate Microspheres with Calcite Equatorial Loops and Vaterite Spherical Cores. *Angew. Chem. Int. Ed.*, **2013**, *52*, 6317-6323.

(81) Cusack, M., Freer, A. Biomineralization: Elemental and Organic Influence in Carbonate Systems. *Chem. Rev.*, **2008**, *108*, 4433-4454.

(82) Wang, L., Nancollas, G.H. Calcium Orthophosphates: Crystallization and Dissolution. *Chem. Rev.*, **2008**, *108*, 4628-4669.

(83) de Bruyn, J.R., Goiko, M., Mozaffari, M., Bator, D., Dauphinee, R.L., Liao, Y., Flemming, R.L., Bramble, M.S., Hunter, G.K., Goldberg, H.A. Dynamic Light Scattering Study of Inhibition of Nucleation and Growth of Hydroxyapatite Crystals by Osteopontin. *Plos One*, **2013**, *8*, e56764.

(84) Rieger, J., Frechen, T., Cox, G., Heckmann, W., Schmidt, C., Thieme, J. Precursor structures in the crystallization/precipitation processes of $CaCO_3$ and control of particle formation by polyelectrolytes. *Fara. Dis.*, **2007**, *136*, 265-277.

(85) Xu, A.-W., Ma, Y., Colfen, H. Biomimetic mineralization. *J. Mater. Chem.*, **2007**, *17*, 415-449.

(86) Delgado-Lopez, J.M., Iafisco, M., Rodriguez, I., Tampieri, A., Prat, M., Gomez-Morales, J. Crystallization of bioinspired citrate-functionalized nanoapatite with tailored carbonate content. *Acta Biomater.*, **2012**, *8*, 3491-3499.

(87) Delgado-Lopez, J.M., Frison, R., Cervellino, A., Gomez-Morales, J., Guagliardi, A., Masciocchi, N. Crystal Size, Morphology, and Growth Mechanism in Bio-Inspired Apatite Nanocrystals. *Adv. Funct. Mater.*, **2014**, *24*, 1090-1099.

(88) Albeck, S., Weiner, S., Addadi, L. Polysaccharides of Intracrystalline Glycoproteins Modulate Calcite Crystal Growth In Vitro. *Chem. Eur. J.*, **1996**, *2*, 278-284.

(89) Giuffre, A.J., Hamm, L.M., Han, N., DeYoreo, J.J., Dove, P.M. Polysaccharide chemistry regulates kinetics of calcite nucleation through competition of interfacial energies. *Proc. Nat. Acad. Sci.*, **2012**, *110*, 9261-9266.

(90) Gebauer, D., Colfen, H., Verch, A., Antonietti, M. The Multiple Roles of Additives in $CaCO_3$ Crystallization: A Quantitative Case Study. *Adv. Mater.*, **2009**, *21*, 435-439.

(91) Xu, A.-W., Antonietti, M., Colfen, H., Fang, Y.-P. Uniform Hexagonal Plates of Vaterite $CaCO_3$ Mesocrystals Formed by Biomimetic Mineralization. *Adv. Funct. Mater.*, **2006**, *16*, 903-908.

(92) Kraji, D., Brecevic, L., Nielsen, A.E. Vaterite growth and dissolution in aqueous solution II. Kinetics of dissolution. *J. Cryst. Growth*, **1994**, *143*, 269-276.

(93) Zhang, Z., Xie, Y., Xu, X., Pan, H., Tang, R. Transformation of amorphous calcium carbonate into aragonite. *J. Cryst. Growth*, **2012**, *343*, 62-67.

(94) He, G., Dahl, T., Veis, A., and George, A. Nucleation of Apatite Crystals in vitro by Self-Assembled Dentin Matrix Protein 1. *Nat. Mater.*, **2003**, *2*, 552–558.

(95) Tsuji, T., Oaki, Y., Yoshinari, M., Kato, T., Shiba, K. Motif-programmed artificial proteins mediated nucleation of octacalcium phosphate on titanium substrates. *Chem. Comm.* **2010**, *46*, 6675-6677.

(96) Tsuji, T., Onuma, K., Yamamoto, A., Iijima, M., Shiba, K. Physicochemical properties of artificial proteins that accelerate nucleation of crystalline calcium phosphate. *J. Cryst. Growth* **2011**, *314*, 190-195.

(97) Tsuji, T., Onuma, K., Yamamoto, A., Iijima, M., and Shiba, K. Direct Transformation from Amorphous to Crystalline Calcium Phosphate Facilitated by Motif-Programmed Artificial Proteins. *Proc. Nati. Acad. Sci. USA*, **2008**, *105*, 16866–16870.

(98) Katsifaras, A. and Spanos, N. Effect of inorganic phosphate ions on the spontaneous precipitation of vaterite and on the transformation of vaterite to calcite, *J. Cryst. Growth*, **1999**, *204*, 183-190.

(99) Akiva-Tal, A., Kababya, S., Balazs, Y.S., Glazer, L., Berman, A., Sagi, A., Schmidt, A. *In situ* molecular NMR picture of bioavailable calcium stabilized as amorphous $CaCO_3$ biomineral in crayfish gastroliths, *Pro. Nat. Acad. Sci. USA*, **2011**, *36*, 14763-14768.

(100) Bentov, S., Weil, S., Glazer, L., Sagi, A., Berman, A. Stabilization of amorphous calcium carbonate by phosphate rich organic matrix proteins and by single phosphoamino acids, *J. Struct. Biol.*, **2010**, *171*, 207-215.

(101) Sato, A., Nagasaka, S., Furihata, K., Nagata, S., Arai, I., Saruwatari, K., Kogure, T., Sakuda, S., Nagasawa, H. Glycolytic intermediates induce amorphous calcium carbonate formation in crustaceans, *Nat. Chem. Biol.*, **2011**, *7*, 197-199.

(102) Prenant, M. Les Forms Mineralogiques du Calcaire Chez les Etres Vivants et le Probleme de Leur Determinisme. *Biol. Rev.*, **1927**, *2*, 365-393.

(103) Kitano, Y., Hood, D.W. Calcium Carbonate Crystals Formed from Sea Water by Inorganic Processes. *J. Oceanograph. Soc. Jpn.*, **1962**, *18*, 141-145.

(104) Falini, G., Albeck, S., Weiner, S., Addadi, L. Control of Aragonite or Calcite polymorphism by Mollusk Shell Macromolecules. *Science*, **1996**, *271*, 67-69.

(105) Turekian, K.K., Armstrong, R.L. Magnesium, Strontium, and Barium Concentration and Calcite-Aragonite Ratios of Some Recent Molluscan Shells. *J. Marine Res.*, **1960**, *18*, 133-151.

(106) EdgerHare, P. Amino Acids in the Proteins from Aragonite and Calcite in the Shells of Mytilus californianus. *Science*, **1963**, *139*, 216-217.

(107) Colfen, H., Mann, S. Higher-Order Organization by Mesoscale Self-Assemblyand Transformation of Hybrid Nanostructures. *Angew. Chem. Int. Ed.*, **2003**, *42*, 2350-2365.

(108) Imai, H. Mesocrystals and Their Related Structures as intermediated between

single crystals and polycrystals. *J. Cera. Soc. Jpn.*, **2014**, *122*, 737-747.

(109) Sommerdijk, N.A.J.M., deWith, G. Biomimetic $CaCO_3$ Mineralization using Designer Molecules and Interfaces. *Chem. Rev.*, **2008**, *108*, 4499-4550.

(110) Aoki, S., Sakamoto, K., Yamaguchi, S., Nakajima, A. Syntheses of Octacalcium Phosphate Containing Dicarboxylic Acids and Effects of the Side Groups on the Crystal Growth of Octacalcium Phosphate. *J. Cera. Soc. Jpn.*, **2000**, *108*, 909-914.

(111) Monma, H., Goto, M. Succinate-complexed Octacalcium Phosphate. *Bull. Chem. Soc. Jpn.*, **1983**, *56*, 3843-3844.

(112) Tsai, T.W.T., Chou, F., Tseng, Y., Chan, J.C.C. Solid-state P-31 NMR study of octacalcium phosphate incorporated with succinate. *Phys. Chem. Chem. Phys.*, **2010**, *12*, 6692-6697.

(113) Markovic, M., Fowler, B.O., Brown, W.E. Octacalcium Phosphate Carboxylates. 2. Characterization and Structural Considerations. *Chem. Mater.*, **1993**, *5*, 1406-1416.

(114) Markovic, M. *Octacalcium Phosphate Carboxylates.* Chow, L.C., Eanes, E.D. (Eds.), In *Octacalcium Phosphate, Monographs in Oral Science Vol. 18*. pp. 77-93. Karger, Basel, Switzerland, **2001**.

Division I

Calcium Carbonate Systems

Chapter 2

Formation control of $H_2PO_4^-$ on phase transformation of amorphous calcium carbonate into vaterite or calcite.

2.1. Introduction

In Chapter 1, the general significance and research scheme of biogenic mineral formation with biocompatible molecules on the basis of crystal growth were described. In Chapter 2, as basic knowledge, it was described how $H_2PO_4^-$ affects into calcium carbonate formation kinetics and polymorph formation.

Calcium carbonates are the main component of the hard tissue in non-vertebrates and are found, for example, in shells and coral reefs.[1] They have at least six polymorphs, including calcite, vaterite, aragonite, ACC, and two hydrous phases.[2] They form as a result of metabolism in biological organisms, a process known as "biomineralization". Biomineralization occurs under normal pressure and temperature in an aqueous solution with neutral to weak basic pH, indicating that it is a gentle crystallization process.[1,3] The final products have various morphologies and crystal structures, and control of these variations can be used to generate new functional materials.

When calcium carbonates form under weak base solutions in the absence of phosphate ($H_2PO_4^-$ or HPO_4^{2-}) ions (in weak basic solutions), ACC appears as an initial phase.[1,4-7] The ACC nucleates by accumulation of calcium carbonate clusters and contains many water molecules in aggregate form, so it has a loose inner structure.[4,8-10] Because the ACC is in a rather unstable phase and has the highest solubility among the calcium carbonate polymorphs, it rapidly transforms into vaterite via direct structure reconstruction in solution.[4,8-10]

Vaterite is also in a metastable phase.[2,8,9,11] The higher solubility of vaterite than that of calcite in neutral to weak basic pH solutions results in vaterite dissolution when the calcite nucleates and grows.[12] Phase transformation of vaterite into calcite proceeds via simple dissolution and growth, in contrast to that of ACC into vaterite.[12] Although calcite is the thermodynamically most stable calcium carbonate under biological conditions, it does not always appear in the hard tissue in non-vertebrates suggesting that biomineralization process is to control the appearance of intermediate unstable phases.[1,3]

The appearance and phase transformation of each calcium carbonate phase described above occurs in the absence of $H_2PO_4^-$. However, the body fluids of non-vertebrates contain $H_2PO_4^-$ although the amount is far smaller than that in the body fluids of vertebrates. This $H_2PO_4^-$ plays an essential role in the nucleation and growth of calcium carbonates. Previous investigations have shown that the $H_2PO_4^-$ extends the lifetime of ACC by stabilizing it, which slows down the formation of crystalline calcium carbonates.[13-15] However, this stabilization mechanism is still quantitatively unclear. In high pH conditions, it was revealed that the presence of HPO_4^{2-} in the precipitating solution stabilized the initially formed vaterite, by decreasing markedly the rate of is transformation to calcite.[16] However, there has been still little investigation for the effect of $H_2PO_4^-$ on the appearance of vaterite in pseudo-physicality conditions.

In Chapter 2, the effect of $H_2PO_4^-$ on the phase transformation of ACC into vaterite in pseudo-physicality conditions was investigated. As a result, it was derived an advanced concept for cluster-based phase transformation, and revealed that small amount of $H_2PO_4^-$ could easily control the nucleation and growth process of calcium carbonate polymorphs.

2.2. Experimental Methods

2.2.1. *Preparation of* $H_2PO_4^-$*-containing calcium carbonate solutions.*

All reagents were dissolved into double-pure water with a specific resistance of 18.2 MΩ and total organic contents (TOC) of them was below 5 ppb. First, four mother solutions were prepared: 1 M of $CaCl_2$ (Wako Pure Chem Co.), 2 M of Na_2CO_3 (Wako Pure Chem Co.), 25 mM of NaCl (Wako Pure Chem Inc.) and KH_2PO_4 (Nakarai Tesque Inc.), and 62.5 mM of tris(hydroxymethyl)aminomethane (Tris: Nakarai Tesque Inc.). The pH of the Tris solution was adjusted to 8.0 using HCl.

Then, two stock solutions (A and B) were prepared. Solution A was made by adding 0.5 mL of $CaCl_2$ solution and 40 mL of Tris solution to 9 mL of H_2O. Solution B was made by mixing 0.25 mL of Na_2CO_3 with various volumes of NaCl and KH_2PO_4. The volume of KH_2PO_4 in solution B ranged from 0 to 0.25 mL and that of NaCl was added so that the ionic strength of the solution was 0.055 $[M/L]^2$.

Supersaturated calcium carbonate solutions were prepared by mixing A and B solutions at a volume ratio of 99:1 using magnetic stirrer at 400-600 rpm. The ionic concentrations in the final solutions were 10 mM of Ca^{2+} and CO_3^{2-} ions, 0-125 μM of $H_2PO_4^-$, and 50 mM of Tris. The pH of the final solutions was at 8.2-8.3. All measurements were performed at room temperature (around 25°C). All experimental were done in glass beakers by using magnetic stirrer at ranging 400-600 rpm. To avoid vaporize from solution surface, the top of beakers was wrapped. Any supplements like Ca electrode and micropipette were put in slit between wrap and glass beaker. There were small headspaces between solution surface and wrap which range was about 1 cm.

2.2.2. Ca^{2+} *ion concentration and pH value as a guide for calcium carbonate*

crystallization.

The change in the Ca^{2+} ion concentration of each solution over time was measured using a Ca^{2+} ion electrode (#6583-10C, Horiba Co., Kyoto, Japan) connected to a multi-meter (D-51AC, Horiba Co., Kyoto, Japan) with stirring by using magnetic stirrer at ranging 400-600 rpm. The electrode was soaked in solution A for at least 30 min prior to measurement to stabilize the electrode intensity. Solution B was then added to solution A to start the reaction by using micropipette. The Ca^{2+} ion concentration of the mixed solution was measured every 2 s, and the nucleation time of the material was determined using a concentration-time curve (as described in the Results section).

The change in pH value of each solution over time was measured using a pH electrode (#6636-10D, Horiba Co., Kyoto, Japan) connected to a multi-meter (D-51AC, Horiba Co., Kyoto, Japan) with stirring as same as Ca^{2+} ion monitoring experiment. Other conditions were as same as Ca^{2+} ion monitoring experiment.

2.2.3. *Observation of calcium carbonate precipitates using electron microscopies.*

The calcium carbonate solutions (about 60 μL) were sampled at specific intervals to observe the change in precipitate morphology and to identify the types of polymorphs present during phase transformation. The interval was 3 min or 20 min.

Two processes were used for the electron microscopy observations. In the first one, 2 mL of 99.5% ethanol or 99.5% acetone was added to the sample solution to immediately stop further reaction. Mixed solution was then centrifuged for 1-2 min. After centrifugation, the precipitates were gathered and washed using ethanol or acetone 2 or 3 times and then left to air dry.

In the second process, the sample solution was directly centrifuged for 1-2 min, and the precipitates were immediately soaked in ethanol sherbet for 1 min. They were then placed in a vacuum vessel for more than 5 h to be freeze-dried.

The precipitates were observed using FE-SEM and TEM and characterized them using XRD and SAED. No differences were observed in the precipitate morphology or polymorph type regardless of the process used.

The treated precipitates were placed on a glass slide for FE-SEM (FE-SEM; S-4300, Hitachi Co., Tokyo, Japan settled on Tohoku University and S-4500, Hitachi Co., Tokyo, Japan settled on Waseda University) observation after Pt-Pd coating or on an amorphous carbon film or amorphous carbon holey film for TEM (H-8100, Hitachi, Co., Tokyo, Japan settled on Tohoku University and HF2200, Hitachi, Co., Tokyo, Japan settled on Waseda University) observation. The films were prepared on conventional Cu grids for TEM. The acceleration voltage and current for the FE-SEM observations were 3-5 kV and 10 μA. The acceleration voltage for the TEM observations was 200 kV. SAED patterns were obtained to characterize the materials. In addition to precipitates observation, total PO_4 concentration into calcium carbonate particles was measured by using EDX (EDAX GENESIS 5000, AMETEK Inc., USA, combined with a HF2200 type STEM-HAADF, settled on Waseda University).

XRD (X'Pert-MPD, PW3050, Philips Co., Nederland, wavelength = 0.15406 nm) measurements at an acceleration voltage of 50 kV and current of 50 mA using a Cu target were done to characterize the materials. The measuring 2θ step was 0.02°. The measured 2θ was from 15° to 80°, time per steps were 37.5 s/θ. Entrance slit size was 5 × 10 mm. The samples were prepared by sampling 5-10 mL solutions and then using 99.5% ethanol or 99.5% acetone more than ten times to stop further reaction. After the samples were centrifuged, they were washed using 99.5% ethanol or 99.5% acetone 2 or

3 times and then left to air dry.

2.3. Results

2.3.1. *Change in Ca^{2+} ion concentration and pH value over time for different $H_2PO_4^-$ concentrations in relation to appearance of calcium carbonate polymorphs.*

It was measured the change in the Ca^{2+} ion concentration in the solutions over time for the different amounts of $H_2PO_4^-$. Figure 1a shows the results of five representative $H_2PO_4^-$ concentrations: 0, 3, 10, 20, and 62.5 μM. The Ca^{2+} ion concentration immediately decreased to 3-5 mM as soon as solution B was added to solution A. It then quickly increased to 6-7 mM except for the 62.5 μM solution,. This process was completed within 10 s. The concentration then gradually increased and reached a local equilibrium (seen as a plateau in the figure). The increased rate gradually decreased over time. The time required to reach the maximum Ca^{2+} ion concentration showed a characteristic relationship with the $H_2PO_4^-$ concentration. It took a minimum when the concentration was 3 μM and then increased with the increase of the $H_2PO_4^-$ concentration.

The Ca^{2+} ion concentration decreased after it reached the maximum point and then stabilized at around at 0.3-0.6 mM. The rate of decrease was lower as higher the $H_2PO_4^-$ concentration. This decrease was not observed for the solution containing 62.5 μM of PO_4.

In addition to Ca^{2+} ion monitoring, it was monitored pH value change with $CaCO_3$ polymorphs forming in the different amount of $H_2PO_4^-$-containing solutions. Four systems were chosed, mainly vaterite formed system ($H_2PO_4^-$ free), both of calcite and vaterite formed system ($H_2PO_4^-$ 10 μM), mainly calcite formed system ($H_2PO_4^-$ 20 μM) and no crystalline system ($H_2PO_4^-$ 62.5 μM) as Fig. 1d.

The precipitates that formed during the plateau interval (before t_{cryst}, the details of t_{cryst} was described below.) were observed using SEM and TEM. The sample solutions contained spherical particles ranging in the size from 10 to 100 nm (Fig. 1b). The SAED pattern for a particle in Fig. 1c shows a halo without any remarkable Debye rings, indicating that the particles were ACC. The formation of ACC particles was observed for all solutions regardless of the $H_2PO_4^-$ concentration. Using STEM-HAADF/EDX, PO_4 from ACC particles were detected. Actually, ACC particles were including some quantum PO_4. For examples, in $H_2PO_4^-$ 20 μM system, atomic ratio of Ca/PO_4 was around 15/1. However, it was impossible to acquire atomic spectrum mapping because PO_4 rate was too low. PO_4 was ranging partially rather than uniformly in ACC particles. As described in the following sections, crystalline phases (vaterite and calcite) subsequently formed after ACC was observed in the solution. It was defined the point at which the Ca^{2+} ion concentration is maximum as the point at which crystalline calcium carbonates start to grow via phase transformation of ACC. This crystallization threshold point was defined as t_{cryst}.

Fig. 1e shows the relationship between t_{cryst} and the $H_2PO_4^-$ concentration. For the solutions containing less than 5 μM PO_4, t_{cryst} decreased with an increase in the $H_2PO_4^-$ concentration up to 2-3 μM (where t_{cryst} was minimum about 70 s) and then it increased. The appearance of a minimum point at around 2-3 μM is consistent with the results shown in Fig. 1a. For the solutions containing 5 to 15 μM $H_2PO_4^-$, t_{cryst} was very sensitive to the $H_2PO_4^-$ concentration. An approximate doubling of concentration increased t_{cryst} about 20 times. When the $H_2PO_4^-$ concentration exceeded 15 μM, the feature observed at 0 to 15 μM was repeated. The t_{cryst} was local minimum at 17 μM

$H_2PO_4^-$ and then exponentially increased when the concentration increased more than 20 μM.

For the solutions containing more than 24 μM $H_2PO_4^-$, the Ca^{2+} ion concentration was very stable over the course of the experiment (about 2.5 h), the same as for the solution containing 62.5 μM $H_2PO_4^-$. The only decrease in the concentration was a rapid one immediately after adding solution B to solution A. This made it impossible to determine t_{cryst} for these solutions.

2.3.2. *Time evolution of calcium carbonate precipitates.*

The growth and phase transformation of calcium carbonates over time depended on the $H_2PO_4^-$ concentration.

2.3.2.1. Solutions containing less than 5 μM $H_2PO_4^-$.

Figure 2 shows a time evolution of precipitates in $H_2PO_4^-$ free solution. ACC particles 10-100 nm in size formed immediately after solution preparation (see Fig. 1b). There was no other calcium carbonate phase except ACC until reaching t_{cryst}. After t_{cryst}, spherulites with a bit awkward shape (1-5 μm in length) appeared (Fig. 2a). They were composed of rigid needle-like crystals 0.5-2 μm in length and 10-100 nm in thickness (Fig. 2b, 2d). These crystals were tightly packed and arranged. The crystals were radially elongated from the center of the spherulites. The spherulites grew over time, and their morphology became spherical by 20 min after solution preparation (Fig. 2c). The needle crystals were separated from each other during this period, and grain boundaries formed (Fig. 2d). The amount of ACC particles rapidly decreased when the spherulites were observed at around t_{cryst}.

The spherulites were observed using SAED to characterize the precipitates at the microscopic level. Three Debye rings, although incomplete, were identified in the outer region of spherulites. They nearly corresponded to the (114), (300), and (118) diffractions of vaterite (Fig. 2e). The rings were not observed in the inner region of spherulite due to the thickness of the materials (too thick for an electron beam to penetrate) (Fig. 2f).

Figure 3 shows XRD patterns for spherulites measured at 20 and 120 min after solution preparation. Both patterns were essentially the same: they consisted of a broad peak at around 2θ = 20-35° (peak maximum at around 25°), which is characteristic of ACC. The sharp peaks (black solid circles) corresponded to vaterite, which is almost consistent with the SAED results (Fig. 2e).

The amount of ACC and intensity of broad peak at around 2θ = 20-35° suggests that the vaterite spherulites contained an ACC-resembling structure, probably in their central region. Since the phase transformation of ACC into vaterite is typically direct structure reconstruction, the outer growth region of ACC aggregates is more likely to have transformed into vaterite, leaving an amorphous-like structure in the central region.

Thus, it was concluded that the spherulites were vaterite, and that no other crystalline calcium carbonate polymorphs (calcite or aragonite) formed when the PO_4 concentration was less than 5 μM.

The morphology of the vaterite spherulites (Fig. 2c) did not show any notable change over the course of the experiment (2.5 h).

2.3.2.2. Solutions containing 5 to 15 μM $H_2PO_4^-$.

Figure 4 shows the time evolution of precipitates in solution containing 12 μM $H_2PO_4^-$. ACC spherical particles 10-100 nm in size formed immediately after solution preparation (Fig. 4a), the same as seen when the $H_2PO_4^-$ concentration was less than 5 μM.

Two kinds of precipitates were observed after t_{cryst}: vaterite spherulites and rhombohedral crystals (0.5-5 μm in size, Fig. 4b), the characteristic morphology of calcite crystals. The surface of the crystals was essentially smooth, and the crystals were sometimes coalesced into the vaterite spherulites (Figs. 4b and c).

The amount and size of the calcite crystals increased over time, indicating that transformation of ACC into calcite and subsequent growth proceeded when the solution contained 12 μM $H_2PO_4^-$. The vaterite spherulites also grew over time but the growth rate was less than that of calcite (Fig. 4d). The growth rates of these polymorphs were, calcite was 150-300 nm/h in whole diameter and that of vaterite was about 200 nm/h in whole diameter. Both of polymorphs were no longer growth after 100 min in FE-SEM observation.

Figure 5 shows XRD patterns for precipitates measured at 20 and 120 min after solution preparation. Peaks corresponding to calcite (black solid reverse triangles) and to vaterite (black solid circles) were identified. The intensities of the peaks corresponding to calcite increased over time, indicating that the volume of calcite relative to that of vaterite gradually increased over time. This was also observed when it was compared the volume of both polymorphs in relation to the concentration of $H_2PO_4^-$ at a particular time. Increasing the $H_2PO_4^-$ concentration resulted in an increase in the calcite ratio. However, the absolute volume of vaterite was far larger than that of calcite during the experimental procedure (about 2.5 h) when the $H_2PO_4^-$ concentration was less than 15 μM. The volume ratio between vaterite and calcite in solution containing 15 μM $H_2PO_4^-$ was estimated at around t_{cryst} to be about 5:1.

2.3.2.3. Solutions containing more than 15 μM $H_2PO_4^-$.

Figure 6 shows the time evolution of precipitates in solution containing 20 μM $H_2PO_4^-$. Immediately after solution preparation, ACC particles 10-100 nm in size appeared, as they did when the $H_2PO_4^-$ concentration was less than 15 μM (Fig. 6a). Fig. 6b shows the SAED pattern for vaterite spherulites. After t_{cryst}, vaterite spherulites and rectangular calcite crystals were observed as they were in the solutions containing 5 to 15 μM $H_2PO_4^-$. (Fig. 6e) Fig. 6d shows the SAED pattern for vaterite spherulites. Four Debye rings corresponding to (112), (114), (300), and (118) diffractions were identified. Each ring contained many Laue spots, indicating that the crystallinity of the outer region was high.

Fig. 6e shows that vaterite and calcite coexisted. Their relative volume was the reverse of that for 5 to 15 μM $H_2PO_4^-$ condition. There was a small amount of vaterite spherulites (1-5 μm in diameter) and a large amount of calcite crystals (0.5-5 μm in size). The ratio between these polymorphs was about 1:3, estimated using the solutions at around t_{cryst} (40 min after preparation). Vaterite and calcite continued to coexist at a constant volume ratio up to 80 min.

A characteristic change in the vaterite morphology was observed at around 80 min after solution preparation. Fig. 6f and 6g shows the vaterite spherulite observed at 100 min. The spherulite had holes in the surface and a hollow structure. TEM observation showed an electron beam was able to penetrate the center of spherulites (Fig. 6g), as expected from Fig. 6c. This morphology suggests that the spherulites dissolved first in their center region. The vaterite eventually disappeared: many vaterite casts remained on the surface of the calcite crystals (Fig. 6h).

XRD measurement showed that the ratio of calcite to vaterite increased over time (Fig. 7). XRD patterns measured 120 min after solution preparation showed that the peaks corresponding to vaterite had disappeared and only those corresponding to calcite were evident. SEM and TEM observations and XRD measurements indicated that the dissolution of vaterite and growth of calcite occurred over time. Phase transformation of vaterite into calcite proceeded via a simple dissolution and growth mechanism. Evidence of direct structure-reconstruction-type transformation between these polymorphs was not observed.

When the $H_2PO_4^-$ concentration exceeded 25 μM, precipitation of calcite was not observed. ACC particles that appeared immediately after solution preparation survived the experimental procedure (about 2.5 h). It was summarized as table 1 about evolution of calcium carbonate precipitate polymorphs and morphology in each $H_2PO_4^-$ concentration solutions.

2.4. Discussion

The relationships between t_{cryst}, polymorph type and $H_2PO_4^-$ concentration showed that $H_2PO_4^-$ inhibited vaterite formation because t_{cryst} increased exponentially with the increase of $H_2PO_4^-$ concentration for that ranging from 5 to 15 μM, where vaterite was observed as the major precipitates. The change in t_{cryst} when the $H_2PO_4^-$ concentration was less than 5 μM is discussed later.

Previous investigations of the formation of calcium carbonate polymorphs in the presence of $H_2PO_4^-$ demonstrated that the $H_2PO_4^-$ extends the lifetime of ACC by stabilizing it. However, this investigation demonstrated that the $H_2PO_4^-$ inhibits vaterite formation and does not affect the nucleation and growth of ACC. ACC formed immediately after solution preparation. The change in the Ca^{2+} ion concentration due to the formation of ACC in this initial stage was independent of the $H_2PO_4^-$ concentration, as seen in Fig. 1a.

The change in the formation of calcium carbonate polymorphs with a change in the $H_2PO_4^-$ concentration suggests that $H_2PO_4^-$ affects the phase transformation (from ACC) and growth of polymorphs kinetically and that it does not control the thermo-dynamical stability of each phase. The solubility of each polymorph, at least the solubility ordering, was not affected by the $H_2PO_4^-$ concentration because the polymorph appearance order obeyed the Ostwald's step law, the same as in the absence of any impurities.

So how does $H_2PO_4^-$ control the formation of polymorphs, especially that of vaterite, at the microscopic level? It was assumed that the inhibition mechanism of $H_2PO_4^-$ is related to the growth unit of calcium carbonates, i.e., the species of molecular clusters. Gebauer et al. proposed the prenucleation cluster model for crystalline calcium carbonate growth. By using extended X-ray adsorption fine structure and ultracentrifuge techniques, they showed that clusters 2-4 nm in diameter form even in undersaturated solutions with respect to calcite and vaterite and that ACC contains these clusters as the essential growth unit.[17] The clusters have particular structures corresponding to those of calcium carbonate polymorphs; therefore the ACCs are assumed to have several kinds of local structure in this model such as ACC1 and ACC2. When ACC transforms into calcite or vaterite, as in this study, particular ACCs have rearranged inner structure corresponding to the final crystalline phases. In EDX-STEM-HAADF observation, there were quite a lot of PO_4 in ACC particles. For this reason, it might be thinking that $H_2PO_4^-$ act any affect to ACC component, i.e. cluster selection.

According to this model, there are two possible mechanisms for $H_2PO_4^-$ inhibiting vaterite formation. One is that the $H_2PO_4^-$ inhibits the structure-reconstruction of ACC into vaterite. The other is that $H_2PO_4^-$ simply hinders the formation (growth) of vaterite clusters in the same manner as impurities do. Regardless of the mechanisms, the behavior of $H_2PO_4^-$ should be monotonic; that is its effectiveness should increase with its concentration. However, the change in t_{cryst} when concentration was less than 5 μM is inconsistent with this assumption. The appearance of a minimum t_{cryst} at a $H_2PO_4^-$ concentration of around 2-3 μM requires a modification of the model to explain the effect of $H_2PO_4^-$ on vaterite formation.

Then, it was assumed that there are several candidate clusters corresponding to the vaterite structure: i.e., there are many isomers. Except for the particular-structure clusters that form the vaterite crystals, many minor clusters would be produced and contained in the initial ACC. The stability of these minor clusters would be controlled by the $H_2PO_4^-$ in solution.

The idea that molecular clusters can take many different structures, all corresponding to the local energy minimum form, was established by Treboux et al.[18] and Kanzaki et al.[19] using *ab initio* calculations for calcium phosphate clusters having a $Ca_9(PO_4)_6$ chemical composition, the essential unit of amorphous calcium phosphate and hydroxyapatite. Yan and Scott[20] also referred to the multi-structures in $Ca_9(PO_4)_6$ clusters.

In this work, this suggestion that vaterite clusters also have several isomers is therefore realistic. The $H_2PO_4^-$ would dissociate these minor clusters (or hinder their formation), which increases the concentration of calcium and carbonate ions in solution. A higher concentration of calcium and carbonates ions would inevitably change the chemical equilibrium between ions and clusters corresponding to those forming the vaterite crystal-structure, and the concentration of these clusters would be increased. This naturally leads to a decrease in t_{cryst} of vaterite. It was assumed that competition between acceleration caused by dissociating isomers and inhibition of the transformation of ACC structure into vaterite ones occurred in the solution and that the minimum t_{cryst} appeared.

The $H_2PO_4^-$ similarly affected the calcite formation when its concentration ranged from 15 to 24 μM, the range in which calcite was the major precipitates. The minimum t_{cryst} appeared at around 17 μM, and t_{cryst} increased exponentially when the concentration exceeded 20 μM. This feature is essentially the same as that seen in vaterite formation thus there would be several isomers in calcite clusters. The difference seen in the calcite formation from vaterite one is a decreasing rate at minimum t_{cryst}. The minimum t_{cryst} observed in vaterite formation was approximately 40% of the t_{cryst} at 0 μM $H_2PO_4^-$. In contrast, that in calcite formation was approximately 20% of the t_{cryst} at 15 μM $H_2PO_4^-$. This suggests that there is less variety of isomers in calcite clusters as compared to that in vaterite clusters, or the $H_2PO_4^-$ has less effective to dissociate the isomers in calcite clusters.

2.5. Conclusion

These experiments showed that a small amount of $H_2PO_4^-$ in the weak basic solution system did not extend the lifetime of amorphous calcium carbonate but did inhibit vaterite formation. Inhibition mechanism was not analyzed as long as it was assumed that the cluster forming vaterite crystal structure was unique form when it was produced in solution and was composed in ACC. The idea that vaterite clusters have several isomers could explain the experimental results. This investigation showed that the appearance and stability of calcium carbonate polymorphs is easily controlled by adjusting the $H_2PO_4^-$ concentration.

Table 2.1. Observed calcium carbonate polymorphs and morphological features in each $H_2PO_4^-$-containing solutions during calcium carbonate crystalline mineralization.

pH	pH = 8.0-8.4, room temperature and pressure			
Ionic strength	Ionic strength = 0.137 $[M/L]^2$, Ca^{2+} = 10 mM/L, total CO_3 = 10 mM/L, $H_2PO_4^-$ = 0-125 μM/L			
Mixing method	Stirring at 400-600 rpm using magnetic stirrer			
Drying method	Washing precipitate in ethanol or acetone to remove water, and eventually dried			
	$H_2PO_4^-$ free	$H_2PO_4^-$ 10 μM	$H_2PO_4^-$ 20 μM	$H_2PO_4^-$ 62.5 μM
0 min	ACC spherical particles	ACC spherical particles	ACC spherical particles	ACC spherical particles
10 min	Vaterite spherulite, ACC spherical particles	ACC spherical particles	ACC spherical particles	ACC spherical particles
20 min	Vaterite spherulite, ACC spherical particles	Vaterite spherulite, Calcite rectangular crystal	ACC spherical particles	ACC spherical particles
40 min	Vaterite spherulite, ACC spherical particles	Vaterite spherulite, Calcite rectangular crystal	Vaterite spherulite, Calcite rectangular crystal	ACC spherical particles
60 min	Vaterite spherulite	Vaterite spherulite, Calcite rectangular crystal	Vaterite spherulite, Calcite rectangular crystal	ACC spherical particles
100 min	Vaterite spherulite	Vaterite spherulite, Calcite rectangular crystal	Vaterite halo like structure, Calcite rectangular crystal	ACC spherical particles
120 min	Vaterite spherulite	Vaterite spherulite, Calcite rectangular crystal	Calcite rectangular crystal	ACC spherical particles

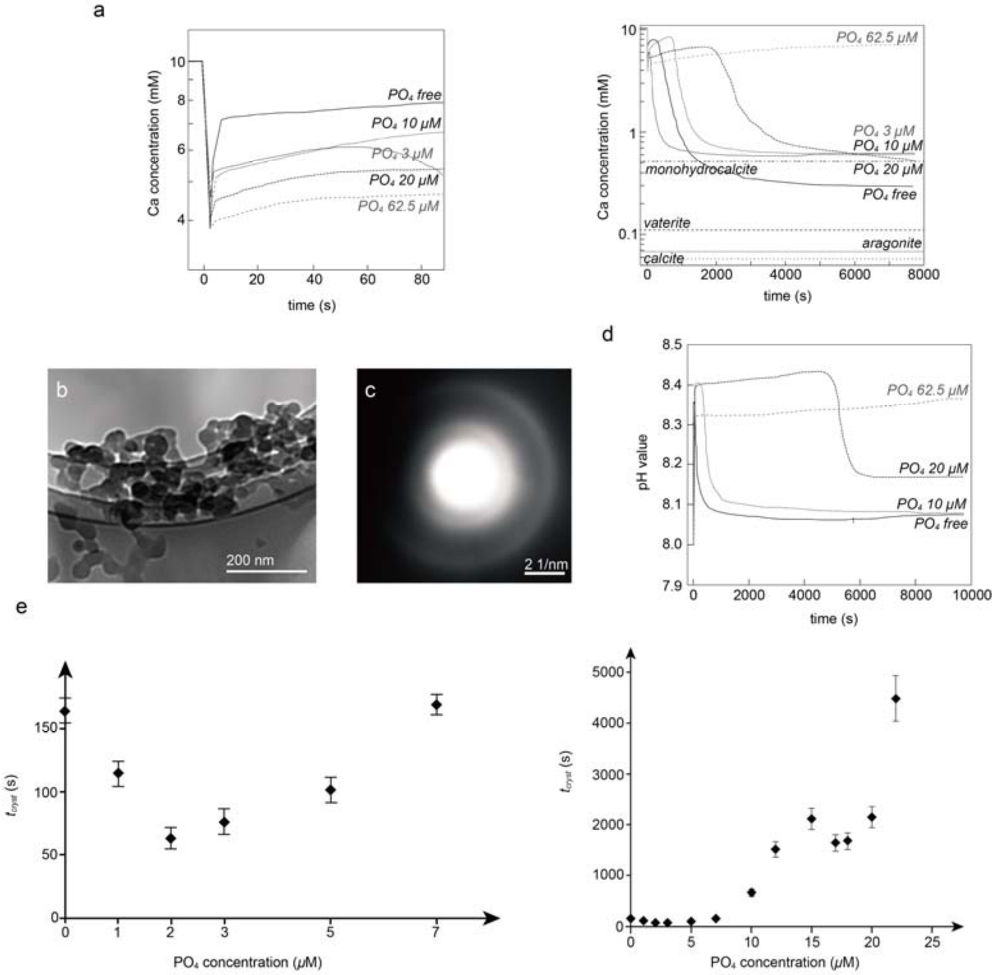

Figure 2.1. Change in Ca^{2+} ion concentration over time as index of calcium carbonate formation. (a) Ca^{2+} ion concentration rapidly dropped immediately after mixing but quickly recovered at initial stage (left graph). It then decreased over time (right graph) and stabilized at around 0.3-0.6 mM, except for 62.5 μM of $H_2PO_4^-$. Solubility lines of calcium carbonate polymorphs were Refs.[11,21] (b) TEM photograph of spherical particles that formed immediately after preparation in $H_2PO_4^-$-free solution. (c) Change in pH value over time as index of calcium carbonate formation. pH value rapidly upped immediately after mixing and stabilized. After that, as crystalline nucleation and growth, pH values were decreasing. (d) SAED pattern corresponding to (b). Particles were ACC as identified by halo region around core and faint broad ring around halo region. (e) Relationship between crystallization threshold point t_{cryst} and $H_2PO_4^-$ concentration: t_{cryst} was minimum at 2-3 μM of $H_2PO_4^-$ (left graph); it then increased exponentially with $H_2PO_4^-$ concentration in the 5 to 15 μM range. Local minimum in t_{cryst} was again observed at 17 μM, and then t_{cryst} increased exponentially above 20 μM (right graph).

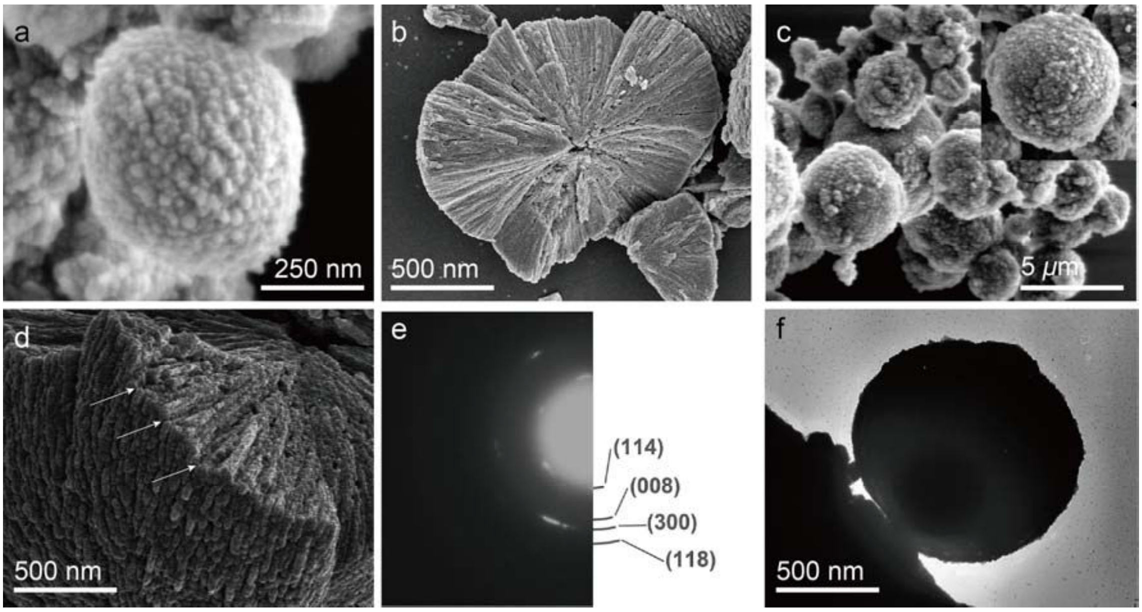

Figure 2.2. Time evolution of precipitates in $H_2PO_4^-$ free solution. (a) SEM photograph of awkward-shape vaterite spherulite observed 10 min after sample preparation. (b) Needle-like crystal in vaterite spherulite observed 20 min after preparation. (c) SEM photograph of vaterite spherulites (sphere shape) observed 20 min after preparation with high magnification image of roundly vaterite spherulite. (d) SEM photograph of edge and inside structure of spherulites. Arrows and white dotted lines showed grain boundaries. (e) SAED pattern corresponding to (b) showing (114), (300), and (118) diffractions of vaterite crystal. (f) TEM photograph of vaterite spherulite observed 120 min after preparation. Center structure was not observed due to thickness.

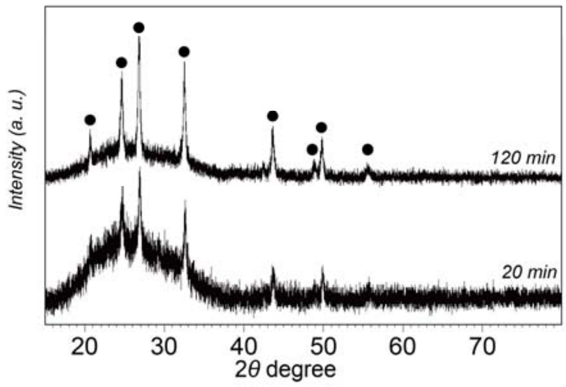

20 min			
2 theta	d spacing	intensity	phase
20.734	4.284	44.3	*V(004)*
24.691	3.606	80.9	*V(110)*
26.875	3.318	100.0	*V(112)*
32.618	2.745	70.3	*V(114)*
42.499	2.127	3.6	*V(008)*
43.682	1.863	23.0	*V(300)*
49.832	1.829	18.0	*V(304)*
55.658	1.651	3.1	*V(224)*

120 min			
2 theta	d spacing	intensity	phase
20.677	4.296	28.7	*V(004)*
24.619	3.616	74.5	*V(110)*
26.799	3.327	100.0	*V(112)*
32.500	2.755	78.9	*V(114)*
42.407	2.131	8.2	*V(008)*
43.889	1.863	32.0	*V(300)*
49.785	1.832	26.2	*V(304)*
55.517	1.655	6.0	*V(224)*

Figure 2.3. XRD pattern of precipitates in $H_2PO_4^-$ free solution measured at 20 and 120 min after preparation. Peaks corresponding to ACC and vaterite (black solid circle) are evident. Table shows crystalline peaks which were corresponding to vaterite (*grey V(hkl)*) d-spacing, intensity and 2 θ.

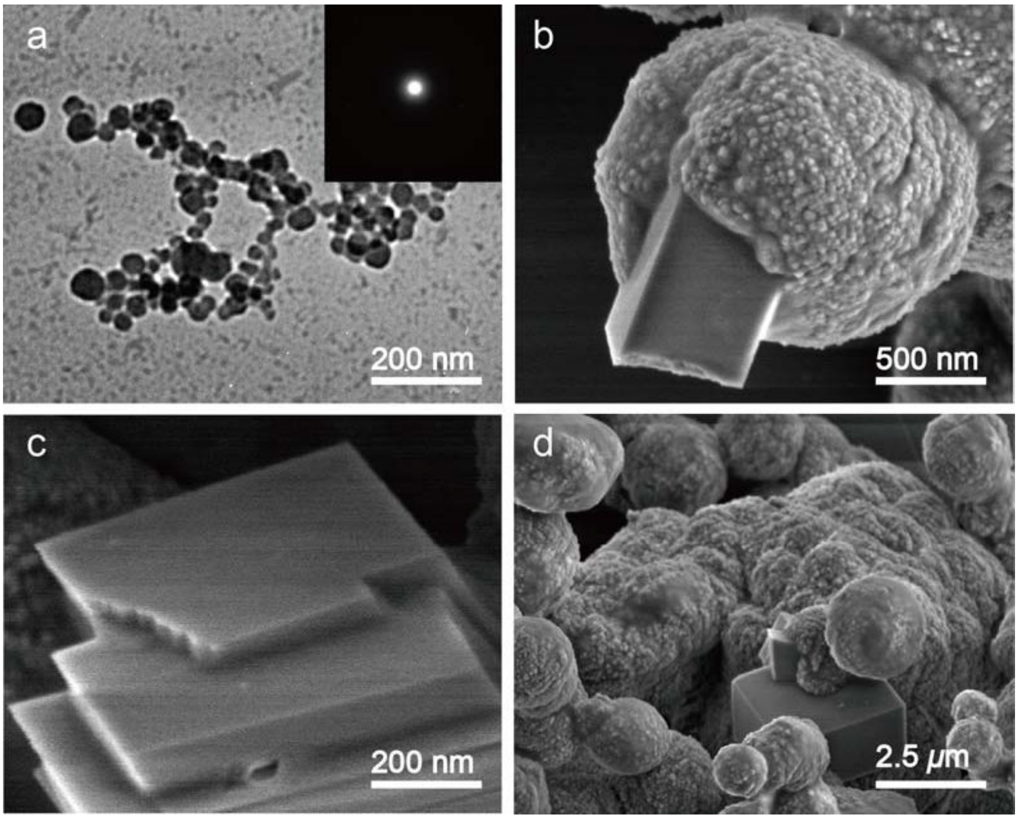

Figure 2.4. Time evolution of precipitates in solution containing 12 μM $H_2PO_4^-$. (a) TEM photograph of ACC spherical particles that formed immediately after preparation. SAED pattern (inset at upper right) showed halo region around core and faint broad ring around halo region. (b) SEM photograph of rectangular calcite crystal and vaterite spherulite 20 min after preparation. Calcite crystal had coalesced into vaterite spherulite. (c) SEM photograph of calcite crystal 20 min after preparation. Surface was essentially smooth indicating that $H_2PO_4^-$ did not have adsorbed on the surface as an inhibitor. (d) SEM photograph showing coexistence of vaterite spherulites with calcite crystals 120 min after preparation. Both vaterite and calcite had continued to grow.

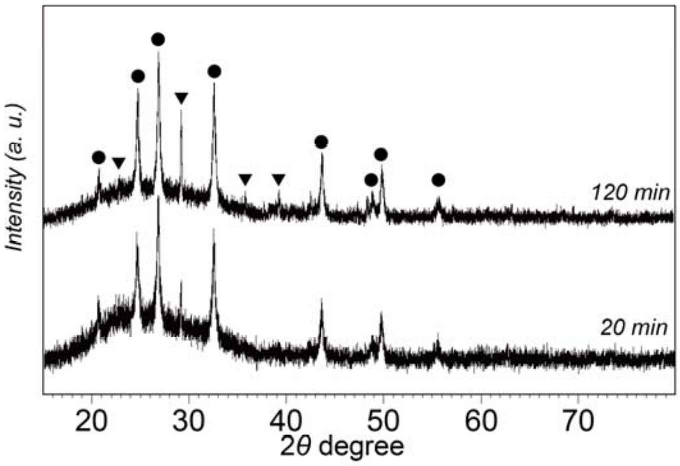

20 min			
2 theta	d spacing	intensity	phase
20.631	4.305	38.3	*V(004)*
24.603	3.618	76.6	*V(110)*
26.771	3.330	100	*V(112)*
29.105	3.068	44.9	**C(104)**
32.487	2.756	74.5	*V(114)*
39.140	2.301	5.9	**C(113)**
42.877	2.109	5.9	**C(202)**
43.617	2.075	29.7	*V(300)*
48.809	1.866	9.58	**C(116)**
49.728	1.834	25.2	*V(304)*
55.572	1.654	6.3	*V(224)*
69.225	1.357	4.7	*V(228)*

120 min			
2 theta	d spacing	intensity	phase
20.777	4.275	18.8	*V(004)*
22.869	3.889	24.0	**C(012)**
24.771	3.594	79.2	*V(110)*
26.903	3.314	100.0	**C(104)**
29.233	3.055	59.4	**C(104)**
32.644	2.743	77.1	*V(114)*
35.912	2.501	6.3	**C(110)**
39.251	2.295	16.7	**C(113)**
42.507	2.127	8.3	**C(018)**
43.717	2.071	38.5	*V(300)*
49.899	1.828	22.9	*V(304)*
55.600	1.651	7.9	*V(224)*

Figure 2.5. XRD patterns for precipitates in solution containing 12 μM $H_2PO_4^-$ at 20 and 120 min after preparation. Peaks corresponding to ACC, vaterite (black solid circle) and calcite (black solid reverse triangle) are evident. The calcite/vaterite ratio increased over time. Table shows crystalline peaks which were corresponding to vaterite (*grey V(hkl)*) and calcite (black C(hkl)) d-spacing, intensity and 2*θ*.

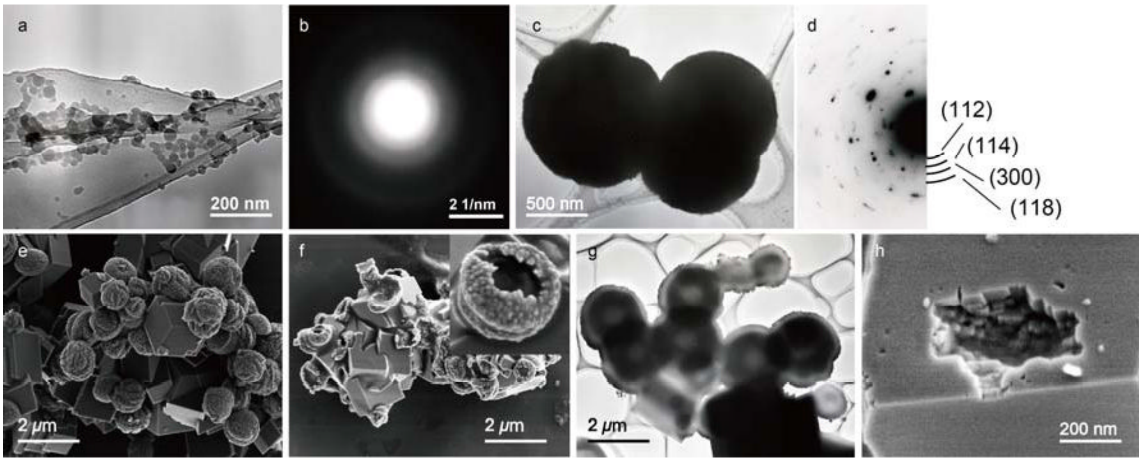

Figure 2.6. Time evolution of precipitates in solution containing 20 μM $H_2PO_4^-$. (a) TEM photograph of ACC spherical particles immediately after preparation. (b) SAED pattern corresponding to (a) with scale bar. (c) TEM photograph of vaterite spherulites observed 40 min after preparation. (d) SAED pattern corresponding to (c). Diffraction indexes coincided with those of vaterite. Vaterite center was too thick for electron beam to penetrate. (e) SEM photograph of calcite rectangular crystals coexisting with vaterite spherulites 40 min after preparation. (f) SEM photograph of calcite rectangular crystals coexisting with hollow vaterite spherulites 100 min after preparation. Core of vaterite spherulites had vanished so that only outer shell remained. (g) TEM photograph of vaterite spherulites. Note that electron beam was able to penetrate center region of spherulites. (h) SEM photograph of calcite crystal 120 min after preparation. Cast where vaterite dissolved and disappeared is evident.

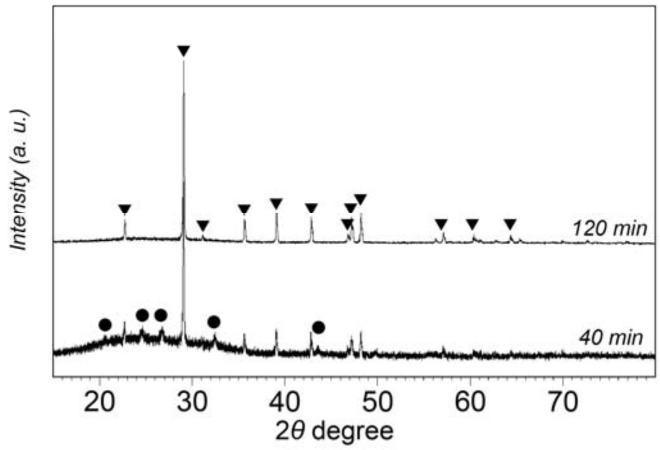

40 min			
2 theta	d spacing	intensity	phase
20.634	4.304	9.1	*V(004)*
22.725	3.913	18.2	**C(012)**
24.586	3.621	13.6	*V(110)*
26.754	3.332	15.1	*V(112)*
29.069	3.072	100.0	**C(104)**
32.465	2.758	11.0	*V(114)*
35.615	2.521	11.7	**C(110)**
39.086	2.305	14.5	**C(113)**
42.823	2.110	13.2	**C(202)**
47.189	1.924	9.8	**C(018)**
48.186	1.887	10.5	**C(116)**
57.080	1.612	4.2	**C(122)**
64.335	1.447	1.7	**C(300)**

120min			
2 theta	d spaceing	intensity	phase
22.756	3.908	11.1	**C(012)**
29.099	3.069	100.0	**C(104)**
35.673	2.517	11.5	**C(110)**
39.112	2.303	15.4	**C(113)**
42.856	2.110	12.6	**C(202)**
47.213	1.925	13.4	**C(018)**
48.212	1.888	15.3	**C(116)**
57.119	1.613	5.7	**C(122)**
60.392	1.533	3.9	**C(214)**
64.384	1.447	4.0	**C(300)**

Figure 2.7. XRD patterns for precipitates in solution containing 20 µM $H_2PO_4^-$ at 40 and 120 min after preparation. Peaks corresponding to ACC, vaterite (black solid circle) and calcite (black solid reverse triangle) are evident for 40 min while only the peaks corresponding to calcite are evident for 140 min. Table shows crystalline peaks which were corresponding to vaterite (*grey V(hkl)*) and calcite (black C(hkl)) d-spacing, intensity and 2 *θ*.

References

(1) Mann, S. *Biomineralization Principles and Concepts in Bioinorganic Materials Chemistry*, Oxford University Press, UK. **2001.**

(2) Ogino, T., Suzuki, T., Sawada, K. The formation and transformation mechanism of calcium carbonate in water. *Geochim. Cosmochim. Acta*, **1987**, *51*, 2757-2767.

(3) Weiner, S. Dove, P.M. *An Overview of Biomineralization Process and the Problem of the Vital Effect.* In *Biomineralization*, *Reviews in Mineralogy and Geochemistry*; Dove, P.M., DeYoreo, J.J., Weiner, S., Eds.; The Mineralogical Society of America: Washington, DC, Vol. 54, p. 1-29. **2003.**

(4) Brecevic, L., Nielsen, A.E. Solubility of Amorphous Calcium Carbonate, *J. Cryst. Growth*, **1989**, *98*, 504-510.

(5) Gebauer, D., Gunawidjaja, P.N., PeterKo, J.Y., Bacsik, Z., Aziz, B., Liu, L., Hu, Y., Bergstrom, L., Tai, C.W., Sham, T.K., Eden, M., Hedin, N. Proto-Calcite and Proto-Vaterite in Amorphous Calcium Carbonates, *Angew. Chem. Int. Ed.*, **2010**, *49*, 8889-8891.

(6) Sohnel, O., Mullen, J.W. Precipitation of Calcium Carbonate, *J. Cryst. Growth*, **1982**, *60*, 239-250.

(7) Addadi, L., Raz, S., Weiner, S. Taking Advantage of Disorder: Amorphous Calcium Carbonate and its Roles in Biomineralization, *Adv. Mater.*, **2003**, *15*, 959-970.

(8) Pouget, E.M., Bomans, P.H.H., Goos, J.A.C.M., Frederik, P.M., deWith, G., Sommerdijk, N.A.J.M. The Initial Stages of Template-Controlled CaCO3 Formation Revealed by Cryo-TEM, *Science*, **2009**, *323*, 1455-1458.

(9) Pouget, E.M., Bomans, P.H.H., Dey, A., Frederik, P.M., deWith, G., Sommerdijk, N.A.J.M. The development of morphology and structure in hexagonal vaterite, *J. Am.*

Chem. Soc., **2010**, *132*, 11560-11565.

(10) Raiteri, P., Gale, J.D. Water Is the Key to Nonclassical Nucleation of Amorphous Calcium Carbonate, *J. Am. Chem. Soc.*, **2010**, *132*, 17623-17634.

(11) Plummer, L.N., Busenberg, E. The solubilities of calcite, aragonite and vaterite in CO_2-H_2O solutions between 0 and 90°C, and an evaluation of the aqueous model for the system $CaCO_3$-CO_2-H_2O, *Geochim. Cosmochim. Acta*, **1982**, *46*, 1011-1040.

(12) Rodriguez-Blanco, J.D., Shaw, S., Benning, L.G. The kinetics and mechanisms of amorphous calcium carbonate (ACC) crystallization to calcite, via vaterite, *Nanoscale*, **2010**, *3*, 265-271.

(13) Akiva-Tal, A., Kababya, S., Balazs, Y.S., Glazer, L., Berman, A., Sagi, A., Schmidt, A. In situ molecular NMR picture of bioavailable calcium stabilized as amorphous $CaCO_3$ biomineral in crayfish gastroliths, *Pro. Nat. Acad. Sci. USA*, **2011**, *36*, 14763-14768.

(14) Bentov, S., Weil, S., Glazer, L., Sagi, A., Berman, A. Stabilization of amorphous calcium carbonate by phosphate rich organic matrix proteins and by single phosphoamino acids, *J. Struct. Biol.*, **2010**, *171*, 207-215.

(15) Sato, A., Nagasaka, S., Furihata, K., Nagata, S., Arai, I., Saruwatari, K., Kogure, T., Sakuda, S., Nagasawa, H. Glycolytic intermediates induce amorphous calcium carbonate formation in crustaceans, *Nat. Chem. Biol.*, **2011**, *7*, 197-199.

(16) Katsifaras, A. and Spanos, N. Effect of inorganic phosphate ions on the spontaneous precipitation of vaterite and on the transformation of vaterite to calcite, *J. Cryst. Growth*, **1999**, *204*, 183-190.

(17) Gebauer, D., Völkel, A., Colfen, H. Stable Prenucleation Calcium Carbonate Clusters, *Science*, **2008**, *322*, 1819-1822.

(18) Kanzaki, N., Treboux, G., Onuma, K., Tsutsumi, S., Ito, A. Calcium Phosphate Clusters, *Biomater.*, **2001**, *22*, 2921-2929.

(19) Treboux, G., Layrolle, P., Kanzaki, N., Onuma, K., Ito, A. Symmetry of Posner's Cluster, *J. Am. Chem. Soc.*, **2000**, *122*, 8323-8324.

(20) Yin, X., Stott, M.J. Biological calcium phosphates and Posner's cluster, *J. Chem. Phys.*, **2003**, *118*, 3717-3723.

(21) Kraji, D., Brecevic, L. Dissolution kinetics and solubility of calcium carbonate monohydrate, *Colloid and Surf. A*, **1995**, *96*, 287-293.

Chapter 3

Dissolution behavior and phase characterization of vaterite spherulite with $H_2PO_4^-$.

3.1. Introduction

As described in Chapter 2, vaterite formation was greatly inhibited in $H_2PO_4^-$-containing solutions In addition, when vaterite formed in small amount of $H_2PO_4^-$-containing solutions, vaterite spherulites formed specific hollow structure through partial dissolution process. It was strongly suggested that an unknown intermediate transition phase whose stability was lower than realistic vaterite located at the core part of vaterite spherulites. In Chapter 3, fine phase characterization of unknown intermediate transition phase which located at the core part of vaterite spherulites and *in situ* observation for hollow vaterite structure formation process from $H_2PO_4^-$-containing vaterite spherulites were demonstrated.

Among the various polymorphs of calcium carbonate, vaterite is a metastable phase with greater solubility and lower stability compared to calcite and aragonite.[1,2] When vaterite crystals into aqueous solutions, vaterite rapidly converted calcite via dissolution and precipitation process.[3] During the dissolution of vaterite in a biological environment, some of the essential elements, such as phosphate, might affect the physicality and kinetics of vaterite. For instance, Katsifaras and Spanos[4] reported that, under high pH conditions (above 12.0), phosphate inhibits the dissolution of vaterite during a phase transformation process; they compared the XRD intensity of the calcite (104) reflection with that of the vaterite (112) reflection. Under weak basic solutions, Chapter 2 demonstrated that even a small amount of phosphate ($H_2PO_4^-$/Ca is about 1/1000) could inhibit the formation of vaterite. As previously mentioned, $H_2PO_4^-$ is considered to strongly affect the dissolution of vaterite. In addition, the results of some studies have suggested that vaterite spherulites contain more unstable phases, such as amorphous-like phases, at the inner parts than at the outer parts.[5,6]

Herein, it was estimated the dissolution rate of each part of vaterite spherulites under various pseudo-physiological conditions. In a typical analysis, the dissolution rate was determined under various phosphate conditions using *in situ* optical measurements. Phase identification of each part of vaterite spherulites, such as the C/Ca ratio, was analyzed using FE-SEM/EDX and cryo-HR-TEM. Furthermore, the crystallinity of the vaterite was quantitatively analyzed using XRD and SAXS. These studies on the dissolution behavior, C/Ca ratio, and crystal features indicate that the vaterite spherulites are composed of three different regions that are clearly distinguishable at high phosphate concentrations.

3.2. Experimental Method

3.2.1. *Solution Preparation.*

Experimental solutions were prepared as describing Chapter 2. The stock solution was prepared by completely dissolving $CaCl_2$ (Wako Pure Chem Co.), NaCl (Wako Pure Chem Co.), $NaHCO_3$ (Wako Pure Chem Co.), K_2HPO_4 (Nakarai Tesque Inc.), KH_2PO_4 (Nakarai Tesque Inc.), FMN (Iwaki Seiyaku Co.), and Tris in double distilled water to final concentrations of 1 M, 1 M, 0.5 M, 0.5 M, 25 mM, 25 mM, and 125 mM, respectively. The pH of the resulting solution was adjusted to 8.0 by the addition of HCl.

3.2.2. *Measurement of the dissolution rate of vaterite spherulite under various*

$H_2PO_4^-$ concentrations.

3.2.2.1. Protocol for measuring the dissolution rate of vaterite spherulite under various $H_2PO_4^-$ concentrations.

The protocol adopted for this experiment consisted of two steps: (1) the preparation of an *in situ* optical observation system and (2) the preparation of the solution for dissolution.

The *in situ* observation system consisted of an optical observation cell and a solution flow system. Figure 1 schematically illustrates the *in situ* observation system used in this study. The observation cell was composed of a glass slide and polypropylene tubes, which were positioned on the Pyrex glass slide coated with vaterite spherulites. The vaterite spherulites on glass slide were prepared by dipping the glass slide into a solution with a composition of 40 mM $CaCl_2$, 40 mM $NaHCO_3$, and 100 mM Tris for 60 min. The glass slides were subsequently washed repeatedly in 99.5% ethanol and dried. The number of vaterite spherulites on the glass slide was adjusted to approximately 5–10 vaterite spherulites particles in the observation eyesight. The diameter of the vaterite spherulites was approximately 5 µm.

The observation cell was placed on an optical microscope (BX-60, Olympus, Tokyo, Japan) using silicon-gum tubes. The optical microscope was connected to a rotary pumping system, which facilitated the flow of dissolution solution into the observation cell at 2 mL/min. Sequence photographs were taken at 1-min intervals.

The dissolution solution used in this study consisted of 500 mM $NaHCO_3$, 500 mM K_2HPO_4, and 1 M NaCl. The concentration of the solution was adjusted using 5 mM $NaHCO_3$ solution and 0, 20, 50, 100, 200, 500, and 1000 µM K_2HPO_4 solutions. The ionic strength of the solution was adjusted by the addition of 1 M NaCl. The pH of the solution was maintained about 8.6. All experiments were performed in a cleanroom under controlled temperature and pressure conditions of 22 ± 0.5 °C and 1 atm.

In addition to simple dissolution experiments, it was investigated the dissolution behavior of $H_2PO_4^-$-doped vaterite spherulites. Vaterite seeds precipitated onto a glass substrate were sealed into the cell, and supersaturated calcium-carbonate solution containing $H_2PO_4^-$ (2 mM $CaCl_2$, 2 mM $NaHCO_3$, and 0.25 mM KH_2PO_4, pH about 8.6, 25°C) was flowed at 2 mL/min for 2 h to dope $H_2PO_4^-$ into the spherulites. An undersaturated solution (2 mM $NaHCO_3$ and 5 mM NaCl, pH about 8.6, 25°C) was then flowed to dissolve the spherulites. $NaHCO_3$ was added to maintain the solution pH. The undersaturation of the solution with respect to calcium carbonates was 100%.

The length of the spherulites was measured in the three directions that were separated at an angle of 60°. The average of the three lengths was defined as the average diameter of the spherulites. At least 50 spherulites were analyzed under each solution condition. The acquired data were subsequently statistically analyzed.

3.2.2.2. Fluorescence microscopy analysis in phosphate-containing environments, including fluorescence materials (FMN).

The protocol adopted for this experiment is similar to that described in Section 2.2. The solution flow system was connected to a fluorescence optical microscope (Olympus BX-53, Olympus, Tokyo, Japan) equipped with a fluorescence optical filter set (Omega Optical Filter Set XF71, Omega Optical, USA), and the Pyrex glass slide in the observation cell was changed to a Si template.

FMN exhibits an excitation wavelength λ_e of 510 nm and a fluorescence wavelength λ_f of 540 nm. FMN, also known as riboflavin-5′-phosphate, is categorized as a phosphate derivative of vitamin B_2.

The reaction solution used in the flow system consisted of 5 mM $NaHCO_3$, 50 µM $CaCl_2$, and 20 µM FMN. This solution was pumped by a rotary pump into the vaterite observation cell at 2 mL/min for 1 h. Subsequently, the observation cell was pumped with 5 mM $NaHCO_3$ for dissolution.

3.2.3. ***Phase characterization of each part of the vaterite spherulites.***

For XRD and SAXS measurements, the precipitates of vaterite spherulites were prepared by mixing 100 mM of Tris, with 40 mM of $CaCl_2$, $NaHCO_3$, and 0.0 or 0.3 mM of KH_2PO_4, under constant stirring at 400–600 rpm for a reaction period of 10 and 120 min. Prior to the analysis, the resulting precipitates were repeatedly washed in 99.5% ethanol and dried.

The details of XRD and FE-SEM/EDX measurement were described in Chapter 2. The dried precipitates were wrapped in polypropylene film, and the crystallite size distribution was measured using SAXS (R-AXIS combined SAXS holder, Rigaku, Tokyo, Japan, $\lambda = 0.15406$ nm); the instrument was operated at an acceleration voltage of 50 kV and a current of 100 mA using a Cu target. The 2θ step size was 0.01° per 0.5 s for each angle; the entrance-slit size was 5×10 mm^2.

For electron microscopy analysis, the vaterite spherulites which synthesized in 100 mM of Tris, with 40 mM of $CaCl_2$, $NaHCO_3$, and 0.3 mM of KH_2PO_4 were mixed with normal temperature (about 20°C) epoxy resin (Logitech 310, Logitech, Scotland, UK; EpoFix-20, Struers, Sweden) and left undisturbed until completely solidified. Subsequently, ultrathin (about 200-nm) cross-sections were prepared using a microtome and positioned like bridges between the Si template for FE-SEM/EDX. The C/Ca ratios were measured at three different locations: core, middle region, and outer region. For comparison, standard calcium carbonate samples were prepared by mixing CaF_2, $CaCO_3$, and Na_2CO_3 at various ratios and were analyzed using EDX. In this study, 10 standard samples with different C/Ca ratios were prepared to obtain a reference curve for C/Ca ratios between 0.85 and 1.50. The measured C/Ca ratios were normalized using this reference curve.

The prepared ultra-thin (about 200 nm) cross-sections were placed on a Cu micro-grid for TEM analysis. The analysis was performed using both a normal observation holder and a liquid-N_2 cryogenic holder (FE-TEM: Hitachi HF3300s, Hitachi, Tokyo, Japan, cryo-FE-TEM, Tecnai 20, FEI, The Netherlands) at acceleration voltages of 300 kV (FE-TEM) and 200 kV (cryo-FE-TEM). The operating temperature was approximately −170 °C.

The reacted solution was mixed with 100 mM of Tris, 40 mM of $CaCl_2$ and $NaHCO_3$, and 0.3 mM of KH_2PO_4. The solution volume was 300 mL.

Sampled calcium carbonate precipitates (about 20 mL) were at specific intervals to measure the changes in the phosphate concentration in the reaction solution. The sampling times were 10 min, 120 min, and 24 h. The sampled precipitates were centrifuged, washed several times using 99.5% ethanol, and eventually dried. It was adding 1 M HCl to approximately 0.05 g of each sample and completely dissolved the sample. It was subsequently added ultra-pure water to bring the total volume of the sample to 5 mL. It was measured the total PO_4 and Ca^{2+} ions concentrations in the react solution using ICP-AES with Ar gas as the carrier gas (SII 7000, Seiko, Tokyo, Japan). It was also measured the XRD patterns and calculated the ratios of vaterite and calcite according to the formulas of Katsifaras and Spanos[4] for estimating vaterite and calcite ratios on the basis of XRD peak intensities.

3.3. Results

3.3.1. *Dynamics of the vaterite spherulite dissolution process and the dissolution rate as a function of $H_2PO_4^-$ concentration.*

Figures 2a and b show the change in the diameter of the vaterite spherulites upon dissolution under various $H_2PO_4^-$ concentrations. The typical dissolution behavior of the vaterite spherulite is as follows. During the dissolution of vaterite spherulites, the diameter of the particles decreased linearly. Irrespective of the $H_2PO_4^-$ concentration, the dissolution process exhibited two inflection points of the dissolution rate. The first point appeared when approximately 0.1–0.5 μm from the surface of the vaterite spherulite dissolved. Until this point, the dissolution rate was much lower in the outer part than in the inner parts. In fact, the dissolution behavior was non-uniform, with some fragments of the outer part remaining, even after the start of the dissolution of the inner parts. The inner parts exhibited a faster dissolution rate than the outer part. As the diameter of the vaterite spherulites reached approximately 1.5–3 μm, the second inflection point appeared. In addition, the dissolution rate accelerated and the vaterite spherulites could be readily categorized into three parts on this basis: the outermost, intermediate, and core parts. In this study, the three parts of vaterite spherulites were designated as the shell (outermost), mantle (intermediate), and core, as shown in Figure 2d. It was further measured and calculated the dissolution rate of each part (Figure 2c).

With an increase in $H_2PO_4^-$ concentration, the dissolution rates decreased (Figures 2a, b, and c). This trend was observed to be stronger in the shell part than in the inner parts. In a phosphate-free system, the average dissolution rate of the shell was

1.58 nm/s, whereas that in a system with 1 mM PO_4 was observed to be 6.87:1 in dissolution rate compare to $H_2PO_4^-$ free system. In contrast, the dissolution rate of the core part was 4.17:1, whereas that of the mantle was 5.10:1, respectively. Furthermore, in systems with a high concentration of $H_2PO_4^-$ (greater than 200 μM), some of the vaterite spherulites exhibited separation among the shell, mantle, and inner parts prior to the dissolution of the shell. Finally, only the shell part remained in the spherulites, which suggests that the shell parts of the vaterite spherulites exhibited greater $H_2PO_4^-$ response than the inner two parts (mantle and core). During separation of the shell and mantle, it was measured the dissolution rates of both the shell and mantle.

3.3.2. ***Morphological evolution of $H_2PO_4^-$-doped vaterite spherulites during the dissolution process and the relationship to $H_2PO_4^-$.***

It was gained further insight by visualizing the $H_2PO_4^-$ response to dissolution dynamics of each part of the vaterite spherulites. Figures 3a, b, and c show the dissolution behavior of the $H_2PO_4^-$-doped vaterite spherulites. The morphology of $H_2PO_4^-$-doped vaterite spherulites before dissolution (Figure 3a) exhibited a radial structure from the core to the outermost part, without non-sequential points. Alternatively, the morphology of $H_2PO_4^-$-doped vaterite spherulites during dissolution (Figures 3b and c) showed boundary separation and the formation of a hollow structure. This result suggests that the $H_2PO_4^-$ affects the shell part of vaterite spherulites more strongly than the inner parts; that is, $H_2PO_4^-$ essentially affects the surface of the vaterite surface without intruding inside. In contrast, no $H_2PO_4^-$ containing vaterite spherulites maintained a radial structure during dissolution process (Figure 3d, e and f). Figure 4 showed the change of $H_2PO_4^-$-doped vaterite spherulite (Figure 3a-c) and no $H_2PO_4^-$

containing vaterite spherulite (Figure 3d-f) during dissolution process. The phosphate-doped vaterite spherulite was inhibited its dissolution process.

In this study, FMN was used as a marker of phosphate (-PO_4^{2-}). The FMN adsorption of each part of vaterite spherulites was detected by *in situ* analysis. Figures 3g and h show photographs of FMN-doped vaterite spherulites in solution under normal light and florescent light, respectively. As evident in Figure 3h, the core region of the vaterite spherulites is much brighter than the outer parts. In particular, the shell region exhibited relatively less fluorescence.

These results suggest that the shell part of the vaterite spherulites exhibits a strong total PO_4 response to dissolution dynamics and low total phosphate adsorption (Figures 2c, 3h), whereas the inner parts exhibit low total phosphate response to dissolution dynamics and high total phosphate adsorption (Figures 2c, 3h).

3.3.3. *Characterization of each part of vaterite spherulites.*

To individually characterize each part of the vaterite spherulites, adopting optimum experimental conditions that resulted in the precipitation of vaterite spherulites with a hollow structure (Figure 5a), which were specifically selected and subsequently analyzed by electron microscopy. For analysis, it was prepared an ultrathin section for TEM observation. Figure 5b shows the inner structure of a vaterite spherulite, indicating the formation of a hollow structure. The core part consisted of spherical particles with diameters ranging from 50 to 100 nm. These particles were highly aggregated, forming a region of 1–1.5 μm. Surrounding the core region, it was observed closely packed needle-like structures with lengths ranging from 2 to 5 μm and thicknesses of 100–200 nm. The roots of the needle-like structures were directly connected to the core region, without clear delineation of the boundary. The needle-like structures almost reached the outermost part, forming the surface of the vaterite spherulite. The boundary between the mantle and shell parts could not be distinguished clearly.

Figures 5c, d, and e show HR-TEM images of each part of the vaterite spherulites (100 mM of Tris, 40 mM of $CaCl_2$ and $NaHCO_3$, and 0.3 mM of KH_2PO_4). During normal observations, the electron beam significantly affected and collapsed the core part. Therefore, the core part was specifically observed under cryogenic conditions to minimize specimen damage during observation. All parts exhibited lattice fringes, which were identified as the crystalline phases, although the degree of crystallinity varied substantially, especially in the region between the core and shell. In the core part, the lattice fringes showed vaterite (111) and (120) faces. The core contained numerous dislocations, including point defects and blade dislocations, whereas the mantle and shell contained few dislocations compared to the core part (Figures 5d and e). The HR-TEM images revealed minor differences between the mantle and shell parts. However, the FE-SEM/EDX analysis showed substantial differences in the chemical compositions. The C/Ca ratio of the shell part was 1.09 ± 0.08, whereas those of the mantle and core parts were 1.28 ± 0.03 and 1.38 ± 0.02, respectively (**N** = >15). It was also observed vaterite spherulites which formed no PO_4 containing solutions. The behaviors of lattice fringes in each part were similar to vaterite spherulites which formed in PO_4 containing solutions. However, there were small amount of dislocations in core and mantle.

It could not detect P ions in the calcium carbonate precipitates using domain measurement methods such as FE-SEM/EDX and X-ray photoelectron spectroscopy. The total PO_4 concentration in the crystalline calcium carbonate during each time sequence was also measured using ICP-AES. It was attempted to calculate the value of PO_4 in the core and outer parts. The PO_4/Ca ratio was 0.18% in the sample reacted for 10 min, 0.14% in the sample reacted for 120 min, and 0.11% in the sample reacted for 24 h, which was completely phase-transformed into calcite. It was calculated the vaterite-to-calcite ratio to estimate the $H_2PO_4^-$ concentration in the core region and outer part of the vaterite spherulites. The $H_2PO_4^-$ concentrations were 0.23% in the core region and 0.15% in the outer region. It could not be estimated the difference between the $H_2PO_4^-$ concentrations in the core and mantle parts. However, the results of FMN experiments suggested that the core part contained more total PO_4 than the mantle part.

The observations of the samples using HR-TEM resulted in the lattice fringes being fused by the focused electron beam. However, this behavior differed from that of the dislocations, such as point defects and edge dislocations, which appeared in the core and mantle regions. Therefore, these defects (Figures 4c and d) are considered to have originated from the samples and not from the damage induced by the HR-TEM observations.

The electron microscopy, FE-SEM/EDX, and HR-TEM results suggested that the vaterite spherulite consisted of several materials with slightly different physical properties. Although these materials were identified as crystalline vaterite, certain parameters of these materials, such as chemical composition, were observed to differ. When vaterite dissolved under $H_2PO_4^-$-containing conditions, the vaterite spherulites retained their hollow structure.[4] It was hypothesized that the vaterite spherulites were formed radially from the core part and grew toward the shell. As a consequence, the reaction time was relatively short. Also, for the same reason, the sample was confirmed to exhibit physicality close to those of the core part. In addition, it was considered that the shell part can be readily obtained because of its self-induced phase transformation to calcite. It was further substantiated this hypothesis by analyzing four different vaterite samples that were obtained after various reaction durations.

Figure 6a shows the XRD patterns of samples collected at different stages of the reaction. The sample collected after a reaction time of 10 min consisted mostly of the core part, whereas that obtained after a reaction time of 120 min exhibited a hollow structure (Figure 5a). The diffraction peaks of the samples indicated the mixed formation of vaterite and calcite phases. It could not be identified some of the minor peaks, such as the broad peaks at 40.0° and 60.5°, on the basis of the crystal structures of LeBail et al.[7] However, these unidentified peaks were observed among all samples and with approximately the same relative intensities. It was concluded that these peaks were vaterite crystal peaks that originated from crystal dislocations such as microtwinning or from unknown structures. It did not detect a peak shift among any sample.

SAXS analysis revealed that the crystallite size distribution in the sample (100 mM of Tris, 40 mM of $CaCl_2$ and $NaHCO_3$, and 0.3 mM of KH_2PO_4) reacted for 10 min was only a few nanometers. In contrast, the SAXS analysis of the sample reacted for 120 min indicated the presence of particles with a bimodal distribution and a diameter of 10 nm, in addition to particle sizes with a distribution of a few nanometers (Figure 6b). Figure 6c showed the SAXS analysis of vaterite spherulites which formed no $H_2PO_4^-$ containing solution (100 mM of Tris, 40 mM of $CaCl_2$ and $NaHCO_3$) at 10 min and 120 min. The particle distributions of both were bimodal distribution and a diameter was larger than vaterite spherulites which formed in $H_2PO_4^-$ containing solutions.

According to the theory of Ostwald ripening, this theory indicated to the relation between size distribution and stability of crystallite particles. Therefore, it was concluded that the shell part is more stable than the inner parts because the particle size distributions tended toward broad distributions because of the absence of disorder. It was defined the shell part as real vaterite, meaning that its physicality and chemical composition are most similar to crystals among all vaterite spherulites composing the materials. However, the inner parts differed from vaterite with respect to certain parameters such as chemical composition and crystallite distribution and were poorly crystalline because of the variation in the dissolution behavior and rate; thus, hence refer to these parts as a vaterite-like phase.

3.4. Discussion

The present study reveals that $H_2PO_4^-$ ions could stabilize vaterite. The FMN experiments revealed that total PO_4 intruded into the vaterite spherulites and stabilized. These results indicate that after vaterite forms in a biological system, it would not easily dissolve because of the relatively high concentration of $H_2PO_4^-$ ions, which inhibit dissolution. Some fish contain otoliths, which mainly consist of vaterite.[8] Thus, the vaterite crystals that composed otoliths were growing as a consequence of the metabolism of biological beings. The present study suggests that PO_4 ions and $-PO_4$ containing molecules stabilizes these tissues, which consist of metastable or unstable mineral phases. In addition, once vaterite has unexpectedly formed in a biological system, it remains and may lead to diseases such as calculus stones. In fact, calculus stones sometimes consist of vaterite.[9]

As previously mentioned, the physical differences of vaterite spherulites poses several problems, especially in an environment where $H_2PO_4^-$ is present, and hence needs to be resolved for these materials to be used in biomedical engineering applications. When vaterite is formed from solution, it does not precipitate directly but proceeds through some precursor stages. Gebauer et al.[10] proposed prenucleation cluster theory to explain this phenomenon. The calcium and carbonate ions in solution form liquid-like ion pairs, which correspond to the final crystalline phase. Subsequently, the ions randomly aggregate as the ACC through the cluster-based reconstruction process finally resulting in the formation of crystalline phase.[11-15] Here the ACC tends to have an essentially loose structure and is strongly affected by the solution conditions.[11,12] In the present study, vaterite spherulites were precipitated from solution, analogous to the precipitation induced by changing the Ca^{2+} ions concentration. Furthermore, the results suggested that the changes in solution conditions affected the ACC physicality, which induced further changes in the physicality of vaterite.[11,12]

It was further evaluated the dissolution behavior and physicality of vaterite spherulites under conditions where $H_2PO_4^-$ ions were present. Recently, other authors have proposed that the vaterite crystal structure is not a single structure but rather has many polytypes and microtwining.[7,15-17] Using *ab initio* calculations, Demichelis et al.[16] demonstrated the difference in phase stability among the different vaterite crystal structures. A clear understanding of the crystal structure of vaterite is highly essential, especially when they are used as biomaterials. The systematic analyses performed in the present study suggest that the physicality of vaterite are not only decided by its crystal structure but also influenced by factors such as chemical composition and crystallite size distribution, e.g., difference between the core and shell parts of vaterite spherulites. In particular, these effects are highly influential when $H_2PO_4^-$ ions are present, such as in biogenic environments.

3.5. Conclusion

In Chapter 3, it was investigated that the dissolution behavior of vaterite in biogenic environments and observed that the behavior of vaterite corresponds to its crystallographic features. Systematic studies indicated that the vaterite spherulites consist of different chemical compositions and crystalline features. Thus, it was determined that the phase stability of the spherulites by measuring their $H_2PO_4^-$ ion response. The results indicate that the more unstable phase exhibits relatively low $H_2PO_4^-$ ion response with respect to dissolution rate and high $H_2PO_4^-$ ion adsorption. In contrast, the most stable phase exhibits a strong $H_2PO_4^-$ ion response and low $H_2PO_4^-$ ion adsorption. These results suggest that vaterite spherulites consist of vaterite and vaterite-like phases, pseudo-vaterite which it could categorize according to their $H_2PO_4^-$ ion response.

To enable the use of vaterite as a biomaterial, its physicality should be measured and understood. It was first examined the physicality on the basis of the particle size probability trends, as determined by the SAXS analysis. The shell part, which corresponds to the solid part with a low $H_2PO_4^-$ ion response, was observed to contain particles with diameters of 10 nm. It was refer to this portion as real vaterite. The second parameter was determined by EDX measurements, which revealed a chemical composition of shell part approximately equal to that of the theoretical vaterite structure and a C/Ca ratio of 1.00.

Table 3.1. Observed vaterite phases and their dissolution behavior under various $H_2PO_4^-$ concentrations.

	core	mantle	shell
Locating region	Center of vaterite spherulite (0.8 – 1.5 μm)	Between core and shell parts.	Outermost, 0.2 – 1.0 μm thickness.
Dissolution rate	1.38 – 5.71 nm/sec	0.63 – 3.19 nm/sec	0.23 – 1.58 nm/sec
$H_2PO_4^-$ response on dissolution process	Low	Relatively high	High
C/Ca rate from EDX measurement	1.38 ± 0.03	1.28 ± 0.03	1.09 ± 0.09
Crystalline structure from TEM and SAXS analysis	Many dislocations. Mono-modal crystallite distributions	Small dislocations. Mono-modal crystallite distributions	Small dislocations. Bi-modal crystallite distributions.

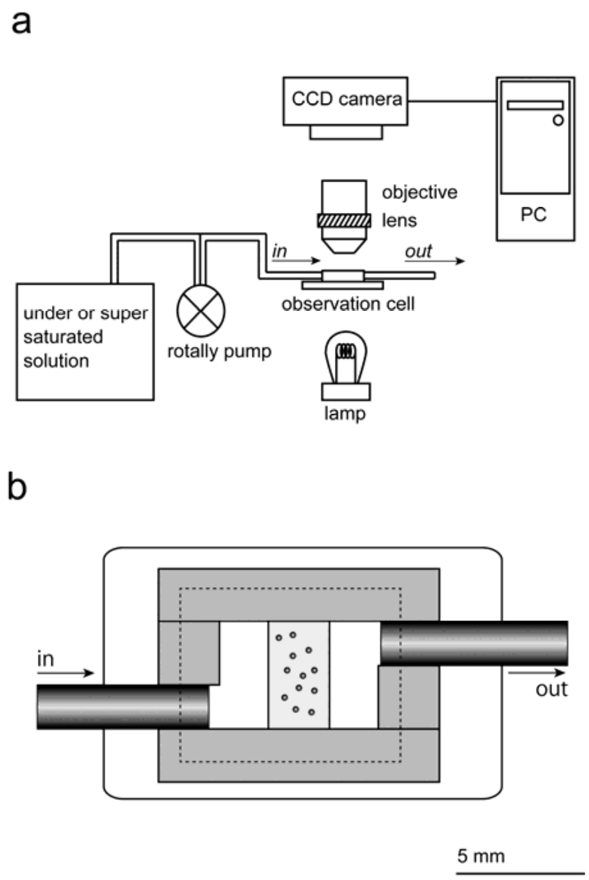

Figure 3.1. Schematic of the *in situ* observation system: (a) overall observation setup and (b) top view of the vaterite-sealed growth cell.

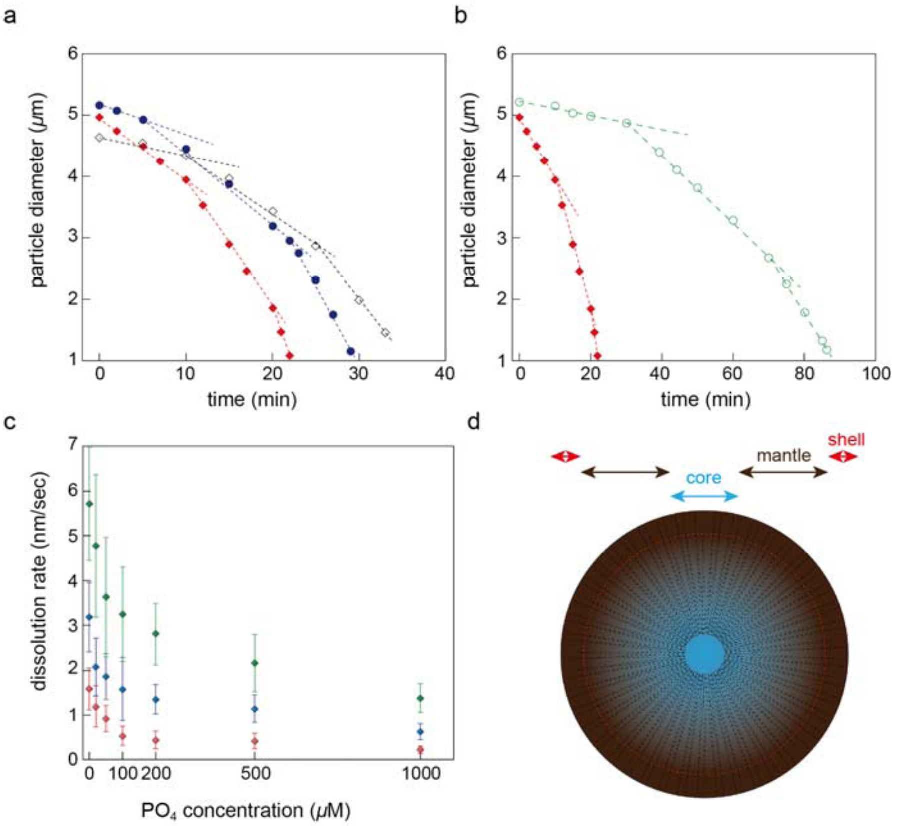

Figure 3.2. The dissolution behavior and rate of vaterite dissolution in solutions with various $H_2PO_4^-$ concentrations. (a) Typical change in the diameter of particles during dissolution of vaterite spherulite under low- $H_2PO_4^-$-concentration conditions; $H_2PO_4^-$-free (red solid squares), 20 µM $H_2PO_4^-$ (dark-blue solid circles), and 50 µM $H_2PO_4^-$ (black open squares). The guided line signifies the two inflection points, which indicate the boundary of shell to the mantle and vice versa. (b) Typical change in particle diameter during dissolution of vaterite spherulites in 1 mM $H_2PO_4^-$ (green open circles). For guidance, the results for $H_2PO_4^-$-free conditions (red solid squares) are also represented. Even under high- $H_2PO_4^-$ concentrations, the dissolution behavior exhibited no significant changes compared with that of the low- $H_2PO_4^-$ system. (c) Dissolution rate vs. $H_2PO_4^-$ concentration of the shell part (red squares), mantle part (blue squares), and core part (green squares). The dissolution rate exponentially decreases with increasing $H_2PO_4^-$ concentration. (d) Schematic illustrating the structures of vaterite spherulites. Vaterite spherulites consist of three parts: shell part, or outermost part, with a thickness of approximately 0.2–1 µm; mantle part, which consists of tightly packed needle-like structures; and core part, which represents the center of spherulites and ranges from 1.5 to 3 µm.

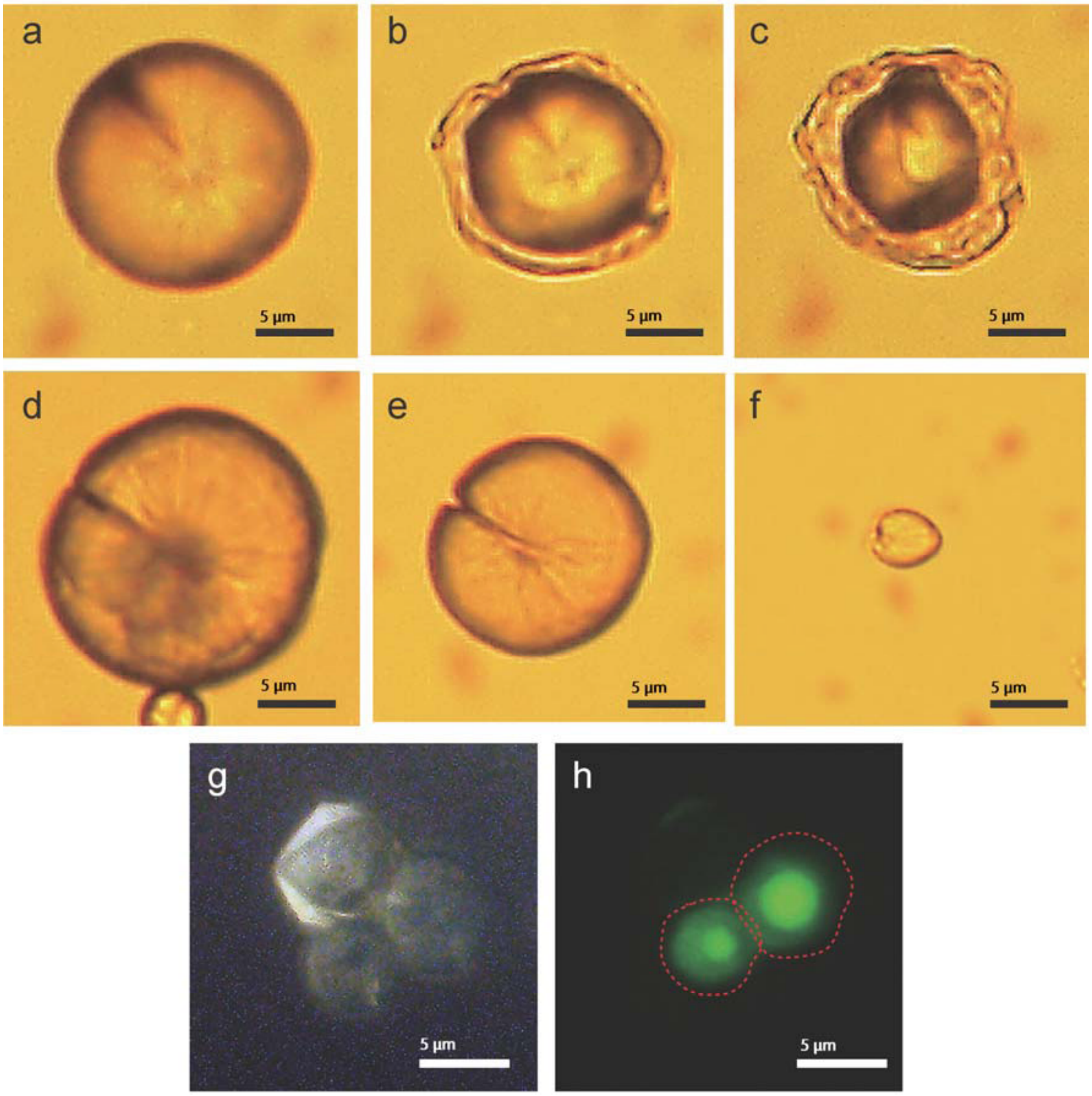

Figure 3.3. Doping $H_2PO_4^-$ altered the vaterite spherulite behavior during the dissolution dynamics. (a, b, and c) Temporal images of the dissolution process of $H_2PO_4^-$-doped vaterite spherulites at (a) 0 min (before dissolution), (b) 30 min, and (c) 60 min. The vaterite spherulites exhibited a hollow structure; the mantle part was dissolved first. (d and e) Photograph of FMN-doped $H_2PO_4^-$-vaterite. Temporal images of the dissolution process of no $H_2PO_4^-$ containing vaterite spherulites (reference) at (d) 0 min (before dissolution), (e) 30 min, and (f) 65 min. (g) Photograph of a normal reflected light image of vaterite spherulites. (h) Photograph of the fluorescence light image of vaterite spherulites. Red broken circles are provided as a guide for the entire scale of vaterite spherulites. The core part was brighter than the other parts. The concentration of FMN was greater in the core part than in the other parts.

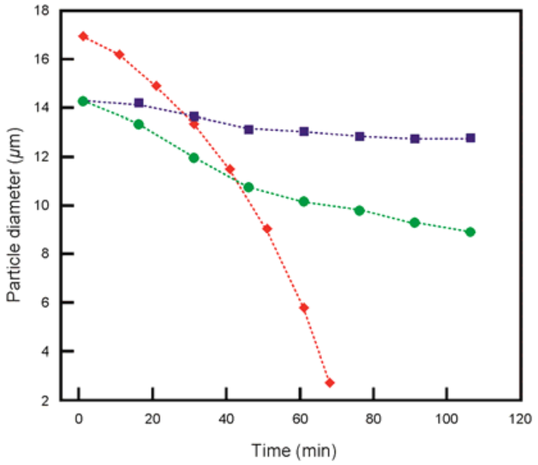

Figure 3.4. Change in the diameter of vaterite spherulites; $H_2PO_4^-$-doped vaterite spherulite (core; green circle, shell; blue square) and no $H_2PO_4^-$ containing vaterite spherulite (red; whole diameter) during dissolution under 5 mM of $NaHCO_3$. $H_2PO_4^-$-doped vaterite spherulite was corresponded to Figure 3(a-c). No $H_2PO_4^-$ containing vaterite spherulite was corresponded to Figure 3(d-f).

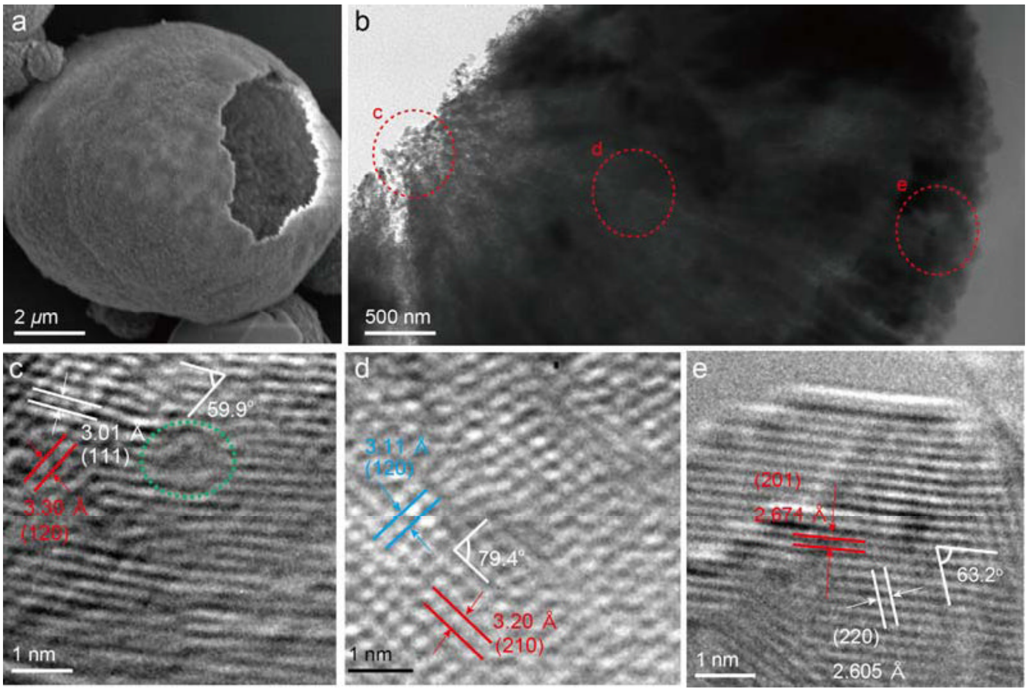

Figure 3.5. Electron microscopy images of vaterite spherulites (100 mM of Tris, 40 mM of $CaCl_2$ and $NaHCO_3$, and 0.3 mM of KH_2PO_4) at 60 min. (a) FE-SEM image showing the hollow structure of a vaterite spherulite. (b) TEM image showing the cross-sectional view of a vaterite spherulite. Red broken circles correspond to each HR-TEM image. (c) Cryo-HR-TEM image of the core part. Lattice fringes corresponding to the *d*-spacings of the (111) and (120) vaterite faces were observed. Several dislocations were observed, as indicated by green circles. (d) Cryo-HR-TEM image of the mantle part. Lattice fringes corresponding to the *d*-spacing of the (120) and (210) of vaterite faces were observed. Several edge dislocations were observed. (e) HR-TEM image of the shell part. Lattice fringes corresponding to the *d*-spacings of the (201) and (220) vaterite faces were observed.

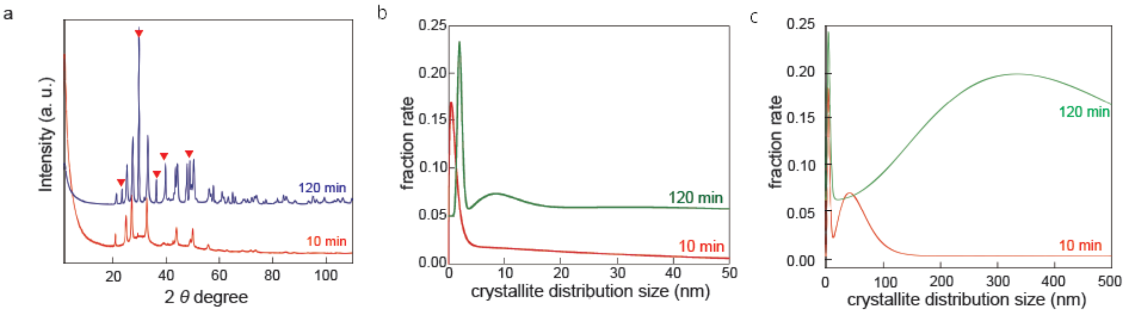

Figure 3.6. X-ray diffraction and scattering analysis of various time periods. (a) XRD pattern of the samples (100 mM of Tris, 40 mM of $CaCl_2$ and $NaHCO_3$, and 0.3 mM of KH_2PO_4). Calcite peaks (red reverse triangles) were observed in the later stages of formation. (b) SAXS analysis of the samples (100 mM of Tris, 40 mM of $CaCl_2$ and $NaHCO_3$, and 0.3 mM of KH_2PO_4). The crystallite distribution of the sample reacted for 10 min exhibited a monomodal trend at approximately 5 nm; however, the crystallite distribution of the sample reacted for 120 min revealed a bimodal trend at approximately 10 nm and a size probability of 5 nm. (c) SAXS analysis of the samples (100 mM of Tris, 40 mM of $CaCl_2$, and $NaHCO_3$) at 10 min and 120 min. Both crystallite distribution of the samples exhibited bimodal trend at 10 nm and 100-300 nm.

Reference

(1) Brecevic, L., Nielsen, A.E. Solubility of Amorphous Calcium Carbonate, *J. Cryst. Growth*, **1989**, *98*, 504-510.

(2) Plummer, L.N., Busenberg, E. The solubilities of calcite, aragonite and vaterite in CO_2-H_2O solutions between 0 and 90°C, and an evaluation of the aqueous model for the system $CaCO_3$-CO_2-H_2O, *Geochim. Cosmochim. Acta*, **1982**, *46*, 1011-1040.

(3) Ogino, T., Suzuki, T., Sawada, K. The formation and transformation mechanism of calcium carbonate in water. *Geochim. Cosmochim. Acta*, **1987**, *57*, 2757-2767.

(4) Katsifaras, A., Spanos, N. Effect of inorganic phosphate ions on the spontaneous precipitation of vaterite and on the transformation of vaterite to calcite, *J. Cryst. Growth*, **1999**, *204*, 183-190.

(5) Zhong, C., Chu, C.C. On the Origin of Amorphous Cores in Biomimetic $CaCO_3$ Spherulites: New Insight into Spherulitic Crystallization. *Cryst. Growth Des.*, **2010**, *10*, 5043-5049.

(6) Suzuki, M., Nagasawa, H., Kogure, T. Synthesis and structure of hollow calcite particles. *Cryst. Growth Des.*, **2006**, *6*, 2004-2006.

(7) LeBail, A., Ouhenia, S., Chateigner, D. Microtwinning hypothesis for a more ordered vaterite model. *Powder Diffr.*, **2011**, *26*, 16-21.

(8) Falini, G., Fermani, S., Vanzo, S., Miletic, M., Zaffino, G. Influence on the Formation of Aragonite or Vaterite by Otolith Macromolecules *Eur. J. Inorg. Chem.*, **2005**, *1*, 162–167.

(9) Sutor, D.J., Wooley, S.E. Gallstone of unusual composition: calcite, aragonite, and vaterite. *Science*, **1968**, *159*, 1113–1114.

(10) Gebauer, D., Völkel, A., and Cölfen, H. Stable Prenucleation Calcium Carbonate

Clusters. *Science*, **2008**, *322*, 1819–1822.

(11) Gebauer, D., Gunawidjaja, P.N., PeterKo, J.Y., Bacsik, Z., Aziz, B., Liu, L., Hu, Y., Bergstrom, L., Tai, C.W., Sham, T.K., Eden, M., Hedin, N. Proto-Calcite and Proto-Vaterite in Amorphous Calcium Carbonates, *Angew. Chem. Int. Ed.*, **2010**, *49*, 8889-8891.

(12) Demichelis, R., Raiteri, P., Gale, J.D., Quigley, D., Gebauer, D. Stable prenucleation mineral clusters are liquid-like ionic polymers. *Nat. Comm.*, **2011**, DOI: 10.1038/ncomms1604.

(13) Rodriguez-Blanco, J.D., Shaw, S., Benning, L.G. The kinetics and mechanisms of amorphous calcium carbonate (ACC) crystallization to calcite, via vaterite, *Nanoscale*, **2010**, *3*, 265-271.

(14) Kanzaki, N., Treboux, G., Onuma, K., Tsutsumi, S., Ito, A. Calcium Phosphate Clusters, *Biomater.*, **2001**, *22*, 2921-2929.

(15) Du, L.W., Bian, S., Gou, B.D., Jiang, Y., Huang, J., Gao, Y.X., Zhao, Y.D., Wen, W., Zhang, T.L., Wang, K. Structure of Clusters and Formation of Amorphous Calcium Phosphate and Hydroxyapatite: From the Perspective of Coordination Chemistry. *Cryst. Growth Des.*, **2013**, *13*, 3103-3109.

(16) Demichelis, R., Raiteri, P., Gale, J.D., Dovesi, R. The Multiple Structures of Vaterite. *Cryst. Growth Des.*, 2013, 13, 2247–2251.

(17) Kabalah-Amitai, L., Mayzel, B., Kauffmann, Y., Fitch, A.N., Bloch, L., Gilbert, P., Pokroy, B. Vaterite Crystals Contain Two Interspersed Crystal Structures. *Science*, **2013**, *340*, 454–457.

Chapter 4

Growth dynamics of vaterite spherulites in the system of $Ca\text{-}CO_3\text{-}H_2PO_4^-$.

4.1. Introduction

As described in Chapters 2 and 3, vaterite spherulites were consisted of at least two phases whose stability was different than each other. An unstable phase called "pseudo-vaterite" formed prior to real vaterite. As a result, the core part of vaterite spherulites was composed of pseudo-vaterite, shell part of that was composed of real vaterite. The difference in their stability was reinforced under $H_2PO_4^-$ containing condition. When they formed or dissolved in $H_2PO_4^-$ containing condition, specific hollow structure was appeared. The dynamics and stability of materials was mainly determined by its surface energy. Thus, in Chapter 4, it was showed that the relationships between surface energy of vaterite and pseudo-vaterite and $H_2PO_4^-$ concentration with related ACC, precursor of calcium carbonate crystalline, dynamics and $H_2PO_4^-$ concentration.

The growth dynamics of calcium carbonate minerals, particularly in simulated biological environments, has been a matter of great research interest in the field of geochemistry and biomineralization.[1-4] Studies in this area may contribute in clarifying complex biological crystallization processes, the origin of life, and biological evolution, and the knowledge gained may be used to generate new functional biomaterials.

Vaterite is an anhydrous crystalline polymorph of calcium carbonate and an intermediate and metastable phase in simulated biological conditions.[1,5-8] It has a higher solubility and a comparatively lower crystallinity than calcite and aragonite.[1,3,5] Although vaterite is an initial crystalline phase in weak basic solution, the growth mechanism of vaterite is unclear compared with those of calcite and aragonite. Olderøy et al.[9] estimated the growth rate of vaterite spherulites in supersaturated solutions. They measured the seeded-vaterite radius *ex situ* and the Ca^{2+} ions concentration as a function of vaterite growth rate. Gomez-Morales et al.[10] and Kawano et al.[11] estimated the surface free energy of vaterite, which is a key parameter in growth, using the incubation time for nucleation in various supersaturated solutions. However, these studies have provided little conclusive information on the growth mechanism of vaterite because there has been a consensus that vaterite crystals do not grow simply by attachment of ionic species in aqueous solutions.[3] Pouget et al.[12] and Gebauer et al.[13] indicated that vaterite is formed via ACC, which is a random aggregate of nanometer-scale essential clusters (called pre-nucleation clusters) that form the vaterite structure through cluster-based structural transformation. Chapter 3 showed that a vaterite-like intermediate phase (called pseudo-vaterite) appeared prior to vaterite nucleation in the presence of $H_2PO_4^-$. This intermediate phase had a more poor structure and a higher C/Ca ratio than those of vaterite, and formed prior to the formation of vaterite. Thus, it is necessary to investigate the relationship between the physico-chemical properties of ACC and the growth dynamics of pseudo-vaterite and vaterite in relation to their structures. In addition, when it was apply the growth model of vaterite estimated *in vitro* to actual living organisms, it should be consider the effect of $H_2PO_4^-$ because it is universally present *in vivo*. Chapter 2 showed that one of the roles of $H_2PO_4^-$ is a strong inhibition of vaterite formation from ACC in simulated biological conditions. They also reported that $H_2PO_4^-$ is easily incorporated into ACC.

Taking into account these considerations, it was provide here a new growth model of vaterite from *in situ* optical microscopic observations in the $Ca–CO_3–H_2PO_4^-$ system under simulated biological temperature, pressure, and pH. In addition to vaterite growth rate, it was characterized ACC structures in relation to vaterite growth using optical spectroscopy and light scattering measurements. It was showed that vaterite only formed via transformation from an ACC phase, and $H_2PO_4^-$ affected the chemical bond structure between Ca^{2+} and CO_3 ions, thus forming a non-vaterite structure in ACC, resulting in inhibition of vaterite nucleation and growth.

4.2. Experimental Methods

4.2.1. *Solution preparation.*

Seven mother solutions were prepared: 1 M $CaCl_2$ and NaCl, 0.5 M $NaHCO_3$, K_2HPO_4 and KH_2PO_4, 25 mM NaCl and KH_2PO_4 solutions as described Chapter 2 methods.

4.2.2. *Measurement of vaterite spherulite growth rate and estimation of surface free energy.*

It was prepared a growth cell for *in situ* observation of vaterite spherulite growth at various levels of supersaturation. Owing to the higher solubility of vaterite than that of calcite, it is difficult to maintain supersaturation with respect to vaterite during experiments with a constant flow of supersaturated solution through the whole system. Thus, it was performed a rapid mixing system of a cation solution with an anion solution in the observation cell to avoid undesirable precipitation before introduction of the solution into the cell.

Fig. 1a shows the schematic solution-flow system. The system consisted of two solution pumps and silicone and Teflon® tubes. Two pumps delivered the cation and anion solutions separately into the observation cell, where the solutions were rapidly mixed. Fig. 1b shows the schematic image of both mixing and observation cell. The cell was composed of pieces of glass slide and polypropylene spacers. It enabled that fresh mixed supersaturated solutions were carried into crystals precipitation and growth part. The observation area was approximately 100 μm thick, 1 mm wide and 7 mm long. The solution was disposed after passing the observation area, and fresh mixed solution was continuously supplied to the area to maintain supersaturation with respect to precipitated vaterite. The flow rates of cation and anion solutions were 2 mL/min, and the Reynolds number just after the mixing was estimated to be about 4500 indicating that the two solutions were completely mixed. The solution pH was maintained at about 8.6 by the buffering effect of HCO_3^-.

The cell was placed on the stage of a transmitted light optical microscope (BX-60, Olympus Co., Tokyo, Japan), using a white-light lamp as a light source. Photographs of vaterite spherulites were taken during a period of 20–60 s, depending on the supersaturation and $H_2PO_4^-$ concentration. It was measured the sizes of spherulites in three directions: the longest dimension and at tilts of ± 60°. The average of the three lengths was defined as the size of the vaterite spherulite. It was measured the size of at least 50 spherulites for each solution condition. The time evolution of spherulite size was fitted using linear approximation and the growth rate was estimated.

The supersaturation of the solution, σ, is defined as

$$\sigma = (C - C_e)/C_e = (I_p/K_{sp})^{1/n} - 1 \qquad (1)$$

where C is the actual concentration, C_e is the equilibrium concentration, I_p is the product of the ionic activity of $CaCO_3$, K_{sp} is solubility product of the corresponding vaterite polytypes, and n is the number of ions in the chemical formula ($n = 2$ in this study).

Each solubility of vaterite and pseudo-vaterite were estimated from the Ca^{2+} ions concentrations of the corresponding equilibrium solutions, which were measured by using ICP-AES, (SI7000, Seiko Instruments Co., Japan) after filtration of solutions using double filtered method; a 0.22-μm pore membrane filter and a 0.1-μm centrifuge filter for complete removal of solid particles.

The ionic activities of vaterite and pseudo-vaterite were given using Ca^{2+} and CO_3^{2-} ions concentrations in the prepared solutions as

$$I_{p(vaterite,\ pseudo\text{-}vaterite)} = [Ca^{2+}][CO_3^{2-}] \qquad (2)$$

The supersaturation ranges in this study are 0.25–2.13 for vaterite and 0.16–1.89 for pseudo-vaterite. (see below)

For vaterite and pseudo-vaterite, the relationship between the growth rate R and σ was fitted using the multiple two-dimensional nucleation model.[14-17] R is expressed using σ as

$$R = K\sigma^{2/3}(1 + \sigma)^{1/3}\{ln(1 + \sigma)\}^{1/6}exp[-\pi\gamma^2/\{3k_B{}^2T^2ln(1 + \sigma)\}] \qquad (3)$$

where K is a experimental constant, k_B is the Boltzmann constant, and T is the absolute temperature.

Eq. 3 is transformed using $1/\ln(1 + \sigma)$ as

$$ln[R/[\sigma^{2/3}(1 + \sigma)^{1/3}\{ln(1 + \sigma)\}^{1/6}]] = lnK - \{\pi\gamma^2/(3k_B{}^2T^2)\} \times 1/ln(1 + \sigma) \qquad (4)$$

where γ is the edge free energy of a two-dimensional island, and is calculated using the slope of the plot for $ln[R/[\sigma^{2/3}(1 + \sigma)^{1/3}\{\ln(1 + \sigma)\}^{1/6}]]$ against $1/ln(1 + \sigma)$.

The surface free energy of vaterite or pseudo-vaterite, ΔG (mJ/m^2), is expressed as follows

$$\Delta G = \gamma/(hV)^{1/2} \qquad (5)$$

where h is the step height, and V is the unit cell volume. Vaterite has a spherulitic morphology; thus, it is difficult to observe its surface directly and estimate the step height. In this study, it was applied the structural model proposed by LeBail et al.[18], in which *h* is assumed to be a half of the *c* unit cell parameter, 0.21 nm.

4.2.3. *Characterization of vaterite polytypes.*

Vaterite spherulites were precipitated in the same manner as described in the previous section. The spherulites precipitated on the glass slide were removed from the surface of the glass and collected. The spherulite residues were washed several times using 99.5 % ethanol to stop further reaction and were dried at room temperature.

The C/Ca ratios in each part of the vaterite spherulites that precipitated under various solution conditions were measured using FE-SEM/EDX using CaF_2-$CaCO_3$-Na_2CO_3 mixture as C/Ca ratio standards. The crystallite sizes of the precipitates were measured using SAXS. The experimental details were described in Chapters 2 and 3.

The ^{13}C and ^{31}P chemical shifts in vaterite polytypes were measured using a solid state NMR (JNM-ECX400 JEOL Co., Japan) with a resonance frequency of 400.0 MHz. For all solid state NMR measurements, MAS with a single pulse mode for ^{31}P and ^{13}C was applied at frequencies of 10000 rpm in 5-mm zirconia rotors. The sample weight was approximately 1 g, the contact time for ^{31}P MAS measurement was 36 ms with relaxation delays of 60 s in each interval. The number of repetitions per measurement was 1400. For ^{13}C MAS measurements, the contact time was 4 ms with relaxation delays of 15 s in each interval. The number of repetitions per measurement was 500. The chemical shifts of ^{13}C and ^{31}P were calibrated as 0.0 ppm using hexamethyl benzene $(CH_3)_6C_6$ and 0.5 M K_2HPO_4–KH_2PO_4 solution with a pH of 8.6.

4.2.4. *Multi-angle Dynamic Light Scattering Measurements (DLS).*

First, cation and anion stock solutions were prepared. The cation solution contained only 1M $CaCl_2$. The anion solutions contained 12.66 mM $NaHCO_3$ with various concentrations of KH_2PO_4. The ionic strength of the anion solutions was adjusted to 0.1 $[M/L]^2$ by adding 1M NaCl. Supersaturated calcium carbonate solutions were prepared by mixing the cation solution with the anion solutions at a volume ratio of 79:1 just before DLS measurement. 0.22-μm pore membrane filters before measurement to remove dust, and were not filtered after mixing. The ionic concentrations in the final solutions were 12.5 mM of Ca^{2+} and CO_3^{2-}, and 0–50 μM of $H_2PO_4^-$. Approximately 15 mL of the final solution was placed into a spherical Pyrex® glass observation cell 29.5 mm in diameter.

A custom-made multi-angle DLS system was used in Kanzaki et al.[19] The light source of the equipment was a semiconductor laser with a wavelength (λ_w) of 532 nm. The second autocorrelation functions, $G^2(q,t)$, were measured at scattering angles, θ, from 30° to 100° at intervals of 10°, to check the angular dependence. The accumulation time to obtain each $G^2(q,t)$ was 120 s.

$G^2(q,t)$ is expressed as

$$G^2(q,t) = <I(q,t) \times I(q,0)>/<I(q,0)>^2 \tag{8}$$

where $I(q,0)$ and $I(q,t)$ denote the scattered intensities at time zero and time difference t between the photon-counting measurement and the brackets denote the time average. The scattering vector, q, is related to the refractive index of the solution, n, λ_w, and scattering angle, θ:

$$q = 4\pi n \sin(\theta/2)/\lambda_w \tag{9}$$

The CONTIN[20] method was applied to analyze the auto-correlation function parameters using the software (ALV-Laser Vetriebsgesellschaft, ALV Co., Germany) and to calculate the decay time, τ, of the scattered particles.

The τ is expressed using q and D, the diffusion coefficient of scattered particles, as

$$1/\tau = q^2D \tag{10}$$

D is affected by the intermolecular interaction between particles, and thus, it is apparent under finite particle concentration. The actual translational diffusion coefficient is estimated by extrapolating D to the zero limit of concentration; however, this was not possible in this study because the aggregation state changed with concentration. Therefore, it was discussed the aggregation of particles using the apparent diffusion coefficient.

The D is converted to apparent particle radius, r_H, using the Einstein–Stokes relation:

$$r_H = k_BT/6\pi\eta D \tag{11}$$

where η is the viscosity of the solution, 0.9452 cP, at a temperature of 22°C.

4.2.5. *Count of calcium-carbonate polymorph ratio.*

Observed how $H_2PO_4^-$ affects the precipitated amount of each calcium carbonate polymorph (vaterite or calcite) in the solutions containing ACC aggregates.

PO_4-containing calcium carbonate solutions ($CaCO_3$: 12.5, 15.0, 17.5, and 20.0 mM and $H_2PO_4^-$: 10 μM) in which ACC formed were prepared. Each solution was cloudy during the initial preparation stage. Some solutions were used without further processing, and others were rapidly filtered using 0.22-μm pore membrane filters within 20 s of mixing Ca with CO_3. Pyrex® glass slide fragments approximately 4 mm × 7

mm^2 in size were soaked in either filtered or non-filtered solution and kept for 60 min. Then, they were removed from the solution, washed several times using 99.5 % ethanol to stop further reaction and dried in air condition.

Photographs of the precipitates on glass slides were taken, and the numbers of each polymorph were counted. It was measured the vaterite/calcite ratio for a minimum of 20 different photographs for each condition. The number of polymorphs counted for each measurement was more than 5000.

4.2.6. *Characterization of ACC structure.*

4.2.6.1. Raman spectroscopy.

They were prepared $H_2PO_4^-$-containing ACC by mixing 20 mL of 12.5 mM $CaCl_2$ with $NaHCO_3$ or Na_2CO_3 containing 0–50 μM K_2HPO_4 immediately in Pyrex® glass bottles, which were stirred using a vortex mixer for several seconds. The pH of the $CaCl_2$ $NaHCO_3$ K_2HPO_4 solution was about 8.6, whereas that of the $CaCl_2$ Na_2CO_3 solution was about 12.0. The ionic strength was adjusted using 1 M NaCl, 0.1 $[M/L]^2$, for both types of solutions.

After stirring, ACC-containing solutions were diluted with 20 times volume of chilled (approximately −60°C) 99.5% ethanol and stirred at 1000 rpm for several seconds to stop further reaction. The mixed solutions were rapidly centrifuged, washed using chilled (approximately −60°C) 99.5% ethanol several times, and freeze-dried under vacuum at −80°C.

The samples were mounted on glass slides. Raman spectra were obtained using microscopic reflection-type Raman spectroscopy (Renishaw InVia, Micro Raman spectrometer, Renishaw Japan Co., Tokyo, Japan) with a semiconductor laser source with λ_w = 532 nm. All spectra were accumulated in static mode, which gives a wave number resolution of 0.5 cm^{-1}. The spectrometer was calibrated using Si spectral lines (520.5 cm^{-1}) as a standard. Measurements were conducted in the range of wavenumber 70–3200 cm^{-1}. The time required to measure each spectrum was about 120 s.

4.2.6.2. Ultraviolet/Visible light (UV/Vis) spectroscopy.

The time evolution of the ACC structure for different $H_2PO_4^-$ concentrations was observed using UV/Vis spectroscopy. Gently mixed 12.5 mM $CaCl_2$ with $NaHCO_3$ containing 0–50 μM KH_2PO_4 for the measurements of UV/Vis absorption. The ionic strength of the sample solutions was adjusted in the same manner as described in the previous sections. Immediately after solution preparation, they were placed into a 4 mL square-quartz (UV/Vis cell) and mounted on the spectrometer (UV/Vis, V-630, Jasco Co., Hachioji, Japan). A reference solution containing the same concentrations of total CO_3 and PO_4 concentrations without $CaCl_2$ was used for baseline calibration. A deuterium lamp was used as a light source. The measured λ_w range was 200–300 nm with a scan rate of 200 nm/min. The interval for each measurement was about 1 min.

It was also measured UV/Vis spectra for solid ACC using reflection-type spectroscopy (UV/Vis, V-550, Jasco Co., Hachioji, Japan located in Waseda University). The samples were prepared in the same way as for Raman spectroscopy measurements using quartz glass slides. The measured λ_w range was 200–300 nm with a scan rate of 80 nm/min using a deuterium lamp as a light source.

4.3. Results

4.3.1. *Growth behaviors and phase characterization of vaterite spherulites.*

Chapter 3 revealed that vaterite spherulites were not a unique phase, but consisted of vaterite and pseudo-vaterite. The latter formed before vaterite and had lower stability, higher solubility, poor crystallinity, and a higher C/Ca ratio compared to those of vaterite. EDX and SAXS analyses can be used to distinguish vaterite from pseudo-vaterite.

Figs. 2a and 2b show vaterite spherulite observed at different growth periods. The spherulite had a well-rounded morphology in the early stage (Fig. 2a); however, became irregular over time (Fig. 2b). It was observed a decrease in the growth rate over time despite constant supersaturation (Fig. 2c).

The rounded spherulite morphology observed during the period of faster growth rate, but changed into an irregular shape after the growth rate became slower.

Irregularly shaped spherulites (Fig. 3a) changed to a hollow-shell structure irrespective of the presence of $H_2PO_4^-$ (Fig. 3b) after washed several times with 10 mM $NaHCO_3$ solution. FE-SEM/EDX measurements showed that the average C/Ca ratio of the outer regions of the shell was 1.03 and that of the inner regions of the shell was 1.28 (Table 1).

The SAXS measurements for irregularly shaped spherulites showed a bi-modal crystallite size distribution with peaks at approximately 5 nm and at 50–200 nm. However, the peak at 5 nm became weak for washed hollow-structure vaterite, and the size distribution changed to almost unimodal with a peak at 50–200 nm (Fig. 3c).

Fig. 4a shows solid state NMR ^{31}P MAS spectra for rounded vaterite and hollow vaterite. It was assumed that the origin of the ^{31}P spectra was the $H_2PO_4^-$ species in the samples. The NMR spectrum of hollow vaterite shows a bi modal distribution with shifts at 3.6 ppm and −0.1 ppm. In contrast, the spectrum for rounded vaterite showed a broad unimodal distribution with a shift from 3.1 ppm to 3.7 ppm.

Fig. 4b shows ^{13}C MAS spectra for rounded vaterite and hollow vaterite. Both samples show a broad unimodal shift centered at 169.5 ppm. This shift corresponds to the vaterite CO_3^{2-} chemical shift (169.07 ppm and 170.12 ppm).[20] The two chemical shifts reported by Nebel et al.[21] were overlapping and detected as a single broad shift in these samples. No difference in shift in the spectra was observed between rounded vaterite and hollow vaterite.

The chemical shifts observed in the ^{31}P spectrum for hollow vaterite nearly corresponded to *P1* site (PO_4^{3-}) of octacalcium phosphate (3.6 ppm) and monetite ($CaHPO_4$) PO_4 site (–0.1 ppm).[22-25] These calcium phosphates have been reported as layered structures containing Ca atoms that are essentially similar to the vaterite structure. Vaterite has a layer structure in which six Ca atoms are bonded as rings. CO_3 ions are located in the interspaces between Ca layers and easily migrate from the structure.[26] These data suggested that $H_2PO_4^-$ ions partly replaces of CO_3 in the vaterite crystal structure (Figs. 4c and d).

The behavior of chemical shifts observed in the ^{31}P spectrum for rounded vaterite, on the other hand, was similar to that of incorporation behavior in calcite.[22,24,27-28] This suggests that $H_2PO_4^-$ was absorbed onto the vaterite surface in rounded vaterite (Fig. 4e).

The growth behavior, SAXS analysis and solid state NMR data suggested that the rounded spherulites appeared in the initial stage of growth were pseudo-vaterite with a higher growth rate, and the irregularly shaped that appeared in the late stage of growth were vaterite with a lower growth rate. Furthermore, the $H_2PO_4^-$ response behavior was clearly different. The discussion below is based on this model.

4.3.2. *Variation in surface free energy with $H_2PO_4^-$ concentration.*

It was assumed and hypothesized that the chemical formula of vaterite or pseudo-vaterite was stoichiometric, $CaCO_3$. The measured solubilities from the Ca^{2+} ions concentrations were

$$K_{sp(vaterite)} = [Ca^{2+}][CO_3^{2-}] = 1.04 \times 10^{-8}\ [M/L]^2 \qquad (12)$$

for vaterite and

$$K_{sp(pseudo\text{-}vaterite)} = [Ca^{2+}][CO_3^{2-}] = 1.44 \times 10^{-8}\ [M/L]^2 \qquad (13)$$

for pseudo-vaterite, in the experimental conditions for ionic strength of 0.1 $[M/L]^2$.

Figs. 5a and 5b show R values for vaterite and pseudo-vaterite depending on σ in $H_2PO_4^-$ solutions. It was measured R for each condition in more than 50 samples; the data were averaged and standard deviations were calculated. The maximum error of R was less than 25%.

R exponentially increased with increasing σ. With increasing $H_2PO_4^-$ concentration, on the other hand, R decreased even when σ was kept constant. At low values of σ (in a $H_2PO_4^-$-free solution, σ was 0.16 for pseudo-vaterite and 0.25 for vaterite, respectively) and higher $H_2PO_4^-$, nucleation of spherulites or growth of spherulite seeds was not detected, despite observation for more than 3 h.

It was applied growth models other than two-dimensional nucleation, spiral growth and adhesive growth models,[16,17] to analyze the growth rate data because it could not observe the surfaces of the crystals directly.

First, it was estimated the growth parameters when the spiral growth model was applied to the growth rate data. In this work, it could not estimate the step kinetic coefficient β, because it is impossible to observed surface condition of vaterite spherulites.[32,33] Thus, this calculate surface energy values of vaterite and pseudo-vaterite is hypothesis parameter.

It was calculated β.[32,33] R is given as $R = vp$ where v is the step velocity and p is the slope of the growth hillock. R is expressed as

$$R = hCe\beta Zk_BT\sigma ln(1 + \sigma)/19\gamma a \tag{14}$$

The a is the radius of growth unit that is considered to be 1 nm.[3] β/γ value was estimated using the slope in the plot for $19aR$ against $hC_ek_BT\sigma ln(1 + \sigma)$. When it was applied the γ value estimated from reasonable value of cluster growth crystals (protein and HAP crystals: $\gamma = 1.8\text{-}3.5k_BT$) to the calculated β/γ, β was 1.2-2.5 cm/s for vaterite and 3.8-7.1 cm/s for pseudo-vaterite, respectively. The equilibrium concentration C_e was 6.14×10^{22} m^{-3} for vaterite and 7.22×10^{22} m^{-3} for pseudo-vaterite.

These values of β are approximately three orders of magnitude larger than those of proteins or HAP ($\beta_{\mathrm{HAP}} = 0.4\times10^{-4}$ cm/s)[34] and are comparable to those of soluble inorganic crystals.[31,36-37] When it was used the cluster-based growth for vaterite (see the discussion part for details), as was confirmed in previous studies,[4,12,13] the application of the spiral growth model to the growth rate data was inadequate.

The adhesive growth model is given as follows:

$$R = C\sigma = (\beta c_0D_sn_{s0}V/x_s^2)\sigma \tag{15}$$

where n_{s0} is the number of growth units in the adsorption layer (per m^2), assumed as $C_e\times10^{-9}$/m^2 and D_s is diffusion constant of growth units in the absorption layer of a crystal face given as 4.93×10^{-9} m^2/s considered by radius of pre-nucleation cluster (1 nm)[4], c_0 is a constant, assumed as 1, because it is assumed that the value of the mean displacement of the growth units on the surface, x_s is much higher than the distance between the neighboring kinks in a step given as x_0. Thus, to avoid the impurity effect, the values of x_s have been estimated for $R^{1/2}$ against $(10^{-5}\beta C_e^2 V\sigma)^{1/2}$ in high σ values. The value of β was 0.4×10^{-4} cm/s which value of HAP.[34]

The values of x_s were 7.75×10^{-2} nm in vaterite and 4.87×10^{-2} nm in pseudo-vaterite, respectively. These values were too small for the mean displacement of growth units. Unless, when the values of β were applied 1.65 cm/s for vaterite and 4.13 cm/s for pseudo-vaterite which inadequate parameter acquired by using spiral growth. The values of x_s were 2.45×10 nm in vaterite and 1.54×10 nm in pseudo-vaterite, respectively. However, the values of β from spiral growth model were unmeanigful. Thus, the application of the adhesive growth model to growth rate data was inadequate.

Using the relationship between R and σ, it was calculated γ for two-dimensional islands nucleated on vaterite or pseudo-vaterite in the $H_2PO_4^-$ solutions. Fig. 6a shows the relationship between $1/ln(1+\sigma)$ and $ln\{R/\sigma^{2/3}(1+\sigma)^{1/3}\{ln(1+\sigma)\}^{1/6}\}$. A change in slope was observed for $1/ln(1+\sigma)$ greater than 1.8 for pseudo-vaterite and greater than 1.5 for vaterite. As has been previously reported for several crystals that grow via a two-dimensional mode,[29,30] it was assumed that growth proceeded via homogeneous nucleation for $1/ln(1+\sigma)$ less than 1.8 and via heterogeneous nucleation for $1/ln(1+\sigma)$ greater than 1.8. The apparent γ values were calculated using the plot in heterogeneous nucleation region.[31] The apparent γ values calculated for the homogeneous nucleation region were $2.43k_BT$ for vaterite and $1.89k_BT$ for pseudo-vaterite in $H_2PO_4^-$-free solutions using two dimensional growth model. The γ values of vaterite and pseudo-vaterite were closed to those of protein and HAP crystals. Thus, the application of the two-dimensional islands growth model to growth rate data was adequate.

The apparent γ values increased with increasing $H_2PO_4^-$ concentration. However, apparent γ for pseudo-vaterite was lower than that for vaterite at all concentration of $H_2PO_4^-$. It was calculated the surface free energy, ΔG, of vaterite and pseudo-vaterite using apparent γ. Fig. 6b shows the relationship between ΔG and $H_2PO_4^-$ concentration. The ΔG values in $H_2PO_4^-$-free solutions were 30.7 mJ/m^2 for vaterite and 23.9 mJ/m^2 for pseudo-vaterite, respectively. Gomez-Morales et al.[10] reported ΔG = 40 mJ/m^2 for vaterite using the relationship between incubation time for three-dimensional nucleation versus σ. These results are close to this value.

The value of ΔG increased with increasing $H_2PO_4^-$ concentration; the rate of increase for vaterite was higher than that for pseudo-vaterite. The ΔG values were 223.9 mJ/m^2 for vaterite and 105.2 mJ/m^2 for pseudo-vaterite in solutions with 10 μM PO_4.

4.3.3. ***Effect of filtering for ACC-containing solution on vaterite formation.***

Figure 7 shows the ratio of vaterite to total precipitates on glass slides soaked in filtered or non-filtered solutions.

All solutions were slightly cloudy before filtration because of the presence of ACC particles, and became transparent after filtration. The ratio of vaterite to total precipitates formed in filtered solutions were markedly lower than that in non-filtered solutions For example, in 12.5 mM $CaCO_3$ solutions, the ratio was 0.58 in the non-filtered solution and 0.08 in the filtered solution, respectively. With increase in the $CaCO_3$ concentration, the ratio of vaterite in the non-filtered solution increased; however, the ratio in the filtered solution was almost constant about 0.08.

The morphology of the vaterite spherulites formed in the filtered solution was similar to that in the non-filtered solution.

4.3.4. ***Spectroscopic analysis for ACC particles in Ca–CO_3–$H_2PO_4^-$ system.***

4.3.4.1. Raman spectroscopic analysis of structure of ACC structure with $H_2PO_4^-$ concentration.

Figs. 8a–d show the Raman spectra of ACC aggregates in $H_2PO_4^-$-containing solutions and the reference spectrum of amorphous calcium phosphate (ACP). The strongest bands of ACC samples were all observed at about 1085 cm^{-1}, which could be attributed to Ca–CO_3 bands corresponding to the symmetric stretching of calcite (1085 cm^{-1}) or vaterite (1089 cm^{-1}) (Figs. 8a and b) according to previous studies.[36,37] Unfortunately, the strongest bands corresponding to the symmetric stretching of non-hydrated calcium carbonate phases are at about 1085 cm^{-1} (1085 cm^{-1} for calcite, 1089 cm^{-1} for vaterite, and 1087 cm^{-1} for aragonite); thus, this band cannot be used for the analysis of ACC structure.

With the increase in $H_2PO_4^-$ concentration, a band at approximately 1075 cm^{-1} corresponding to an extra symmetric stretching vibration mode of vaterite was observed. A slight shift was observed with an increase in $H_2PO_4^-$ concentration, and the band of transmitte increased with increasing $H_2PO_4^-$. For example, the band had a relative intensity of about 10 without any bands in the $H_2PO_4^-$-free solution; however, it changed to bi modal bands in the 50 μM $H_2PO_4^-$ solutions with a relative intensity of about 60. This indicates that Ca–CO_3 chemical bonds similar to those observed in the ration of vaterite structure increased with increasing $H_2PO_4^-$ concentration. In addition to symmetry-stretching vibration, Raman vibrations corresponding to lattice mode and plane bending were observed in the vaterite structure with an increase in $H_2PO_4^-$ concentration. The intensities corresponding to the Raman bands for vaterite (around 118 cm^{-1} and 301 cm^{-1} in the lattice mode, 740.4 cm^{-1} and 751.1 cm^{-1} in the plane bending mode, respectively) increased with the PO_4 concentration (Figs. 8c and d).

The band corresponding to the Raman shift, 301 cm^{-1}, shifted toward higher wavenumber with the $H_2PO_4^-$ concentration such that the 301.2 cm^{-1} band in the $H_2PO_4^-$-free solution shifted to 306.5 cm^{-1} in the 50 μM $H_2PO_4^-$-containing solution. The band at 118 cm^{-1}, on the other hand, shifted toward a lower wavenumber with increasing $H_2PO_4^-$ concentration such that the 118.4 cm^{-1} band in the $H_2PO_4^-$-free solution shifted to 111.8 cm^{-1} in a 50 μM $H_2PO_4^-$-containing solution (Fig. 8c).

In contrast to the Raman shift observed in the lattice mode, a slight shift was observed in the plane bending mode of Raman bands (740.4 cm^{-1} and 751.1 cm^{-1}) with changes in the $H_2PO_4^-$ concentration (Fig. 8d).

An extra broad band appeared at approximately 210 cm^{-1} with an increase in the $H_2PO_4^-$ concentration, which corresponds to the lattice mode of aragonite, although aragonite was not observed in the precipitates.

Large shifts in the Raman bands corresponding to symmetric stretching and lattice modes of the vaterite structure were observed and a slight shift of the plane bending mode was observed. A summary of the shift in Raman bands is shown in Table 2. The asymmetric stretching bands corresponding to the vaterite structure were too weak to be detected.

Evidence of attributed bands for Ca–PO_4 (Ca-$H_2PO_4^-$ or Ca-HPO_4^{2-}) in ACC samples was not detected under these solution conditions.

4.3.4.2. UV/Vis spectroscopy measurement for ACC in different $H_2PO_4^-$ concentrations.

Fig. 9a shows the UV/Vis absorption spectra for supersaturated calcium carbonate solutions for different $H_2PO_4^-$ concentrations at immediately after mixing. A broad absorption band was only observed at approximately 235 nm for all $H_2PO_4^-$ concentrations. Absorption intensities were enhanced with $H_2PO_4^-$ concentration. When the concentration of $H_2PO_4^-$ exceeded 5 μM, the absorption intensity gradually increased until 10 min after preparation of the solutions, and then became constant during experimental period (about 120 min). It was observed that the spectra shifted toward short wavelengths when the band intensities increased.

It was frequently observed that the absorption Raman shifted to short wavelengths with an increase in the $H_2PO_4^-$ concentration. For example, the absorption band was at 240 nm in the $H_2PO_4^-$-free solution, at 229 nm in the 10 μM PO_4 and at 224 nm in the 50 μM $H_2PO_4^-$, respectively.

Fig. 9b shows reflection UV/Vis spectra for solid calcium-carbonate polymorphs: calcite, vaterite, and ACCs ($H_2PO_4^-$-free ACC and ACC containing 50 μM $H_2PO_4^-$). The maximum band of the spectrum for calcite was at 213 nm. The spectrum intensity of calcite gradually decreased from 213 nm to 230 nm and showed a sharp drop between 230 nm and 260 nm. It showed a plateau between 260 nm and 280 nm.

The maximum band of the spectrum for vaterite was at approximately 236 nm. The behavior of the vaterite spectrum was markedly different from that of calcite. The spectrum intensity rapidly increased at 200–210 nm and gradually increased at 210–225 nm. The intensity gradually decreased at 225–260 nm and showed a small sharp drop at approximately 265 nm. Finally, the plateau appeared at 265–280 nm following a sharp drop.

The band of the spectrum for $H_2PO_4^-$-free ACC was at 209 nm. The band showed a sharp drop at the edge of short wavelength. The spectrum showed two plateaus at approximately 220–240 nm and at 260–280 nm.

ACC containing 50 μM $H_2PO_4^-$ showed a broad reflection spectrum with a band at 224 nm. The spectrum had two plateaus as well as that of $H_2PO_4^-$-free ACC at 240–255 nm and 265–280 nm. The position of one of the plateaus was consistent with that observed for vaterite.

4.3.4.3. ICP-AES measurement for total PO_4/Ca ratio of ACC particles.

Fig. 10 shows the total PO_4/Ca ratio of ACC formed immediately after solution preparation in the presence of total PO_4 ions. The ratio increased linearly with increasing $H_2PO_4^-$ concentration. The ratio was 3.8×10^{-3} in 20 μM $H_2PO_4^-$ and 9.7×10^{-3} in 50 μM $H_2PO_4^-$ both of which contained 12.5 mM $CaCO_3$. The band positions and intensities observed in the Raman and UV/Vis spectra of ACC, and the total PO_4/Ca ratios in $H_2PO_4^-$-containing solutions are summarized in Table 2.

4.3.5. ***Time evolution of ACC particles revealed by DLS measurements.***

The solutions containing low concentrations of $H_2PO_4^-$ (for example, 5 μM $H_2PO_4^-$) showed abnormal autocorrelation functions that exceeded 2 as a result of abrupt increases in intensity during measurement (Fig. 11a) compared with a solution with a high $H_2PO_4^-$ concentration. It was excluded these data from the results. Solutions with $H_2PO_4^-$ concentrations greater than 10 μM showed normal autocorrelation functions (Fig. 11b).

The relationship between $1/\tau$ and q^2 using autocorrelation function data was obtained for all samples to estimate D with high accuracy (less than 5% error) (Fig. 11c). It was checked that the relationships was linear to assess the reliability of the measured autocorrelation functions.

Fig. 11d shows the time evolution of particle radius in $H_2PO_4^-$ solutions. The time evolution can be classified into three stages for all solutions: particle radius simply increased over time (stage 1), reached equilibrium (stage 2), and then it decreased over time (stage 3). The particle radius in each solution was larger than 80 nm immediately after solution preparation, suggesting that nucleation of ACC rapidly occurred after mixing of the cation and anion solutions.

The particle radius compared at a fixed time increased with the increase in $H_2PO_4^-$ concentration for stage 1. The duration of this stage and the growth rate of particles during this stage both slightly increased with increasing $H_2PO_4^-$ concentration.

Conversely, the duration of stage 2, in which the particle radius was almost constant, increased with an increase in $H_2PO_4^-$ concentration. Approximately 40 min of duration in the 10 μM $H_2PO_4^-$-containing solution decreased to approximately 5 min in the 20 μM $H_2PO_4^-$-containing solution.

The change in particle radius over time in stage 3 was strongly dependent on the $H_2PO_4^-$ concentration. At low concentrations of $H_2PO_4^-$, such as 10 μM, a simple decrease in the radius and number of particles, estimated from the scattering intensity decrease, were observed over time. When the particle radius decreased to 100 nm, an autocorrelation function could not be obtained because the scattering intensity was too low.

At high concentrations of $H_2PO_4^-$, such as 50 μM, the radius did not show a simple decrease over time. The calculated particle radius distribution showed a bimodal nature: one band (corresponding to smaller particles) showed a decrease in radius over time, and the other band (corresponding to larger particles) showed an increase in radius over time, although the average scattering intensity of the solutions decreased over time. The bimodal distribution was observed at the start of stage 3. Although the larger radius particles increased and reached about 500 nm after 120 min in the stage 3, measurement had to cease because the scattering intensity corresponding to smaller particles became too lower for detection.

Sampled solutions and quenched ACC particles had done at each stage. Figs. 11e and f show FE-SEM photographs of samples prepared at different stages for two different $H_2PO_4^-$ solutions. The ratios of supersaturated calcium carbonate solutions were 1.21 in vaterite and 1.04 in pseudo-vaterite.

ACC was present as an aggregated form composed of small spherical particles around 20 nm in radius when the concentration of $H_2PO_4^-$ was low (5 μM) in stage 1. The autocorrelation function was not detected here because the size of the ACC aggregates was too large (Fig. 11e). When the $H_2PO_4^-$ concentration was high (20 μM), ACC aggregates were not present and ACC particles about 50 nm in radius were observed (Fig. 11f).

4.4. Discussions

Calcium carbonate crystalline particles precipitated on the walls and at the bottom of cells. In low-concentration $H_2PO_4^-$ solutions, they mainly consisted of vaterite spherulites, and the amount of calcite increased with increasing in $H_2PO_4^-$ concentration.

This study revealed the characteristics of vaterite growth dynamics in the Ca–CO_3–$H_2PO_4^-$ system under simulated biological conditions. In $H_2PO_4^-$-free solutions, the values for apparent edge free energy was $\gamma = 2.43k_BT$ for vaterite and $\gamma = 1.89k_BT$ for pseudo-vaterite. Malkin et al.[29] investigated the growth dynamics of the (101) face of ammonium dihydrogen phosphate crystal, which is a representative soluble inorganic crystal. The (101) face grew by two-dimensional nucleation and γ was estimated to be $0.7k_BT$. Sazaki et al.[35] investigated the (101) face of the lysozyme crystal of a protein crystal, and found that γ was $2.8k_BT$. These studies indicate that the value of γ greatly depends on the size of the essential growth unit of crystals, i.e., whether a crystal is an ionic species or a macroscopic molecule. Onuma et al.[31] investigated the (0001) face of a hydroxyapatite crystal with a homogeneous two-dimensional nucleation growth mode, and showed γ to be $3.3k_BT$. This large value of γ suggested that the growth unit of hydroxyapatite is not an ionic species but large molecular clusters, which was confirmed by light scattering measurements and *ab initio* calculations.[38-40]

The value of apparent γ for vaterite and pseudo-vaterite was two or three times larger than that of soluble inorganic crystals; this value is comparable to those of protein crystals and hydroxyapatite, the representative biomaterial, as well as calcium carbonates. The large γ of vaterite and pseudo-vaterite is consistent to the conclusion of previous studies concerning the growth unit of calcium carbonates, i.e., that they are clusters.

Next, it was discuss the inhibiting effect of $H_2PO_4^-$ on vaterite growth. On the basis of the growth rate measurements, there are two possibilities for the mechanism causing the $H_2PO_4^-$ effect. First, $H_2PO_4^-$ is simply adsorbed onto the surface of vaterite and stops vaterite growth. Second, $H_2PO_4^-$ changes the ACC structure and inhibits its transformation into vaterite.

One of the important pieces of evidence for distinguishing between these two possibilities is the filtration experiment, which suggests that ACC is one of precursors in the formation of vaterite and pseudo-vaterite. The Raman spectra indicated that the structure of ACC changed from calcite-like amorphous into vaterite-like amorphous with an increase in PO_4 concentration. This result was revealed from the behavior of Ca–CO_3 bands such as those at approximately 1085 cm^{-1}, where the bands changed from a unimodal calcite-like pattern to a bi modal vaterite-like pattern. The shifts of the absorption band in the UV/Vis spectra were consistent with the conclusion from Raman measurements that ACC particles had vaterite-like structures in the $H_2PO_4^-$-containing solutions.

However, this conclusion is seemingly inconsistent with the results of the growth rate measurements because both vaterite and pseudo-vaterite growth were strongly inhibited in $H_2PO_4^-$-containing solutions, despite the increase in vaterite-like structure in ACC in the presence of $H_2PO_4^-$. It was assumed that the increase in vaterite-like structures in ACC with $H_2PO_4^-$ did not correspond to *actual vaterite structure*; therefore, they could not be transformed into crystalline vaterite. These vaterite-like structures are "junk parts," and their increase resulted in a marked reduction in the actual vaterite growth rate.

Demichelis et al.[41] investigated the structure of pre-nucleation clusters of calcium carbonate under various pH conditions using molecular dynamics calculations. They showed that the size, distribution, and coordination number of the cluster increased with an increase in solution pH. The essential chemical bond between Ca and CO_3 in ACC is Ca–C, corresponding to a calcite-like structure at relatively lower pH condition about 8.5, which is comparable to this experimental condition, and O–C, corresponding to a vaterite-like structure, at relatively higher pH condition about 11.5. This conclusion was also supported by experiments.[21] At lower pH, HCO_3^- ion pairs are formed in which H^+ bonds O of CO_3. This inhibits the formation of O–Ca bonds, resulting in ACC particles with small particle distributions. They also indicated that the average size of ACC particles increases at higher pH because of the absence of H^+ ions, which acts to block ACC aggregation.

The conclusion concerning the effect of $H_2PO_4^-$ on ACC structure is comparable to that caused by increasing the pH of the solutions. When the results obtained by Demichelis et al.[41] are applied to this case, it appears that $H_2PO_4^-$ binds H^+ in ACC and changes the ACC structure. This drastically reduces the number of growth units that originally construct the vaterite structure via cluster-based phase transformation from ACC. Some previous studies had investigated the effect of H^+ on amorphous phases, and they support these conclusion.[42-43]

The effect of $H_2PO_4^-$ on vaterite growth can be summarized as follows. $H_2PO_4^-$ is not only absorbed on the surface of vaterite as a conventional impurity but also changes the structure of the growth unit in ACC *before* the vaterite forms via phase transformation from ACC. This modified structure is vaterite-like, but is never the actual vaterite structure. It is highly likely that PO_4 binds H^+ in ACC particles, thus reducing the free space in ACC and resulting in the ACC structure being more closely packed. These closely packed ACC particles cannot form the growth unit of vaterite. The supersaturation of the solution is defined using the $CaCO_3$ concentration. However, PO_4 reduces the growth units of vaterite, which decreases the supersaturation with respect to vaterite despite the average $CaCO_3$ concentration being kept constant. Because of this decrease in actual supersaturation, a higher supersaturation of the bulk solution than would be expected required for nucleation and growth of vaterite, which causes an increase in the apparent surface energy of vaterite in $H_2PO_4^-$-containing solutions.

Because of the difference in apparent surface free energy, pseudo-vaterite phase is likely to precipitate under high $H_2PO_4^-$ concentrations. When the $H_2PO_4^-$ concentration further increases, crystalline vaterite dose not precipitate, and ACC with a vaterite-like chemical structure is stable.

It was obtained conclusive information in this study to explain why vaterite is rarely observed in biological hard tissues. Small amounts of $H_2PO_4^-$ ($H_2PO_4^-/CaCO_3$ = below 1/1000), which is essential for all living organisms, are sufficient to inhibit vaterite nucleation and growth. It was also observed that fluctuations in $H_2PO_4^-$ concentration caused the formation of non-uniform vaterite-like structures, which are inadequate for stable hard tissues *in vivo*.

4.5. Conclusions

In Chapter 4, it was investigated the growth dynamics of vaterite and pseudo-vaterite in the $Ca–CO_3–H_2PO_4^-$ system under simulated biological conditions in relation to the physico-chemical properties of ACC, the precursor of vaterite. A possible inhibition mechanism of $H_2PO_4^-$ on vaterite growth is that the apparent surface free energy was increased by decreasing supersaturation with respect to vaterite, which is caused by the reduction of cluster numbers corresponding to vaterite structure in ACC. This effect is more evident in vaterite than in pseudo-vaterite because the structure of pseudo-vaterite is looser than that of vaterite. Therefore, in higher $H_2PO_4^-$ solutions, the unstable phase of vaterite is likely to appear because of its lower surface free energy. With an increase in the $H_2PO_4^-$ concentration, the dominant phase in the solutions changes from vaterite to pseudo-vaterite.

There have been several reported about the phase diagrams of precipitated mineral polymorphs in the Ca–CO_3–$H_2PO_4^-$ system.[44-46] However, there have been few studies concerning the dynamics of minerals in the Ca–CO_3–$H_2PO_4^-$ system, particularly in relation to the physico-chemical properties of amorphous material despite the fact that it forms an initial phase for all minerals. These results will contribute to the understanding of biomineralization in the Ca–CO_3–$H_2PO_4^-$ system.

Table 4.1. Summary of the physico-chemical properties of vaterite and pseudo-vaterite in the Ca–CO_3–$H_2PO_4^-$ system.

	Vaterite	Pseudo-vaterite
Crystal structure	Highly crystalline phase. Crystallite size was around 200 nm	Low crystalline phase. Crystallite size distribution was bi-modal, around 10 nm and 150 nm.
Chemical composition, C/Ca ratio	1.08 ± 0.08	1.28 ± 0.15
Solubility, K_{sp} $[M/L]^2$	1.04×10^{-8}	1.44×10^{-8}
$H_2PO_4^-$ responce	High response and low absorption	Relatively low response and high absorption

Table 4.2. Summary of Raman spectra, UV/Vis spectra, and total PO_4/Ca ratio of ACC particles for solutions with different $H_2PO_4^-$ concentrations.

Sample conditions	$H_2PO_4^-$ free	$H_2PO_4^-$ 20 μM	$H_2PO_4^-$ 50 μM
Lattice mode	118.4, 301.2 cm^{-1}	113.4, 304.5 cm^{-1}	111.8, 306.1 cm^{-1}
In plane bending	740.4, 751.1 cm^{-1}	740.4, 751.1 cm^{-1}	740.4, 751.1 cm^{-1}
Symmetry stretching	1079.8 cm^{-1}, and one which cannot divide calcite	1076.9 cm^{-1}, and one which cannot divide calcite	1075.4 cm^{-1}, and one which cannot divide calcite
UV/Vis-Abs band at immediately after mixing	239 nm	231 nm	226 nm
UV/Vis-Abs band at 10 min	240 nm	229 nm	224 nm

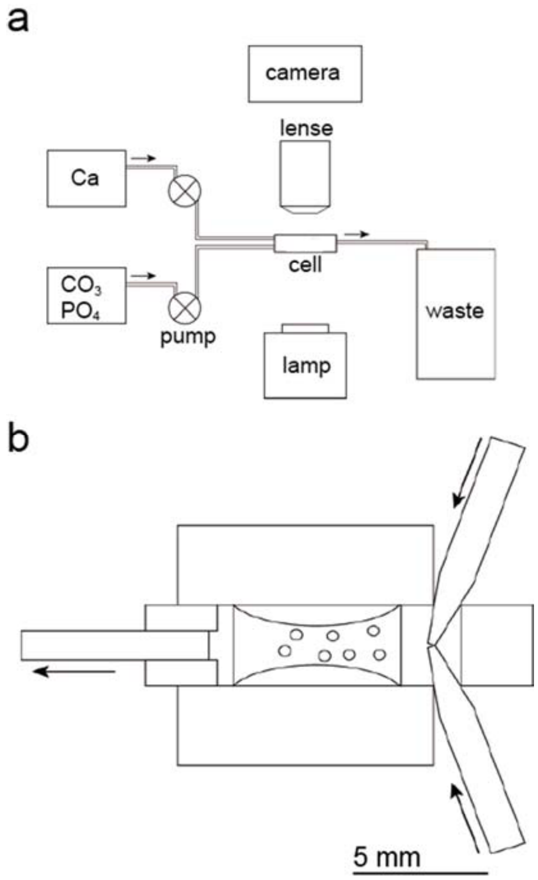

Figure 4.1. Experimental setup for vaterite growth rate measurement. (a) Overall diagram of the observation system. The arrows indicate the flow direction of the solutions. (b) Schematic of the growth cell. The cell consists of three parts: the solution mixing part, the observation part, and the waste part. The circles indicate vaterite spherulites, the rectangular area containing circles denotes the observation part, and the arrows indicate the flow direction of the solutions.

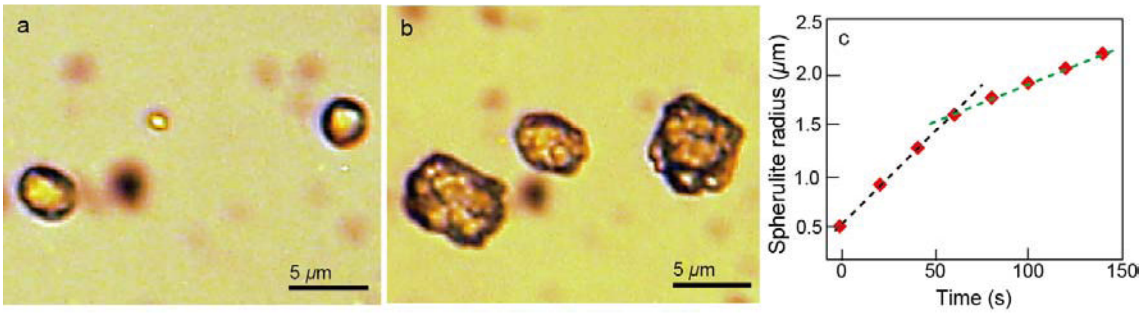

Figure 4.2. Growth behavior of precipitated spherulites in supersaturated solutions. (a) Optical microscopic photograph of spherulites 20 s after the start of growth. Supersaturation σ was 1.80 for vaterite and 1.58 for pseudo-vaterite ($H_2PO_4^-$-free condition). The spherulites exhibit a well-rounded morphology. (b) Optical photomicrograph of spherulites 140 s after the start of growth. The well-rounded shape observed in (a) has changed into an irregular one. (c) Change in average spherulite radius over time measured around at center of spherulites. Growth rate (slope of line) of spherulites decreased after 60 s. The black dotted line corresponds to the growth rate of pseudo-vaterite and the green dotted line to that of vaterite.

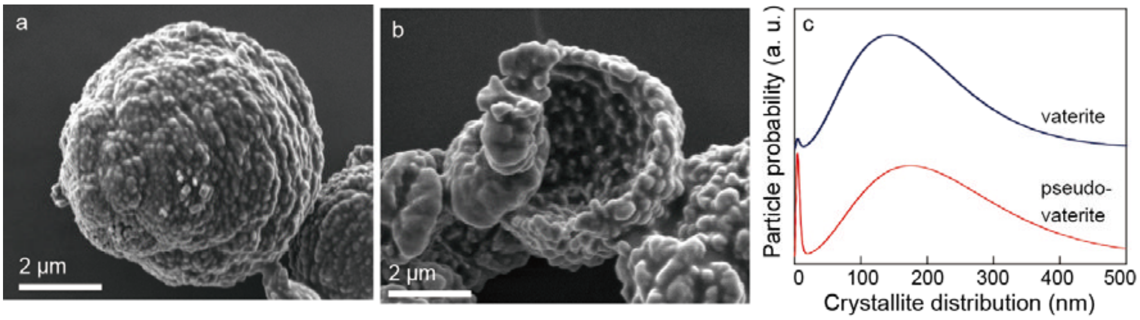

Figure 4.3. Phase characterization of spherulites. (a) FE-SEM photograph of irregularly shaped spherulites precipitated in the same solution as Fig. 2. The photograph was taken 300 s after the start of growth. (b) FE-SEM photograph of hollow spherulites obtained by washing the spherulites in (a) using 10 mM $NaHCO_3$ solution. (c) SAXS measurements for (a) and (b). The crystallite probability of (a) and (b) is indicated respectively.

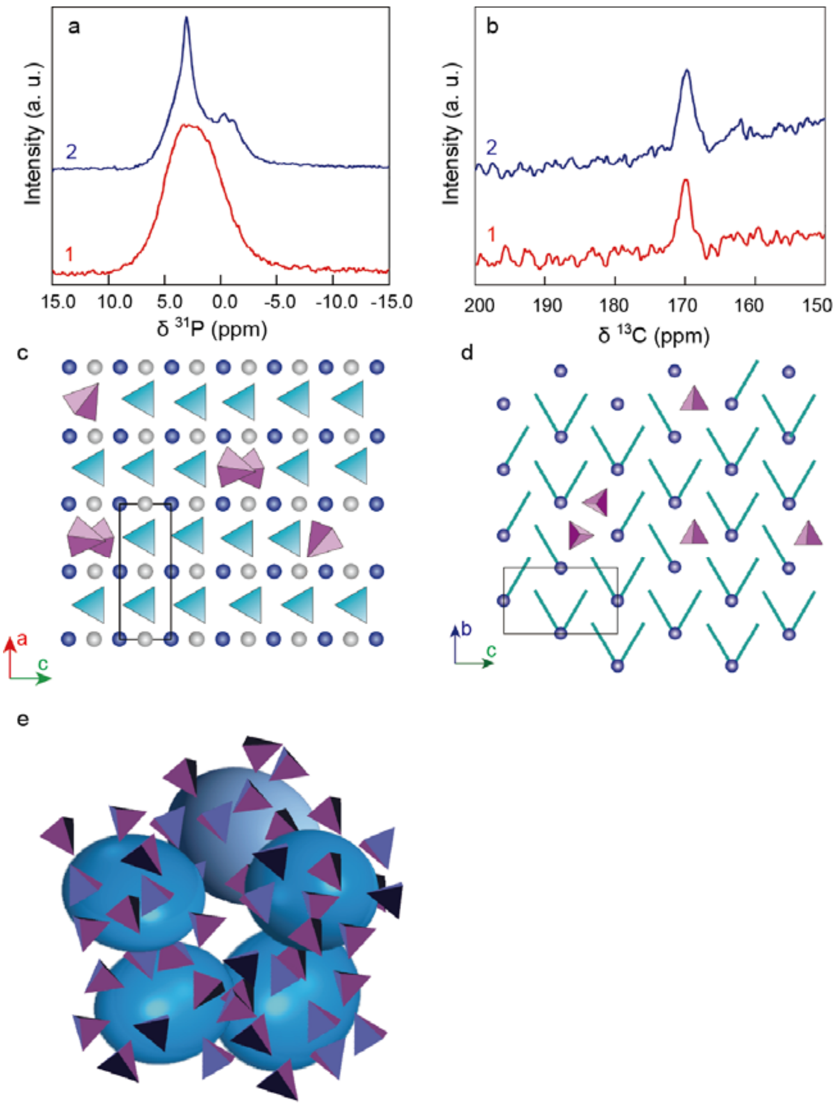

Figure 4.4. ^{31}P MAS and ^{13}C MAS NMR spectra of rounded vaterite and hollow vaterite, and schematic images of vaterite and pseudo-vaterite in relation to incorporated PO_4. (a) ^{31}P solid state MAS NMR spectra. 1: rounded whole spherulite. 2: hollow spherulite. (b) ^{13}C solid state MAS NMR spectra. 1: rounded whole spherulite. 2: hollow spherulite. (c) Schematic image of incorporation PO_4 ions into the vaterite crystal structure viewed from the *b*-axis. PO_4 (triangular pyramids) has replaced CO_3 (triangles) in the spaces between the Ca layers (Ca atoms are indicated as light grey (near side) and blue (back side) spheres). (d) Schematic image of incorporation of PO_4 ions into the vaterite structure viewed from the *a*-axis. Blue rods correspond to CO_3. The open black square of (c) and (d) denote a unit cell in the vaterite crystal structure. (**e**) Schematic image for adsorption of $H_2PO_4^-$ onto pseudo-vaterite. Spheres indicate pseudo-vaterite crystallites, and triangular pyramids indicate $H_2PO_4^-$ adsorbed onto the surface of the pseudo-vaterite crystallite.

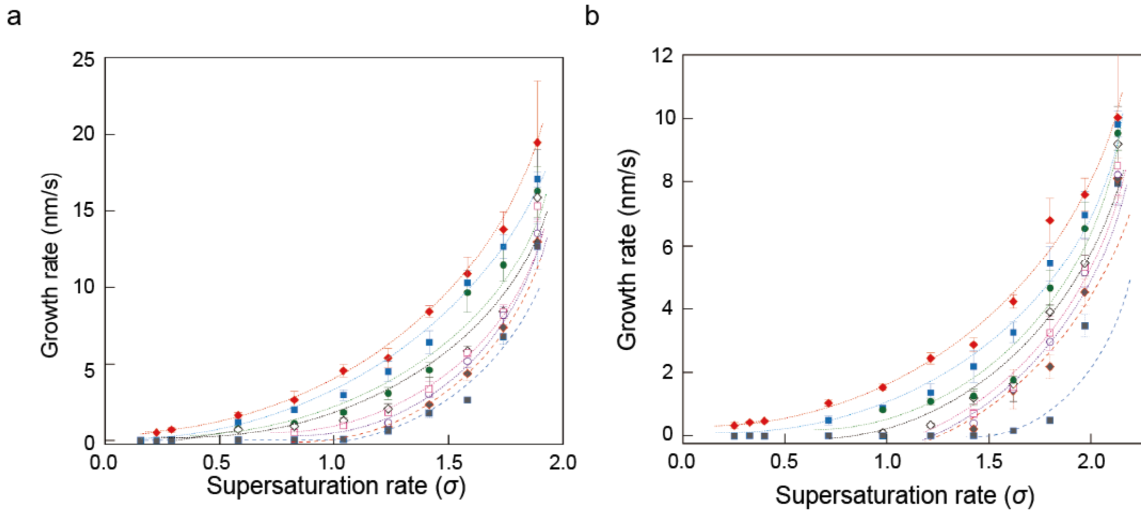

Figure 4.5. Relationship between *R* and *σ* in $H_2PO_4^-$-containing solutions. (a) Pseudo-vaterite. (b) Vaterite. The symbols and fitting lines by 2D nucleation models correspond to data measured at various $H_2PO_4^-$ concentrations: red solid diamonds with fine broken line ($H_2PO_4^-$-free solution), light blue solid squares with fine broken line (1.25 µM $H_2PO_4^-$-containing solution), green solid circles with fine broken line (2.50 µM $H_2PO_4^-$-containing solution), pink open diamonds with fine broken line (5.00 µM $H_2PO_4^-$-containing solution), purple open squares with fine broken line (6.25 µM $H_2PO_4^-$-containing solution), grey open circles with fine broken line (7.50 µM $H_2PO_4^-$-containing solution), grey solid diamonds with roughly broken line (8.75 µM $H_2PO_4^-$-containing solution) and grey solid squares with roughly broken line (10.00 µM $H_2PO_4^-$-containing solution).

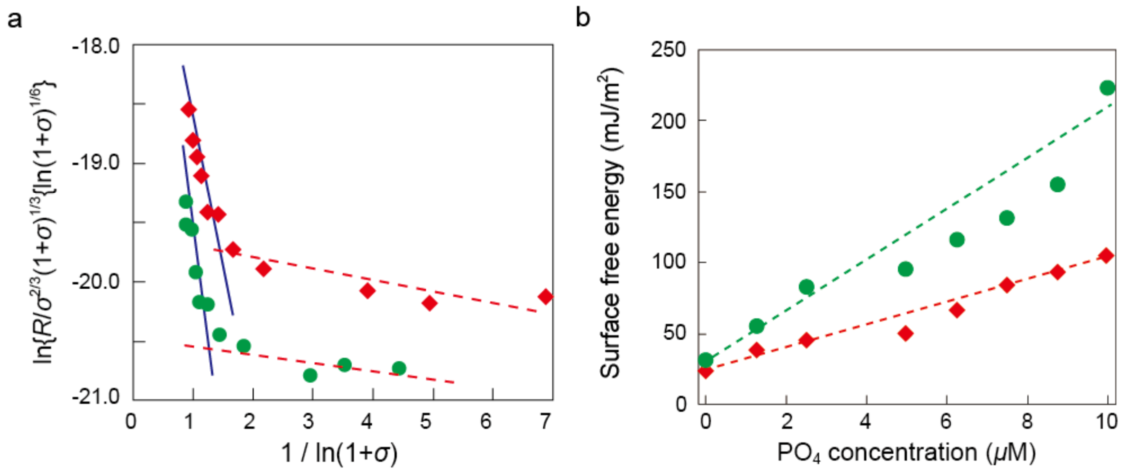

Figure 4.6. (a) Logarithmic plots of growth rate of the vaterite (solid circles) and pseudo-vaterite (solid circles) for calculation of edge free energy under $H_2PO_4^-$ free conditions using two dimensional nucleation theory. (b) Change in surface free energies of vaterite (solid circles with dotted line) and pseudo-vaterite (solid diamonds with dotted line) with $H_2PO_4^-$ concentration.

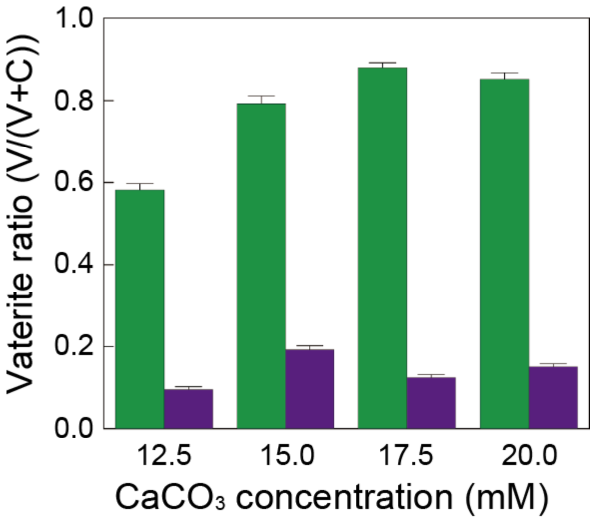

Figure 4.7. Ratio of vaterite in total calcium carbonate precipitates in filtered (purple bars) and non-filtered (green bars) solutions.

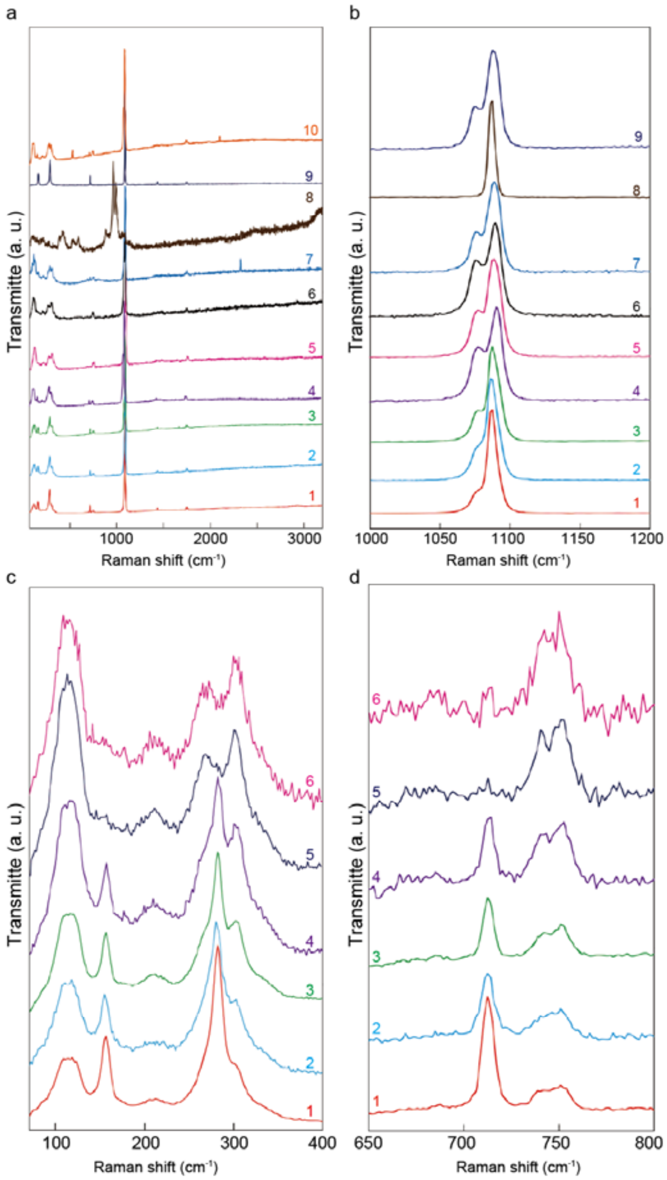

Figure 4.8. (a) Raman spectra of ACC at 70–3200 cm^{-1} precipitated in solutions containing no $H_2PO_4^-$ (1), 5 µM $H_2PO_4^-$ (2), 10 µM $H_2PO_4^-$ (3), 15 µM $H_2PO_4^-$ (4), 20 µM $H_2PO_4^-$ (5) and 50 µM $H_2PO_4^-$ (6). The spectrum of ACC precipitated in Na_2CO_3-$CaCl_2$ solution is (7) and that of ACP precipitated in K_2HPO_4–$CaCl_2$ solution is (8). Spectrum of vaterite is (9) and that of calcite is (10). (b) Expanded Raman spectra at 1000–1200 cm^{-1} for the same samples as in (A). $H_2PO_4^-$-free (1), 5 µM $H_2PO_4^-$ (2), 10 µM $H_2PO_4^-$ (3), 15 µM $H_2PO_4^-$ (4), 20 µM $H_2PO_4^-$ (5), 50 µM $H_2PO_4^-$ (6), Na_2CO_3–$CaCl_2$ ACC (high pH ACC) (7), calcite (8), vaterite (9). A bi modal trend was observed with increasing $H_2PO_4^-$ concentration. (c) Expanded Raman spectra at 70–400 cm^{-1} for the same samples as (1) to (6) in (a). (d) Expanded Raman spectra at 650–800 cm^{-1} for the same samples as (1) to (6) in (a).

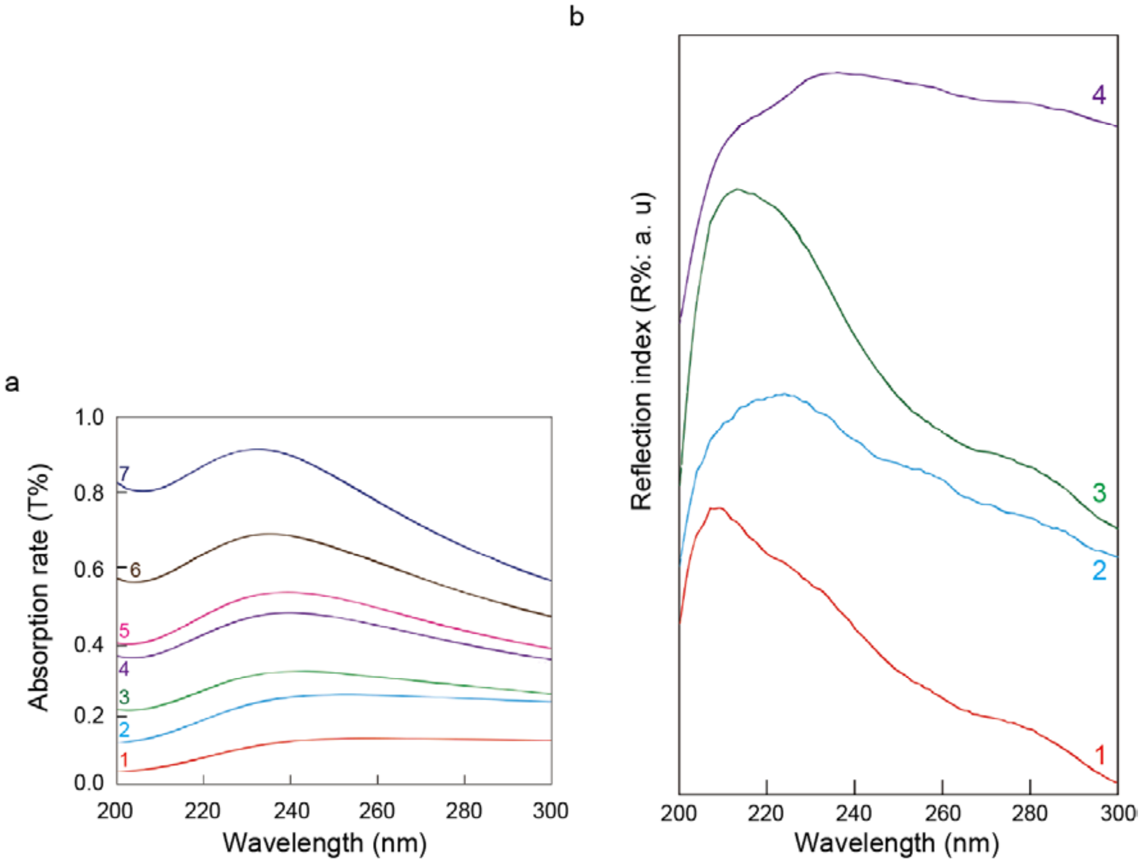

Figure 4.9. UV/Vis spectra of ACC in $H_2PO_4^-$-containing solutions and those of solid calcium carbonate polymorphs. (a) *In situ* UV/Vis spectra of ACC in solutions measured immediately after mixing. The absorption intensities were enhanced with increasing $H_2PO_4^-$ concentration. The $H_2PO_4^-$ concentrations in solutions were $H_2PO_4^-$-free (1), 5 µM (2), 10 µM (3), 15 µM (4), 20 µM (5) and 50 µM (6). (b) Solid UV/Vis spectra of ACC precipitated in $H_2PO_4^-$ solutions and those of calcium carbonate polymorphs. The $H_2PO_4^-$ concentrations in solutions were $H_2PO_4^-$-free (1) and 50 µM (2). The spectrum of calcite is (3), and that of vaterite is (4).

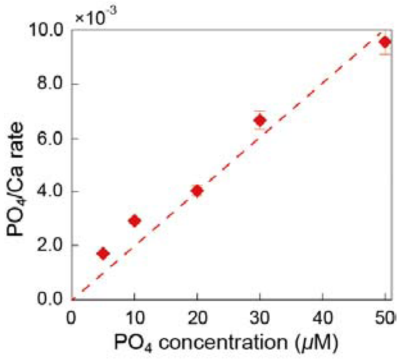

Figure 4.10. Total PO_4/Ca ratio of ACC precipitated in $H_2PO_4^-$-containing solutions.

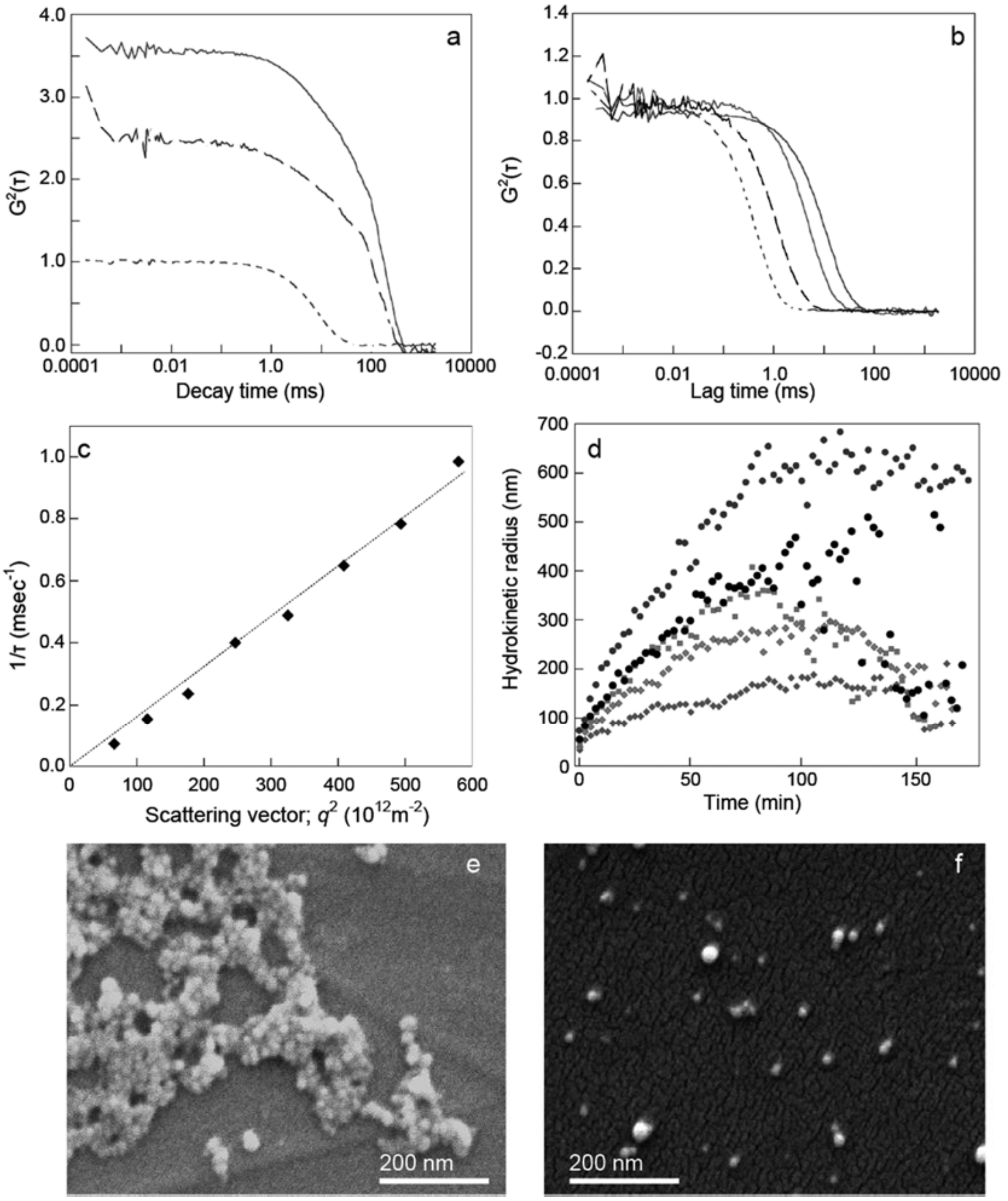

Figure 4.11. Multi-angle DLS measurements for the time evolution of ACC particles in $H_2PO_4^-$-containing solutions. (a) Auto correlation functions measured in $H_2PO_4^-$-containing solutions. The solid and roughly broken black curves indicate data for 5 μM $H_2PO_4^-$ taken immediately after solution preparation (solid: scattering angle 40°, roughly broken: scattering angle 90°). The fine broken grey curve shows data for 20 μM $H_2PO_4^-$ taken immediately after solution preparation (scattering angle: 30°). The auto correlation functions showed abnormal values (>2) for low concentrations of $H_2PO_4^-$ just after solution preparation. (b) Autocorrelation functions for high $H_2PO_4^-$

concentrations measured immediately after solution preparation. Solid black (scattering angle 40°) and broken roughly grey (scattering angle 80°) curves were measured for 20 μM $H_2PO_4^-$-containing solution. Solid grey (scattering angle 40°) and finely broken grey (scattering angle 80°) curves were taken in 50 μM $H_2PO_4^-$-containing solution. (c) Relationships between $1/\tau$ and q^2 in 30 μM $H_2PO_4^-$-containing solution measured 2 min after solution preparation. (d) Change in hydrodynamic radius of ACC particles over time in $H_2PO_4^-$-containing solutions. Dark grey diamonds correspond to data taken at 10 μM $H_2PO_4^-$, light grey diamonds correspond to 15 μM $H_2PO_4^-$, grey square to 20 μM $H_2PO_4^-$, black circles to 30 μM $H_2PO_4^-$, and grey circles to 50 μM $H_2PO_4^-$. (e) An SEM image of aggregated ACC particles precipitated in 5 μM $H_2PO_4^-$-containing solution taken 20 min after solution preparation. (f) An SEM image of separated ACC particles precipitated in 20 μM $H_2PO_4^-$-containing solution taken 1 h after solution preparation.

Reference

(1) Ogino, T., Suzuki, T., Sawada, K. The formation and transformation mechanism of calcium carbonate in water. *Geochim. Cosmochim. Acta*, **1987**, *57*, 2757-2767.

(2) Mann, S. *Biomineralization, Principles and Concepts in Bioinorganic Materials Chemistry*. Oxford University Press, USA, **2003**.

(3) Colfen, H., Antonietti, M. *Mesocrystals and Nonclassical Crystallization.* John Wiley and Sons Ltd., England, **2008**.

(4) Gebauer, D., Volkel, A., Colfen, H. Stable pre-nucleation clusters for calcium carbonate. *Science,* **2008**, *322*, 1819–1822.

(5) Plummer, L.N., Busenberg, E. The solubilities of calcite, aragonite and vaterite in CO_2-H_2O solutions between 0 and 90°C, and an evaluation of the aqueous model for the system Ca–CO_3–H_2O. *Geochim. Cosmochim. Acta*, **1982**, *46*, 1011-1040.

(6) Brecevic, L., Nielsen, A.E. Solubility of amorphous calcium carbonate. *J. Cryst. Growth*, **1989**, 98, 504-510.

(7) Deer, W.A., Howie, R.A., Zussman, J. *An introduction to the Rock-Forming Minerals 2nd ed.* Pearson Prentice Hall Co., UK, **1992**.

(8) Rodriguez-Blanco, J.D., Shaw, S., Benning, L.G. The kinetics and mechanisms of amorphous calcium carbonate (ACC) crystallization to calcite, *via* vaterite. *Nanoscale*, **2010**, *3*, 265–271.

(9) Olderøy, M.Ø., Xie, M., Strand, B.L., Flaten, E.M., Sikorski, P., Andreassen, J.P. Growth and nucleation of calcium carbonate vaterite crystals in presence of alginate. *Cryst. Growth Des.*, **2009**, *9*, 5176-5183.

(10) Gomez-Morales, J., Torrent-Burgues, J., Rodriguez-Clemente, R. Nucleation of calcium carbonate at different initial pH conditions. *J. Cryst. Growth*, **1996**, *169*,

331-338.

(11) Kawano, J., Shimobayashi, N., Miyake, A., Kitamura, M. Precipitation diagram of calcium carbonate polymorphs: its construction and significance. *J. Phys. Condens. Matter*, **2009**, *21*, 425102-425109.

(12) Pouget, E.M., Bomans, P.H.H., Goos, J.A.C.M., Frederik, P.M., deWith, G., Sommerdijk, N.A.J.M. The initial stages of template-controlled $CaCO_3$ formation revealed by cryo-TEM. *Science*, **2009**, *323*, 1455-1458.

(13) Gebauer, D., Gunawidjaja, P.N., PeterKo, J.Y., Bacsik, Z., Aziz, B., Liu, L., Hu, Y., Bergstrom, L., Tai, C.W., Sham, T.K., Eden, M., Hedin, N. Proto-Calcite and Proto-Vaterite in Amorphous Calcium Carbonates. *Angew. Chem. Int. Ed.*, **2010**, *49*, 8889–8891.

(14) Bennema, P. Analysis of crystal growth models for slightly supersaturated solutions. *J. Cryst. Growth*, **1967a**, *1*, 278-286.

(15) Bennema P. Interpretation of the relation between the rate of crystal growth from solution and the relative supersaturation at low supersaturation. *J. Crystal Growth*, **1967b**, *1*, 287-292.

(16) Ookawa, A. Chapter 1: Growth of complete crystal. Crystal growth. Syokabo Co., Japan, pp.2-28, **1977**. (in Japanese)

(17) Saito, Y. Chapter 5: Surface kinetics. Crystal growth. Syokabo Co., Japan. pp. 81-90, **2002**. (in Japanese)

(18) LeBail, A., Ouhenia, S., Chateigner, D. Microtwinning hypothesis for a more ordered vaterite model. *Powder Diffr.*, **2011**, *26*, 16-21.

(19) Kanzaki, N., Uyeda, Q.P.T., Onuma, K. Intermolecular interaction of action revealed by a dynamic light scattering technique. *J. Phys. Chem. B*, **2006**, *110*,

2881-2887.

(20) Provencher, S.W. *Users Manual for CONTIN, Technical Report EMBL-DAO5*, Queens University Belfast, UK, **1982**.

(21) Nebel, H., Neumann, M., Mayer, C., Epple, M. On the structure of amorphous calcium carbonate–A detailed study by solid-state NMR spectroscopy. *Inorg. Chem.*, **2008**, *47*, 7874-7879.

(22) Hinedi, Z.R., Goldberg, S., Chang, A.C., Yesinowski, J.P. A ^{31}P and ^{1}H MAS NMR study of phosphate sorption onto calcium carbonate. *J. Coll. Interf. Sci.*, **1992**, *152*, 141-160.

(23) Bak, M., Thomsen, J.K., Jakobsen, H.J., Petersen, S.E., Petersen, T.E., Nielsen N.C. Solid-state ^{13}C and ^{31}P NMR analysis of urinary stones. *J. Urol.*, **2000**, *164*, 856-863.

(24) Tseng, Y.H., Zhan, J., Lin, K.S.K., Mou, C.Y., Chan, J.C.C. High resolution ^{31}P NMR study of octacalcium phosphate. *Solid State NMR*, **2004**, *26*, 99-104.

(25) Tsai, T.W.T., Chan, J.C.C. Recent progress in the solid-state NMR studies of biomineralization. *Annu. Rep. NMR Spectr.*, **2011**, 73, 1-61.

(26) Demichelis, R., Raiteri, P., Gale, J.D., Quigley, D., Gebauer, D. Stable prenucleation mineral clusters are liquid-like ionic polymers. *Nat. Comm.*, **2011**, 2, 590-597.

(27) deKanel, J., Morse, J.W. The chemistry of orthophosphate uptake from seawater on to calcite and aragonite. *Geochim. Cosmochim. Acta*, **1978**, *42*, 1335-1340.

(28) Gertman, R., Shir, I.B., Kababya, S., Schmidt, A. *In situ* observation of the internal structure and composition of biomineralized *Emiliania huxleyi* calcite by solid state NMR spectroscopy. *J. Am. Chem. Soc.*, **2008**, *130*, 13425-13432.

(29) Malkin, A.I., Chernov, A.A., Alexeev, L.V. Growth of dipyramidal face of

dislocation-free ADP crystals; free energy of steps. *J. Cryst. Growth*, **1989**, *97*, 765-769.

(30) Onuma, K., Oyane, A., Tsutsui, K., Tanaka, K., Treboux, G., Kanzaki, N., Ito, A. Precipitation kinetics of hydroxyapatite revealed by the continuous-angle laser light-scattering technique. *J. Phys. Chem. B*, **2000**, *104*, 10563-10568.

(31) Onuma, K., Kanzaki, N., Ito, A., Tateishi, T. Growth kinetics of the hydroxyapatite (0001) face revealed by phase shift interferometry and atomic force microscopy. *J. Phys. Chem. B*, **1998**, *102*, 7833-7838.

(32) Chernov, A.A. Stability of faceted shapes. *J. Cryst. Growth*, **1974**, *24/25*, 11-31.

(33) Chernov, A.A., Rashkovich, L.N. Spiral crystal growth with nonlinear dependence of step growth rate on supersaturation: the {110} faces of KH_2PO_4 crystals in aqueous solution. *J. Cryst. Growth*, **1987**, *84*, 389-393.

(34) Onuma, K., Ito, A., Tateishi, T. Investigation of a growth unit of hydroxyapatite crystal from the measurements of step kinetics. *J. Cryst. Growth*, **1996**, *167*, 773-776.

(35) Sazaki, G., Kurihara, K., Miyashita, S., Komatsu, H., Nakada, T. *In situ* observation of the concentration distribution around a lysozyme crystal by two-beam interferometry. *J. Jpn. Asso. Cryst. Growth*, **1996**, *23*, 413-421. (in Japanese)

(36) Kontoyannis, C.G., Vagenas, N.V. Calcium carbonate phase analysis using XRD and FT-Raman spectroscopy. *The Anal.*, **2000**, *125*, 251-255.

(37) Gopi, S., Subramanian, V.K., Palanisamy, K. Aragonite-calcite-vaterite: A temperature influenced sequential polymorphic transformation of $CaCO_3$ in the presence of DTPA. *Mater. Res. Bull.*, **2013**, *48*, 1906-1912.

(38) Onuma, K., Ito, A. Cluster growth model for hydroxyapatite. *Chem. Mater.*, **1998**, *10*, 3346-3351.

(39) Treboux, G., Layrolle, P., Kanzaki, N., Onuma, K., Ito, A. Symmetry of Posner's

cluster. *J. Am. Chem. Soc.*, **2000**, *122*, 8323-8324.

(40) Kanzaki, N., Treboux, G., Onuma, K., Tsutsumi, S., Ito, A. Calcium phosphate clusters. *Biomater.*, **2001**, *22*, 2921-2929.

(41) Demichelis, R., Raiteri, P., Gale, J.D., Dovesi, R. The multiple structure of vaterite. *Cryst. Growth Des.*, **2013**, *13*, 2247-2251.

(42) Wang, C.G., Liao, J.W., Gou, B.D., Huang, J., Tang, R.K., Tao, J.H., Zhang, T.L., Wang, K. Crystallization at multiple sites inside particles of amorphous calcium phosphate. *Cryst. Growth Des.*, **2009**, *9*, 2620-2626.

(43) Sugiura, Y., Onuma, K., Kimura, Y., Miura, H., Tsukamoto, K. Morphological evolution of precipitates during transformation of amorphous calcium phosphate into octacalcium phosphate in relation to role of intermediate phase. *J. Cryst. Growth*, **2011**, *332*, 58-67.

(44) Sendroy, J.J., Hastings, A.B. Studies of the solubility of calcium salts. III. The solubility of calcium carbonates and tertiary calcium phosphate under various conditions. *J. Biol. Chem.*, **1927**, *71,* 797-846.

(45) Greenwald, I. The effect of phosphate on the solubility of calcium carbonate and of bicarbonate on the solubility of calcium and magnesium phosphates. *J. Biol. Chem.*, **1945**, *161,* 697-704.

(46) Christoffersen, M.R, Christoffersen, J., Kibalczyc, W. Apparent solubilities of two amorphous calcium phosphates and of octacalcium phosphate in the temperature range 30–42°C. *J. Cryst. Growth*, **1990**, *106*, 349-354.

Chapter 5

Calcium carbonate polymorph selection effect of HPO_4^{2-} and $-PO_4^{2-}$.

5.1. Introduction

As described in Chapter 2 to 4, inorganic phosphate ion is great inhibitor of calcium carbonate formation. As described in Chapter 2 to 4, under weak basic solution, the inhibit effect of phosphate to vaterite was stronger than that to calcite. Around weak basic pH value, it is described that phosphate ions reveal mono charge described as $H_2PO_4^-$. However, it is indicated that the charge of phosphate ions is flexible, easily transformed double charges (HPO_4^{2-}) and non-charge (H_3PO_4) depending on solution pH.[1] It is natural that the affection of different charged phosphate into calcium carbonate formation was different. In addition, phosphate molecules were contained in numerous organic molecules as phosphate (forming as $-HPO_4^-$ or $-PO_4^{2-}$) functional groups. It was quite natural that the phosphate functional groups in organic molecules effect on calcium carbonate formation. However, it was also considered that their effect into calcium carbonate formation was different to that of HPO_4^{2-} or $H_2PO_4^-$, because of different charge of phosphate functional group under weak basic solutions. Thus, in this chapter, focusing on how dose HPO_4^{2-} affect to calcium carbonate crystalline phases, calcite and vaterite formation using phosphate-functional groups containing organic molecules which reveal $-PO_4^{2-}$ under weak based solutions or in high pH solution.

Calcite is a stable phase in weak basic solutions and formed as rhombohedral crystals.[2-5] The calcite crystal has well-developed crystal structure and completely cleavage surface. Vaterite is a metastable calcium carbonate phase present in weak basic solutions.[2-5] Vaterite shows higher solubility and comparatively lower crystallinity than calcite and aragonite.[2,6,7] Previous works showed that there are vaterite crystals with various morphologies, such as well-rounded spherulite, plate-like crystals, and dendritic forms.[8–11]

When calcium carbonate precipitated in a weakly basic solution, the intermediate transition phase, pseudo-vaterite and ACC, with lower stability and higher solubility than vaterite, formed prior to vaterite. These tendencies were reinforced in the increasing of phosphate ions.[12,13] When vaterite preferentially formed, mostly inorganic phosphate ions have $H_2PO_4^-$ structures.[1] Thus, it is considered that the effect of phosphate ions into vaterite (and calcite) is mono-charged ion effect. However, phosphate structure emerged not only inorganic ions but also phosphate-functional group of organic molecules. It is still unclear how HPO_4^{2-} and $-PO_4^{2-}$ act into calcium carbonate mineralization. In this work, using FMN as $-PO_4^{2-}$ in weal base solution, it was investigated how HPO_4^{2-} and $-PO_4^{2-}$ act in calcium carbonate mineralization. Furthermore, it is also investigated how HPO_4^{2-} ions affect into calcite formation especially morphology and surface roughness using high pH solutions.

5.2. Experimental Method

5.2.1. *Solution preparation.*

Experimental solutions were prepared as describing Chapter 2. In Chapter 3, five mother solutions were prepared: 1 M of $CaCl_2$, 2 M of Na_2CO_3, 25 mM of NaCl and KH_2PO_4 and FMN.

5.2.2. *The neutralization titration of FMN from HCl-acidic condition using NaOH.*

The 50 mL of 20 mM FMN and 100 mM HCl-containing solution was used for neutralization titration. It was stirred using magnetic stirrer bar at 400-600 rpm. The solution pH was monitored using pH electrode (#9615-10D, Horiba Co., Kyoto, Japan). 100 mM NaOH was added per 2 μL and recorded pH values.

5.2.3. *Preparation of FMN-containing supersaturated calcium carbonate solutions and their dynamics.*

Two stock solutions (cationic and anionic) were prepared. The cationic solution contained 1 M $CaCl_2$. The anionic solution was obtained by mixing H_2O (96.5 mL) and $NaHCO_3$ (2 mL) with various volumes of NaCl and FMN for a total volume of 0.5 mL. The FMN concentration in the anionic solution was 10 μM, and the ionic strength of the solution was maintained at 0.055 $[M/L]^2$ using NaCl.

FMN-containing supersaturated calcium carbonate solutions were prepared by mixing cationic and anionic solutions at a volume ratio of 1:99. This mixture was stirred at 400–600 rpm. Final ionic concentrations equaled 10 μM for FMN and 10 mM for Ca^{2+} and CO_3^{2-}. The pH of the final solutions amounted to about 8.6. Solutions were stirred at 400–600 rpm during the reaction.

5.2.4. *Observation and characterization of calcium carbonate precipitates.*

The FMN-containing calcium carbonate solutions were sampled at specific intervals to examine precipitate morphology and identify the polymorphs present during phase transformation.

Aliquots were centrifuged to separate precipitates from solution. The isolated precipitates were washed several times using a 1:1 mixture (v/v) of 99.5% ethanol and isopropanol. They put at room environment and eventually dried for FE-SEM and TEM observation.

Precipitate morphologies were observed by FE-SEM. Crystal phases were measured by XRD. The details were described in former chapters. Each step took 0.5 s. Chemical shifts were measured by an attenuated total reflection (ATR) type of FT-IR spectrometer (FT-IR: Nicolet 6300, ThermoScientific Co., USA) equipped with a triglycine sulfate (TGS) detector (32 scans, resolution 2 cm^{-1}). The background of measurements was atmosphere. The determination of the FMN-containing hollow structural vaterite relative surface area [m^2/g] was realized by low temperature nitrogen adsorption based on the method Brunauer et al.[14] and is termed Brunauer-Emmett-Teller (BET) surface area. The measurements were performed by BELSORP-minII, Nippon BEL Co., Osaka, Japan. The sample were evacuated at 40 °C over night and nitrogen was introduced in eleven pressure steps (P/P_0 = 0.05-0.30) at a temperature of -196 °C.

5.2.5. *In situ monitoring of the dissolution behavior of FMN-containing vaterite spherulites and FMN-calcite interactions by fluorescence optical microscopy.*

The morphological evolution of FMN-containing vaterite spherulites during dissolution and the interactions between FMN and the calcite surface were monitored by fluorescence microscopy (Olympus BX-53, Olympus, Tokyo, Japan). These experiments involved (1) setting up the *in situ* observation system as well as (2) preparing and reacting the solution for dissolution.

The *in situ* observation system consisted of a disposal self-built observation cell and a solution flow system, as previously described by Chapter 3. Briefly, the observation cell comprised a glass slide and polypropylene tubes, which were positioned on a Si plate coated with FMN-containing vaterite spherulites. To examine the morphological evolution of FMN-containing vaterite spherulites during dissolution, Si plates were dipped into a solution composed of 10 mM $CaCl_2$, 10 mM $NaHCO_3$, and 10 μM FMN for 2 h. The vaterite spherulite-coated plates were subsequently washed in double-distilled water and dried.

The Si plates were also dipped into a solution composed of 10 mM $CaCl_2$ and Na_2CO_3 for 2 h to form calcite crystals on the surface. The calcite crystals-coated plates were subsequently washed in double-distilled water and dried.

The observation cell was placed on a fluorescence optical microscope (Olympus BX-53, Olympus, Tokyo, Japan) equipped with a fluorescence optical filter set (Omega Optical Filter Set XF71, Omega Optical USA). FMN exhibits an excitation wavelength λ_e of 474 nm and a fluorescence wavelength λ_f of 540 nm.

The dissolution solution of vaterite spherulites used in the flow system contained 10 mM $NaHCO_3$, that of calcite crystals contained 10 mM $NaHCO_3$ and 10 μM FMN, were pumped using a rotary pump into the observation cell at 2 mL/min for 1 h.

5.2.6. *Synthesis of FMN-containing hollow vaterite by partial dissolution method.*

Vaterite spherulites were prepared in 2 h from 10 mM $CaCO_3$ and 10 μM FMN. Vaterite spherulites (about 0.1 g) were dispersed into 10 mM $NaHCO_3$ (500 mL) by stirring at 200–300 rpm for 2 h. Samples were treated and characterized, as previously described at section 2.3.

5.3. Result

5.3.1. *The neutralization titration of 20 mM FMN-containing aqueous solution.*

Figure 1 shows the acid-base titration curve of FMN. FMN aqueous solution showed two-plateau positions around pH 6-7 and 9-11. Ionic charge conversion induced plateau condition during titration. Then, these plateau conditions were corresponding to -PO4H$_2$ to -PO$_4$H$^-$ around pH 6-7 and -PO$_4$H$^-$ to -PO$_4$$^{2-}$ around pH 9-10, respectively. It is indicated that in weak basic solutions (pH around 9.0), phosphate-functional group of FMN showed mainly -PO$_4$$^{2-}$ form. Thus, when FMN molecules affect in calcium carbonate formation process, they act as PO$_4$$^{2-}$ form into calcium carbonate formation in weak basic conditions.

5.3.2. *Phase characterization of calcium carbonate formed in FMN-containing solutions.*

Figure 2 shows X-ray diffraction (XRD) patterns of calcium carbonate precipitates formed after 2, 6 and 12 h of stirring (400–600 rpm) at room temperature and 1 atm. These precipitates resulted from a mixture of 10 mM $CaCl_2$ and 10 mM $NaHCO_3$ (pH 8.6) in the presence or absence of FMN (10 μM FMN). The FMN-free samples (Fig. 2a) show peaks of calcite (closed reverse triangles) and vaterite (closed circles). The ratio of calcite increased with increasing reaction time. Conversely, FMN-containing samples showed only peaks for vaterite (Fig. 2b). FMN-free samples displayed peaks only for calcite after 12 h of reaction whereas calcite phase was not observed in 10 μM FMN-containing precipitates after 12 h.

FE-SEM micrographs (Figure 3) revealed that these precipitates mainly consisted of spherical vaterite crystals with diameters ranging from 2 to 5 μm formed in both FMN free or 10 μM FMN-containing solutions after 2 h of reaction. FMN-free precipitates mostly displayed irregular spherical shapes and aggregates (Fig. 3a). In addition, rectangular calcite crystals were often observed. In contrast, FMN-containing samples mainly comprised well-defined spherical crystals showing 1–5 μm diameters and a few irregularly shaped spherulites with 0.5–2 μm diameters (Fig. 3b). The results suggested that FMN acts as a homogenizer for the vaterite morphology, leading to the conversion of irregularly shaped particles to well-defined spherical particles. The well-defined spherical crystals consisted of 0.5–2 μm long and 10–100 nm thick rigid crystals. These fibrous crystals were tightly packed and radially elongated from the sphere centers. The average diameter of well-defined spherulite equaled 4.3 ± 0.8 μm by the counting method. The average radius of irregularly shaped spherulites was not calculated because they formed complex aggregates.

Figure 4a shows an FE-SEM image of an entire hollow FMN-free vaterite structure after partial dissolution. During the dissolution, the hollow structure maintained a well-defined spherical morphology resulting from the fibrous crystal aggregates. However, the FE-SEM image revealed a gap in the particle center. The structure comprised 50–100 nm thick shells of fibrous crystal aggregates (insert image of Fig. 4a), which were separated from each other. Their grain boundaries were clearly defined. Fig. 4b shows the XRD pattern of 10 μM FMN-containing vaterite obtained by partial dissolution. This XRD pattern was essentially the same as that before partial dissolution. The XRD sharp peaks corresponded to vaterite and no peaks of calcite were detected. The average diameter of the hollow centers in the particles was 1.5 ± 0.6 μm as determined using the counting method. The specific surface area of the resulting particle was 13.6 ± 5.3 m^2/g.

Note that the analysis of the FT-IR spectrum revealed the presence of small amount of an amorphous calcium phosphate phase (broad absorbance peak at approximately 986 cm^{-1}) in the FMN containing hollow vaterite spherical particles (Fig. 5a).[15] Fig. 5b showed FT-IR spectra in the calcium carbonate ν_3 vibration frequencies regions of the samples. Both samples revealed broad absorption peaks at 1398, 1440 and 1480 with 1490 cm^{-1} as a shoulder, which corresponded to poorly crystallinity vaterite or amorphous calcium carbonate (ACC).[16,17] However, they also showed shape peaks in the internal modes region (black solid circles in Fig. 5a). Thus, it was concluded that both samples were identified as low crystallinity vaterite rather than ACC.[16,17]

5.3.3. *Dissolution dynamics of FMN-containing vaterite spherulites.*

The dissolution behavior of FMN-containing vaterite formed in an undersaturated solution (10 mM $NaHCO_3$) was monitored *in situ* to clarify its formation mechanisms. Figure 6 shows the fluorescence image of vaterite spherical crystals that were settled on a silicon plate in a solution flow cell prior to dissolution. It can be seen that the spherical vaterite crystals exhibited no internal discontinuities. In addition, FMN was detected throughout the spherical crystals. The fluorescence image of the spherical crystals after 1 h of dissolution indicated boundary separations (Figure 5b). This result suggested that FMN affected the outer portions of the spherical crystals strong than their cores, thus inducing the formation of hollow structural vaterite spherulites, as previously observed for phosphate.[12,13] In general, vaterite is rapidly converted to calcite in aqueous solutions via a dissolution-reprecipitation process.[7] However, under FMN containing condition, this process was strongly inhibited. The key of this phenomenon was calcite surface interact between FMN in aqueous solutions.

5.3.4. *HPO_4^{2-} or -PO_4^{2-} interaction on calcite surface.*

Figure 7a showed fluorescence micrograph of calcite crystals in

FMN-containing solutions. It is clearly evidenced that the surface of calcite crystals were brightness. It was indicated that FMN absorbed onto calcite surface. Thus, it is concluded that the calcite formation inhibition effect of FMN is regarded as FMN absorbed onto the surface of calcite. Figure 7b showed FE-SEM micrograph of calcite crystals formed in 3 mM $CaCl_2$ and Na_2CO_3 and, 10 μM FMN-containing solutions at 2hours. Calcite crystals revealed porous structures.

It is suggested that HPO_4^{2-} absorbed onto calcite surface. When calcite formed under HPO_4^{2-}-containing high pH (above 12.0) condition, the surface and morphology of calcite was greatly altered. Figure 8 showed FE-SEM micrographs of calcite crystals formed in high pH condition (Fig. 8a: HPO_4^{2-} free, Fig. 8b: 10 μM HPO_4^{2-} and, Fig. 8c: 100 μM HPO_4^{2-}). In HPO_4^{2-}-containing solution, calcite crystals revealed porous structures. It suggested that HPO_4^{2-} ion absorbed onto calcite crystals and altered their morphologies. Furthermore, high HPO_4^{2-} induced vaterite (Fig. 8c). TEM observation with microtome method indicated porous calcite crystals were essentially consisted of randomly aggregation of pillar like calcite crystals ranging 5 nm in width and 20 nm in length, respectively (Fig. 8d-f). This structure was essentially regarded as *mesocrystal*.

Figure 9 showed XRD pattern of precipitates formed in various HPO_4^{2-}-containing solutions at high pH (above 12.0). In HPO_4^{2-} free or low concentration solutions, the precipitates were essentially calcite. However, in 100 μM HPO_4^{2-}-containing solution, precipitates showed a few amounts of vaterite peaks with large amount of calcite peaks. It indicated that HPO_4^{2-} induced vaterite formation in pH conditions.

5.4. Discussion

This tendency was clearly contrast to $H_2PO_4^-$ as described Chapter 2, 3 and 4. Briefly, the inhibit affection of vaterite is much stronger than that of calcite. However, it is clearly contrast that the affection of HPO_4^{2-} into calcium carbonate formation compare to $H_2PO_4^-$. It is strongly suggested that surface attraction of calcite and, HPO_4^{2-} or $-PO_4^{2-}$ play an essential role in inhibiting affection. The HPO_4^{2-} and $-PO_4^{2-}$ selective absorbed onto calcite surface and inhibit its growth. This tendency was similar to calcite-aragonite problems.[18-20] Some kind of polypeptide and protein selectively adhered onto calcite as if epitaxy. Phosphate ions were selective absorption should cause polymorph alternation even stabilized metastable phases.

Phosphate ions are easily converted H_3PO_4 ($-H_2PO_4$), $H_2PO_4^-$ ($-HPO_4^-$) and HPO_4^{2-} ($-PO_4^{2-}$) owing to the physico-chemical properties (for example, pH and ionic strength) of solution and chemical reactions.[1,21-23] It may be a factor of controlling to create process of their hard tissues using biological metabolisms. On the basis of molecular biology, biological beings may have altered phosphate ion charge (or functional groups) using their biological metabolisms to a suitable form to create calcium carbonate crystals. Furthermore, the selective effect onto calcium carbonate formation enables the development of advanced material synthesis methods using only simple molecules with switching process to translate their forms. For examples, it is hope to synthesis calcite-vaterite lamella crystal structures using phosphate conversion process.

5.5. Conclusion

FMN inhibited calcite formation even at low concentration ($FMN/CaCO_3$ = 1/1000). The HPO_4^{2-} and $-PO_4^{2-}$ adhered the surface of calcite by their selective adsorption onto calcite surface. The HPO_4^{2-} and $-PO_4^{2-}$ inhibited calcite formation and induced vaterite formation.

Metastable calcium carbonate phases are highly relevant to numerous industrial fields because of their highly flexible morphologies and sizes. However, their purification has proven challenging. Metastable calcium carbonate phases are highly relevant to numerous industrial fields but their purity is crucial. This basic knowledge contributes a fundamental technology that may provide control over metastable calcium carbonate polymorphs for advanced industrial science and technology using biocompatible materials.

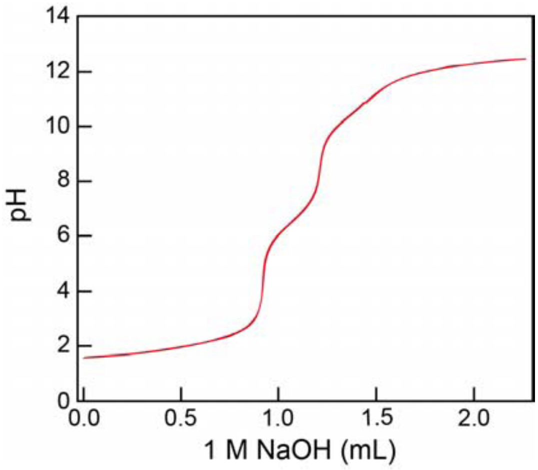

Figure 5.1. The neutralization titration curve of 100 mL of 20 mM FMN in HCl-NaOH systems.

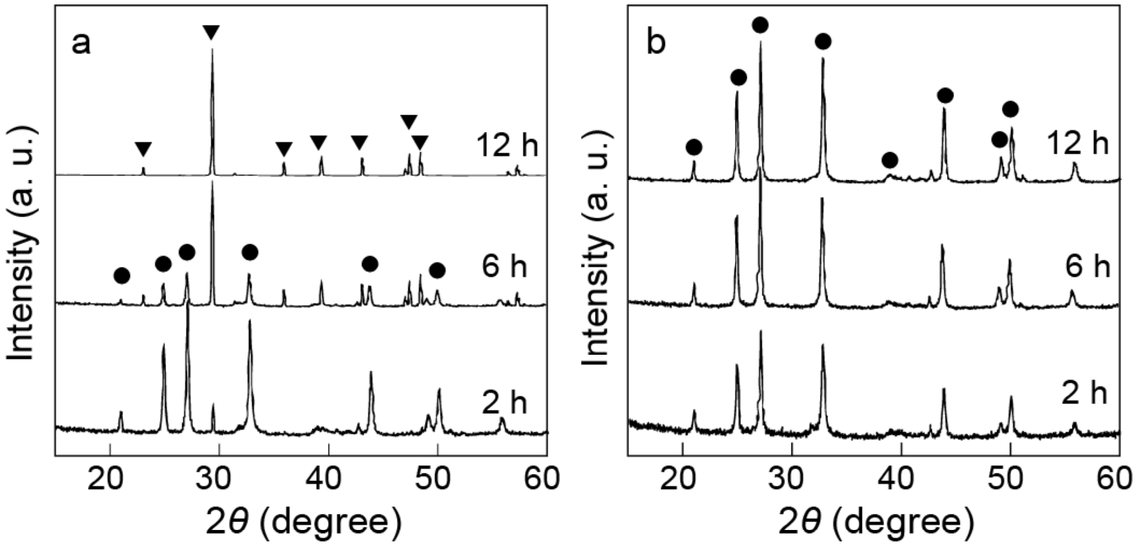

Figure 5.2. XRD patterns of precipitates generated from supersaturated calcium carbonate solutions after 2, 6 and 12 h. (a) FMN-free sample. (b) FMN-containing sample ([FMN] = 10 μM). Solid circles and solid reverse triangles indicate vaterite and calcite peaks, respectively.

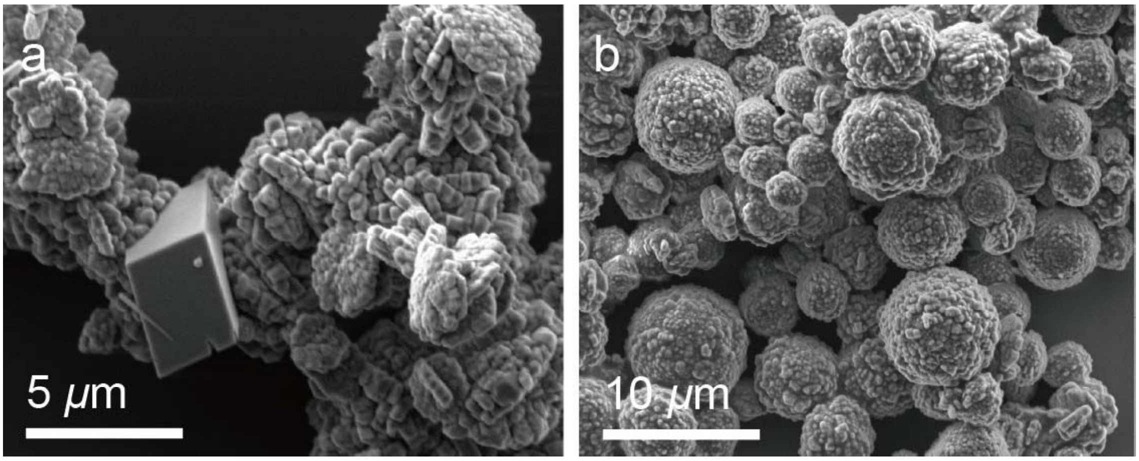

Figure 5.3. FE-SEM micrograph of precipitates generated from supersaturated calcium carbonate solutions. (a) FMN-free sample. (b) FMN-containing sample ([FMN] = 10 μM).

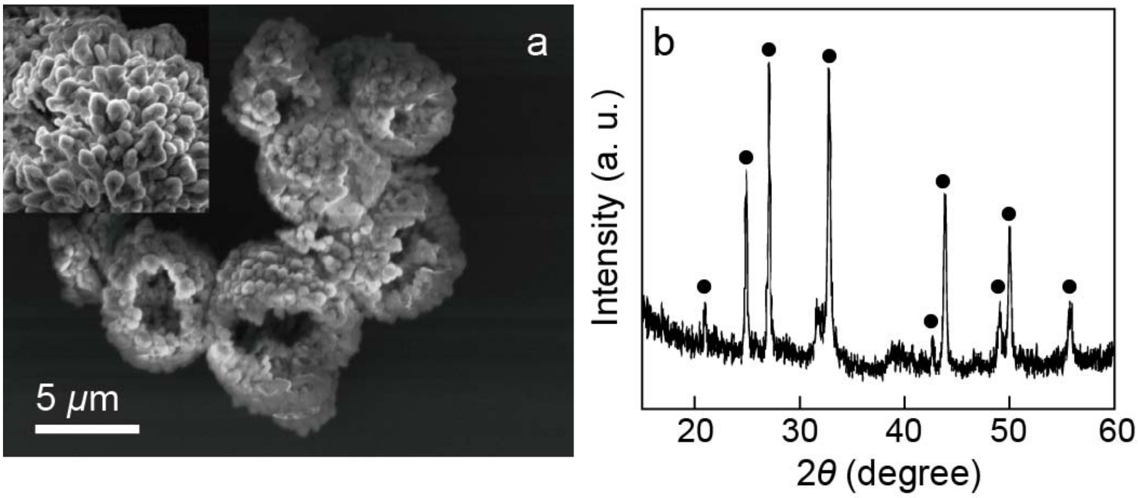

Figure 5.4. (a) FE-SEM micrograph and (b) XRD pattern of hollow vaterite spherulites after partial dissolution. Insert micrograph of (a) is surface structure of hollow vaterite. Solid circles in (b) indicate vaterite peaks.

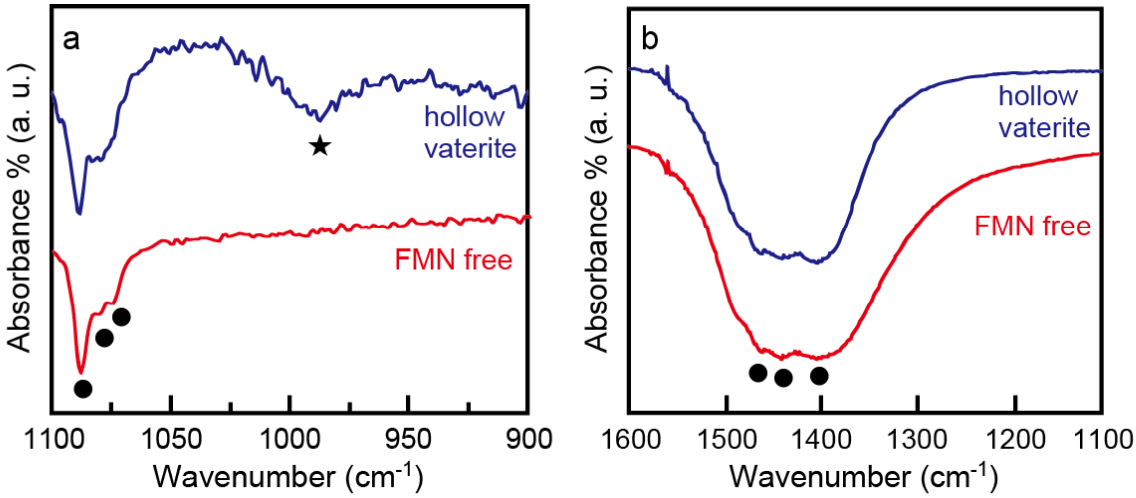

Figure 5.5. FT-IR spectra of hollow structural FMN-containing vaterite and FMN-free vaterite particles. (a) 900-1100 cm-1, which corresponding to internal modes region. (b) 1100-1600 cm^{-1}, which corresponding to v_3 vibration frequencies region. The black solid star and black solid circles indicate PO_4 vibration of ACP and CO_3 vibrations of vaterite, respectively.

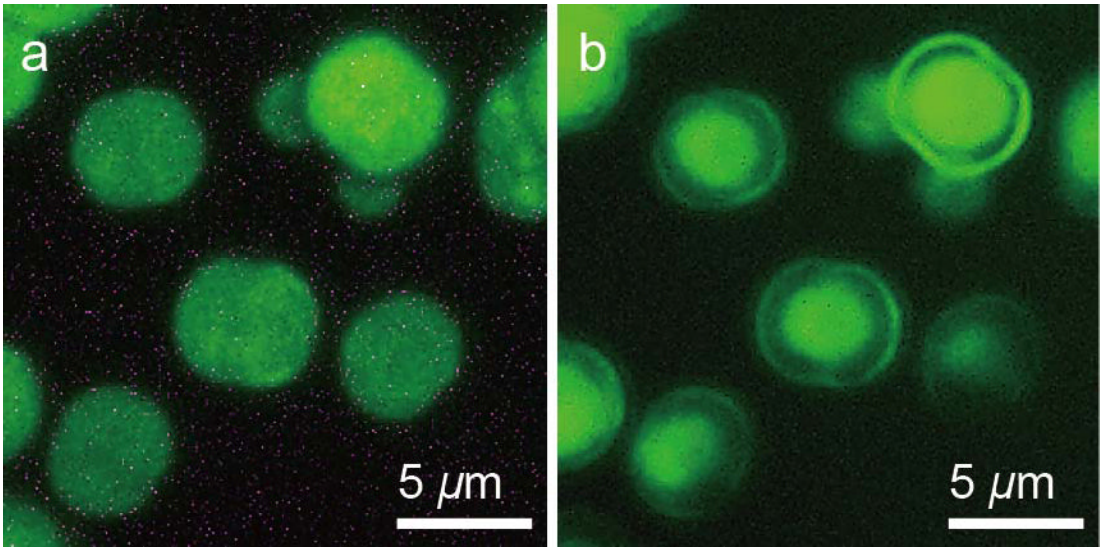

Figure 5.6. *In situ* fluorescence micrographs of FMN-containing vaterite spherulites during partial dissolution. (a) Before dissolution. (b) After 1 h.

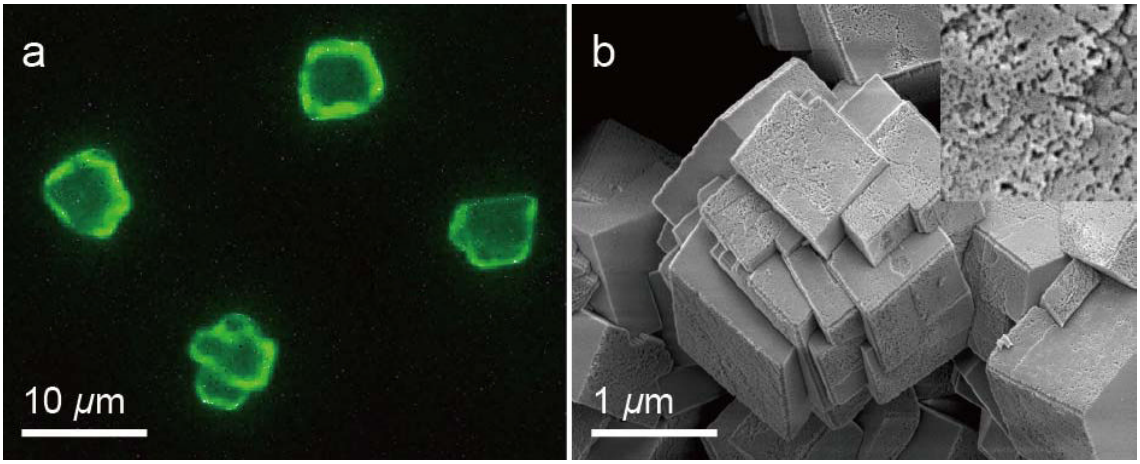

Figure 5.7. (a) *In situ* fluorescence micrographs of calcite crystals in 10 μM FMN-containing solution. (b) FE-SEM micrograph of calcite crystals formed in 3 mM $CaCl_2$ and Na_2CO_3 and, 10 μM FMN at 2 hours. Insert micrograph of (b) is surface structure of porous calcite.

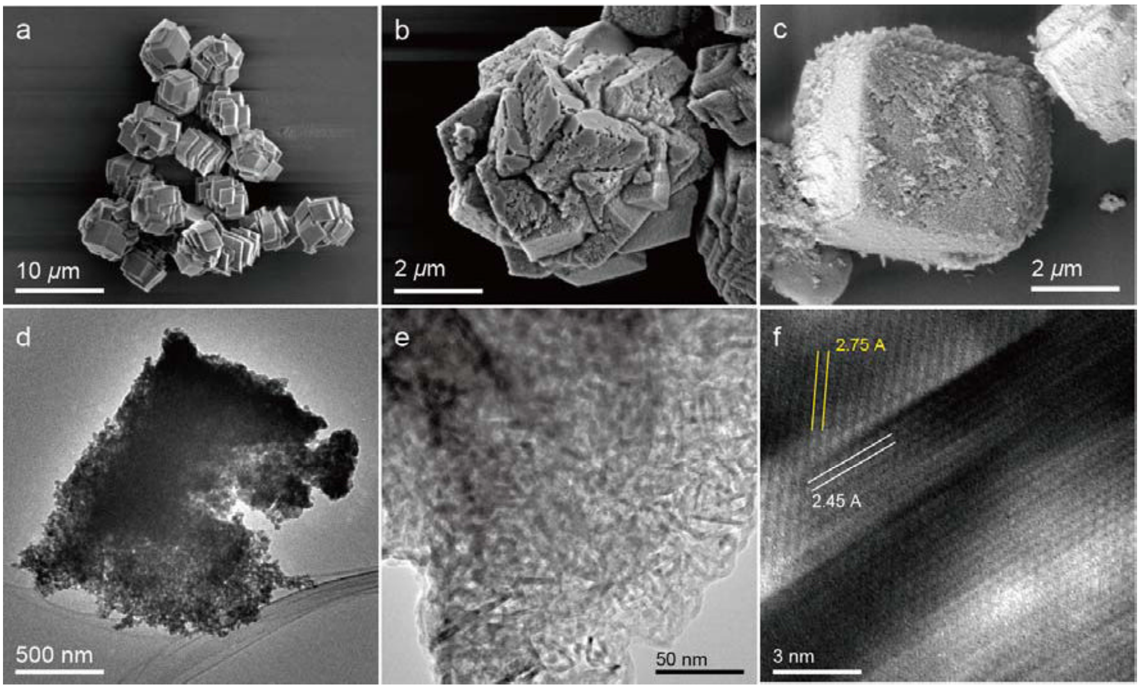

Figure 5.8. FE-SEM micrograph of porous calcite formed in high pH (above 12.0) solutions containing various HPO_4^{2-} ions at 2 hours. (a) HPO_4^{2-} free. (b) 10 μM HPO_4^{2-}. (c) 100 μM HPO_4^{2-}. TEM micrographs of ultrathin section of (b). (d) Low magnified micrograph of ultrathin section of porous calcite. (e) Mesoscale structure of (d). (f) HR-TEM micrograph of (e).

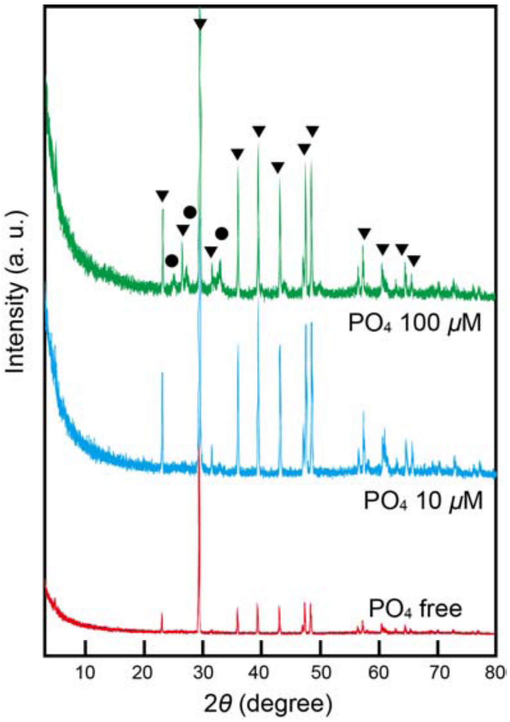

Figure 5.9. XRD patterns of precipitates formed in high pH (above 12.0) solutions containing various HPO_4^{2-} ions at 2 hours. Solid black triangle and solid black circle corresponded to calcite and vaterite, respectively.

Reference

(1) Arsic, J., Kaminski, D., Poodt, P., Vlieg, E. Liquid ordering at the Brushite-[010]-water interface. *Phys. Rev. B.*, **2004**, *69*, 245406, DOI: 10.1103/PhysRevB.69.245406.

(2) Ogino, T., Suzuki, T., Sawada, K. The formation and transformation mechanism of calcium carbonate in water. *Geochim. Cosmochim. Acta*, **1987**, *57*, 2757-2767.

(3) Mann, S. *Biomineralization Principles and Concepts in Bioinorganic Materials Chemistry*, Oxford University Press, UK. **2001.**

(4) Weiner, S., Dove, P.M. *An Overview of Biomineralization Process and the Problem of the Vital Effect.* In *Biomineralization*, *Reviews in Mineralogy and Geochemistry*; Dove, P.M., DeYoreo, J.J., Weiner, S., Eds.; The Mineralogical Society of America: Washington, DC, Vol. 54, p. 1-29. **2003.**

(5) Deer, W.A., Howie, R.A., Zussman, J. *An introduction to the Rock-Forming Minerals 2nd ed.* Pearson Prentice Hall Co., UK, **1992**.

(6) Plummer, L.N., Busenberg, E. The solubilities of calcite, aragonite and vaterite in CO_2-H_2O solutions between 0 and 90°C, and an evaluation of the aqueous model for the system $CaCO_3$-CO_2-H_2O, *Geochim. Cosmochim. Acta*, **1982**, *46*, 1011-1040.

(7) Rodriguez-Blanco, J.D., Shaw, S., Benning, L.G. The kinetics and mechanisms of amorphous calcium carbonate (ACC) crystallization to calcite, via vaterite, *Nanoscale*, **2010**, *3*, 265-271.

(8) Colfen, H., Antonietti, M. *Mesocrystals and Nonclassical Crystallization.* John Wiley and Sons, Ltd., UK, **2008**.

(9) Xu, A.W., Antonietti, M., Colfen, H., Fang, Y.P. Uniform Hexagonal Plates of Vaterite $CaCO_3$ Mesocrystals Formed by Biomimetic Mineralization. *Adv. Funct.*

Mater., **2006**, *16*, 903-908.

(10) Kuther, J., Seshadri, R., Knoll, W., Tremel, W. Templated growth of calcite, vaterite and aragonite crystals on self-assembled monolayers of substituted alkylthiols on gold. *J. Mater. Chem.*, **1998**, *8*, 641-650.

(11) Beck, R., Andreassen, J.P. The influence of crystallization conditions on the onset to dendritic growth of calcium carbonate. *Cryst. Res. Tech.*, **2012**, *47*, 404-408.

(12) Sugiura, Y., Onuma, K., Kimura, Y., Tsukamoto, K., Yamazaki, A. Acceleration and inhibition effects of phosphate on phase transformation of amorphous calcium carbonate into vaterite, *Am. Min.*, **2013**, *98*, 262-270.

(13) Sugiura, Y., Onuma, K., Nagao, M., Momma, K., Kimura, Y., Yamazaki, A. Dissolution behavior of vaterite spherulites in solution containing phosphate ions, *J. Cera. Soc. Jpn.*, **2014**, *122,* 679-684.

(14) Brunauer, S., Emmett, P.H., Teller, E. Adsorption of Gases in Multimolecular Layers. *J. Am. Chem. Soc.*, **1938**, *60*, 309-319.

(15) Nakamura, J., Kasuga, T. Enhancement of crystalline plane orientation in silsesquioxane-containing vaterite particles towards tuning of calcium ion release. *J. Mater. Chem. B*, **2014**, *2*, 1250-1254.

(16) Gago-Duport, L., Briones, M.J., Rodríguez, J.B., Covelo, B. Amorphous calcium carbonate biomineralization in the earthworm's calciferous gland: pathways to the formation of crystalline phases. *J. Struct. Biol.*, **2008**, *162*, 422-435.

(17) Andersen, F.A., Brecevic, L. Infrared Spectra of Amorphous and Crystalline Calcium Carbonate. *Acta Chimica Scandinav.*, **1991**, *45*, 1018-1024.

(18) Elhadj, S., Salter, E.A., Wierzbicki, A., DeYoreo, J.J., Han, N., Dove, P.M., Peptide Controls on Calcite Mineralization: Polyaspartate Chain Length Affects Growth

Kinetics and Acts as a Stereochemical Switch on Morphology. *Cryst. Growth. Des.*, **2006**, *6*, 197-201.

(19) Elhadj, S., DeYoreo, J.J., Hoyer, J.R., Dove, P.M. Role of molecular charge and hydrophilicity in regulating the kinetics of crystal growth. *Proc. Nati. Acad. Sci. USA*, **2006**, *103*, 19237 - 19242.

(20) Falini, G., Albeck, S., Weiner, S., Addadi, L. Control of Aragonite or Calcite polymorphism by Mollusk shell Macromolecules, *Science*, **1996**, *271*, 67-69.

(21) Abbas, C.A., Sibirny, A.A. Genetic Control of Biosynthesis and Transport of Riboflavin and Flavin Nucleotides and Construction of Robust Biotechnological Producers. *Microbiol. Mol. Biol. Rev.*, **2011**, *75*, 321-360.

(22) Linari, M., Caremani, M., Lombardi, V. A kinetic model that explains the effect of inorganic phosphate on the mechanics and energetics of isometric contraction of fast skeletal muscle. *Proc. Royal Soc. B Biol. Sci.*, **2010**, *277*, 19-27.

(23) Swanson, M.A. Studies of the non-oxidative exchange between inorganic phosphate and ATP, as catalyzed by intact mitochondria. *Biochim. Biophys. Acta*, **1956**, *20*, 85-91.

Division II
Calcium Phosphate Systems

Chapter 6

Formation behavior of HAP in CGNs-containing solutions.

6.1. Introduction

In *Division I*, calcium carbonate systems were investigated. In *Division II*, calcium phosphate systems are investigated. In calcium phosphate systems, carboxylic-functional group (-COOH) was used as one of additives. In Chapter 6, it was investigated how immobilized -COOH (CGNs) affect into formation dynamics of HAP from ACP in weak basic solution.

HAP ($Ca_{10}(PO_4)_6(OH)_2$) is a stable phase of calcium phosphates in weak acidic to basic solutions and main inorganic component of vertebrate biological hard tissues such as teeth and bones.[1-4] It is thus very important to control and accelerate HAP mineralization in tissue engineering and regeneration medicine, such as for application to rapid fracture treatment and advanced teeth implant. The key to achieve this is to find the factors and materials that accelerate HAP formation under pseudo physiological conditions.

Various proteins and polypeptides are assumed to interact with HAP, therefore, their roles on HAP crystallization has been investigated energetically.[5-8] Tsuji et al.[9] synthesized artificial proteins with various molecular weights and isoelectric points, all of which contained peptide motifs present in dentin matrix protein 1 (DMP1). These motifs accelerate HAP formation when they are immobilized on a substrate. [8,10] Tsuji et al. [9,11] investigated several combinations of DMP1 motifs and containing their motifs in the synthesized proteins, and succeeded to accelerate HAP formation from transformation of ACP by approximately 20 % as compared to the case without proteins.[11] It should be noted that the acceleration of HAP formation was achieved even though the protein molecules were dispersed in the solutions, not immobilized on substrates. However, the detail mechanism of acceleration was not clarified although the specific functional group of proteins, such as immobilized -COOH one, may have important role on acceleration.

Here it is assumed that the immobilized -COOH itself and their quantity have definitive effect on acceleration of HAP formation irrespective of the three-dimensional conformation of protein molecules. Indeed, artificial proteins by Tsuji et al. [11] did not have any particular conformation in the solutions. It is still unclear what factors, for example isoelectric point of protein, which reflects the number of immobilized -COOH, morphology of sub-chain of protein molecules determine the transformation rate from ACP to HAP.

In Chapter 6, it is hypothesized that immobilized -COOH amounts in solutions were main factor for the transformation rate form ACP to HAP. It was prepared the hybrid materials of carboxylic mercaptan (MUA: mercapt-undecanolic acid, $HS(CH_2)_{10}COOH$) and gold nanoparticles colloids called CGNs, which could be used as simulated -COOH rich proteins. It was investigated how the CGNs contributed the transformation dynamics from ACP to HAP and discussed the possible mechanism of acceleration of HAP formation based on the data obtained using pH monitoring, time-resolved static light scattering (TR-SLS), *in situ* FT-IR, and HR-TEM.

6.2. Experimental Method

6.2.1. *Preparation of stock solution used in the experiments of ACP into HAP phase transformation.*

$CaCl_2$ (Special grade, Wako Pure Chem. Inc., Tokyo, Japan), K_2HPO_2, KH_2PO_4, and NaCl (Special grade or molecular analysis grade, Nakarai Tesque Inc., Kyoto, Japan) were dissolved in double distilled water (specific resistance of 18.2 MΩ and total organic contents (TOC) of >5 ppb). Mercapt-undecanolic acid (MUA: $HS(CH_2)_{10}COOH$) (Sigma-Aldrich Co., USA) was were dissolved in 99.5 % ethanol (Wako Pure Chem. Inc.). Prepared four water stock solutions and a ethanolic solution were: 1M $CaCl_2$, 0.5 M KH_2PO_4, 0.5 M K_2HPO_4, 2 M NaCl and 20 mM MUA ethanolic solution. Mixed the KH_2PO_4 and K_2HPO_4 solutions were to obtain 0.5 M KDP-KAP solution with a pH of 8.0 (22℃).

6.2.2. *Preparation and characterization of CGNs.*

The gold nanoparticles were a commercial-grade gold colloid (Gold Colloid 5 nm, BBI solutions Co., UK) that contained approximately 300 µM of gold. A 20 mM MUA (99 %, Sigma-Aldrich Japan K.K., Tokyo, Japan) ethanolic solution (5 mL) was added to this solution (5 mL) and the mixture was left at room temperature for more than 3 h to allow the formation of self-assembled MUA layers on the gold particles in a glass bottle. The mixed solution was then dialyzed for more than 120 h into 3 L ultra-pure water through a cellophane membrane. The water was changed at 12 h intervals. The pH of the final solution containing CGNs was approximately 4.5. For comparison purposes, a reference colloid solution containing gold nanoparticles was also dialyzed into ultra-pure water.

The CGNs were characterized using, dynamic light scattering (DLS), zeta potential analysis, and visible-light adsorption spectroscopy analysis. The detail of multi-angle DLS[12] measurement and visible-light adsorption spectroscopy was described in Chapter 4.

Apparent Zeta-potential, ζ measurements revealed the presence of a double electric layer of colloidal particles in the solutions. The surface charge of the CGNs was compared with that of the dialyzed gold nanoparticles (reference) to estimate the formation of Au-S bonds on the gold nanoparticles using an ELSZ-1000Z photoelectric spectrometer (Otsuka Electric Co., Osaka, Japan). The particle concentration in both measured solutions was 50 μM. The solution temperature and pH were 25 °C and 6.5 (buffered using 5 mM KDP-KAP), respectively. A 30 mV semiconductor laser (λ_w=660 nm) was used as the light source and the impressed voltage between the electrodes was 10 kV. The detection angle of the scattered light was 15° with avalanche photodiode (APD) detector. The ζ potential was given by using Smoluchowski equation[13] followed as

$$u = (\varepsilon_0 \varepsilon_r / \eta)\, \zeta \qquad (1)$$

The u is relative velocity between interface and solution; η is viscosity of solution as 0.89 mPa, ε_0 is electric permittivity of vacuum as 8.85×10^{-12} Fm^{-1}, and ε_r is relative electric permittivity of solution as 78.5 Fm^{-1}.

The formation of Au-S bonds on the gold nanoparticles was also estimated using visible-light absorption spectroscopy.

6.2.3. *Monitoring of changing pH values of supersaturated calcium phosphate solution with various CGNs concentrations as phase transformation.*

All experiments were done under 22℃ and 1 atm conditions. The various CGNs-containing supersaturated calcium phosphate solution was prepared by mixing stock solutions. As they were mixed, they were stirred at 400-600 rpm with a magnetic stirrer. It was prepared three different calcium phosphate concentrations ($CaPO_4$: 3, 3.25

and 4 mM).

The change in the pH value of each solution over time as it was stirred at 400-600 rpm was measured using a pH electrode (LAQUA standard ToupH electrode 9615-10D, Horiba Co., Kyoto, Japan) connected to a multi-meter (D-51AC, Horiba Co., Kyoto, Japan). The electrode was soaked in Ca^{2+} ion free reaction solution for few minutes to stabilize the electrode condition. The pH value of the mixed solutions were recorded every 2 s, and the phase transformation time of the materials was determined using a concentration time curve (the details were described in the Result section).

6.2.4. *TR-SLS observation of time evolution of particles molecular mass (M_w), gyration radius (R_g) and fractal dimension (D_f) in various CGNs-containing concentration.*

The theory and setup of TR-SLS are described in Ref.[15-17] The main components of the instrument are an ellipsoidal mirror and a high-speed charge-coupled-device (CCD) camera. TR-SLS obtained the scattering intensity of dispersed particles as scattering angles ranging from 10° to 170°, with an angle resolution of 1° and a maximum time resolution of 1 s. The measurement temperature was 22℃.

The light source was a He-Ne laser (λ_W=632.8 nm). It was prepared two kind of solutions for measurement: cation solution (1 M $CaCl_2$) and anion solution (mixture of 3.26 mM KDP-KAP, 401.17 mM NaCl and 0-30.09 μM CGNs-containing solutions buffered at pH 7.6. Both solutions were filtered 220 nm filters (syringe- and centrifuge filter) to remove dusts which disturb measurements before mixing. The two solutions were quickly mixed in the measurement cells; the volume ratio of cation and anion solutions was 1: 306.7. The final solutions contained 3.25 mM Ca and PO_4, 400 mM

NaCl and, 0-30 μM CGNs. The amount of solutions was 18.0 mL. After solution preparation, the scattering intensity with angular dependence was recorded every 2 s, the changes in molecular mass, M_w and the gyration radius, R_g were calculated from measured scattering intensity and behavior.

The relationship between the scattering intensities and scattering angles was analyzed by Zimm-square-root plot which is suitable for lineally analysis because its data are likely to show lineally trend in low angular compare to those of Zimm-square plot. The excess Rayleigh ratio ΔR of the sample solution (difference in scattering intensity between the sample and buffer solutions) depends on q, M_w, Rg, particle concentration c, second virial coefficient of the particles $A2$, and the optical constant K, which includes the refractive index increment of the sample solution with the particle concentration. The Rayleigh ratio is given by,

$$(Kc/\Delta R)^{1/2} = (1/M_w)^{1/2}(1+q^2R_g^2/6)+2A^2c. \qquad (2)$$

Because Eq. (1) cannot be extrapolated to the $c \rightarrow 0$ limit in TR-SLS measurements, it was specified M_w as apparent rather than actual. The contribution of the $A2c$ term is usually neglected in TR-SLS measurements because it is much smaller than the first term on the right-hand side of Eq. (1). Fractal dimension, D_f was also obtained using relationships between q and interparticle scattering factor which related I_s as followed

$$I_s = \mathrm{A}q^{-D_f} \qquad (3)$$

The A is constant. In this work, the scattering intensity of dispersed particles was calculated for scattering angles ranging from 10° to 80° for D_f of aggregate, so as to avoid any stray light and large size aggregate effect. Molecular analysis grade of toluene used as standard of scattering intensity ($I_s/I_0 = 7.0$, I_0 is reference scattering intensity.).

6.2.5. *In situ FT-IR measurement of chemical bond evolution in various CGNs concentration during ACP-HAP phase transformation.*

Measured solutions were previously mixed in 2 mL polypropylene tubes after filtration using 220 nm syringe filters. Approximately 5 μL solution of measured solutions were mounted on horizontal diamond single crystal of attenuated total reflection prism of infrared spectra (ATR-FT-IR; Nicolet 6300, ThermoScientific Co., USA) equipped with a TGS-detector (32 scans, resolution 2 cm^{-1}). The measured interval was approximately 90 s. To avoid evaporation, it was covered measured solution by silicon gum caps.

6.2.6. *Phase identification of calcium phosphate phases formed in various CGNs concentration solutions during ACP-HAP phase transformation.*

The calcium phosphate solutions were sampled at all reaction stages (during transformation from the amorphous to the crystalline phase and the subsequent precipitation stage) to determine how the material phases, structures and morphologies changed over time using TEM, XRD and FE-SEM/EDX. In EM observation, ACP particles and precipitates obtain methods were below. 2 mL reaction solutions were sampled into polypropylene tubes and centrifuged for 30 s. After centrifugation, the precipitates were gathered and washed using mixed alcohol (ethanol: isopropyl alcohol = 1: 1 in volume wait) for several times and dropped on TEM Cu microgrid covered carbon holey films and air dried on KimWipes® for TEM observation. The treated ACP particles and precipitates were also mounted on 11 nine pure Si plate for FE-SEM/EDX measurement. In FE-SEM/EDX measurement, at least 15 samples were measured in each condition. The calibration was operated as auto calibration mode.

The prepared ultra-thin (about 200 nm) cross-sections were placed on a Cu micro-grid for TEM analysis. The analysis was performed using a normal observation holder (TEM: JEM2200, JEOL Co.,, Tokyo, Japan) at acceleration voltages of 200 kV.

XRD (RINT40, Rigaku Co., Japan, λ_w = 0.15406 nm) analyses were performed at an acceleration voltage of 50 kV and a magnitude of 100 mA using a Cu target. The 2θ value was varied from 3° to 60° in 0.01° increments. The time required per step was 0.5 s. The entrance slit size was 5 mm × 10 mm.

6.3. Results

6.3.1. *Characterization of the reference gold nanoparticle and CGNs-containing solutions*

Figure 1 plots the results of the dynamic light scattering (DLS) measurements for the reference gold nanoparticle and CGNs solutions. The $G^2(q, t)$s values (Fig. 1a) obtained for the solubilized CGNs at two concentrations were sufficiently clarified (high S/N ratio) to calculate the value for τ. The value of D for each type of solution was then calculated using Eq. (3) (Fig. 1b), and its concentration dependence was measured for both solutions containing reference gold nanoparticles and CGNs (Figs. 1c and d, respectively). Using D_0, the r_H values for the gold nanoparticles and CGNs were calculated as 3.0 ± 0.2 nm and 6.9 ± 0.6 nm, respectively, indicating that -COOH were immobilized on gold nanoparticles. The errors in r_H in this study were larger compared with a previous study using the same equipment because a number-weight analysis was adopted for the calculation of the τ values.[18] Note that D increased linearly as the concentration of reference gold nanoparticles increased, suggesting a repulsive intermolecular interaction. In contrast, the negative relationship between D and the

CGNs concentration indicates that the contribution of an attractive force was increased with concentration decreasing.

The apparent ζ of the 50 μM reference gold nanoparticles and 50 μM CGNs in solution were -45.5 and -48.1 mV, respectively. These results indicate that the surfaces of the CGNs were more negatively charged than those of the gold nanoparticles because of the ionized -COOH in reacting condition. The larger attractive interaction and hydrodynamic radius of the particles in the CGNs-containing solution compared with those in the reference solution (Figs. 1 c and d) suggested that the van der Waals forces of the particles increased owing to the presence of -COOH, leading to aggregation of the particles, although the increase in the average surface charge would be expected to disperse the particles.

Figure 2 shows visible-light absorption spectra of both solutions. The reference gold nanoparticles-containing solution was red, whereas the CGNs-containing solution was *sakura-iro* (a traditional pink similar to mauve Japanese color). The -COOH shifted the band of the absorption spectrum from 515.5 nm (reference solution) to 518.5 nm (CGNs-containing solution). Because the wavelength can be resolved to below 0.5 nm, this shift in the absorbance band is real.

6.3.2. *Change in pH over time for CGNs-containing solutions in relation to initial calcium phosphate concentrations and phase characterization of precipitates formed in control or various CGNs or reference gold nanoparticles-containing solutions.*

Figures 3 and 4 show the change in pH over time for CGNs-containing solutions with stirring. The concentrations of initial calcium and phosphate ions were 3.00 (Fig. 3a), 3.25 (Fig. 3b), and 4.00 mM (Fig. 4a), respectively. Figures 3a and b show the data when the concentration of CGNs in the solution was widely varied (from 0.25 to 10 μM in 3a and from 3 to 30 μM in 3b). In each solution, the pH immediately decreased when $CaCl_2$ was added to phosphate solution independent of the CGNs' concentrations. Then, it quickly increased and reached local maximum within 20 s. After the local maximum, the solution pH gradually decreased and reached a critical point where the pH showed rapid decrease. In this critical pH, crystalline phases appeared in ACP particles that were confirmed by lattice fringes in HR-TEM observation (see detail in below section). After a rapid decrease, the solution pH was stabilized at about 6.2. In 3.00 and 3.25 mM calcium phosphate concentrations, solutions were clouded when the pHs were stabilized. The solution clouding was not due to the rapid decrease in pH, but to the formation of crystalline phases in the ACP.

Crystallization threshold time, t_{cryst}, was defined as the point where the tangent of initial rapid pH-decrease curve crossed to that of subsequent gradual pH-decrease curve (see Figure 3c).

Figures 3d and e show the relationship between t_{cryst} and CGNs concentration in 3.00 and 3.25 mM calcium phosphate solutions. In the 3.00 mM solution (Fig. 3d), the t_{cryst} was minimum when the concentration of CGNs was 1.75 μM, indicating that the crystallization was accelerated to the maximum at this CGNs concentration. The acceleration degree for crystallization was defined by $t_{cryst}/t_{cryst\ (\mathrm{CGNs}=0)}$, and hereafter called as acceleration index. The index observed in Fig. 3d was about 45%, which was much larger than that observed by using artificial proteins (at maximum 20%).[9,11] When the initial concentration of calcium phosphate increased to 3.25 mM (Fig. 3e), the maximum index was about 25%, indicating that the index was controlled by the calcium phosphate concentration. The relationship between t_{cryst} and CGNs concentration in the solution without stirring (Figure 5) showed similar feature with that in Fig. 3d or e.

After the minimum point of t_{cryst}, it continuously increased with the increase in CGNs concentration in both 3.00 and 3.25 mM solutions, although the shapes of increasing curves were different from each other. Above 10 μM CGNs in 3.00 mM calcium phosphate solution or 30 μM CGNs in 3.25 mM calcium phosphate solution, there were no sign of rapid pH drop until the final stage of reaction (8h), indicating that neither nucleation nor precipitation of crystalline phases occurred in the solutions.

XRD patterns of precipitates formed in the clouded solutions containing 3.00 mM calcium phosphate with CGNs less than 10 μM and 3.25 mM calcium phosphate with CGNs less than 30 μM at 2 h after solution preparation showed broad peak at around 2θ= 24-32°, which corresponded to calcium phosphate crystalline phases with low crystallinity indicated cluster based phase transformation. Although this peak can be attributed to that of OCP, β-TCP, DCPD and DCPA except HAP, it did not find any specific peaks of other calcium phosphates than HAP in the XRD patterns (Figure 6). HR-TEM images showed that the lattice fringes observed in the precipitates were mainly attributed to those of HAP (see Figs. 9 and 10). Thus, it was concluded that the precipitates formed in the solutions containing 3.00 mM and 3.25 mM calcium phosphates were both HAP. Above 10 μM CGNs in 3.00 mM calcium phosphate solution or 30 μM CGNs in 3.25 mM calcium phosphate solution, it did not find any crystalline phases in XRD measurements and HR-TEM observations (see Figs. 9 and 10).

6.3.3. ***TR-SLS measurement for ACP-HAP phase transformation dynamics depending on concentration of CGNs in solution.***

The changes in apparent molecular weight (M_w) and gyration radius (R_g) of calcium phosphate particles at early stage during ACP-HAP transformation were measured using TR-SLS. Fig. 7a shows the typical relationship between modified scattering intensity (I_s/I_0) and angular dependence. As is seen, the intensity decreases smoothly with the scattering angles for each period. This indicates the wide size distribution of the aggregate particles. Based on this data, the apparent molecular weight and radius of gyration of the aggregates were calculated using Zimm-square-root plot. Fig. 7b shows the typical Zimm-square-root plot determined from the scattering intensity of $CaPO_4$ particles in solution (3.25 mM $CaCl_2$ and KDP-KAP, CGNs free). As seen from the figure, the plot tends to curve at higher angles, indicating the aggregation of the particles. Conversely, the plot corresponding to lower angles (30° to 70°) is relatively linear. Therefore, the linear part of the plot was considered for calculation, so as to avoid the effect of aggregation in determining M_w, R_g, and D_f of the $CaPO_4$ particles (see green line in Fig. 7b).

The average R_g of initial ACP particles appeared just after solution preparation was around 200 nm and it was kept constant until the final precipitation stage independent of the CGNs concentration. On the other hand, M_w of particles decreased rapidly within initial 500 s although R_g was constant. Because the particles smaller than around 50 nm showed no angular dependence on scattering intensity and did not affect the calculation of R_g in SLS measurement, the data suggested the rapid vanishing of these small particles during initial stages. Except 10 μM CGNs-containing solution, rapid decrease of M_w just after starting reaction was observed independent of the CGNs concentration. After rapid decrease, the M_w gradually increased and reached local maximum (green arrows in Fig 2), which corresponded to the period that the solution pH rapidly dropped and calcium phosphate crystalline (HAP and OCP) specific bands appeared in the FT-IR spectra (see Figure 10). The M_w then gradually decreased and reached local minimum point. The duration to reach the minimum point depended on the CGNs concentration at CGNs molar ratio about 1/1000 of Ca concentrations. After this period, the M_w showed drastic increase with the increase in R_g, and the precipitates appeared in the solutions.

In the 10 μM CGNs-containing solution, in which the rapid drop in pH was not observed, the M_w kept constant over time (Figure 8) that was consistent to the data in pH measurement.

Unlike the time evolutions of R_g and M_w, the D_f values of $CaPO_4$ aggregate particles that formed in the solutions exhibited a peculiar time evolution, which indicates the internal evolution and construction of $CaPO_4$ particles. Immediately after mixing, D_f simply increased during the initial M_w decreasing stage. With the exception of the 10 μM CGNs-containing solution, the time evolutions of D_f of the aggregate $CaPO_4$ particles showed a contrast till the pH dropped. After the pH dropped, the D_f values of the aggregate $CaPO_4$ particles exhibited an increasing trend until the precipitation period. In the CGNs-free solution, the increasing trend of D_f was consistent with that of R_g. It indicated that HAP formed when the crystals attained critical size, showing nucleation and growth trends. On the other hand, in the 5 μM CGNs-containing solution, with the exception of the final precipitation period, D_f increased while R_g was maintained constant. It indicated that HAP formed through the cluster rearrangement of internal structural reconstruction in ACP particles.[9,15]

In the 10 μM CGNs-containing solution, D_f reached 1.8 at 2000 s, and it was maintained constant over time as in the case of M_w.

The duration until the rapid increase in both M_w and R_g was shortened with CGNs concentration up to 5 μM (Figs. 8c,d). In this concentration range of CGNs, the increasing degree of M_w and R_g was also changed exponentially to lineally increasing mode. From 5 to 10 μM of CGNs concentration, the duration up to precipitation was elongated but both M_w and R_g increasing period (precipitation period) had been shortened. Above 10 μM, it could not be observed M_w and R_g rapidly increasing which corresponded to precipitation in experiment periods (around 3 h).

6.3.4. *In situ FT-IR measurement for ACP-HAP phase transformation dynamics in control, reference gold nanoparticles or CGNs-containing solutions.*

The change in local structure of calcium phosphates over time in the solutions was investigated using *in situ* FT-IR. Figure 9 shows the change in the bands corresponding to P-O stretching band over time measured in 3.25 mM calcium phosphate solutions without CGNs (Fig. 9a), with 5 μM CGNs (Fig. 9b) and 5 μM reference gold nanoparticles (Fig. 9c). Calcium phosphate minerals have two characteristic bands corresponding to the P-O stretching band; at around 1000-1050 cm^{-1} as a main band and 1100-1150 cm^{-1} as a sub band.

In both solutions, broad spectra corresponding to ACP appeared in the initial solutions. During the solution pH dropped rapidly (1000-1800 s), spectra of calcium phosphate crystalline (HAP and OCP) appeared and increased intensities over time, and finally they were stabilized. In the reference solution, the bands at 1021, 1038 and 1128 cm^{-1}, which corresponded to OCP, were observed after pH drop. The bands corresponded to HAP (1030 and 1142 cm^{-1}) also appeared; however, their intensities were smaller than those of OCP. The spectrum showed that OCP was rich in the precipitates.

On the other hand, in the 5 μM CGNs-containing solution, most of all bands in the initial reaction stage were attributed to HAP, especially in the sub-band region. For example, HAP 1030 and 1142 cm^{-1} bands were well developed in this condition and the later was hardly detected in the reference solution. It is obvious that the only CGNs developed the band corresponded to HAP in all reaction stages (Fig. 9b and c).

6.3.5. *TEM observations of calcium phosphate phases appeared during phase transformation from ACP to HAP depending on CGNs concentration.*

The macroscopic morphologies and inner structures of calcium phosphates formed during transformation from ACP to HAP in stagnant solutions were observed using TEM in relation to the CGNs concentration. The data of pH monitoring were used to the guide to determine the pick-up time of materials from the solutions. TEM observations were performed for materials taken from four kinds of solutions with various CGNs concentration depending on the reaction behaviors. They were categorized as the reference solution (CGNs free), the solution in which HAP formation was accelerated (5 μM CGNs), the solution in which the pH drop was observed but no precipitation occurred (10 μM CGNs), and the solution in which neither pH drop nor precipitation was observed (30 μM CGNs), respectively.

In the reference solutions, spherical particles (around 100 nm) were observed at the initial stage before the solution pH rapidly dropped (Fig. 10a). SAED pattern of the particles revealed a halo region around the core and a faint broad ring around the halo region, indicating that the particles were ACP1 (Fig. 10a inserts right hands). HR-TEM observation showed no lattice fringes structure (Fig. 10b). Formation of ACP1 just after solution preparation was also observed in other solutions (see Fig. 11).

After the solution pH rapidly dropped, high contrast regions ranging 5-20 nm in diameter were observed in the ACP structures. These regions contained well-arranged lattice fringes corresponded to HAP (*hkl*) structures (Figs. 10c and d). These regions were extended in ACP particles over time; however, the spherical morphology of ACPs particles was maintained as long as the solution was transparent. When the solution was clouded, precipitates were pasty materials (Fig. 10e), which consisted of numerous block structures ranging from 10 to 50 nm. These blocks were arranged randomly (Fig. 10f). This block structure was similar to that observed in ACP particles. In the reference solution, most block structures showed lattice fringes corresponded to HAP (Fig. 10g), but some of these showed lattice fringes corresponded to OCP (Fig. 10h).

On the other hand, OCP lattice fringes were not observed in the pasty materials precipitated in CGNs-containing solutions (Fig. 11). In 5 μM CGNs-containing solution, high contrast regions in the ACP particles were observed after pH drop (Figs. 11a and c). The precipitates were pasty materials (inset upper right of Fig. 11b) and each block (5-20 nm) in it showed lattice fringes corresponding to HAP (Fig. 11b and d). It did not be observed OCP structures in the materials formed in 5 μM CGNs-containing solutions.

In the solutions containing more than 10 μM CGNs, no precipitation of crystalline calcium phosphates particles except ACP spherical particles occurred during all reaction stages (Fig. 11). Although these ACP particles maintained their specific spherical forms (inset upper right of Fig. 11e) during reaction, many irregular complex lattice fringes appeared in the ACP particles after pH drop (Fig. 11e). The widths and angles of these fringes were hardly determined; however, some of these corresponded to *d*-spacing of

HAP crystal. These loose crystalline structures in ACP spherical particles were probably defined to be low crystalline HAP in the previous XRD measurements, because the intensity of diffraction from crystalline phase was much stronger than that from amorphous.

In 30 μM CGNs-containing solution, no lattice fringes appeared in the ACP particles in solutions during all reaction stages (Fig. 11f).

The Ca/PO_4 molar ratio of calcium phosphate particles (ACP and precipitates) was measured using FE-SEM/EDX. The ratio increased when the solution pH drop and precipitation proceeded. It was indicated that increase in the ratio was attributed to the evolution of HAP (and OCP?) crystalline region.

The Ca/PO_4 ratio of precipitated calcium phosphate particles decreased with the increase in CGNs concentration in the precipitate stages (**N** is >15 in each materials). In the ACP without any lattice fringes (before pH drop), the ratios were 1.33 ± 0.04 independent on the CGNs concentration. However, when the solution pH dropped, the ratio increased to 1.44 ± 0.07 in control and 1.45 ± 0.04 in 5 *μ*M CGNs, respectively. In the precipitation stage, it was 1.75 ± 0.05 in control, 1.54 ± 0.04 in 2 μM and 1.54 ± 0.04 in 5 μM of CGNs, respectively. Thus, it was concluded that CGNs inhibit crystallization process in ACP spherical particles.

6.4. Discussion

The pH monitoring, TR-SLS measurement and HR-TEM observation showed that calcium phosphate particles formed as ACP at the initial reaction stage. The ACP particles repeated partial dissolution and aggregation until HAP (and OCP) regions appeared in them. These regions were observed as the block structure ranging 5-20 nm in diameter. At first looks, it is ambitious that TR-SLS observation showed that the average density of each ACP particle decreased by the formation of block structures. In natural, in TR-SLS observation, crystallization in amorphous induce M_w increasing.[9,14] It is suggested that the phenomenon revealed HAP crystallization induced not only phase transformation from ACP but also ACP dissolution. Many previous works showed that ACP has many structures.[19-23] Thus, it is totally natural that occurring phase transformation and junk ACP dissolution were at the same times during M_w decreasing stage, junk ACP dissolution process more contributed to M_w changing than M_w increasing process is described as phase transformation process. Finally, HAP blocks coalesced forming mesocrystal structure and precipitated.[24]

TR-SLS and *in situ* FT-IR measurements indicated that CGNs altered HAP formation kinetics as compared to the condition without CGNs. When HAP formed in biological environment, they formed through some intermediate phases such as Ca-deficient OCP.[21] CGNs altered reaction path of HAP from ACP throughout OCP structures. The key effect of CGNs in HAP formation is the evolution of specific chemical bond as shown by *in situ* FT-IR. *In situ* FT-IR measurement and HR-TEM observation showed that CGNs inhibited the formation of OCP structure (exactly, HPO_4-OH layer structure) in precipitated calcium phosphates. Previous investigations showed that the phase transformation from OCP to HAP proceeds via hydrolysis of OCP and subsequent growth of HAP.[25-27] This process should be slower than the transformation from ACP to HAP via direct structure reconstruction.[15,19,20] Therefore, it was assumed that the transformation from OCP (and even from Ca-deficient OCP) to HAP needs high activation energy, and CGNs skip this process that resulted in direct HAP formation from ACP. This change in the reaction path made great acceleration of

HAP formation.

As discussed in Chapter 6 (and Chapter 7), there are no evidences of covalent bond formation in CGNs still maintained after being dispersed in $CaPO_4$ during the mineralization process. Accordingly, the effect of CGNs on the mineralization of $CaPO_4$ can be considered in two ways. First, the large CGNs molecules directly alter the internal crystalline structure of $CaPO_4$ through mineralization process. In particular, the CGNs-containing ACP show different physico-chemical properties when compared to those formed in control. It is suggested that the interaction between Ca^{2+} or phosphate ions and CGNs affected cluster formation and its aggregation behavior during early stage of ACP formation. For examples, He et al.[29] indicated DMP molecules binding effect altered cluster structures and mineralization. Actually, *in situ* FT-IR spectra showed the evidence of intermolecular affection between Ca^{2+} ion and CGNs (see Chapter 7, Fig. 11). HR-TEM observation indicated the formation of crystalline phases in ACP. Clearly, the physico-chemical properties are altered.

Second, the effect of MUA separated from CGNs on the $CaPO_4$ particles. The following chapter (see Chapter 7) describes the NMR study of CGNs-containing OCP, which showed typically -COOH intercalated patterns (see Chapter 7, Fig. 7).[30-36] This indicates that the separated MUA intercalates and alters the mineralization of $CaPO_4$ crystalline in ACP rather than directly affecting the CGNs.

In any cases, it is strongly suggested that molecular interaction of immobilized -COOH and calcium phosphate ions during early stage of HAP mineralization controlled physico-chemical properties of later minerals and their formation dynamics. This tendency has been revealed in calcium carbonate systems.[37-39]

6.5. Conclusions

It has been well known that immobilized -COOH of materials accelerates HAP formation.[9-11,28] However, it has been unclear which kind of physico-chemical properties such as molecular mass, isoelectric point, molecular structure and co-existed other functional groups of materials control the HAP mineralization kinetics. Used simple -COOH immobilized on chemically stable gold nano-particles and clarified the role of these on HAP mineralization kinetics. The data clearly showed that the concentration of immobilized -COOH controlled the HAP formation. They were both accelerator (1/1000 of Ca concentration) and inhibitor (over 1/500 of Ca concentration). The maximum acceleration index for HAP formation was about 45%, which was much larger than that achieved by using artificial proteins in the previous investigation.[15] It was also strongly suggested that CGNs altered reaction path of HAP to without OCP intermediate.

This tendency was similar to $H_2PO_4^-$ affection into formation dynamics of calcium carbonate (Chapter 2). This investigation would contribute to high speed synthesis of novel functional biomaterials in tissue engineering and regeneration medicine fields such as use for repair of bone fracture.

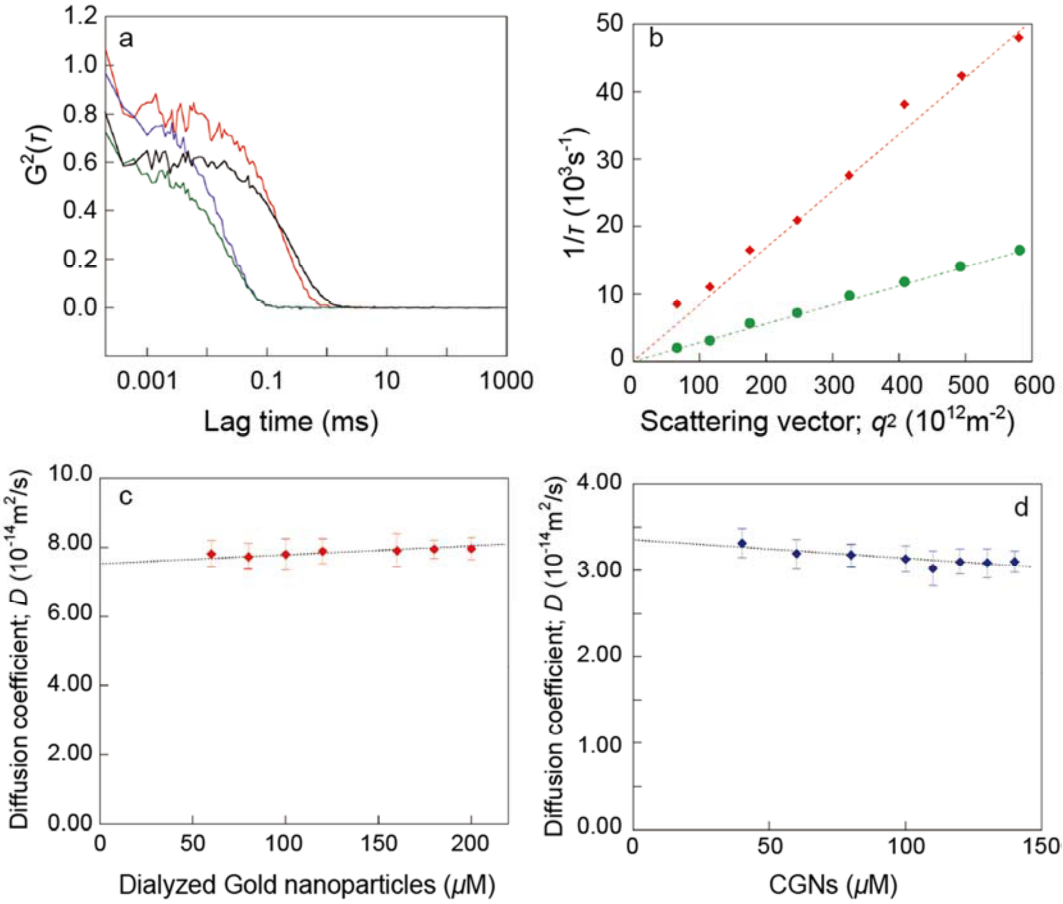

Figure 6.1. DLS measurements of the solutions containing the reference gold nanoparticles and CGNs. (a) Second autocorrelation functions at $\theta = 30°$ (red line) and 90° (purple line) for the solution containing 150 μM CGNs and at $\theta = 30°$ (black line) and 90° (green line) for the solution containing 37.5 μM CGNs. (b) Relationship between $1/\tau$ and q^2 for the solutions containing 60 μM reference gold nanoparticles (red diamonds) and 120 μM CGNs (green circles). (c) Relationship between D and the concentration of reference gold nanoparticles. (d) Relationship between D and the CGNs concentration.

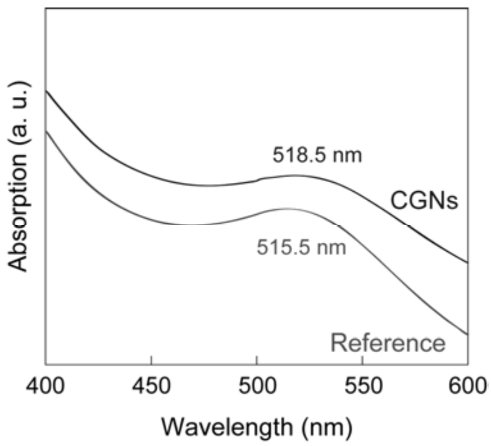

Figure 6.2. Visible-light absorption spectra of the solution containing CGNs (black line) and reference gold nanoparticles (grey line).

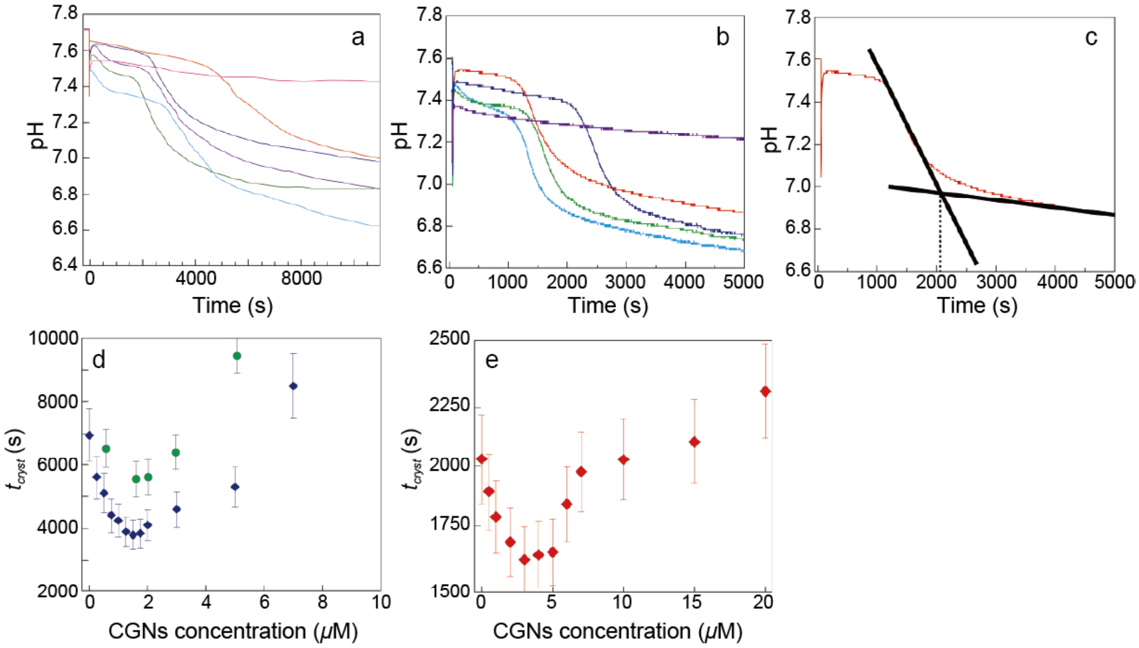

Figure 6.3. The pH drop experiments. (a) pH drop profiles in solutions containing 3 mM Ca^{2+} and phosphate ions of various concentration CGNs-containing solutions. (red line, control; light blue line, 250 nM; green line, 1750 nM; purple line, 3 μM; dark blue line, 5 μM; pink line, 10 μM) (b) pH drop profiles in solutions containing 3.25 mM Ca^{2+} and phosphate ions of various concentration CGNs-containing solutions. (red line, control; light blue line, 3 μM; green line, 7 μM; dark blue line, 25 μM; pink line, 30 μM) (c) The method of define, t_{cryst} value. (d, e) Relationship between crystallization threshold point t_{cryst} and CGNs concentration. (d) 3 mM. (e) 3.25 mM.

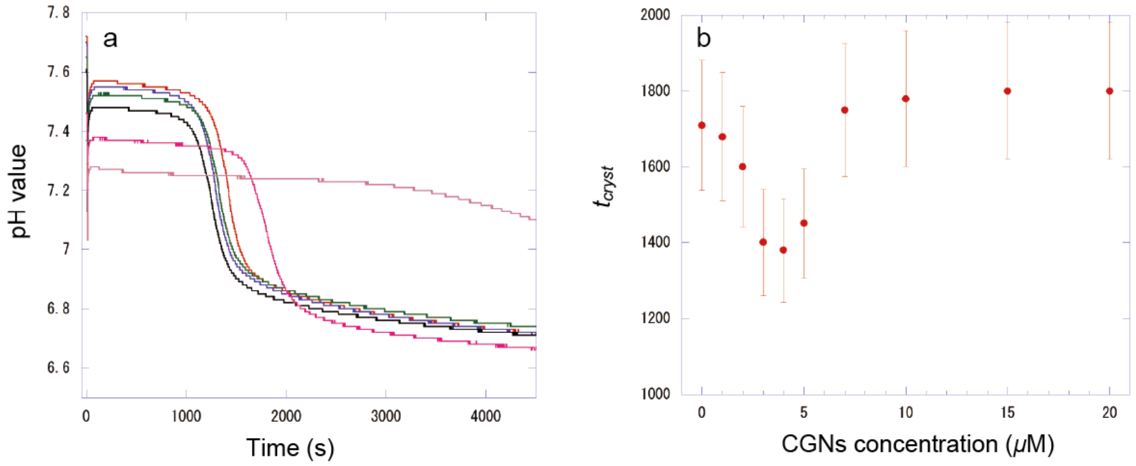

Figure 6.4. The pH drop experiments of 4 mM Ca-PO$_4$. (a) pH drop profiles in solutions of various concentration CGNs. (red line, control; black line, 3 μM; purple line, 5 μM; pink line, 50 μM; mauve line, 100 μM). (b) Relationship between crystallization threshold point t_{cryst} and CGNs concentration.

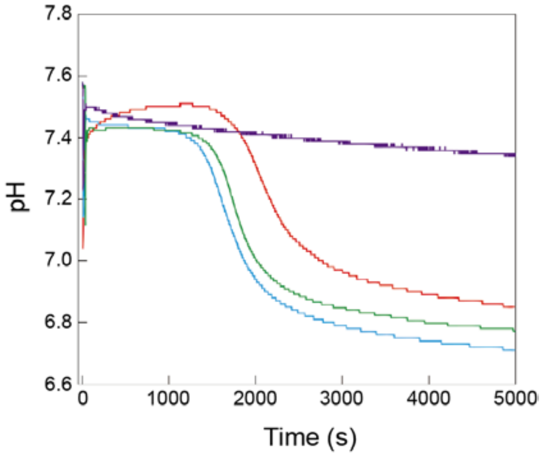

Figure 6.5. pH drop profile of 3.25 mM Ca-PO_4 in various CGNs-containing solutions without stirring. red line, control; light blue line, 2 μM; green line, 5 μM; purple line, 30 μM.

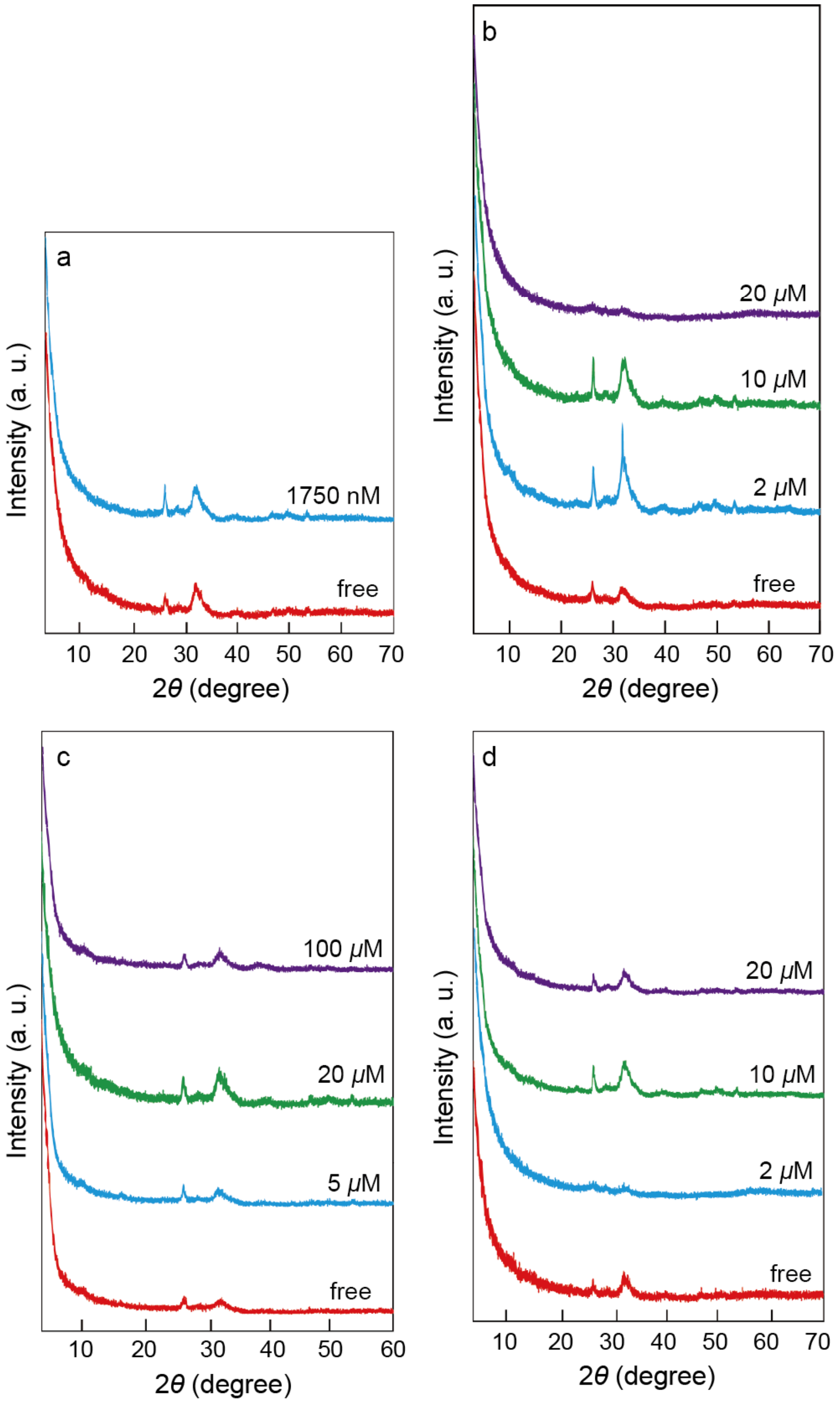

Figure 6.6. XRD pattern of materials formed in various Ca-PO_4 and CGNs-containing solutions at 2 hours. (a) 3 mM with stirring. (b) 3.25 mM with stirring. (c) 4 mM with stirring. (d) 3.25 mM without stirring.

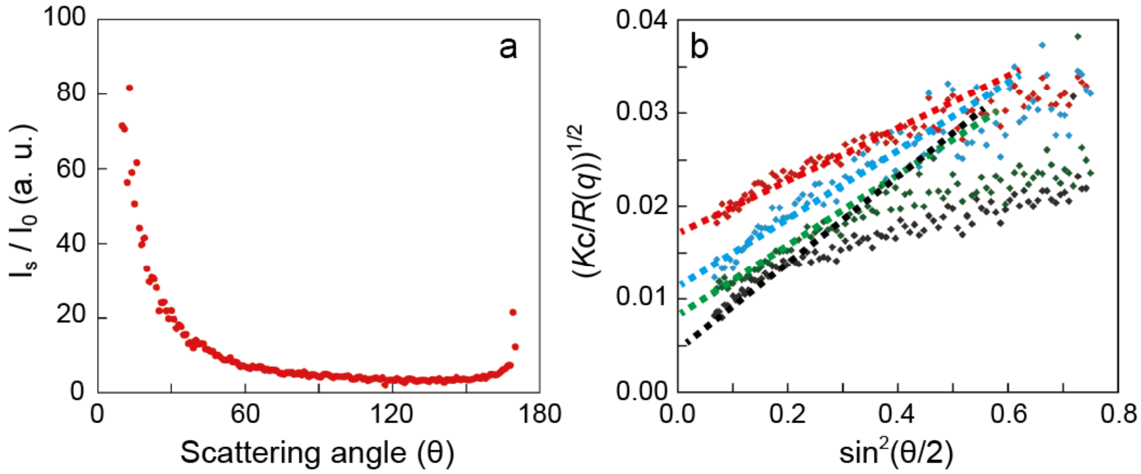

Figure 6.7. (a) Relationships between scattering angle and scattering relative intensity of 3.25 mM $CaCl_2$ and KDP-KAP solutions at 10 min. (b) Zimm-square-root plot of (a). Red 10 min; Light blue 30 min; Green 60 min and Black 120 min. Broken lines indicated calculation part of plot (θ = 30 to 70°).

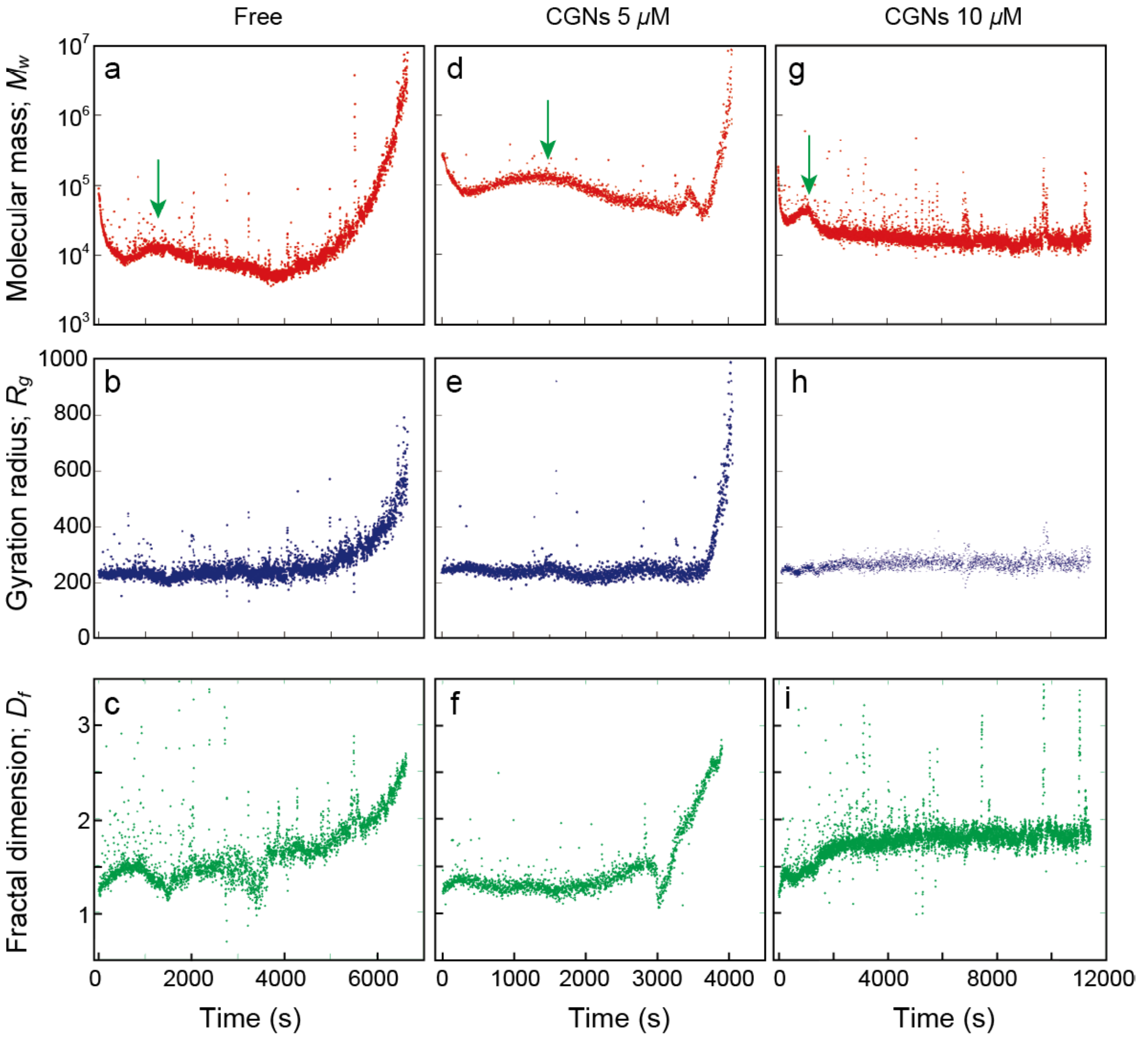

Figure 6.8. TR-SLS measurement of HAP formation in various concentration CGNs-containing solutions. Time dependent changes of the calculated apparent molecular mass, M_w (a, d, g), gyration radius, R_g (b, e, h) and fractal dimension, D_f (c, f, i). Green arrows indicate the start point of pH dropping.

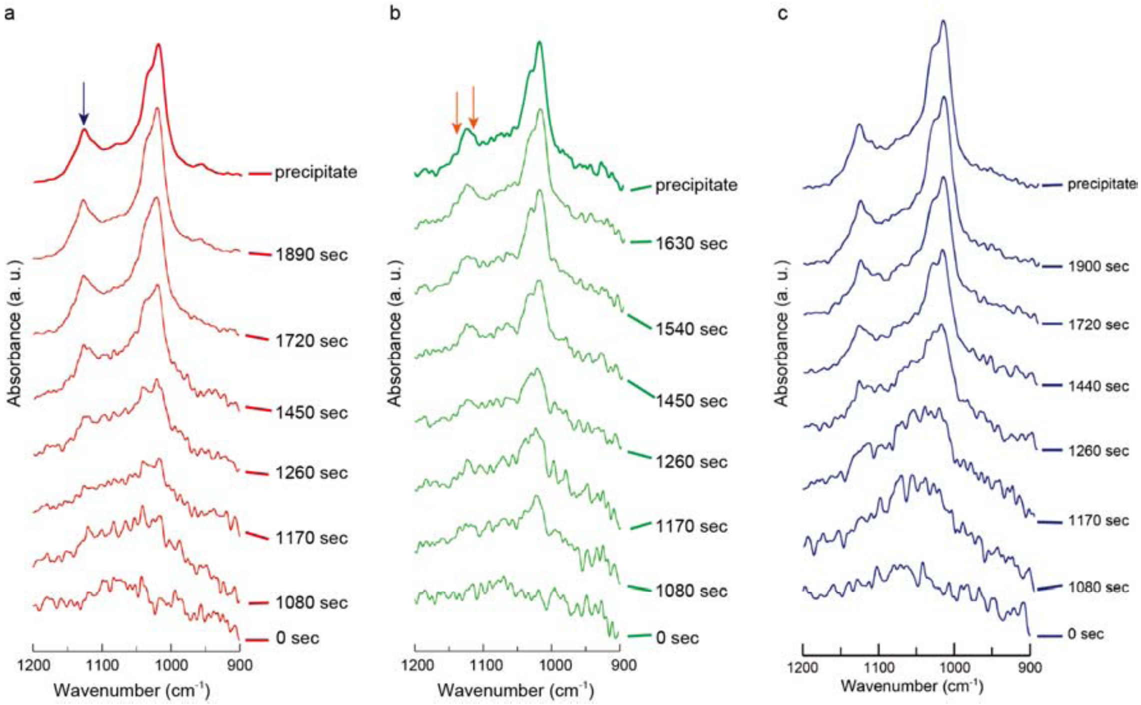

Figure 6.9. *In situ* FT-IR spectra in the P-O stretch region of materials formed in control (a), 5 μM CGNs-containing (b) and 5 μM reference gold nanoparticles-containing (c) solutions. Dark blue arrow indicated OCP band. Orange arrows indicated HAP bands.

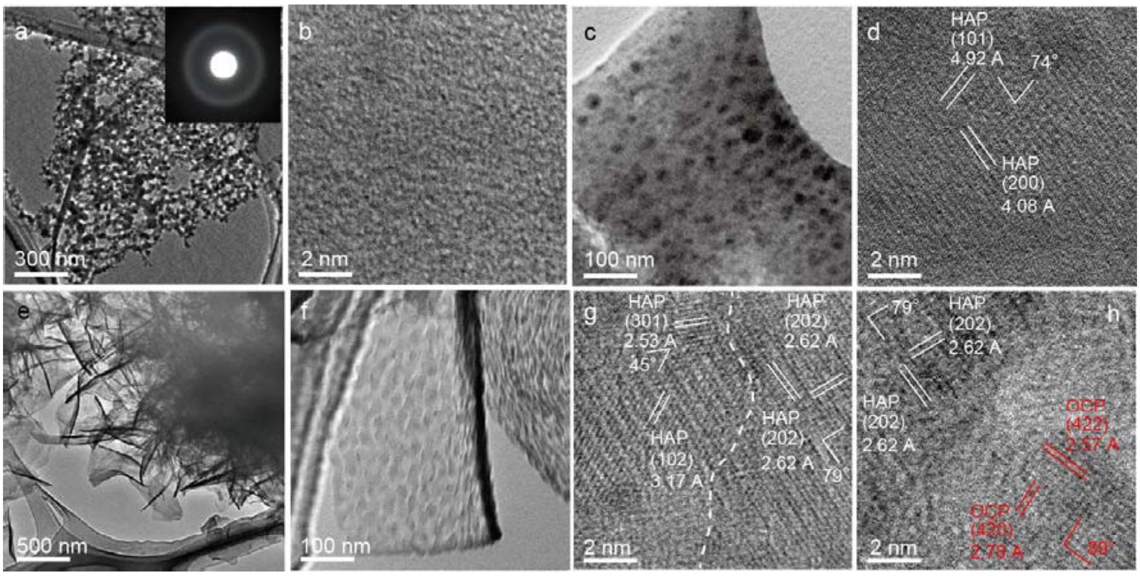

Figure 6.10. TEM photograph of morphology and crystallinity of calcium phosphate particles appeared during precipitation experiments in control solution. (a) TEM photograph of ACP spherical particles aggregate with SAED pattern formed at 10 min. (b) HR-TEM photograph of completely random structure of ACP in control solution formed at 10 min. (c) TEM photograph of ACP formed at pH dropping. There are black dots ranging 2–10 nm. (d) HR-TEM photograph of dots. (e) TEM photograph of initial precipitate. (f) Magnified image of initial precipitate. Plate like crystal was consisted of many block like structures. (g) HR-TEM photograph of well-arranged HAP lattice fringes in initial precipitates. (h) HR-TEM photograph of OCP lattice fringes in HAP crystals.

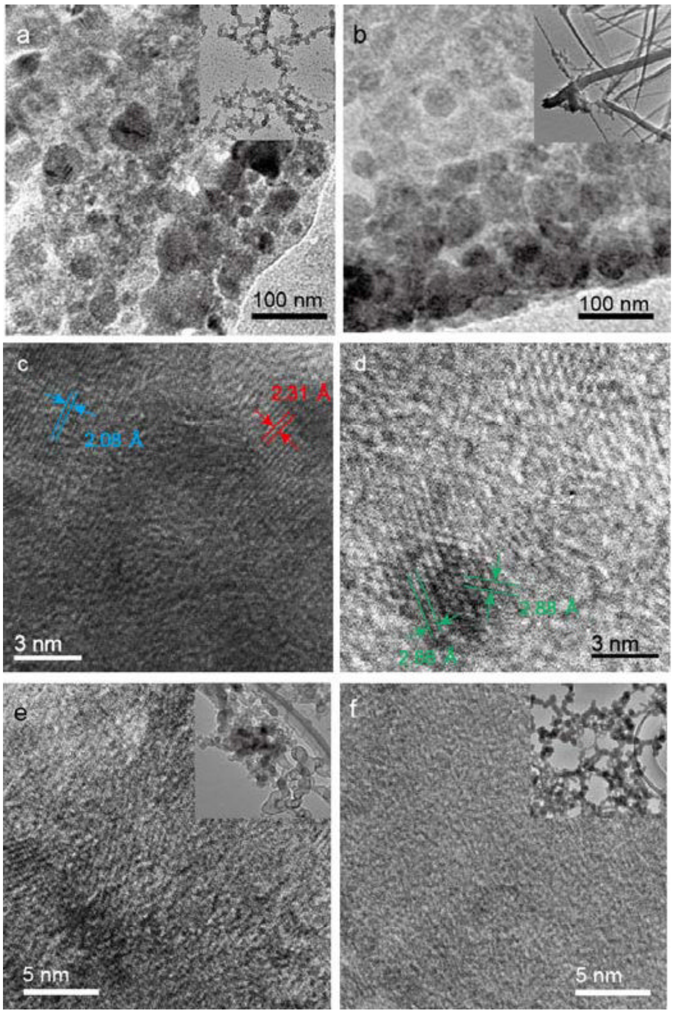

Figure 6.11. TEM photograph of morphology and crystallinity of calcium phosphate particles appeared during precipitation experiments in the various concentration CGNs-containing solution. (a) Magnified TEM photograph of block-like structures in ACP formed in 5 μM CGNs-containing solution, and whole spherical morphology at pH dropping (upper right). (b) Magnified TEM photograph of block-like structure in pasty like precipitate formed in 5 μM CGNs-containing solution, and whole pasty morphology at pH dropping (upper right) at 1 hour. (c) Single dimensional lattice fringes formed in ACP spherical particles formed in 5 μM CGNs-containing solution at 30 min. (d) Double dimensional lattice fringes in precipitates formed in 5 μM CGNs-containing solution at 1 hour. (e) HR-TEM photograph of poorly complex lattice fringes in materials formed in 10 μM CGNs-containing solution, and whole spherical morphology at 1 hour (upper right). (f) HR-TEM photograph of completely amorphous structures in materials formed in 30 μM CGNs-containing solution, and whole spherical morphology at 2 hour (upper right).

Reference

(1) Berkovitz, B.K.B., Boyde, A., Frank, R.M., Hohling, H.J., Moxham, B.J., Nalbandian, J., Tonge, C.H. *Handbook of Microscopic Anatomy, Volume V/6: Teeth.* Springer-Verlag, Berlin Heidelberg, **1989**.

(2) Weiner, S., Dove, P.M. *An Overview of Biomineralization Processes and the Problem of the Vital Effect.* In *Biomineralization, Reviews in Mineralogy and Geochemistry Vol. 54.* Dove, P.M., DeYoreo, J.J., Weiner, S. Eds. Mineralogical Society of America, USA., pp. 1-29, **2003**.

(3) Nudelman, F., Lausch, A.J., Sommerdijk, N.A.J.M., Sone, E.D. *In vitro* models of collagen biomineralization. *J. Struct. Biol.* **2013**, *183*, 258-269.

(4) Wang, L., Nancollas, G.H. Calcium Orthophosphates: Crystallization and Dissolution. *Chem. Rev.* **2008**, *108*, 4628-4669.

(5) Dey, A., Bomans, P.H.H., Muller, F.A., Will, J., Frederick, P.M., deWith, G., Sommerdijk, N.A.J.M. The role of prenucleation clusters in surface-induced calcium phosphate crystallization. *Nat. Mater.* **2010**, *9*, 1010-1014.

(6) Hunter, G.K., Hauschka, P.V., Poole, A.R., Rosenberg, L.C., Goldberg, H.A. Nucleation and inhibition of hydroxyapatite formation by mineralized tissue proteins. *Biochem. J.* **1996**, *317*, 59-64.

(7) O'Young, J., Liao, Y., Xiao, Y., Jalkanen, J., Lajoie, G., Karttunen, M., Goldberg, H.A., Hunter, G. Matrix Gla Protein Inhibits Ectopic Calcification by a Direct Interaction with Hydroxyapatite Crystals. *J. Am. Chem. Soc.* **2011**, *133*, 18406-18412.

(8) He, G., Dahl, T., Veis, A., George, A. Nucleation of apatite crystals in vitro by self-assembled dentin matrix protein 1. *Nat. Mater.* **2003**, *2*, 552-558.

(9) Tsuji, T., Onuma, K., Yamamoto, A., Iijima, M., Shiba, K. Direct transformation

from amorphous to crystalline calcium phosphate facilitated by motif-programmed artificial proteins. *Pro. Nat. Acad. Sci. USA* **2008**, *105*, 16866-16870.

(10) Tsuji, T., Oaki, Y., Yoshinari, M., Kato, T., Shiba, K. Motif-programmed artificial proteins mediated nucleation of octacalcium phosphate on titanium substrates. *Chem. Comm.* **2010**, *46*, 6675-6677.

(11) Tsuji, T., Onuma, K., Yamamoto, A., Iijima, M., Shiba, K. Physicochemical properties of artificial proteins that accelerate nucleation of crystalline calcium phosphate. *J. Cryst. Growth*, **2011**, *314*, 190-195.

(123) Kanzaki, N., Uyeda, Q.P.T., and Onuma, K. Intermolecular interaction of actin revealed by a dynamic light scattering technique. *J. Phys. Chem. B*, **2006**, *110*, 2881–2887.

(13) Smoluchowski, M. Drei Vortrage uber Diffusion, Brownsche Molekularbewegung und Koagulation von Kolloidteilchen. *Physik. Z*, **1916**, *17*, 557-571. (in German)

(14) Provencher, S.W. *Users Manual for CONTIN*, Technical Report EMBL-DAO5, Queens University Belfast, UK, **1982**.

(15) Onuma, K., Oyane, A., Tsutsui, K., Tanaka, K., Treboux, G., Kanzaki, N., and Ito, A. Precipitation Kinetics of Hydroxyapatite Revealed by the Continuous-Angle Laser Light Light-Scattering Technique. *J. Phys. Chem. B*, **2000**, *104*, 10563–10568.

(16) Tseng, Y., Fedorov, E., McCaffery, J.M., Almo, S.C., and Wirtz, D. Micromechanics and Ultrastructure of Actin Filament Networks Crosslinked by Human Fascin: A Comparison with α-Actinin. *J. Mole. Biol.*, **2001**, *310*, 351–366.

(17) Lehner, D., Kellner, G., Schnablegger, H., and Glatter, O. Static Light Scattering on Dense Colloidal Systems: New Instrumentation and Experimental Results. *J. Coll. Interface Sci.*, **1998**, *201*, 34–47.

(18) Onuma, K., Furubayashi, N., Shibata, F., Kobayashi, Y., Kaito, S., Ohnishi, Y., and Inaka, K. Anomalous effect of poly(ethylene)glycol on intermolecular interaction and protein association. *Cryst. Growth Des.*, **2009**, *9*, 2517–2524.

(19) Onuma, K., Ito, A. Cluster growth model for hydroxyapatite. *Chem. Mater.* **1998**, *10*, 3346-3351.

(20) Posner, A., Betts, F. Synthetic amorphous calcium phosphate and its relation to bone mineral structure. *Acc. Chem. Res.* **1975**, *8*, 273-281.

(21) Habraken, W.J.E.M., Tao, J.T., Brylka, L.J., Friedrich, H., Bertinetti, L., Schenk, S.A., Verch, A., Dmitrovic, V., Bomans, P.H.H., Frederik, P.M., Laven, J., van der Schoot, P., Aichmayer, B., deWith, G., DeYoreo, J.J., Sommerdijk, N.A.J.M. Ion-association complexes unite classical and non-classical theories for the biomimetic nucleation of calcium phosphate. *Nat. Comm.* **2013**, DOI: 10.1038/ncomms2490.

(22) Christoffersen, J., Christoffersen, M.R., Kibalczyc, W., Anderson, F.A. A Contribution to the Understanding of the Formation of Calcium Phosphate. *J. Cryst. Growth*, **1989**, *94*, 767–777.

(23) Christoffersen, M.R., Christoffersen, J., Kibalczyc, W. (1990) Apparent Solubilities of Two Amorphous Calcium Phosphates and of Octacalcium Phosphate in the Temperature Range 30-42 °C. *J. Cryst. Growth*, **1990**, *106*, 349–354.

(24) Colfen, H., Antonietti, M. *Mesocrystals and Nonclassical Crystallization.* Wiley and Sons, Ltd., USA. **2008**.

(25) Brown, W.E. Octacalcium phosphate and hydroxyapatite: Crystal structure of octacalcium phosphate. *Nature* **1962**, *196*, 1048- 1050.

(26) Nelson, D.G.A., McLean, J.D. High-resolution electron microscopy of octacalcium phosphate and its hydrolysis products. *Carcif. Tissue Int.* **1984**, *36*, 219-232.

(27) Kamitakahara, M., Ito, N., Murakami, S., Watanabe, N., Ioku, K. Hydrothermal synthesis of hydroxyapatite from octacalcium phosphate: effect of hydrothermal temperature. *J. Ceram. Soc. Jpn* **2009**, *117*, 385-387.

(28) Nonoyama, T., Kinoshita, T., Higuchi, M., Nagata, K., Tanaka, M., Sato, K., Kato, K. Multistep Growth Mechanism of Calcium Phosphate in the Earliest Stage of Morphology-Controlled Biomineralization. *Langmuir* **2011**, *27*, 7077-7083.

(29) He, G., Gajjeraman, S., Schulz, D., Cookson, D., Qin, C., Butler, W.T., Hao, J., George, A. Spatially and temporally controlled biomineralization in facilitated by interaction between self-assembled dentin matrix protein 1 and calcium phosphate nuclei in solution. *Biochem.*, **2005**, *44*, 16140-16148.

(30) Monma, H., Goto, M. Succinate-complexed Octacalcium Phosphate. *Bull. Chem. Soc. Jpn.*, **1983**, *56*, 3843-3844.

(31) Markovic, M. *Octacalcium Phosphate Carboxylates*. Chow, L.C., Eanes, E.D. (Eds.), In *Octacalcium Phosphate, Monographs in Oral Science Vol. 18*. pp. 77-93. Karger, Basel, Switzerland, **2001**.

(32) Markovic, M., Fowler, B.O., Brown, W.E. Octacalcium Phosphate Carboxylates. 2. Characterization and Structural Considerations. *Chem. Mater.*, **1993**, *5*, 1406-1416.

(33) Aoki, S., Sakamoto, K., Yamaguchi, S., Nakajima, A. Syntheses of Octacalcium Phosphate Containing Dicarboxylic Acids and Effects of the Side Groups on the Crystal Growth of Octacalcium Phosphate. *J. Cera. Soc. Jpn.*, **2000**, *108*, 909-914.

(34) Monma, H., Goto, M. Succinate-complexed Octacalcium Phosphate. *Bull. Chem. Soc. Jpn.*, **1983**, *56*, 3843-3844.

(35) Davies, E., Muller, K.H., Wong, W.C., Pickard, C.J., Reid, D.G., Skepper, J.N., Duer, M.J. Citrate bridges between mineral platelets in bone. *Proc. Nati. Acad. Sci. USA*,

2014, *111*, E1354-E1363.

(36) Tsai, T.W.T., Chou, F., Tseng, Y., Chan, J.C.C. Solid-state P-31 NMR study of octacalcium phosphate incorporated with succinate. *Phys. Chem. Chem. Phys.*, **2010**, *12*, 6692-6697.

(37) Gebauer, D., Gunawidjaja, P.N., PeterKo, J.Y., Bacsik, Z., Aziz, B., Liu, L., Hu, Y., Bergstrom, L., Tai, C.W., Sham, T.K., Eden, M., Hedin, N. Proto-Calcite and Proto-Vaterite in Amorphous Calcium Carbonates, *Angew. Chem. Int. Ed.*, **2010**, *49*, 8889-8891.

(38) Gebauer, D., Völkel, A., Colfen, H. Stable Prenucleation Calcium Carbonate Clusters, *Science*, **2008**, *322*, 1819-1822.

(39) Demichelis, R., Raiteri, P., Gale, J.D., Quigley, D., Gebauer, D. Stable prenucleation mineral clusters are liquid-like ionic polymers. Nat. Comm., **2011**, DOI: 10.1038/ncomms1604.

Chapter 7

Formation dynamics of octacalcium phosphate (OCP) via intermediate phase and its physico-chemical properties.

7.1. Introduction

As described in Chapter 6, CGNs accelerate not only HAP mineralization but also altered reaction path skipping OCP structures in weak basic solutions HAP during mineralization process. In Chapter 7, it is focused on how CGNs affect into OCP formation, particularly, it is mainly investigated for still unclear purpose how dynamics and formation path of OCP from ACP were affected by immobilized -COOH-containing molecules (CGNs).

OCP is a crystalline phase of calcium phosphate, which is preferentially formed in weak acidic to neutral solutions (pH 5.5 to 7.0).[1-4] OCP crystals are often formed as plate-like crystals, and its unit cell contains an HAP-like structure.[1-3,5] (Figure 1) Furthermore, OCP is indicated to be a precursor of HAP through solid-solid phase transformation.[1,6-8]

The crystal structures of OCP can be categorized as three layers along the *a*-axis: HAP-like structure, transition structure, and HPO_4-OH layer structure.[5] OCP structure has highly flexibility and it often exhibits partial structural alteration while maintaining the their whole structure and morphology by thermal and additive effects.[6-12] In particular; some previous studies have been reported that the HPO_4-OH layer structure of OCP is easily affected by some –COOH-containing molecules. Monma and Goto[9] showed that succinate, a bi-carboxylic acid, easily intercalated into the HPO_4-OH layer structure instead of HPO_4^{2-} ions, altering the lattice parameters of OCP. Markovic et al.[10] investigated how various –COOH-containing molecules affect the OCP crystal structure and described their effects in terms of intercalation in the HPO_4-OH layer structure. Using high-resolution NMR spectroscopy, Davies et al.[11] demonstrated the lattice alternation behavior of citrate-containing OCP. As described, a variety of evidence has been reported for the intercalation of –COOH-containing molecules in OCP and the resulting structural alteration. However, it remains unclear how -COOH-containing molecules affect the formation dynamics of OCP. As described in Chapter 6, some previous reports indicated that -COOH-containing molecules affect into formation dynamics of HAP, especially intermediate OCP phase.[13-15]

When OCP formed in aqueous solution even though weak acidic solution under supersaturated condition, ACP is formed as the initial phase and precursor phase at normal temperature and pressure under relatively high supersaturated solutions.[1,2,16-19] ACP has essentially loose and absence long range order but containing short range order assumed as aggregation of Ca-PO_4 clusters.[13,20,21] The structural similarity between the minimum unit of ACP and HAP strongly suggests that ACP plays an essential role during HAP formation as precursor.[19-24] For example, using HR-TEM, Wang et al.[25] reported HAP lattice fringes formed and dispersed inside ACP particles during early stage of HAP mineralization in aqueous solution. The OCP crystal structure contains HAP-like structures. Therefore, it is natural that there were strongly relationships between ACP and OCP and suggested that ACP is precursor phases of OCP. Furthermore, Habraken et al.[26] reported that ACP is also a precursor of OCP (Ca-deficient OCP) during HAP mineralization in aqueous solutions. Thus, when ACP formed as initial phases under weak acidic conditions, OCP is considered to formed inside ACP, which is thought to be a cluster based phase transformation process.[20-26]

In Chapter 7, on the basis of cluster base phase transformation, it is investigated how CGNs affect in the dynamics of the ACP–OCP phase transformation. CGNs were dispersed in a bit acidic calcium phosphate solution which OCP preferentially formed. The time evolution of the phase transformation was observed using TR-SLS and *in situ* FT-IR, and the phases appeared throughout the transformation were characterized by XRD, TEM with cryo-HR-TEM, SAED, FE-SEM/EDX, NMR spectroscopy and Raman spectroscopy.

7.2. Experimental Methods

7.2.1. *Preparation of the solutions used for the ACP–OCP phase transformation studies.*

CaCl$_2$ (reagent grade, Wako Pure Chem. Inc., Tokyo, Japan), KH$_2$PO$_4$, K$_2$HPO$_4$, and NaCl (reagent grade, Nakarai Tesque Inc., Kyoto, Japan) were dissolved in ultra-pure water with a specific resistance of 18.2 MΩ and total organic contents (TOC) of them was <5 ppb. Three stock solutions were prepared: 1 M CaCl$_2$, 0.5 M KH$_2$PO$_4$, and 0.5 M K$_2$HPO$_4$. First, the KH$_2$PO$_4$ and K$_2$HPO$_4$ solutions were mixed together to obtain a 0.5 M phosphate solution (KDP–KAP) with a pH of 6.5. The final solution was prepared by mixing the KDP–KAP solution with the CaCl$_2$ solution, such that both the Ca^{2+} and phosphate ions concentrations were 5 mM (pH 6.5 ± 0.1 at 22 °C). Because the volume ratio of the CaCl$_2$ solution to the phosphate solution was less than 1/100, the solution pH remained constant throughout the mixing process.

7.2.2. *Observation of the ACP–OCP phase transformation dynamics in solutions containing reference gold nanoparticles and CGNs using TR-SLS and in situ FT-IR.*

The theory and application of TR-SLS and the details of the optical instrument are described previously.

Two types of reaction solutions were prepared for the TR-SLS analyses: a cationic solution (1 M $CaCl_2$) and an anionic solution (5.03 M KH_2PO_4–K_2HPO_4 buffered at pH 6.5 with 10.01 μM reference gold nanoparticles or 10.01 μM CGNs). Both solutions were filtered through a 0.22 μm syringe-type membrane filter or a 0.22 μm centrifuge filter to remove any dust particles. Sixty microliters of the cationic solution was added to 11.94 mL of the anionic solution, and the two solutions were quickly mixed in the measurement cells. The final solutions contained 5 mM Ca and phosphate and 10 μM reference gold nanoparticles or CGNs. After solution preparation, the changes in the molecular mass M_w and the gyration radius R_g of the particles were measured.

In addition, the relationship between the scattering intensity and scattering angle for each solution was analyzed using Zimm-square-root plots.

For *in situ* FT-IR analyses, after the stock solutions were filtered using 0.22 μm centrifuges and syringe filters, the measured solutions were mixed in 2 mL polypropylene tubes. Approximately 5 μL of each mixed solution was mounted on the horizontal diamond single crystal of the attenuated total reflection prism of an IR spectrometer. The measurement interval was approximately 90 s. The solutions were covered with silicon gum caps to avoid evaporation.

7.2.3. *Characterization of the calcium phosphate phases formed in the solutions containing reference gold nanoparticles and CGNs.*

The treated materials, or their ultrathin cross-sections prepared using a microtome, were placed on an amorphous-carbon-coated Cu microgrid for transmission electron microscopy (TEM, JEM-2200, JEOL Co., Japan) observation. The phases of the materials were characterized according to their selected-area electron diffraction (SAED) patterns. The prepared ultrathin cross-sections (about 200 nm) were placed on a Cu microgrid for high-resolution (HR-TEM) TEM observation. The HR-TEM observation was performed using a TEM: at acceleration voltages of 200 kV. Cryo-HR-TEM observation was performed using a liquid-N_2 cryogenic holder (FE-TEM: Hitachi HF-3000S, Hitachi High Technologies Co., Ibaraki, Japan, FE-TEM, Tecnai G^2 20, FEI, the Netherlands) at acceleration voltages of 200 kV (JEM-2200 for TEM and Tecnai G^2 20 for cryo-HR-TEM) and 300 kV (HF-3000S for cryo-HR-TEM). The operating temperature of the cryo-HR-TEM observation was approximately −180 °C.

The OCP formed during precipitated crystalline phases formed in the solutions containing various acetate acid were mounted on 11 nine Si plate and determined their Ca/PO_4 ratio using FE-SEM/EDX (FE-SEM: FEI40, FEI Co., The Netherlands; EDX: EDAX GENESIS, EDAX Japan Co., Japan) using auto calibration operating. In FE-SEM/EDX measurement, at least 15 samples were measured in each condition.

The chemical shifts were measured by an attenuated total reflection (ATR)-type Fourier-transform infrared spectrometer (FT-IR: Nicolet 6300, ThermoScientific Co., USA) equipped with a triglycine sulfate (TGS) detector (32 scans, resolution 2 cm^{-1}). The background of the measurements was the ambient atmosphere.

The ^{31}P chemical shifts of the $CaPO_4$ samples were determined using a solid-state NMR spectrometer (JNM-ECX400 JEOL Co., Japan, and AVANCE III HD 600WB, Bruker AXS Co., US) with a resonance frequency of 400.0 (JNM-ECX400) and 600 MHz (AVANCE III HD 600WB). For all of these measurements, magic-angle spinning (MAS) with a single-pulse mode for ^{31}P was applied at frequencies of 10000 or 15000 rpm in 4 or 5 mm zirconia rotors. The sample weight was approximately 0.2 g and the contact time for the ^{31}P MAS measurements was 36 ms with relaxation delays of 60 s or 5 ms with relaxation delays of 10 s in each measurement interval. The number of repetitions per measurement was 1400. The chemical shift of ^{31}P was calibrated as 0.0 ppm using a 0.5 M K_2HPO_4 solution.

XRD (RINT40, Rigaku Co., Japan, λ_w = 0.15406 nm) analyses were performed at an acceleration voltage of 50 kV and a magnitude of 100 mA using a Cu target. The 2θ value was varied from 3° to 60° in 0.01° increments. The time required per step was 0.5 s. The entrance slit size was 5 mm × 10 mm.

7.3. Results

7.3.1. *TR-SLS measurements of the ACP–OCP phase transformation dynamics in the reference gold nanoparticles and CGNs-containing solutions.*

Using TR-SLS, changes in the M_w and R_g of the calcium phosphate particles formed in both solutions were observed during ACP–OCP phase transformation. Figure 2 showed the relationships between I_s/I_0 and scattering angle (a) and Zimm-square-root plot of them (b) (5 mM $CaCl_2$ and KDP-KAP and 10 μM CGNs-containing solution). Around all time periods, at low angle region (θ = 30° to 70°), linearly trends were showed.

Figure 3 plots the changes in M_w, R_g, the relative density (D_r; M_w/R_g^3) and D_f of the calcium phosphate particles formed in solutions containing 10 μM reference gold nanoparticles (Fig. 3a to d) and CGNs (Fig. 3e to h). The D_r was controlled by the number and rigidity of the particles. The evolution behavior of M_w and R_g of calcium phosphate particles formed in both solutions were essentially categorized as rapidly increasing stage during the first 10 min (stage *I*), gradually increase period (stage *II*) and second rapidly increasing period which indicated precipitation (stage *III*).

In the reference gold nanoparticle-containing solution, the initial M_w and R_g of the particles were approximately 2500 and 80 nm, respectively (Figs. 3a and b). Both values rapidly increased during the first 10 min (stage *I*), and then continued to gradually increase throughout the next 45 min (stage *II*). After 55 min, both values again increased drastically, and the solution became cloudy at about 70 min regard as precipitation (stage *III)*. The D_f (Fig. 3d) of the particles typically showed as crystalline phases nucleation on amorphous template, because the increasing of D_f was closely linked increasing of M_w and R_g.[25] It indicated that sequent phase transformation was occurred in reference gold nanoparticles-containing solution.

In contrast, the M_w and R_g of initial particles (stage *I*) in the CGNs-containing solution (approximately 600 and 50 nm, respectively) were much smaller than those in the reference solution (Figs. 3e and f). Throughout the first 10 min, both M_w and R_g rapidly reached local equilibrium values and remained unchanged for 40 min. Between 40 and 50 min, M_w again increased rapidly, reaching a local equilibrium value that was maintained up to 80 min. After 80 min, M_w further increased to a value that was maintained up to 170 min (stage *III*). The change in D_r (Fig. 3g) was consistent with that of M_w. Therefore, it can be concluded that the stepwise increases in M_w at 40 and 80 min manifested chiefly from increased particle rigidity.[27] However, the D_f showed no obviously changing in this time period. If the number of particles controlled the change in M_w, the sizes of the particles formed in the solution (indicated by the average R_g) should have varied widely. After 170 min, the solution became cloudy, and both M_w and R_g increased drastically (stage *III*). In the CGNs-containing solution, it was delayed relative to the reference solution by a factor of approximately 3. These initial precipitates formed in both solutions were characterized using XRD and Raman spectroscopy (see below).

7.3.2. *TEM analysis of the ACP formed in the reference gold nanoparticles and CGNs-containing solutions.*

The changes in the ACP structure over time prior to the appearance of the initial precipitates in the reference gold nanoparticles and CGNs-containing solutions were investigated by evaluating the morphologies of the particles using TEM and analyzing their corresponding SAED patterns and lattice fringes. Figure 4 shows TEM micrographs of the ACP obtained from the reference solution (Fig. 4a-d) and CGNs-containing solution (Fig. 4e-h), along with their corresponding SAED patterns, and cryo-HR-TEM images of their lattice fringes. The solutions were transparent in both cases. In previous works, it is assumed that ACP is an essential precursor of calcium phosphate crystalline phases.[13-24] Wang et al.[25] reported HAP crystalline domain formed inside of ACP. Thus, it is also assumed that OCP crystalline domain also formed inside of ACP particles because OCP crystal structure containing HAP-like structures.

At 10 min, the particles in the reference solution had assembled into a liquid-like form with faint broad Debye rings corresponding to a *d*-spacing of 3.75 Å, (Fig. 4a) which are characteristic of ACP1.[16] At 60 min (Fig. 4b), spherical morphology and broad Debye rings of ACP were observed, which are characteristic of ACP2.[16] This result agrees with the TR-SLS analysis, which revealed changes in the internal structure of the ACP during this period (Fig. 3c).[16] Cryo-HR-TEM observation showed that, at 60 min, the structure of the ACP in the reference solution was essentially random with uniform contrast to the electron beam and small areas that appeared as black spots ranging from 2 to 10 nm in diameter (Fig. 4c), which is larger than the size of calcium phosphate clusters (0.7-1.4 nm).[21,22] A magnified cryo-HR-TEM image of these areas is shown in Fig. 4d. They consisted of weak but well-ordered lattice fringes with a *d*-spacing of 3.05 Å. A fast Fourier transform (FFT) image of the lattice fringes showed that the direction of the fringes was constant, which was in stark contrast to that of the lattice fringes of the ACP formed in the CGNs-containing solution (see below).

The morphological evolution of the ACP particles in the CGNs-containing solution essentially matched that of the reference solution. At 10 min, the particles had assembled into a liquid-like form (Fig. 4e). The corresponding SAED pattern showed a halo with no clear rings, indicating ACP1. At 60 min, which was the point when the first local increase in M_w was completed, the ACP morphology was spherical, and a broad Debye ring corresponding to a *d*-spacing of 3.75 Å appeared in the SAED pattern. This pattern typifies ACP2 (Fig. 4f). However, as can be seen in the cryo-HR-TEM images of the ACP2 particles formed at 60 min in the CGNs-containing solution (Figs. 4g and h), the ACP particles consisted of a major region showing a random-structure (Fig. 4g) and a minor region (<1 % of the observation area) showing complex lattice fringes (Fig. 4h). In addition, in the fringe region, the interspace distance between the neighboring lattice fringes varied from 2.5 to 5.0 Å, and thus it was impossible to identify the actual *d*-spacing. The direction of the lattice fringes was also random. The Ca/P ratios for the ACP in both solutions were 1.06 at 10 min and then rapidly increased, reaching 1.25 prior to initial precipitation (about 70 min and 170 min in the reference and CGNs-containing solutions, respectively) (see Fig. 6).

7.3.3. *In situ FT-IR analysis of the ACP and subsequent precipitates formed in the solution containing the reference gold nanoparticles or CGNs.*

Figure 5 shows the *in situ* FT-IR spectra in the P-O stretch region (800–1300 cm^{-1}) of ACP in the initial transparent solutions and the subsequent cloudy solutions with precipitates. Figs. 5a and b correspond to the spectra of the solutions containing the reference gold nanoparticles and CGNs, respectively. The reference solution was transparent until 70 min, while the CGNs-containing solution was transparent until 170 min. Immediately after initiating the reaction, intensities of both spectra were too low to identify; however, ACP particles formed in both solutions as shown by TEM observations. A low-intensity spectrum was observed until 25 min for the reference solution and until 40 min for the CGNs-containing solution. The spectra then showed several specific bands that gradually evolved, with different band evolution for each solution.

In the reference solution, the spectrum at 25 min exhibited seven separated bands at 804, 862, 963, 1024 (with a shoulder at 1034 cm^{-1}), 1049, 1126 and 1189 cm^{-1}. These bands corresponded to OCP vibrations, with the band at 963 cm^{-1} attributed to the PO_4^{3-} vibration mode ($\nu_1(PO_4)$) and the remaining bands attributed mainly to the HPO_4^{2-} ion vibration ($\nu_n(HPO_4)$) or OH^- with HPO_4^{2-} ($\delta_{OH}(HPO_4)$) vibration.[27] Combined with the XRD data (see section below), we concluded that the initial precipitate in the reference solution was crystalline OCP.

Alternatively, only major calcium phosphate bands at 1024 (with a shoulder at 1034 cm^{-1}), and 1126 cm^{-1} appeared in the spectrum of the CGNs-containing solution at

40 min. Note that these bands corresponding to OCP were clearly seen (broken lines in Figs. 4a and b); however, the bands at 804, 862, 963, 1049 and 1189 cm^{-1}, which appeared in the reference solution, were not observed in the CGNs-containing solution.

The *in situ* FT-IR spectrum of the initial precipitate in the CGNs-containing solution (after 170 min) lacked the specific bands corresponding to OCP HPO_4^{2-} ion vibrations ($v_n(HPO_4)$) such as those at 804, 864, 1049, 1105, and 1189 cm^{-1}, which were clearly observed in the spectrum of the precipitate in the reference solution (gray arrows in Fig. 3a). In addition, the spectra of the materials formed in the CGNs-containing solution at all reaction stages lacked the characteristic band for HAP at 1146 cm^{-1}. These results suggested that CGNs did not induce HAP formation prior to OCP formation under the present reaction conditions. On the basis of this information, combined with the results of the XRD and Raman spectroscopy analyses of the isolated precipitates (see details below), thus, it was inferred that the initial precipitate in the CGNs-containing solution is HPO_4-OH-structure-deficient OCP.

7.3.4. *Chemical composition of the ACP and precipitates determined using FE-SEM/EDX.*

Figure 6 shows the Ca/PO_4 ratios of the ACP and precipitates formed at various stages in the reference and CGNs-containing solutions (**N** is over 15). The Ca/PO_4 ratios of the materials taken from both the reference and CGNs-containing solutions increased gradually. The ratios for the ACP in both solutions were 1.06 ± 0.05 at 10 min and then rapidly increased, reaching 1.25 ± 0.03 prior to initial precipitation (70 min and 170 min in the reference and CGNs-containing solutions, respectively). After precipitation, the ratios of the precipitates in both solutions slowly increased and reached 1.35 ± 0.05 three days after starting the reactions. There were no significant difference between precipitate and ACP formed in the reference solutions and those formed in CGNs-containing solutions.

Figure 3, 4 and 5 indicate that, in each solution, the structural rearrangement of the ACP to a crystalline phase occurred from 10 to 60 min.

7.3.5. *XRD, NMR, and Raman analyses of the precipitates formed in the reference gold nanoparticles and CGNs-containing solutions.*

Figure 7 shows the XRD patterns of the precipitates taken from the reference solution (a) and CGNs-containing solution (b). The pattern of the initial precipitate taken from the reference solution (at 70 min after solution preparation) was characteristic of OCP crystals with a (100) peak at $2\theta = 4.7°$. This XRD pattern was essentially the same for up to 1 week. In contrast, the XRD pattern of the initial precipitate taken from the CGNs-containing solution (at 170 min after solution preparation) showed no peak at $2\theta = 4.7°$. Instead, the pattern exhibited a broad peak at around 24°–32°, which corresponded to several calcium phosphate crystalline phases; HAP, OCP, and β-TCP. Therefore, it was not possible to assign this peak to a particular calcium phosphate. At 12 h after solution preparation, a weak peak corresponding to the (100) orientation of crystalline OCP ($2\theta = 4.7°$) appeared in the XRD pattern of the precipitate taken from the CGNs-containing solution. Notably, the intensity of this peak gradually increased, and the final OCP was also stable for up to at least one week in the CGNs-containing solution. Note that none of the XRD patterns of the materials precipitated from the CGNs-containing solution included the characteristic HAP peak at

2θ = 10.5°. However, the intensities of weak peaks corresponding to the (-110) and (010) orientations (2θ = 9.2 and 9.4°, respectively) increased for two days in the CGNs-containing solution, but disappeared at one week. The crystalline OCP structure was consists of two HAP-like structures with transition zone and an HPO_4-OH-layer structure between them. The appearance of these two peaks suggested the development of a HAP-like structure with transition zone in OCP. Because the decrease in the intensities of these two peaks corresponded to the development of the conventional OCP structure, it was assumed that the precipitated OCP in the CGNs-containing solution had a HAP-like structure with transition zone during the initial precipitation stage, which then transformed to conventional OCP.

Figure 8 presents the ^{31}P solid-state NMR spectra of the initial precipitates taken from the reference solution at 70 min (initial precipitate), and from CGNs-containing solution at 170 min (initial precipitate) and two days after starting the reaction. The spectrum of the initial precipitate from the CGNs-containing solution exhibited a broad ^{31}P peak at 3.0 ppm as the main peak, with shoulder at 1.9 and -0.4 ppm. The main peak correspond to the doublet OCP *P1* and *P2/P4* sites of a poorly crystalline nanometric OCP phase, and the shoulder peaks correspond to OCP *P3* (1.9 ppm) and *P5/P6* (-0.4 ppm) site, which was confirmed by comparison with the spectrum of initial precipitate (crystalline OCP) from the reference solution shown as dotted spectrum in Fig. 6.[28] Note that the position of each peak observed in the precipitate from CGNs-containing solution was essentially equivalent to that from the reference solution. The spectrum of the initial precipitate taken from CGNs-containing solution had essentially weak a *P5/P6* peak corresponding to HPO_4^{2-} sites, indicating that the initial precipitate was mainly consisted of PO_4^{3-} rich structures and contained other minor structures corresponding to HPO_4^{2-} structures. The NMR spectra indicated that the structure of the initial precipitate formed in the CGNs-containing solution was low crystalline OCP, and not HAP.

The spectrum of the precipitate at two days after the reaction exhibited typical OCP peaks at -0.4, 1.9, 3.1, and 3.6 ppm with an additional peak at -1.2 ppm.[28,31] The presence of the -1.2 ppm peak was evidence that the -COOH altered the HPO_4-OH structure of the OCP lattice through either intercalation or adsorption.[9-12]

Raman spectra of the precipitates from the reference solution (from 70 min to 1 week) showed similar patterns independent of time (Fig. 9a). Typical OCP peaks at 417, 591 and 961 cm^{-1} and sub-peaks at 609, 1011 and 1048 cm^{-1} were observed. The results of the XRD and Raman analyses of the precipitates taken from the reference solution indicate that OCP was directly formed from ACP without passing through other crystalline intermediate phases.

The time evolution of the Raman spectra of the precipitates taken from the CGNs-containing solution (from 170 min to one week) is shown in Fig. 9b. All the spectra showed weak peaks attributable to OCP (417, 591, and 961 cm^{-1}) with sub-peaks at 609, and 1048 cm^{-1}. These sub-peaks were also attributed to OCP and their intensities increased over time. However, the intensity of a sub peak at 1011 cm^{-1}, which corresponded to $v_1(HPO_4)$ stretch, of the precipitate formed in the CGNs-containing solution was much weaker at all-time points than that of precipitate formed in the reference solution (black arrow in Fig. 9b). Additional broad peaks in the spectra at 170 and 200–300 cm^{-1} were attributed to the glass slide, and were observed in the CGNs-containing solution due to the weaker crystallinity of the precipitates relative to that of the precipitates observed in the reference solution. Consistent with the cryo-HR-TEM observation, the Raman spectra of the precipitates formed in the CGNs-containing solution indicated a HPO_4-OH-deficient OCP structure than that observed for the spectra of the precipitates formed in the reference solution.

The precipitates formed in both solutions were observed using TEM (Figs. 10 and 11). Briefly, both initial precipitates were spherical particles (1–2 μm in diameter) consisting of plate-like (reference) or needle-like (CGNs) crystals. In both solutions, the typical OCP plate-like morphology developed at 12 h. Cryo-HR-TEM observation showed the precipitates formed in the CGNs-containing solution consisted almost exclusively of complex lattice fringes, such as those seen in Fig. 4h, which is in contrast to the initial precipitates formed in the reference solution (Fig. 10). Well-ordered lattice fringe regions were also observed, although they were rare (Fig. 11). Gold nanoparticles were sometimes observed on the edge and inside of OCP crystals in randomly.

7.4. Discussions

HR-TEM observation indicated that the crystalline structures which considered as OCP lattice were formed in ACP spherical particles in both solutions. XRD and Raman analysis showed that CGNs not only altered dynamics of phase transformation of ACP-OCP but also induced unknown intermediate phase lacked HPO_4 and OH structures OCP during phase transformation from ACP into conventional OCP. At first glance, the physico-chemical properties of this unknown intermediate phase were similar to that of HAP rather than that of OCP because typically OCP peak at $2\theta = 4.7°$ was absent. However, Raman and NMR spectra indicated that unknown intermediate phase is an OCP-like material which deficient HPO_4-OH structure rather than HAP. In addition, the XRD pattern showed no evidence of HAP in the precipitates (lack of

HAP-specific peaks at $2\theta = 10.5°$). Furthermore, under high supersaturation conditions, the relatively larger surface energy of HAP ($\gamma_{\mathrm{HAP}} = 3.3k_B\mathrm{T}$, $\gamma_{\mathrm{OCP}} = 2.0k_B\mathrm{T}$) can be overcome.[29,30] Thus, in the CGNs-containing solution, it is summarized that ACP first transformed to OCP-like material which deficient HPO_4-OH structure, and then converted to conventional OCP over time.

Based on the TR-SLS results, the phase transformation from ACP to OCP in the reference solution can be explained as rearrangement of the internal structure from loose (ACP) to rigid (OCP) or as simple nucleation of OCP crystals using ACP as a template. However, the results of the cryo-HR-TEM and *in situ* FT-IR analyses indicated the presence of OCP in the initial ACP, suggesting that the transformation occurred via direct structural rearrangement in the particles. Structural rearrangement of the initial ACP to the final crystalline phase also occurred in the CGNs-containing solution. However, direct rearrangement to OCP was inhibited, and an additional intermediate phase appeared prior to formation of conventional crystalline OCP. Thus, it was inferred that CGNs act as a negative catalyst, increasing the activation energy of the ACP–OCP phase transformation and inhibiting HPO_4-OH-layer structure evolution. Consequently, CGNs not only delayed the phase transformation from ACP to OCP but also changed the reaction path, resulting in the formation of an OCP-like intermediate phase (HPO_4-OH layer structure deficient OCP).

The HPO_4-OH layer structure is unique structure for OCP.[5] Habraken et al.[26] showed OCP (Ca-deficient OCP) is precursor of HAP. The HPO_4-OH layer formation skip effect by CGNs may be a core of acceleration effect of HAP formation which described in Chapter 6. Furthermore, it is suggested that physico-chemical properties of initial amorphous phases were essential for crystalline mineralization process.[18-20,22,24,26,32-34] It is suggested that CGNs affect into clustering formation process, especially ionic pair formation stage. Thus, it is also suggested that ionic interaction between CGNs and Ca^{2+} ions were controlled final polymorph formation processes. This suggests that CGNs has strong affinity for Ca^{2+} ions and there is a strong chemical bonding effect between Ca^{2+} ions of the OCP crystal structures.[11,12] Briefly, using high resolution NMR, Davies et al.[11] showed that citrate bridged Ca^{2+} ions of transition zone instead of HPO_4 and OH molecules. This suggested that molecular interaction between Ca^{2+} ions and -COOH molecules controlled the OCP mineralization, especially the HPO_4-OH layer structures during OCP mineralization from ACP.

7.5. Conclusions

In Chapter 7, this study has provided new insights into the role of immobilized -COOH-containing material in OCP mineralization. In weak acidic solutions, CGNs act as negative catalyst of OCP formation process. CGNs altered not only physico-chemical properties of ACPs as precursor and reaction path of OCP formation via HPO_4-OH layer deficient OCP as intermediate transition phase.

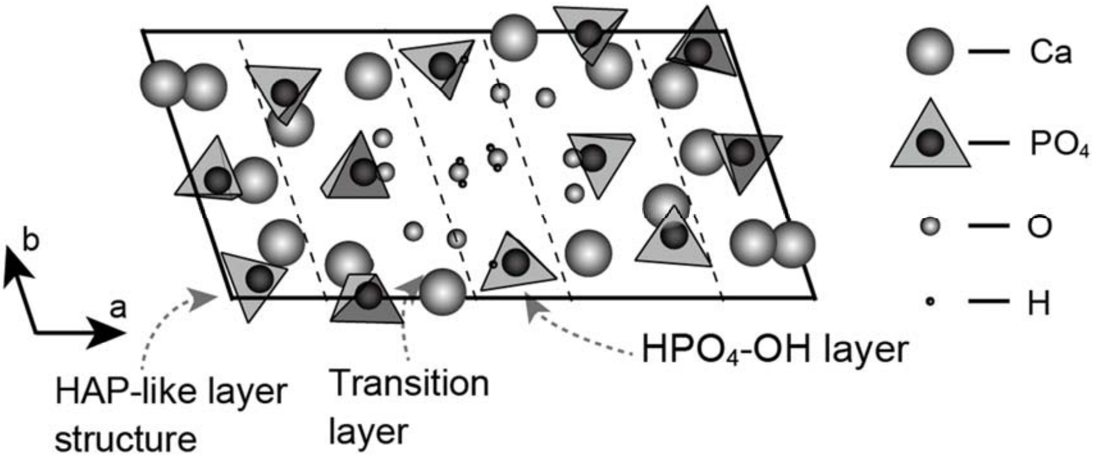

Figure 7.1. OCP unite lattice toward to *c*-axis from Brown et al.[5]

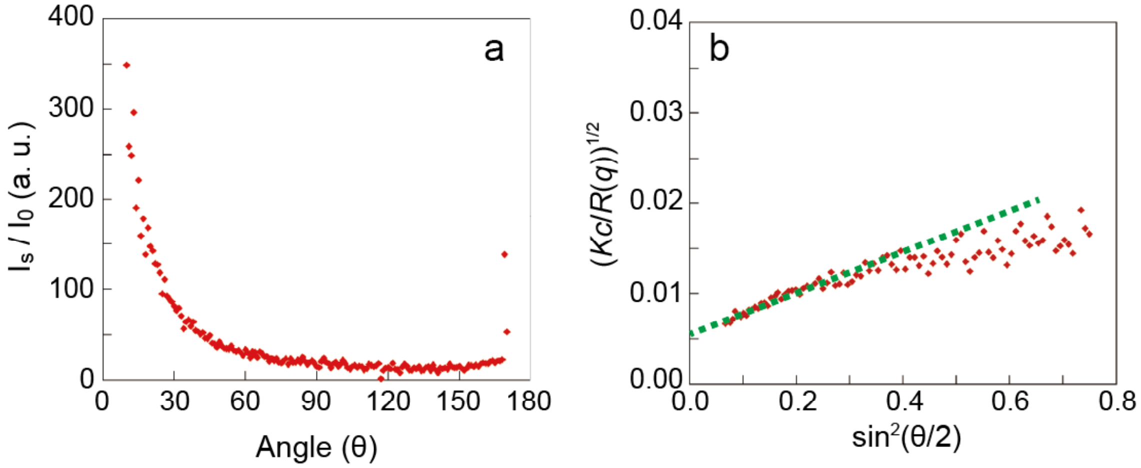

Figure 7.2. (a) Relationships between scattering angle and scattering relative intensity of calcium phosphate formed in reference gold nanoparticles-containing solution at 10 min. (b) Zimm-square-root plot of (a). Green broken line indicated calculation part of plot ($\theta = 30°$ to 70°).

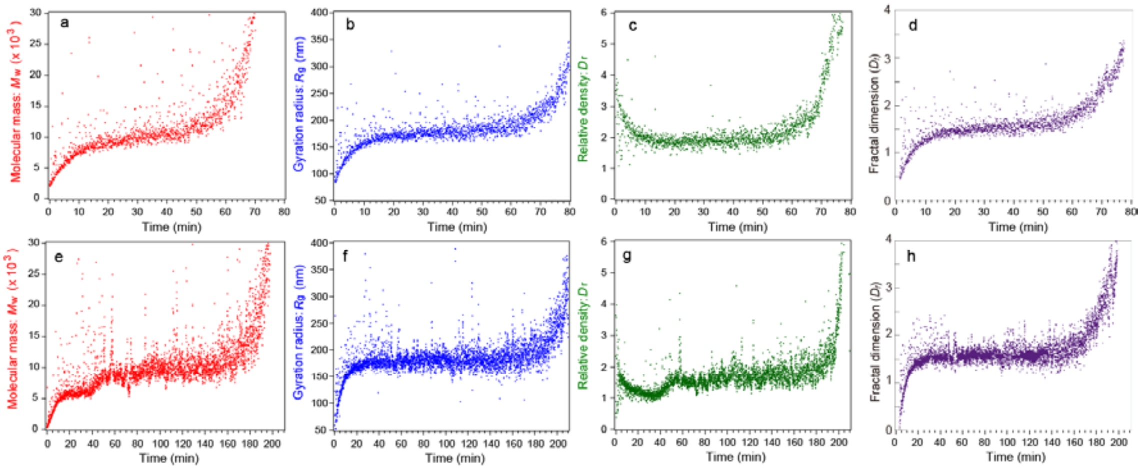

Figure 7.3. TR-SLS analysis results for the solutions containing 10 µM reference gold nanoparticles (upper panels; (a)–(d)) and 10 µM CGNs (bottom panels; (e)–(h)). Shown are the temporal changes in the apparent M_w, R_g, D_r and D_f of the particles in solution.

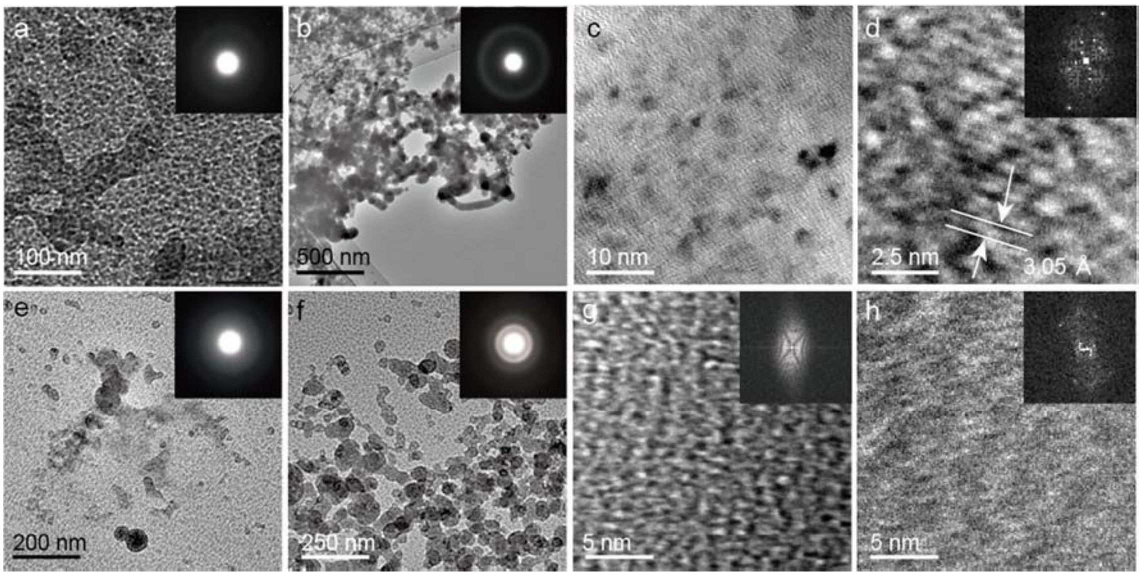

Figure 7.4. TEM photographs with SAED patterns (inset) and FFT images of the ACP formed in the reference and CGNs-containing solutions. (a) Liquid-like ACP in the reference solution at 10 min. (b) Spherical ACP in the reference solution formed at 60 min. (c) Cryo-HR-TEM photograph of the ACP in the reference solution formed at 60 min. Black dots ranging from 2–10 nm can be seen. (d) Cryo-HR-TEM photograph of the dots in (c) with the corresponding FFT image. (e) Liquid-like ACP formed at 10 min in the CGNs-containing solution. (f) Spherical ACP formed at 60 min in the CGNs-containing solution. All times correspond to those after solution preparation. (g) Cryo-HR-TEM photograph of the completely random structure of the ACP in formed at 60 min in the CGNs-containing solution with the corresponding FFT image. (h) Cryo-HR-TEM photograph of the ACP in the CGNs-containing solution at 60 min. Complex lattice fringes are observed, but the FFT image shows poor symmetry.

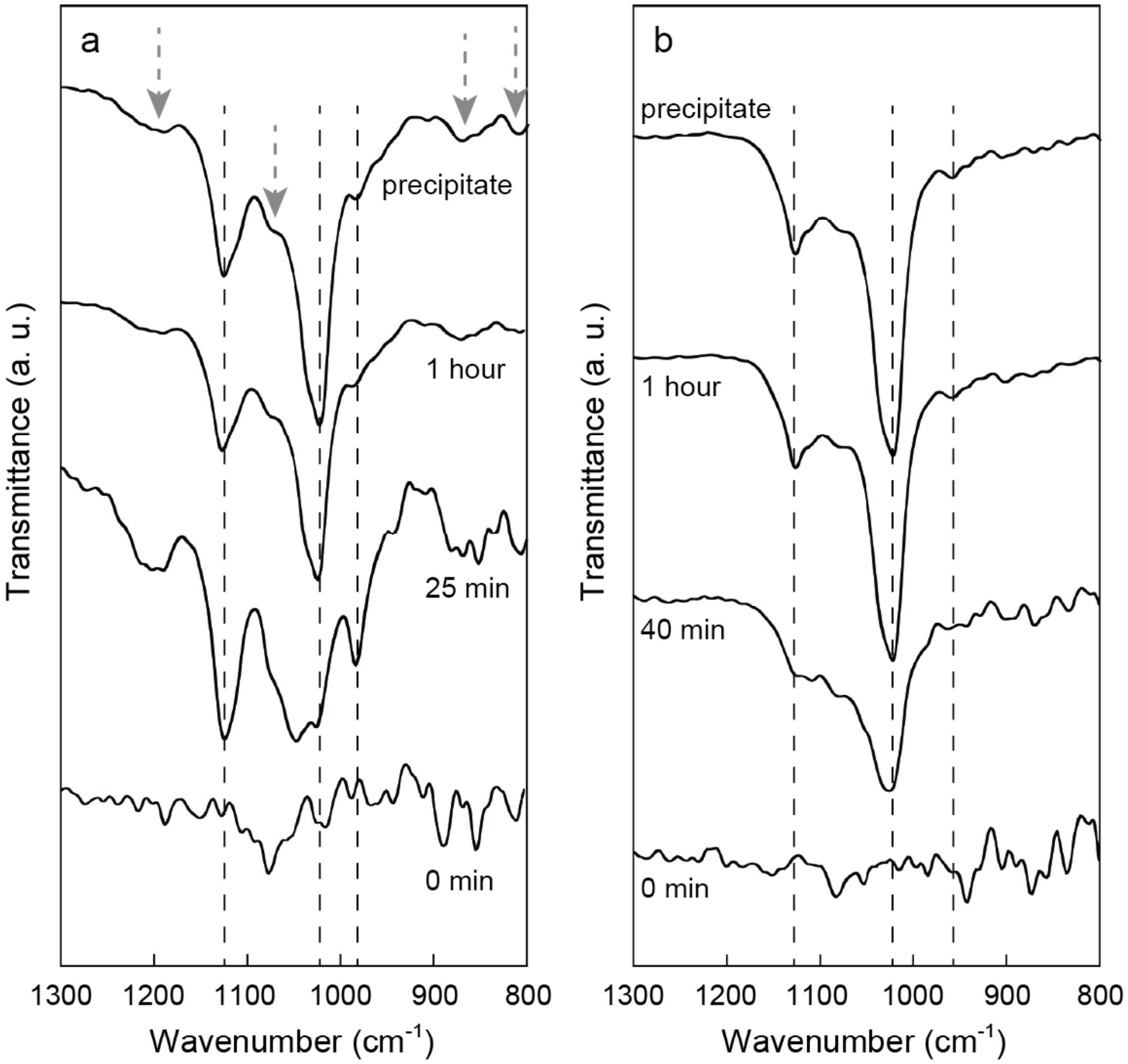

Figure 7.5. *In situ* FT-IR spectra of ACP in the reference (a) and CGNs-containing (b) solutions at various reaction stages. Broken black lines indicate typical OCP peaks: 963, 1021 and 1124 cm^{-1}. Broken grey arrows indicate OCP peaks that disappear in the ACP and precipitate formed in the CGNs-containing solution.

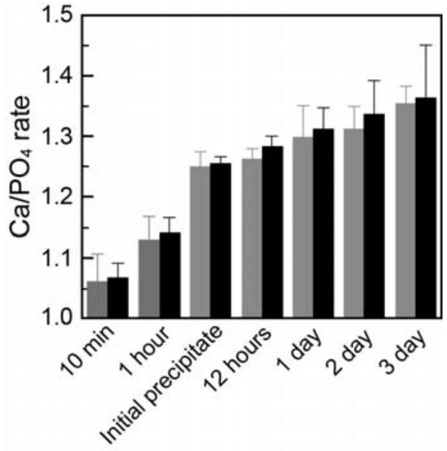

Figure 7.6. FE-SEM/EDX data for the Ca/PO4 ratios of the materials formed in the reference (grey bar) and CGNs-containing (black bar) solutions at various reaction stages.

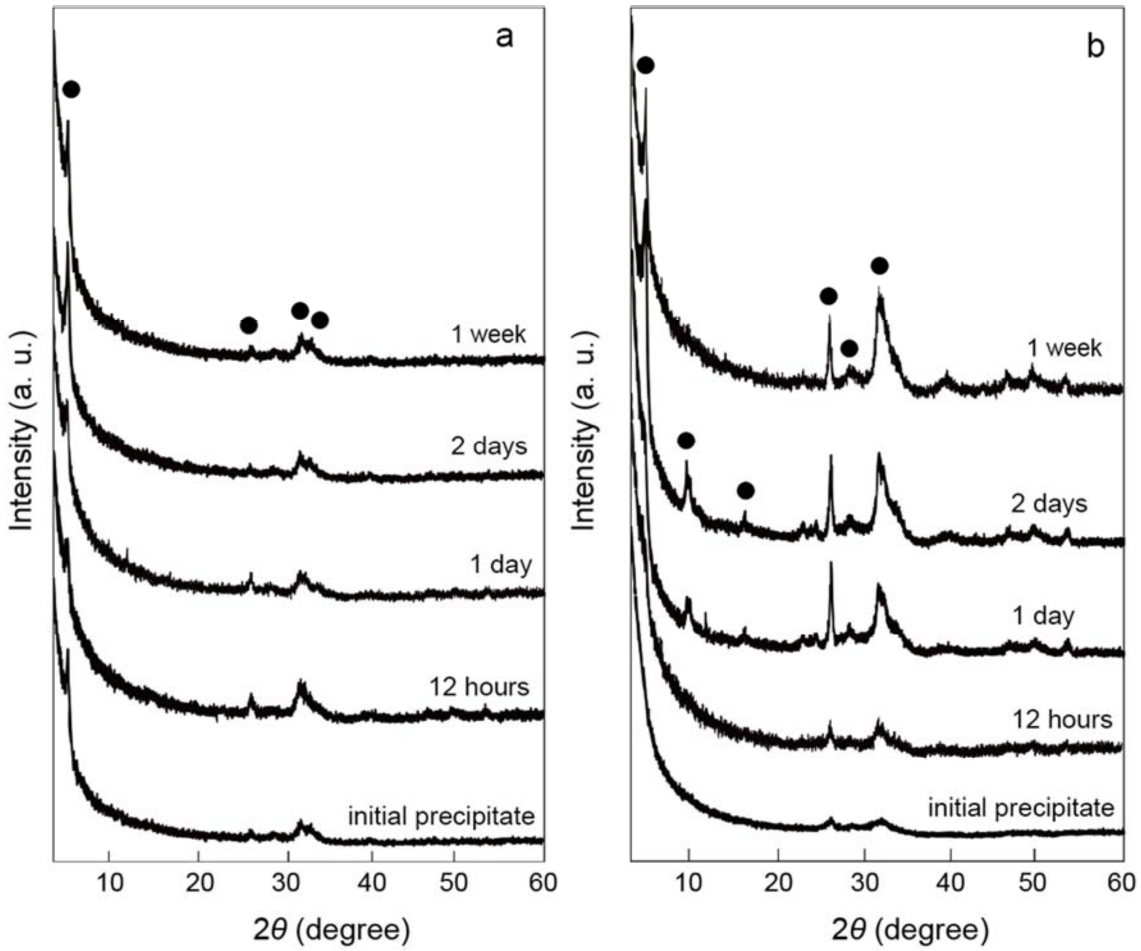

Figure 7.7. Time evolution of the XRD patterns of the precipitates taken from the (a) reference solution and (b) CGNs-containing solution. The solid black circles correspond to the OCP peaks.

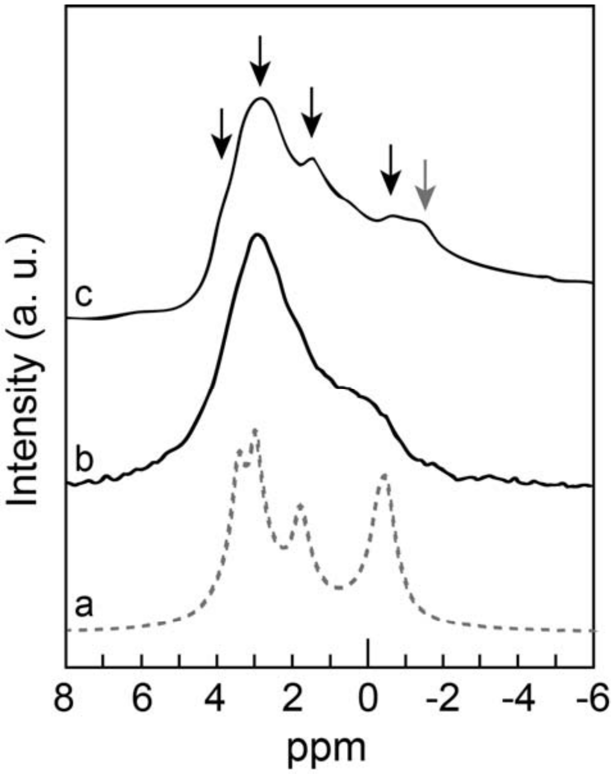

Figure 7.8. Solid-state NMR ^{31}P spectra of (a) the initial precipitate from reference solution (grey broken line) and (b) the initial precipitate and material (c) after 2 day from CGNs-containing solution (solid black line). Black arrows indicate the OCP peaks. Grey arrow indicates the -COOH-containing OCP peak.

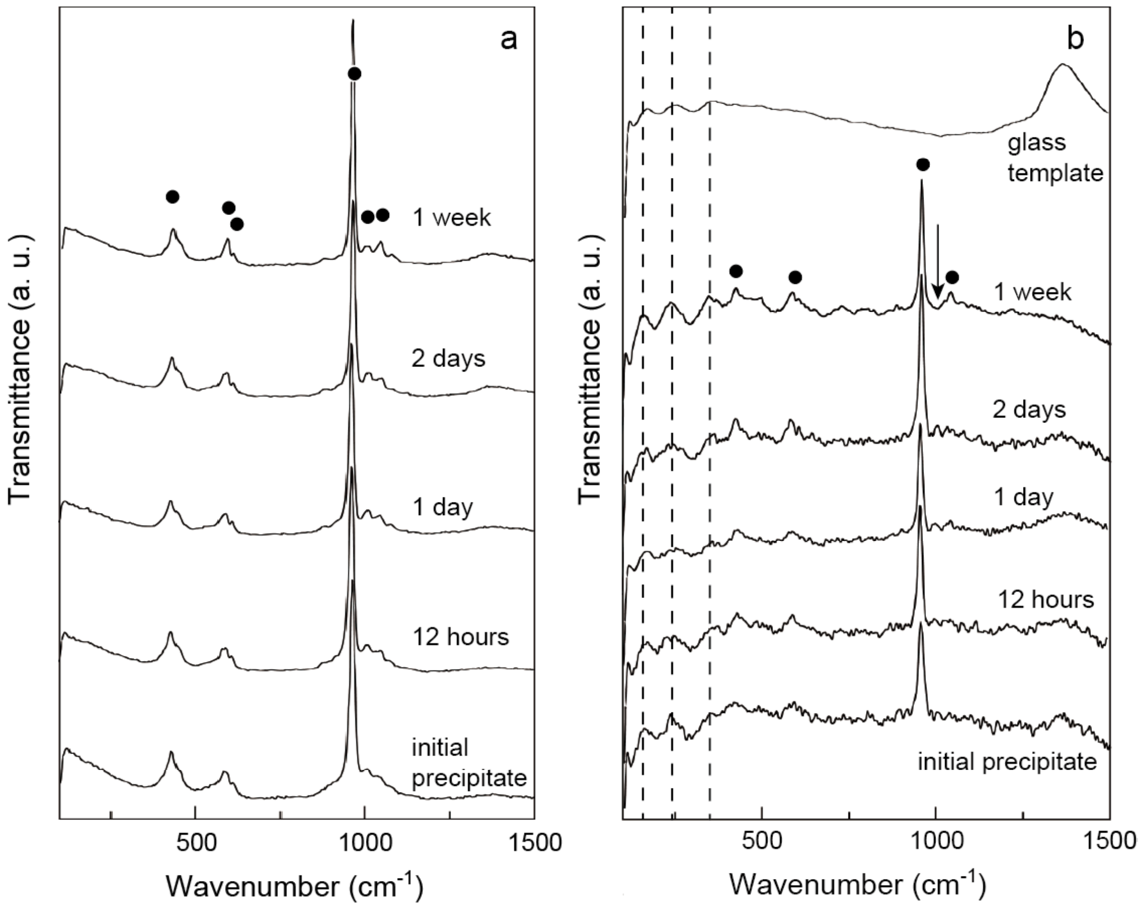

Figure 7.9. Time evolution of the Raman spectra of the precipitates taken from the (a) reference solutions and (b) CGNs-containing solutions. The solid black circles correspond to the OCP peaks. The black arrow in (b) indicates a peak at 1011 cm^{-1} correspond to $\nu_1(HPO_4)$ stretch.

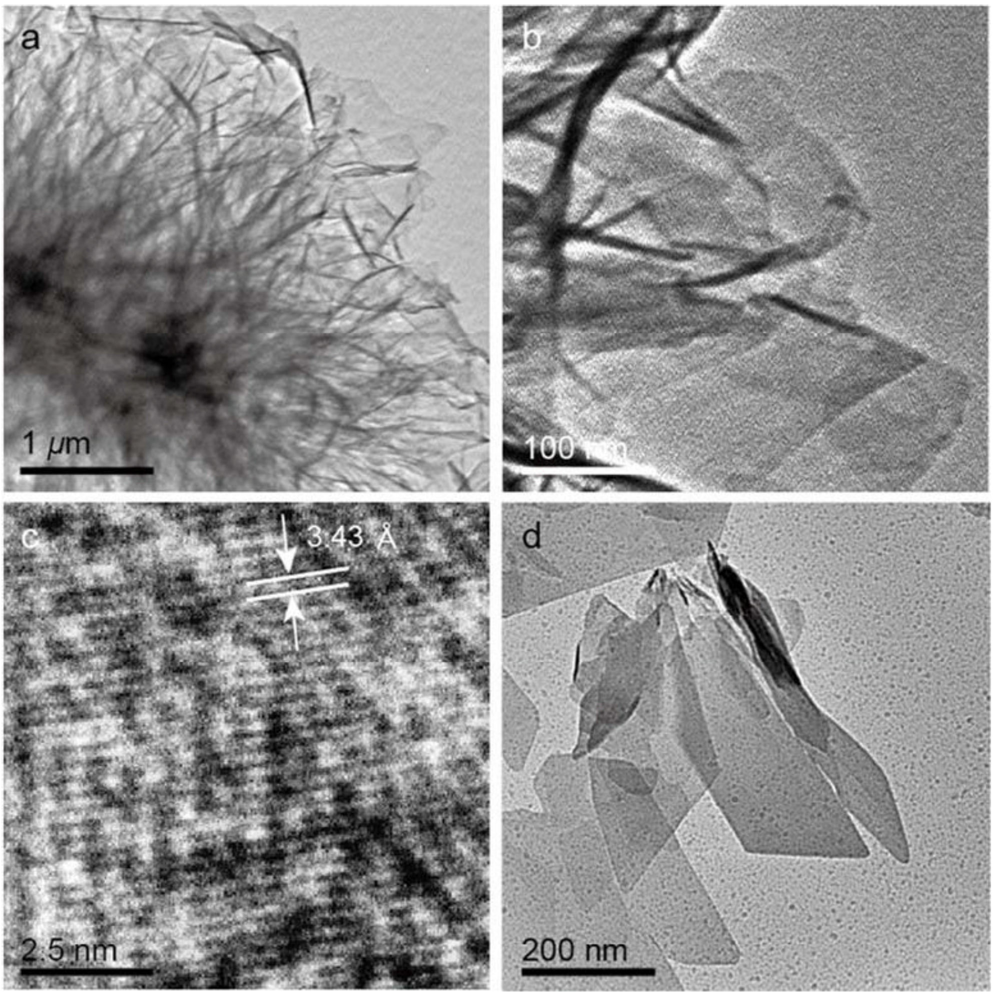

Figure 7.10. TEM photographs of the precipitates formed in the reference solutions. (a) TEM photograph of the initial precipitate. (b) Magnified image of (a). (c) Cryo-HR-TEM photograph of the well-ordered lattice fringes in the initial precipitates. (d) TEM photograph of the OCP plate-like crystals formed at 12 h.

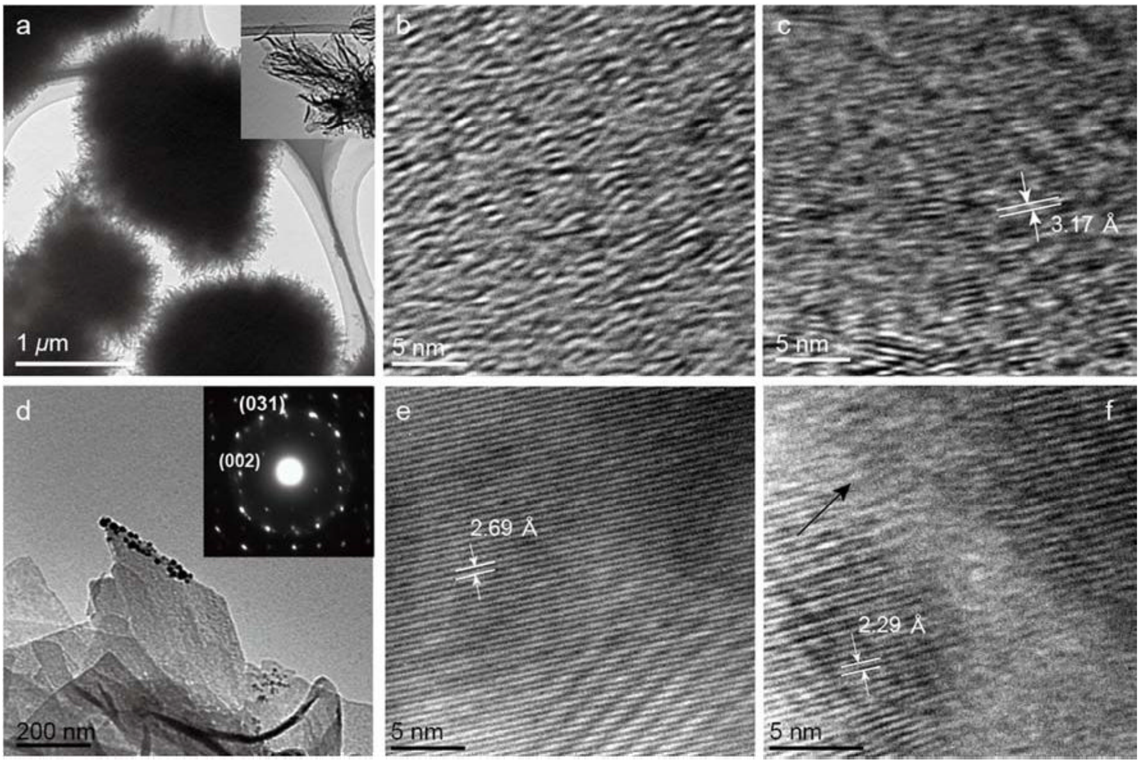

Figure 7.11. TEM photographs of the precipitates formed in the CGNs-containing solution. (a) TEM photograph of the initial precipitate (a magnified image is shown in the upper left). (b) Cryo-HR-TEM photograph of the complex poorly lattice fringe region for the initial precipitate. (c) Cryo-HR-TEM photograph of the partially well-ordered lattice fringes in the initial precipitate. (d) TEM photograph with the SAED pattern of the plate-like precipitates formed after 1 day. The gold nanoparticles observed at the edges of the plate-like crystals. (e) Cryo-HR-TEM photograph of the precipitates formed after 1 day. Well-ordered lattice fringes and moiré fringes (lower right) are observed. (f) Cryo-HR-TEM photograph of the separated well-ordered lattice fringes. The black arrow indicates the region of the complex poorly lattice fringes.

Reference

(1) Wang, L., Nancollas, G.H. Calcium Orthophosphates: Crystallization and Dissolution. *Chem. Rev.*, **2008**, *108*, 4628-4669.

(2) Johnsson, M.S., Nancollas, G.H. The role of brushite and octacalcium phosphate in apatite formation. *Crit. Rev. Oral. Biol. Med.*, **1992**, *3*, 61-82.

(3) Newesely, H. Darstellung von "Oktacaliumphosphat" (Tcracalcium hydrogentrisphosphat) durch homogene Kristallisation. *Monatch. Chem.*, **1960**, *249*, 1020-1023.

(4) Vereecke, G., Lemaitre, J. Calculation of the solubility diagrams in the system $Ca(OH)_2$-H_3PO_4-KOH-HNO_3-CO_2-H_2O. *J. Cryst. Growth*, **1990**, *104*, 820-832.

(5) Brown, W.E. Octacalcium Phosphate and Hydroxyapatite. *Nature*, **1962**, *196*, 1048-1050.

(6) Nelson, D.G.A., McLean, J.D. High-Resolution Electron Microscopy of Octacalcium Phosphate and its Hydrolysis Products. *Caldif. Tiss. Int.*, **1984**, *36*, 219-232.

(7) Kamitakahara, M., Okano, H., Tanihara, M., Ohtsuki, C. Synthesis of octacalcium phosphate intercalated with dicarboxylate ions from calcium carbonate and phosphoric acid. *J. Cera. Soc. Jpn.*, **2008**, *116*, 481-485.

(8) Brown, W.E., Schroeder, L.W., Ferris, J.S., Interlayering of crystalline octacalcium phosphate and hydroxyapatite. *J. Phys. Chem.*, **1979**, *83*, 1385-1388.

(9) Monma, H., Goto, M. Succinate-complexed Octacalcium Phosphate. *Bull. Chem. Soc. Jpn.*, **1983**, *56*, 3843-3844.

(10) Markovic, M., Fowler, B.O., Brown, W.E. Octacalcium Phosphate Carboxylates. 1. Preparation and Identification. *Chem. Mater.*, **1993**, *5*, 1401-1405.

(11) Davies, E., Muller, K.H., Wong, W.C., Pickard, C.J., Reid, D.G., Skepper, J.N., Duer, M.J. Citrate bridges between mineral platelets in bone. *Proc. Nati. Acad. Sci. USA*, **2014**, *111*, E1354-E1363.

(12) Tsai, T.W.T., Chou, F., Tseng, Y., Chan, J.C.C. Solid-state P-31 NMR study of octacalcium phosphate incorporated with succinate. *Phys. Chem. Chem. Phys.*, **2010**, *12*, 6692-6697.

(13) Tsuji, T., Onuma, K., Yamamoto, A., Iijima, M., and Shiba, K. Direct Transformation from Amorphous to Crystalline Calcium Phosphate Facilitated by Motif-Programmed Artificial Proteins. *Proc. Nati. Acad. Sci. USA*, **2008**, *105*, 16866–16870.

(14) Tsuji, T., Oaki, Y., Yoshinari, M., Kato, T., Shiba, K. Motif-programmed artificial proteins mediated nucleation of octacalcium phosphate on titanium substrates. *Chem. Comm.* **2010**, *46*, 6675-6677.

(15) He, G., Dahl, T., Veis, A., and George, A. Nucleation of Apatite Crystals in vitro by Self-Assembled Dentin Matrix Protein 1. *Nat. Mater.*, **2003**, *2*, 552–558.

(16) Christofferesen, J., Christofferesen, M.R., Kibalczyc, W. Apparent solubilities of two amorphous calcium phosphates and octacalcium phosphate in the temperature range 30-42°C. *J. Cryst. Growth*, **1990**, *105*, 349-354.

(17) Sugiura, Y., Onuma, K., Kimura, Y., Miura, H., Tsukamoto, K. Morphological evolution of precipitates during transformation of amorphous calcium phosphate into octacalcium phosphate in relation to role of intermediate phase. *J. Cryst. Growth*, **2011**, *322*, 58-67.

(18) Eanes, E.D., Gillessen, I.H., Posner, A.S. Intermediate states in the precipitation of hydroxyapatite. *Nature*, **1965**, *208*, 365-367.

(19) Christoffersen, J., Christoffersen, M.R., Kibalczyc, W., Anderson, F.A. A Contribution to the Understanding of the Formation of Calcium Phosphate. *J. Cryst. Growth*, **1989**, *94*, 767–777.

(20) Posner, A., Betts, F. Synthetic amorphous calcium phosphate and its relation to bone mineral structure. *Acc. Chem. Res.* 1975, *8*, 273-281.

(21) Treboux, G., Layrolle, P., Kanzaki, N., Onuma, K., Ito, A. Symmetry of Posner's Cluster, *J. Am. Chem. Soc.*, **2000**, *122*, 8323-8324.

(22) Onuma, K., Oyane, A., Kokubo, T., Treboux, G., Kanzaki, N., Ito, A. Nucleation of Calcium Phosphate on 11-Mercaptoundecanoic Acid Self-assembled Monolayer in a Pseudophysiological Solution. *J. Phys. Chem. B*, **2000**, *104*, 11950-11956.

(23) Dey, A., Bomans, P.H.H., Muller, F.A., Will, J., Frederick, P.M., deWith, G., and Sommerdijk, N.A.J.M. The Role of Prenucleation Clusters in Surface-Induced Calcium Phosphate Crystallization. *Nat. Mater.*, **2010**, *9*, 1010–1014.

(24) Onuma, K., Ito, A. Cluster Growth Model for Hydroxyapatite. *Chem. Mater.*, **1998**, *10*, 3346–3351.

(25) Wang, C.G., Liao, J.W., Gou, B.D., Huang, J., Tang, R.K., Tao, J.H., Zhang, T.L., Wang, K. Crystallization at multiple sites inside particles of amorphous calcium phosphate. *Cryst. Growth Des.*, **2009**, *9*, 2620-2626.

(26) Habraken, W.J.E.M., Tao, J.T., Brylka, L.J., Friedrich, H., Bertinetti, L., Schenk, S.A., Verch, A., Dmitrovic, V., Bomans, P.H.H., Frederik, P.M., Laven, J., van der Schoot, P., Aichmayer, B., deWith, G., DeYoreo, J.J., Sommerdijk, N.A.J.M. Ion-association complexes unite classical and non-classical theories for the biomimetic nucleation of calcium phosphate. *Nat. Comm.* **2013**, DOI: 10.1038/ncomms2490.

(27) Onuma, K., Oyane, A., Tsutsui, K., Tanaka, K., Treboux, G., Kanzaki, N., Ito, A.

Precipitation Kinetics of Hydroxyapatite Revealed by the Continuous-Angle Laser Light Scattering Technique. *J. Phys. Chem. B*, **2000**, *104*, 10563-10568.

(28) Berry, E.E., Baddiel, C.B. Some assignments in the infra-red spectrum of octacalcium phosphate. *Spectroshim. Acta*, **1967**, *23A*, 1781-1792.

(29) Tsai, T.W.T., Chan, J.C.C. Chapter 1: Recent Progress in the Solid-State NMR Studies of Biomineralization, *Annual Reports on NMR Spectroscopy*, Volume 73, pp.1-61, Elsevier Ltd., the Netherland, **2011**.

(30) Onuma, K., Kanzaki, N., Ito, A., Tateishi, T. Growth Kinetics of the Hydroxyapatite (0001) Face Revealed by Phase Shift Interferometry and Atomic Force Microscopy. *J. Phys. Chem. B*, **1998**, *102*, 7833-7838.

(31) Wu, W., Nancollas, G.H. Nucleation and Crystal Growth of Octacalcium Phosphate on Titanium Oxide Surfaces. *Langmuir*, **1997**, *13*, 861-865.

(32) Gebauer, D., Gunawidjaja, P.N., PeterKo, J.Y., Bacsik, Z., Aziz, B., Liu, L., Hu, Y., Bergstrom, L., Tai, C.W., Sham, T.K., Eden, M., Hedin, N. Proto-Calcite and Proto-Vaterite in Amorphous Calcium Carbonates, *Angew. Chem. Int. Ed.*, **2010**, *49*, 8889-8891.

(33) Gebauer, D., Völkel, A., Colfen, H. Stable Prenucleation Calcium Carbonate Clusters, *Science*, **2008**, *322*, 1819-1822.

(34) Demichelis, R., Raiteri, P., Gale, J.D., Quigley, D., Gebauer, D. Stable prenucleation mineral clusters are liquid-like ionic polymers. *Nat. Comm.*, **2011**, DOI: 10.1038/ncomms1604.

Chapter 8

The effect of soluble -COOH (acetic acid) into OCP crystal structures.

8.1. Introduction

As described in Chapter 6 and 7, immobilized carboxylic functional groups (CGNs) selectively inhibited the HPO_4-OH layer structure, which is essential for OCP crystal formation during HAP and OCP mineralization. However, Newesely et al.[1] suggested that a soluble -COOH, acetic acid, is essential for inducing large size and well-crystalline OCP crystals. In addition, as described in *Division I*, the same ions and molecules which have difference physico-chemical properties influenced different effect into biogenic mineralization. Therefore, in Chapter 8, crystallographical studies focusing on the effect of hydrate -COOH on the OCP mineralization using acetic acid as hydrate -COOH are described. On the basis of acetic acid effect on OCP crystallinity, how acetic acid affect into OCP formation process was discussed.

OCP is known as a metastable crystalline phase of calcium phosphate and a precursor, especially for HAP formation through specific solid-solid transformation.[1-6] It preferentially forms in slightly acidic to neutral solutions (pH = 5.0–7.0).[7-9] Previous studies have been reported that the chemical formula of OCP is described as $Ca_8(HPO_4)_2(PO_4)_4{\cdot}5H_2O$ (Ca/PO_4 ratio 1.33, $Ca:PO_4 = 8:6$), and its crystal symmetry is $P{-}1$ triclinic space group.[2,3,8,10] The OCP crystal structure is consisted of three sub-layer-structures along the *a*-axis, namely a HAP-like layer structure (*Apa*: Ca/PO_4 ratio 2.00, $Ca:PO_4 = 4:2$), a transition structure (*Tra*: Ca/PO_4 ratio 1.33, $Ca:PO_4 = 4:3$), and a HPO_4–OH layered structure (*Lay*: Ca/PO_4 ratio 0.00, $Ca:PO_4 = 0:2$).[3,8,10] Thus, the OCP crystal structure is thought to have a layered structure with *Apa–Tra–Lay–Tra–Apa* stacking along the *a*-axis. Therefore, OCP crystals have long range *a*-axis (18.3-21.2 Å)

04compare to *b*- (9.63 Å) and *c*-axis (6.87 Å) parameters. Because of the large *a*-axis parameter, a strong reflection at a low angle (2θ = around 4.7°) is observed in the XRD pattern as a typical OCP peak.[2,5-10]

Some previous studies have been reported that the OCP crystal structure can be easily altered by thermal fluctuations, and that some kind of -COOH-containing molecules.[4-6,11-14] This effect was described as a molecular intercalation and releasing effect of phosphate ions in *Lay*. Monma and Goto[11] showed that succinate incorporated OCP crystals have an elongated *a*-axis at 21.5 Å. During the interaction between -COOH-containing molecules and *Lay* in OCP, lattice parameter of OCP, especially the *d*-spacing of *a*-axis, was widely altered. Recently, direct evidence of molecular intercalation in OCP crystal structures maintaining the whole structure was showed by high resolution NMR.[15,16] Markovic et al.[12,17] investigated change in lattice parameter of OCP formed in various -COOH-containing molecules in a bit acidic aqueous solutions. In acetic acid, a simple -COOH molecules, incorporated systems, there were no evidence of change in lattice parameters and no evidence of -COOH-containing OCP formation.

After Newesely et al.[1] found that large size (around 1 mm) single crystals of OCP could be synthesized using acetic acid, Mathew et al.[18] reported the formation of large sized OCP through DCPD crystals hydrolysis reaction in a solution containing 100 mM acetic acid. Thus, the results of the studies by Markovic et al.[12,17] conflict with those obtained by Newesely et al.[1] and Mathew et al.[18]. Therefore, knowledge on this phenomenon, i.e., how acetic acid molecules affect OCP mineralization, would provide further interests into the OCP mineralization process. Previous studies mainly focused on changing in lattice parameters,[12] especially *a*-axis, and changing the *Lay* structures of

OCP.[15,16] However, it is suggested that -COOH-containing molecules affect not only *Lay* structure of OCP but also affect *Apa* structure of OCP because some previous report indicated that -COOH-containing molecules essentially affect into HAP structures and formation.[19-21] Thus, it would be natural that -COOH-containing molecules affect the *Apa* structure of OCP; however, this phenomenon remains unclear.

In Chapter 8, the effect of acetic acid on the OCP crystal structure mineralization process, especially *Apa* structures is investigated.

8.2. Experimental Methods

8.2.1. *Preparation of solutions used for crystalline OCP synthesis.*

All reagents were reagent grade or mass analysis grade and dissolved in double-distilled water (resistance at 18.2 Ω and <5 ppb in TOC). The reaction solutions were prepared using 1 M $CaCl_2$, 1 M CH_3COONa, 1 M CH_3COOH, 0.5 M KH_2PO_4, and 0.5 M K_2HPO_4. The CH_3COONa and CH_3COOH solutions were mixed to obtain a 1 M CH_3COONa–CH_3COOH solution (acetic buffer solution) with a pH of 5.7 at 25 °C.

8.2.2. *Synthesis of dicalcium phosphate dihydrate (DCPD) by solution chemistry processes.*

DCPD was used as the OCP precursor. 25 mL of 0.5 M KH_2PO_4 and 5 mL of K_2HPO_4 were mixed with a magnetic stirrer in a glass beaker. After thorough mixing, 15 mL of 1 M $CaCl_2$ was immediately added into the phosphate solution with stirring. The prepared solution contained 0.33 mM total PO_4 and Ca^{2+} ions. This supersaturated calcium phosphate solution was stirred at 400–600 rpm for 1 h at room temperature and pressure.

The precipitated materials were separated by centrifugation for 30 s, and then washed five times with 2 mL of H_2O. The solid phases were immediately rewashed with 2 mM of a mixed alcohol solution (ethanol: isopropanol = 1:1 v/v) several times to remove any residual water, and then dried at room temperature. The obtained materials were characterized as DCPD crystals by XRD analysis and FE-SEM observation. The details are described below.

8.2.3. *OCP synthesis methods in various COOH-containing solutions from DCPD.*

Different concentration acetic buffer solutions (0, 2.5, 5.0, 7.5, 10.0, 12.5, 15.0, 17.5, 20.0, 50.0, 100, 200 and 500 mM) were prepared at 65 °C in 2 mL polypropylene tubes. To the solutions of acetic buffer, 50 mg of DCPD was added and mixed using a vibrational mixer. After mixing, all of the vessels were caped to avoid evaporation and placed in a zirconia sand bath at the temperature of 65 °C. The pH values of each solution were monitored using a pH electrode (LAQUA standard ToupH electrode 9615-10D, Horiba Co., Kyoto, Japan) connected to a multimeter (D-51AC, Horiba Co., Kyoto, Japan). The electrode was soaked in Ca-free reaction solution for a few minutes to stabilize the electrode condition. The pH values of the mixed solutions were recorded every 2 s. After reacting for 15 h, the precipitates were separated by centrifuging, washed five times with 2 mL double-distilled water, and well ejected water using micropipettes, after that they dried at 65 °C for 1 h. The precipitate washing methods were referred by Ref investigated on phase transformation process from OCP into HAP.[22]

8.2.4. *Material characterization methods.*

To determine how the material phases, structures and morphologies, the calcium phosphate precipitates were sampled at 15 hours. In microscopic observation, precipitates obtain methods were below. 2 mL reaction solutions were sampled into polypropylene tubes and centrifuged for 30 s. After centrifugation, the precipitates were gathered and washed using mixed alcohol (ethanol: isopropyl alcohol = 1: 1 in volume wait) for several times and dropped on TEM Cu microgrid covered carbon holey films and air dried on KimWipes® for TEM observation. The treated precipitates were also mounted on 11 nine pure Si plate for FE-SEM/EDX measurement. In FE-SEM/EDX measurement, at least 15 samples were measured in each condition. The calibration was operated as auto calibration mode.

The details of observation and measurement (TEM, FE-SEM/EDX, XRD, Raman and NMR) were described in previous chapters.

8.3. Results

8.3.1. *Characterization of DCPD for OCP synthesis.*

Figure 1a shows a FE-SEM micrograph of the precipitate formed in 0.33 M Ca and PO_4 solution after 1 h reaction time. The rhombohedral plate-like crystals were up to about 50 μm in length and 10 μm in width, and spherical aggregates of the crystals were also observed. The precipitate roughly consisted of one phase crystals. Figure 1b shows the XRD pattern of the rhombohedral plate-like crystal precipitate. The patterns of the precipitates showed four shapes and strong peaks at $2\theta = 11.8°$, 21.2°, 23.4°, and 29.2°, corresponding to the (020), (12−1), (040), and (14−1) reflections of DCPD, respectively.[19] Therefore, the precipitates were determined to be DCPD.

8.3.2. ***pH monitoring during OCP formation in various concentration acetic acid-containing solutions.***

Figure 2 shows the pH curves of OCP formation in various concentrations of acetic acid. In low concentration solutions of acetic acid (<100 mM), the pH values increased at the initial mixing stage because of the DCPD dissolution process. In the control solution (acetic acid free solution), the pH reached at 7.5 and then rapidly decreased to reach a value of around 5.4. After the rapid decrease of the pH value, the solution pH gradually decreased (0.025/h). The pH values of the final stage (15 h) were around 5.1. For high concentration of acetic acid (>200 mM), there were no obvious maximum pH points. However, the final pH values were around 5.1, the same as at the condition of low concentration. Thus, all materials were synthesized under acidic solutions (pH 5.0–5.5) with or without acetic acid.

8.3.3. ***XRD, FT-IR, NMR, and FE-SEM/EDX analysis of OCPs formed in various c acetic acid-containing solutions.***

Figure 3a shows the XRD patterns of the precipitates formed at 15 h in solutions with various concentrations of acetic acid. The patterns of the precipitates obtained from every solution indicated the presence of the OCP phase with a (100) reflection at 2θ = 4.7°. The other peaks were also similar to those of OCP. The relative intensities of some peaks were increased by increasing the concentration of acetic acid. The relative intensity ratios of the (100) peaks increased, and the relative intensity ratios of the strongest peak of OCP ((100) peak, 2θ = 4.7°) to the second strongest peak ((4-1-2) peak, 2θ around 26°) were 100:90 in the control, 100:50 in 5 mM acetic acid, 100:25 in 10 mM acetic acid, and 100:3 in 100 mM acetic acid. This suggests that the layered structure of OCP along the *a*-axis developed in the presence of acetic acid. The typically HAP peak at 2θ = 10.8° was not observed in XRD pattern of precipitates formed in various acetic acid-containing solutions.

Figure 3b shows enlarged XRD patterns of the precipitates formed at 15 h with various concentrations of acetic acid. The pattern of the control precipitate shows a single peak at 2θ = 26.5°, a broad single peak at 2θ = 26.5°, and fused peaks around 2θ = 30.4°–35.5°. For the precipitates formed in low concentration (<5 mM) of acetic acid, the fused peaks around 2θ = 30.4°–35.5° showed typical *hk* diffraction band reflections. This indicates that the precipitates had layer stacking defects along the *a*-axis direction. However, increasing the concentration of acetic acid drastically changed the XRD patterns.

The sharp single peak around 2θ = 33.5° corresponding to the (700) reflection of OCP[19] was enhanced with increasing concentration of acetic acid. The relative intensity of the peak reached 30 of OCP formed in 500 mM acetic acid-containing solution, where the (100) reflection intensity of OCP is considered 100 (relative intensity). The single peak at 2θ = 26.8° was also enhanced with attenuation of the peak intensity at 2θ = 26.5° with increasing concentration (>15 mM) of acetic acid. This peak was attenuated at high concentration of acetic acid. In addition, many small reflections in the region 2θ = 27.0°–30.0° were enhanced. The *hk* diffraction band reflection was attenuated and separated into two peaks at 2θ = 31.8° and 32.0°. The fused peaks were attenuated and sharp peaks were enhanced with increasing concentration of acetic acid. This indicated that crystallinity and symmetry of OCP crystals developed with the increase in the concentration of acetic acid. This is supported by TEM observation. In addition, FT-IR and NMR spectroscopic measurements showed *Lay* structures were developed with increase of acetic acid (see below).

Figure 4 shows FT-IR spectra of the precipitates formed with various concentrations of acetic acid. The FT-IR spectra of OCP exhibited monomodal strong absorption corresponding to v_3''' (PO_4) stretching at 1025 cm^{-1}, and many weak sub-absorptions bands of OCP at 864, 917, 963, 1038, 1058, and 1080 cm^{-1} because of PO_4 vibrations and at 1105, 1123, 1130, and 1185 cm^{-1} because of HPO_4 vibrations.[20] The spectra of the precipitates formed in acetic acid solutions showed an extra absorption band of OCP at 1005 cm^{-1} corresponding to v_3'' of HPO_4, which is the strongest absorption of OCP.[21] The band at 1005 cm^{-1} was enhanced with increasing concentration of acetic acid. Thus, the FT-IR results indicate that acetic acid enhances the *Lay* structure of OCP.

Figure 5 shows solid state ^{31}P NMR spectra of the precipitates formed in the control, and 5 mM and 100 mM acetic acid solutions at 15 h. The NMR spectrum of OCP shows four chemical shifts corresponding to *P1* at 3.6 ppm (PO_4 from *Apa*), *P2/P4* at 3.1 ppm (PO_4 from *Apa*), *P3* at 1.9 ppm (PO_4 from *Tra*), and *P5/P6* (HPO_4 from *Lay*).[2,12,13,15,22] The spectrum of the precipitate formed in the control solution shows a strong *P3* shift and weak and broad *P1* and *P2/P4* shifts. We could not detect obvious chemical shifts corresponding to *P5/P6* in the control precipitate.

However, the spectrum of the precipitate formed in 5 mM acetic acid solution showed a bimodal shift owing to *P1* and *P2/P4* and monomodal shifts owing to *P5/P6* with *P3* shift, which is the typical NMR spectrum of OCP. Furthermore, the spectrum of the precipitate formed in 100 mM acetic acid solution showed a strong *P1* shift, indicating a well-developed HAP structure in the OCP phase. The NMR results indicate that acetic acid induced the *Apa* and *Lay* structures in OCP. In addition, there was no evidence for shift separation of the *P5/P6* shift, such as is observed for OCPS.[24] This tendency was consistent for both the XRD and FT-IR results.

Figure 6 shows the Ca/PO4 ratios of the materials formed with various concentrations of acetic acid measured with FE-SEM/EDX. The Ca/PO4 ratios of the materials formed in the control solution was 1.45 ± 0.07 (N=15). At low concentration (<20 mM) of acetic acid, this value rapidly decreased to 1.15 ± 0.03 at 20 mM. Above 20 mM concentration of acetic acid, this value stabilized approximately at 1.15. The Ca/PO4 ratios of OCP decreased with increasing concentration of acetic acid.

8.3.4. *Microscopy observation of the precipitates formed in various acetic acid-containing solutions.*

8.3.4.1. The average sized of OCP crystals formed in various acetic acid-containing solutions.

The average sizes of OCP crystals formed in acetic acid-containing solutions were increased with increasing concentration of acetic acid but remained below 50 mM. For example, in acetic acid-free conditions, precipitates mainly comprised crystals 10 μm in length and 200 nm in thickness. In 50 mM acetic acid-containing solutions, precipitates mainly comprised rigid crystals over 200 μm in length and 200 nm in thickness. Above 100 mM, there were little correlation between the average sizes of OCP crystals and acetic acid concentration. However, even in high acetic acid concentration solutions, a few of crystals formed were the same size as those formed in low acetic acid concentrations.

8.3.4.2. Precipitate formed in the control solution.

Figure 7a shows FE-SEM micrographs of the OCP crystal precipitate formed in the control solution. The OCP crystals showed a typical elongated ribbon-like morphology 10–20 μm in length, approximately 2 μm in width, and 200 nm in thickness. The edge of single crystals were often rectangular (insert image of Fig. 7a), sometimes formed blade-like morphologies, and sometimes formed spheritic aggregates.

Figure 7b shows TEM photographs of typical single OCP crystals perpendicular to the plate-like plane. The SAED image of Fig. 7b shows the positions of the diffraction spots of the (010) and (001) diffractions of OCP (Fig. 7c). It indicates that the plate-like plane of OCP is the *bc* plane. HR-TEM showed well-ordered lattice fringes with a moiré pattern along the *bc* plane (Fig. 7d). This indicates that atomic disorder is present along the *a*-axis of the crystal. Furthermore, small regions of the OCP crystals showed poor lattice fringes (Fig. 7e). Figure 7f shows a low-magnification TEM micrograph of an ultrathin section of OCP large-scale plate-like crystals in the vertical direction along the *a*-axis. Figure 7g and 7h show a HR-TEM image of an ultrathin section in the vertical direction along the *a*-axis. The HR-TEM observations showed that the structure of the OCP crystals formed in the control solution consisted of well-ordered lattice fringes (see Fig. 8) with a few poor lattice (Fig. 7g) and polycrystalline regions (Fig. 7h).

8.3.4.3. Precipitate formed in 100 mM acetic acid-containing solution.

Figure 8a shows a transmission optical micrograph of the OCP crystals formed in 100 mM acetic acid-containing solution. The OCP crystals had a rigid plate-like morphology 50–100 μm in length, 10–20 μm in width, and 0.2–5 μm in thickness. The OCP crystals sometimes formed polycrystalline spherulites. The edges had a sword-like shape, not a rectangular shape.

Figure 8b shows a TEM image and a SAED pattern of the OCP crystals. The SAED pattern of the plate-like OCP crystals along the *a*-axis shows clear Laue spots corresponding to the single crystal. HR-TEM image showed the tendency of well-ordered lattice fringes (Fig. 8c). The ultrathin section of the large-scale plate-like OCP crystals (Fig. 8d) revealed that they mainly consisted of well-ordered lattices in the vertical direction along the *a*-axis with a lattice spacing of 2.47 Å (Fig. 8e).

TEM observation indicated that in acetic acid the layer structure formed along the *a*-axis was well-developed. NMR and FT-IR spectroscopic measurements showed that acetic acid plays an important role in the formation of the *Lay* structure in OCP.

8.4. Discussions

Kamitakahara and colleagues[5,23-25] showed using hydrothermal synthesis method of HAP from OCP. According to their researches, the heating degree at 65 °C, 1 h is too small to transform OCP into HAP during drying processes. Thus, it is considered that the results were originated from OCP structures alternation by acetic acid.

In Chapter 8, when OCP formed with increasing concentrations of acetic acid, NMR and FT-IR measurements showed that *Apa* and *Lay* structures of OCP were well developed with increasing acetic acid concentration. XRD measurements also indicated that OCP showed high symmetric structure with increasing acetic acid concentration, because *hk* diffraction band structures were attenuated. This indicated that the development of *Apa* structure by acetic acid was one of the main factors responsible for well-crystallized OCP crystal formation. Considering the OCP crystal structure, i.e., *Apa*-*Tra*-*Lay*-*Tra*-*Apa* layer structures, it is suggested that a well-developed *Apa* structure enables a well-developed *Lay* structure because the *Apa* structure acts as a connector of *Lay* bridge structures. This tendency was also confirmed by microtome-HR-TEM methods.

The reason why acetic acid enhanced not only *Lay* structure but also *Apa* structure of OCP. Although it could not be detected how acetic acid developed the *Apa* structure in precursor phases, furthermore, there were no evidence that acetic acid incorporated into OCP lattices, a hint was derived by Mathew et al.[17] who acquired large OCP crystals formed in 100 mM acetic acid at 40 °C. At approximately 40 °C, ACP phases formed as an initial phase.[26,27] ACP phases played an essential role in calcium phosphate crystalline formation on the basis of cluster-based phase transformation.[26,28-30] In this work, although experiments were conducted at a relatively high temperature of 65 °C, OCP crystals were synthesized from ACP in aqueous solutions because OCP formed in aqueous solutions. Thus, in this work, it is considered that ACP formed as precursor phase of OCP.

In Chapter 7, OCP crystals formed in ACP particles are shown, suggesting that the alteration physico-chemical properties of ACP or cluster which component of ACP by -COOH-containing molecules may control OCP formation, reaction path, and its structure. Based on this suggestion, acetic acid may affect the early stages of OCP formation. Habraken et al.[29] showed that OCP (Ca-deficient OCP) formed via some precursor stages, ACP, that are described as an ionic-pair and cluster in aqueous solutions. Kanzaki et al.[30] analyzed potential free energy of Ca-PO_4 cluster structures using *ab initio* calculations. Du et al.[31] also reported Ca-PO_4 cluster structures in aqueous solutions using X-ray adsorption near edge spectroscopy (XANES). Some Ca-PO_4 clusters which component of ACP particles did not have structural similarity between crystalline phases, and it was suggested that these cluster types are isomers and later attenuated crystallinity of crystalline phases. Based on these results, acetic acid may attenuate isomer of Ca-PO_4 clusters formation process during the OCP formation and develop well-crystallized *Apa* structures of OCP.

With regard to cluster based mineralization, it was suggested that multiple structures that could be identified as minerals was formed. For example, vaterite, a metastable phase of calcium carbonate, formed several different structures through cluster based mineralization. Demichelis et al.[37] showed using *ab initio* calculation, vaterite has multiple type of crystal structures having the same basic Ca^{2+} ions locations but different CO_3^{2-} ions locations. In XRD analysis, the main peaks of these crystals coincided well and were identified as vaterite, but minor peaks did not coincided as well. In Chapter 8, it is considered that OCP also has multiple structures which showed typically OCP peak at $2\theta = 4.7°$ but their structures were slightly different. Numerous previous works[2-5,11-18,22,23] reported different lattice parameters of OCP; thus, it was suggested that the OCP phase could be categorized as an OCP group structure rather than a strictly single strictly structure such as calcite and NaCl.

8.5. Conclusions

Chapter 8 investigated how acetic acid effects OCP crystal structure formation. Acetic acid enhanced the *Apa* structure in addition to *Lay* structure, which is important for acquiring well-crystallized and large sized OCP crystals. It is suggested that well-crystalline OCP formation by acetic acid could be explained by the elimination isomers, which attenuated *Apa* structure crystallinity, during precursor ACP stage. The idea that Ca-PO_4 clusters have several forms which including isomer could explain the calculation results.[32-36] This investigation shows that the process through which the *Apa* structure is formed has an additive effect on the final crystallinity of OCP and is related to the entire OCP formation process.

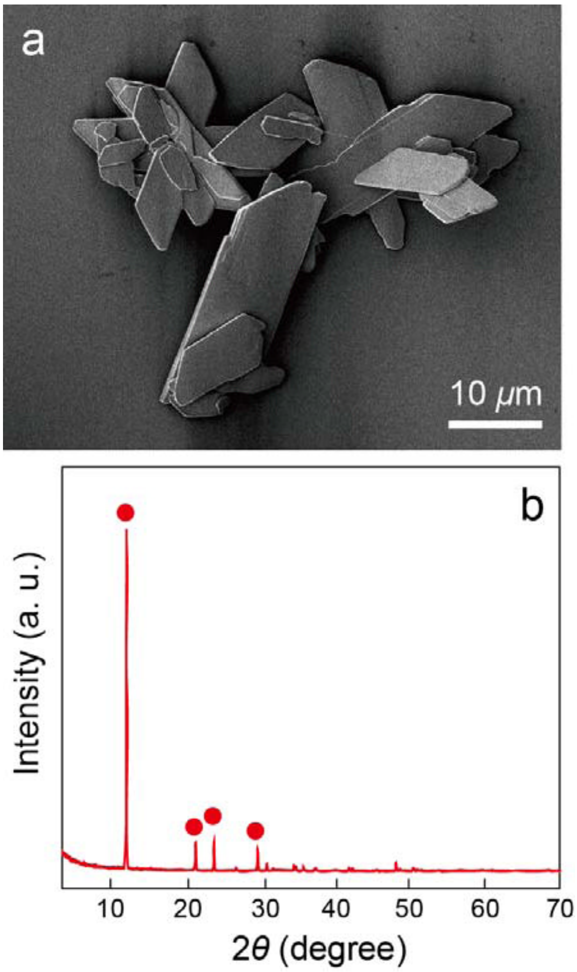

Figure 8.1. FE-SEM micrograph and XRD pattern of DCPD (the starting material for OCP synthesis). (a) DCPD formed in 0.33 M Ca and PO_4 solutions at 1 h showing the aggregation of rhombohedral crystals. (b) XRD pattern of the sample in (a). Red solid circles correspond to DCPD peaks.

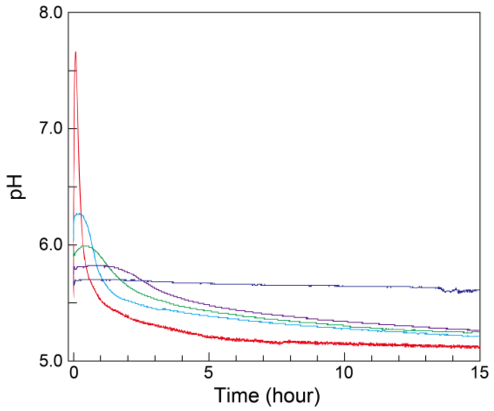

Figure 8.2. Change in pH values as a function of time as an indicator of OCP formation in different concentration acetic acid solutions: red line, control; light blue line, 20 mM; green line, 50 mM; purple line, 100 mM; and dark blue line, 800 mM.

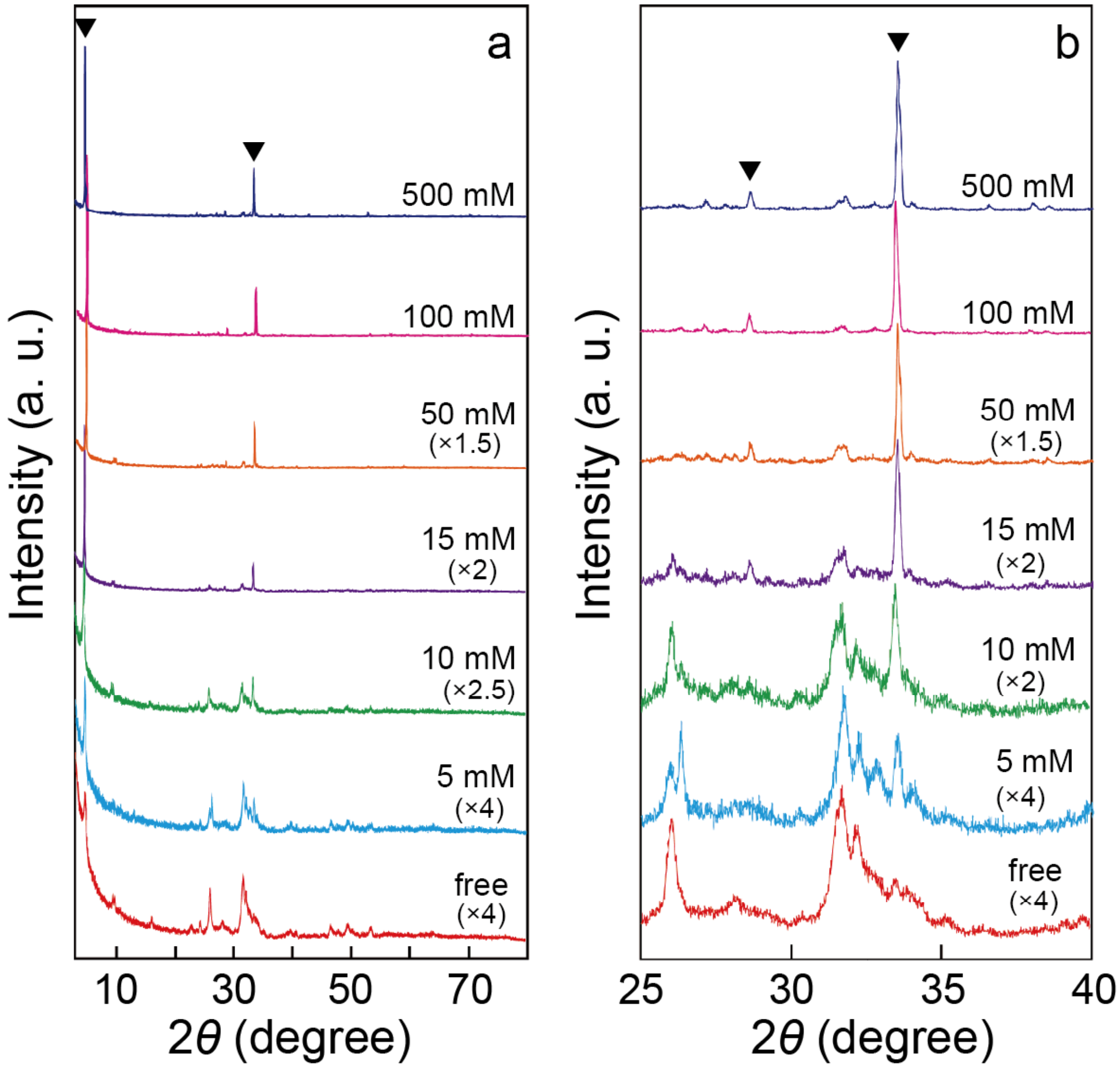

Figure 8.3. XRD patterns of the precipitates formed with various concentrations of acetic acid. XRD patterns of the (a) wide-angle range and (b) narrow-angle range from 2θ = 25°–40°. The reflections indicated by upside-down solid triangles correspond to a phase that appeared by increasing the concentration of acetic acid.

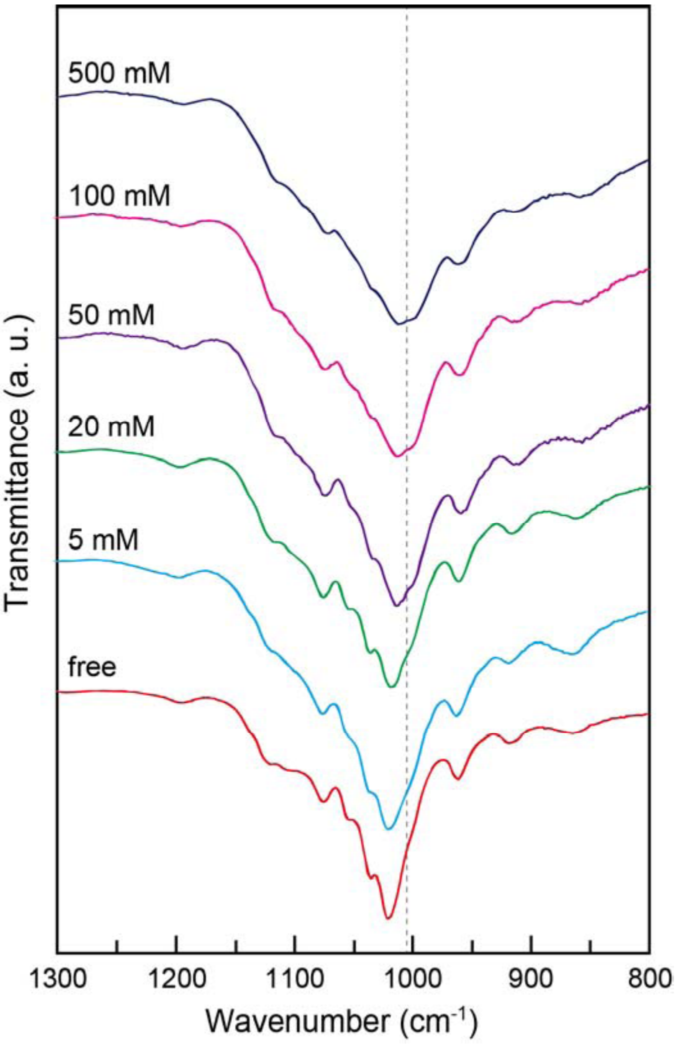

Figure 8.4. FT-IR spectra of the precipitates formed in different concentration acetic acid solutions. The grey dotted line at 1008 cm^{-1} indicates absorption owing to HPO_4 vibration.

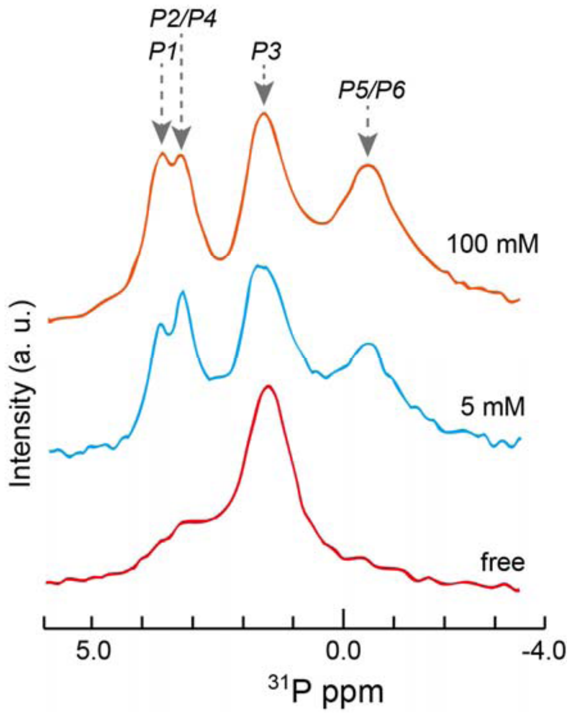

Figure 8.5. ^{31}P solid-state NMR spectra of precipitates formed in 0, 5, and 100 mM acetic acid solutions.

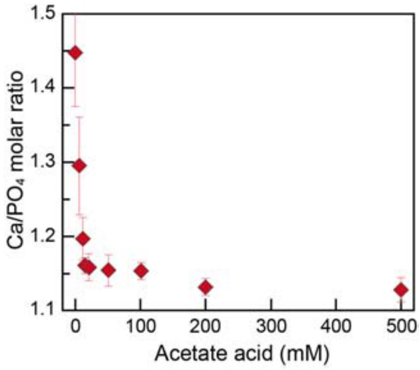

Figure 8.6. Ca/P ratios of the products formed in various concentration acetic acid solutions.

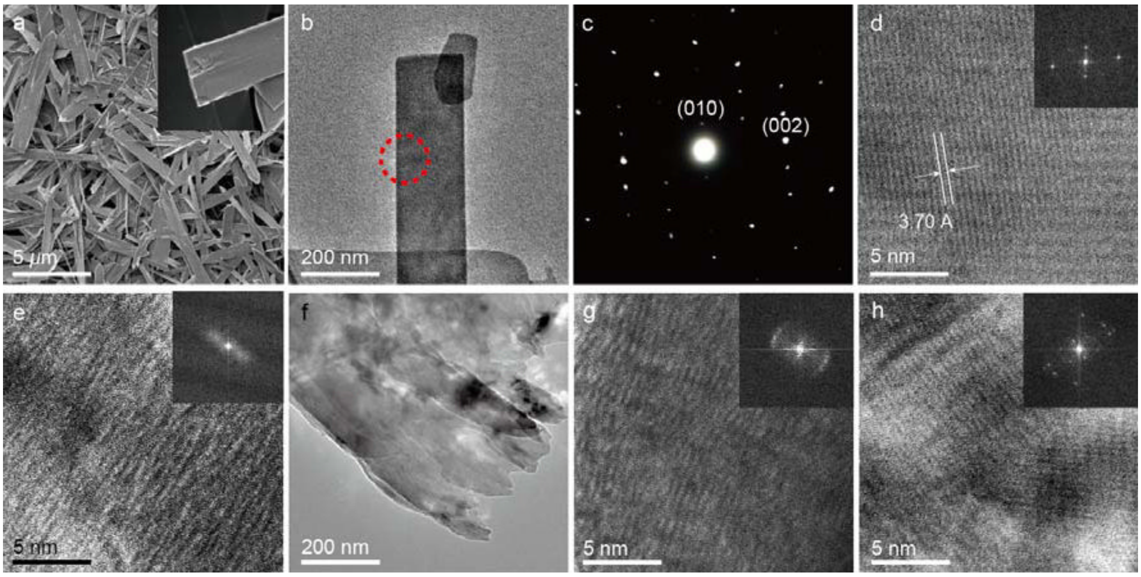

Figure 8.7. Electron microscopic data of the precipitate formed in acetic acid-free solution. (a) FE-SEM image of the precipitate and magnified image of the edge of the plate-like crystals. (b) Bright-field image of plate-like crystals along the *a*-axis. Red broken circle indicated SAED pattern area. (c) SAED pattern of the crystal of (b). (d) HR-TEM image with FFT pattern showing well-ordered lattice fringes in plate-like crystals along the *a*-axis. (e) HR-TEM image with FFT pattern showing poor complex lattice fringes in plate-like crystals along the *a*-axis. (f) Low magnification bright-field image of ultrathin section of the crystal in the vertical direction along the *a*-axis. (g) HR-TEM image and FFT pattern of OCP showing poor complex lattice fringes in the vertical direction along the *a*-axis in the ultrathin section. (h) HR-TEM image and FFT pattern of OCP showing polycrystalline lattice fringes in ultrathin section in the vertical direction along the *a*-axis.

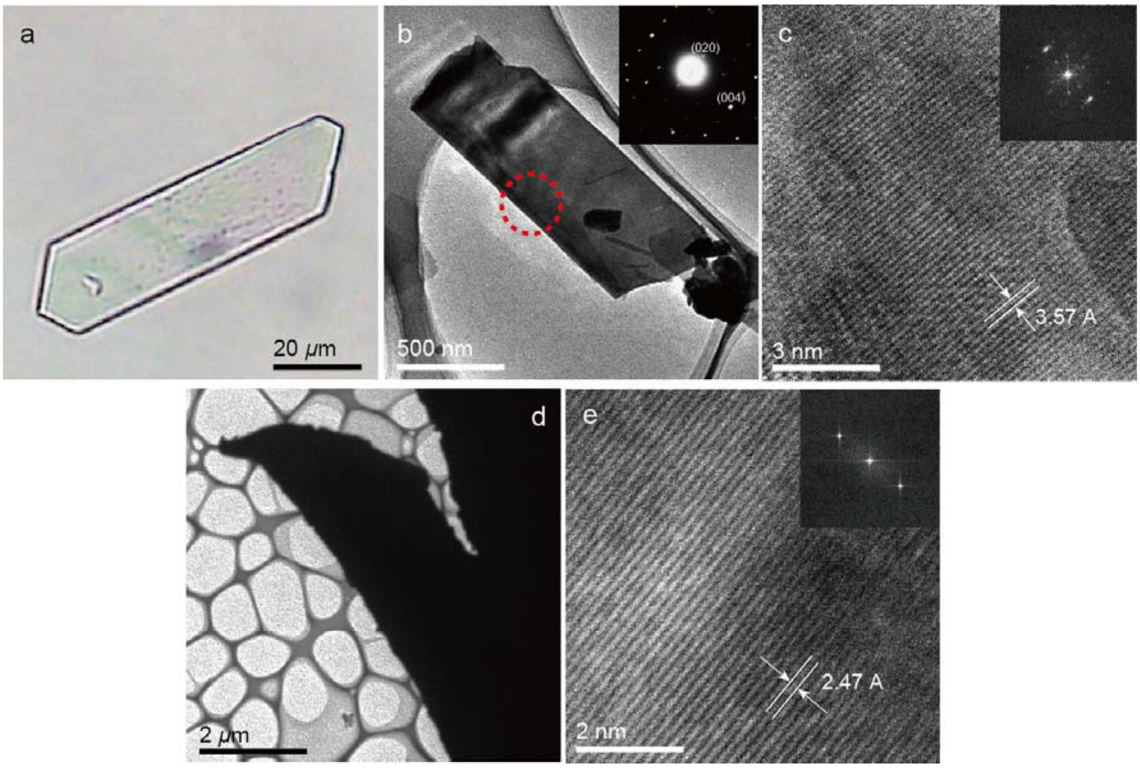

Figure 8.8. Electron micrograph data of the precipitate formed in 100 mM acetic acid solution. (a) Optical micrograph of a single crystal of the precipitate. (b) Bright-field image of plate-like crystals along the *a*-axis with SAED pattern. Red broken circle indicated SAED pattern area. (c) HR-TEM image and FFT pattern of plate-like crystals showing well-ordered lattice fringes along the *a*-axis. (d) Low magnification bright-field image of the same sample in the ultrathin section in the vertical direction along the *a*-axis. (e) HR-TEM image and FFT pattern of plate-like crystals showing well-ordered lattice fringes along the *a*-axis.

Reference

(1) Newesely, H. Darstellung von “Oktacaliumphosphat” (Tcracalcium hydrogentrisphosphat) durch homogene Kristallisation. *Monatch. Chem.*, **1960**, *249*, 1020-1023.

(2) Aoba, T., Ishida, T., Yagi, T., Hasegawa, K., Moriwaki, Y. X-ray crystallographic studies on the conversion of octacalcium phosphate into hydroxyapatite. *Jpn. J. Oral Biol.*, **1975**, *17*, 1-7. (in Japanese)

(3) Brown, W.E., Smith, J.P, Lehr, J.R., Frazier, A.W. Octacalcium Phosphate and Hydroxyapatite. *Nature*, **1962**, *196*, 1050–1055.

(4) Brown, W.E., Schroeder, L.W., Ferris, J.S., Interlayering of crystalline octacalcium phosphate and hydroxyapatite. *J. Phys. Chem.*, **1979**, *83*, 1385-1388.

(5) Kamitakahara, M., Okano, H., Tanihara, M., Ohtsuki, C. Synthesis of octacalcium phosphate intercalated with dicarboxylate ions from calcium carbonate and phosphoric acid. *J. Cera. Soc. Jpn.*, **2008**, *116*, 481-485.

(6) Nelson, D.G.A., McLean, J.D. High-Resolution Electron Microscopy of Octacalcium Phosphate and its Hydrolysis Products. *Calcif. Tiss. Int.*, **1984**, *36*, 219-232.

(7) Vereecke, G., Lemaitre, J. Calculation of the solubility diagrams in the system $Ca(OH)_2$-H_3PO_4-KOH-HNO_3-CO_2-H_2O. *J. Cryst. Growth*, **1990**, *104*, 820-832.

(8) Wang, L., Nancollas, G.H. Calcium Orthophosphates: Crystallization and Dissolution. *Chem. Rev.*, **2008**, *108*, 4628-4669.

(9) Johnsson, M.S., Nancollas, G.H. The role of brushite and octacalcium phosphate in apatite formation. *Crit. Rev. Oral. Biol. Med.*, **1992**, *3*, 61-82.

(10) Davies, E., Duer, M.J., Ashbrook, S.E., Griffin, J.M. Applications of NMR

Crystallography to Problems in Biomineralization: Refinement of the Crystal Structure and ^{31}P Solid State NMR Spectral Assignment of Octacalcium Phospahte. *J. Am. Chem. Soc.*, **2012**, *134*, 12508-12515.

(11) Monma, H., Goto, M. Succinate-complexed Octacalcium Phosphate. *Bull. Chem. Soc. Jpn.*, **1983**, *56*, 3843-3844.

(12) Markovic, M., Fowler, B.O., Brown, W.E. Octacalcium Phosphate Carboxylates. 1. Preparation and Identification. *Chem. Mater.*, **1993**, *5*, 1401-1405.

(13) Markovic, M., Fowler, B.O., Brown, W.E. Octacalcium Phosphate Carboxylates. 2. Characterization and Structural Considerations. *Chem. Mater.*, **1993**, *5*, 1406-1416.

(14) Aoki, S., Sakamoto, K., Yamaguchi, S., Nakajima, A. Syntheses of Octacalcium Phosphate Containing Dicarboxylic Acids and Effects of the Side Groups on the Crystal Growth of Octacalcium Phosphate. *J. Cera. Soc. Jpn.*, **2000**, *108*, 909-914.

(15) Tsai, T.W.T., Chou, F., Tseng, Y., Chan, J.C.C. Solid-state P-31 NMR study of octacalcium phosphate incorporated with succinate. *Phys. Chem. Chem. Phys.*, **2010**, *12*, 6692-6697.

(16) Davies, E., Muller, K.H., Wong, W.C., Pickard, C.J., Reid, D.G., Skepper, J.N., Duer, M.J. Citrate bridges between mineral platelets in bone. *Proc. Nat. Acad. Sci. USA.*, **2014**, E-1354-E1363.

(17) Markovic, M. *Octacalcium Phosphate Carboxylates*. Chow, L.C., Eanes, E.D. (Eds.), In *Octacalcium Phosphate, Monographs in Oral Science Vol. 18*. pp. 77-93. Karger, Basel, Switzerland, **2001**.

(18) Mathew, M., Brown, W.E., Schroeder, L.W., Dickens, B. Crystal structure of octacalcium bis(hydrogenphosphate) tetrakis(phosphate) pentahydrate, $Ca_8(HPO_4)_2(PO_4)_4 \cdot 5H2O$. *J. Crystallog. Spectro. Res.*, **1988**, *18*, 235-250.

(19) Delgado-Lopez, J.M., Frison, R., Cervellino, A., Gomez-Morales, J., Guagliardi, A., Masciocchi, N. Crystal Size, Morphology, and Growth Mechanism in Bio-Inspired Apatite Nanocrystals. *Adv. Funct. Mater.*, **2014**, *24*, 1090-1099.

(20) Delgado-Lopez, J.M., Iafisco, M., Rodriguez, I., Tampieri, A., Prat, M., Gomez-Morales, J. Crystallization of bioinspired citrate-functionalized nanoapatite with tailored carbonate content. *Acta Biomater.*, **2012**, *8*, 3491-3499.

(21) Xie, B.Q., Nancollas, G.H. How to control the size and morphology of apatite nanocrystals in bone. *Proc. Nat. Acad. Sci. USA*, **2010**, *107*, 22369-22370.

(22) Tseng, Y.-H., Mou, C.-Y., Chan, J.C.C. Solid-State NMR Study of the Transformation of Octacalcium Phosphate to Hydroxyapatite: A Mechanistic Model for Central Dark Line Formation. *J. Am. Chem. Soc.*, **2006**, *128*, 6909-6918.

(23) Kamitakahara, M., Ito, N., Murakami, S., Watanabe, N., Ioku, K. Hydrothermal synthesis of hydroxyapatite from octacalcium phosphate: effect of hydrothermal temperature. *J. Cera. Soc. Jpn.*, **2009**, *117*, 385-387.

(24) Ito, N., Kamitakahara, M., Murakami, S., Watanabe, N., Ioku, K. Hydrothermal synthesis and characterization of hydroxyapatite from octacalcium phosphate. *J. Cera. Soc. Jpn.*, **2010**, *118*, 762-766.

(25) Kawachi, G., Misumi, H., Fujimori, H., Goto, S., Ohtsuki, C., Kamitakahara, M., Ioku, K. Fabrication of porous blocks of calcium phosphate through hydrothermal processing under glycine coexistence. *J. Cera. Soc. Jpn.*, **2010**, *118*, 559-563.

(26) Onuma, K., Oyane, A., Tsutsui, K., Tanaka, K., Treboux, G., Kanzaki, N., Ito, A. Precipitation Kinetics of Hydroxyapatite Revealed by the Continuous-Angle Laser Light Scattering Technique. *J. Phys. Chem. B*, **2000**, *104*, 10563-10568.

(27) Christofferesen, J., Christofferesen, M.R., Kibalczyc, W. Apparent solubilities of

two amorphous calcium phosphates and octacalcium phosphate in the temperature range 30-42°C. *J. Cryst. Growth*, **1990**, *105*, 349-354.

(28) Posner, A., Betts, F. Synthetic amorphous calcium phosphate and its relation to bone mineral structure. *Acc. Chem. Res.* 1975, *8*, 273-281.

(29) Onuma, K., Ito, A. Cluster Growth Model for Hydroxyapatite. *Chem. Mater.*, **1998**, *10*, 3346–3351.

(30) Onuma, K., Oyane, A., Kokubo, T., Treboux, G., Kanzaki, N., Ito, A. Nucleation of Calcium Phosphate on 11-Mercaptoundecanoic Acid Self-assembled Monolayer in a Pseudophysiological Solution. *J. Phys. Chem. B*, **2000**, *104*, 11950-11956.

(31) Habraken, W.J.E.M., Tao, J.T., Brylka, L.J., Friedrich, H., Bertinetti, L., Schenk, S.A., Verch, A., Dmitrovic, V., Bomans, P.H.H., Frederik, P.M., Laven, J., van der Schoot, P., Aichmayer, B., deWith, G., DeYoreo, J.J., Sommerdijk, N.A.J.M. Ion-association complexes unite classical and non-classical theories for the biomimetic nucleation of calcium phosphate. *Nat. Comm.* **2013**, DOI: 10.1038/ncomms2490.

(32) Kanzaki, N., Treboux, G., Onuma, K., Tsutsumi, S., Ito, A. Calcium Phosphate Clusters, *Biomater.*, **2001**, *22*, 2921-2929.

(33) Du, L.-W., Bian, S., Gou, B.-D., Jiang, Y., Huang, J., Gao, Y.-X., Zhao, Y.-D., Wen, W., Zhang, T.-L., Wang, K. Structure of Clusters and Formation of Amorphous Calcium Phosphate and Hydroxyapatite: From the Perspective of Coordination Chemistry. *Cryst. Growth Des.*, **2013**, *13*, 3103-3109.

(34) Treboux, G., Layrolle, P., Kanzaki, N., Onuma, K., Ito, A. Symmetry of Posner's Cluster, *J. Am. Chem. Soc.*, **2000**, *122*, 8323-8324.

(35) Dey, A., Bomans, P.H.H., Muller, F.A., Will, J., Frederick, P.M., deWith, G., and Sommerdijk, N.A.J.M. The Role of Prenucleation Clusters in Surface-Induced Calcium

Phosphate Crystallization. *Nat. Mater.*, **2010**, *9*, 1010–1014.

(36) Yin, X., Scott, M.J. Biological calcium phosphates and Posner’s cluster. *J. Chem. Phys.*, **2003**, *118*, 3717-3723.

(37) Demichelis, R., Raiteri, P., Gale, J.D., Dovesi, R. The Multiple Structures of Vaterite. *Cryst. Growth. Des.*, **2013**, *13*, 2247-2251.

Chapter 9

General Summary

Based on cluster growth models, in calcium carbonate and calcium phosphate systems, the dynamics of phase transformation from amorphous into the crystalline phases and how physico-chemical properties, ionic charge, and hydration of additives affect into these behaviors were investigated. For both systems, fine characterization of intermediate transition phases during phase transformation from the amorphous to the crystalline phase was mainly performed, and their dynamics were determined in relation to the use of different physico-chemical properties of additives, phosphate ions or carboxylic-functional-groups.

In Chapter 2, the effects of $H_2PO_4^-$ ions on the formation dynamics of crystalline calcium carbonate formation and its polymorphism in weak basic solutions were investigated. Although a small amount of $H_2PO_4^-$ ions (molar ratio of $H_2PO_4^-/Ca^{2+}$ approximately 1/5000) accelerated vaterite formation, $H_2PO_4^-$ ions essentially inhibited calcium carbonate formation. It inhibited vaterite more than calcite, and calcite was likely to form only under relatively high $H_2PO_4^-$ ions concentrations.

In Chapter 3, the vaterite spherulite dissolution process was studied in $H_2PO_4^-$-containing solutions, and the vaterite-like intermediate transitional phase (pseudo-vaterite) was characterized. The vaterite spherulites consisted of at least two phases. Although their physico-chemical properties were very similar, their responses to $H_2PO_4^-$ were different. Thus, when $H_2PO_4^-$-containing vaterite or vaterite was dissolved in $H_2PO_4^-$-containing solutions, the vaterite spherulites developed a hollow structure during dissolution, because pseudo-vaterite formed before vaterite.

In Chapter 4, the surface energies of vaterite and pseudo-vaterite in solutions with different $H_2PO_4^-$ ions concentrations were determined. The surface energies of vaterite and pseudo-vaterite are 30.7 mJ/m^2 and 23.9 mJ/m^2, respectively, and were found to increase with increasing $H_2PO_4^-$ ions concentration. In 10 μM $H_2PO_4^-$-containing solution, the surface energies of vaterite and pseudo-vaterite were 223.9 mJ/m^2 and 105.2 mJ/m^2 using two dimensional models, respectively. In $H_2PO_4^-$-rich-containing solutions, therefore, the formation of vaterite was difficult because it was dependent on the surface energy. As a result, a low-stability phase was likely to appear instead.

In Chapter 5, the behavior of HPO_4^{2-} and $-PO_4^{2-}$ additives during the calcium carbonate mineralization process was investigated. FMN, a PO_4 derivative of vitamin B_2, was used as the $-PO_4^{2-}$ source in weak basic solutions. Small amounts of FMN (molar ratio of FMN/Ca^{2+} of approximately 1/1000) inhibited calcite and induced vaterite formation. This tendency was also confirmed in HPO_4^{2-}-containing solutions with pH values greater than 12.0, in which porous calcite crystals formed. Thus, it can be concluded that HPO_4^{2-} and $-PO_4^{2-}$ selectively effect calcium carbonate polymorph formation by adsorbing onto the calcite surface and inhibiting calcite formation. Therefore, the effect of oxygenated phosphorous ions on calcium carbonate formation depends on the charge of the phosphate ions.

In Chapter 6, the effect of immobilized –COOH (CGNs) on the formation dynamics of HAP were studied. CGNs not only accelerated HAP formation by approximately 45% (molar ratio of CGNs/Ca^{2+} of approximately 1/1000), but they also altered the formation path of HAP. Rather than forming an intermediate OCP-like structure was generated first, in the presence of CGNs, directly from ACP. Conversely, the OCP-like structure was not observed under weak basic conditions in the presence of

CGNs.

In Chapter 7, the effect of CGNs on OCP formation was investigated. In particular, CGNs inhibited formation of the HPO_4–OH layer during OCP formation from ACP and induced an intermediate transition phase, an HPO_4-OH layer-deficient OCP, which lacked the characteristic OCP peak at $2\theta = 4.7°$ in the XRD pattern. Thus, the CGNs acted as a negative catalyst for calcium phosphate mineralization.

In Chapter 8, the effect of the hydration state of the carboxylic acid, acetic acid on the OCP structure was studied. NMR and FT-IR spectroscopic analyses revealed that acetic acid favored not only the HPO_4–OH layer, but also the HAP-like layer structure for the OCP, which was in contrast to the result obtained with CGNs.

In both calcium carbonate and calcium phosphate systems, the intermediate transition phases have relatively loose structures compared to those of the crystalline phases, and their responses to different additives were consequently different from those of the crystalline phases. Thus, it may be possible to control intermediate transition phase formation during biogenic mineralization in aqueous solutions by selecting the appropriate additive. Furthermore, even with the same ions or functional groups, the charges and hydration states of the additives can have different effects on the transformation from the amorphous to the crystalline state in these materials, with the opposite effects observed for calcium carbonate and calcium phosphate mineralization.

Acknowledgement

In first, I would like to say absolutely thank for two great teachers, Prof. Atsushi Yamazaki, Waseda University and Dr. Kazuo Onuma, National Institute of Advanced Industrial Science and Technology (AIST) for their helpful and fruitful suggestions and tutorships. Without their warmly and kindly support ship, this Ph.D thesis has never written.

I also have a lot to be thankful for Prof. Katsuo Tsukamoto, Osaka University (Tohoku University) for his suggestions and support-ships during I had been a student at Tohoku University, and Dr. Atsuo Ito (AIST), Dr. Motohiro Hirose (AIST), Dr. Yu Sogo (AIST), Dr. Ayako Oyane (AIST), Dr. Xiupeng Wang (AIST), Ms. Yumi Sugiura (AIST), Ms. Kazuo Yoshiyuki (AIST) and Ms. Fumiko Kobayashi (AIST), for helpful advices and supporting at AIST, the past Prof. Ichiro Sunagawa (Tohoku Univ.), Prof. Yuki Kimura (Hokkaido Univ.), Prof. Hitoshi Miura (Nagoya City Univ.), Dr. Koichi Momma (National Museum of Nature and Science), Dr. Ken Nagashima (Hokkaido Univ.), Dr. Jun Nozawa (Tohoku Univ.), Dr. Mihoko Maruyama (Osaka Univ.), Dr. Fumiko Watanabe-Nara (Tohoku Univ.) and Mr. Hiromasa Niinomi (Nagoya Univ.) for lots of suggestions and supports.

Prof. Alexander A Chernov (LRNI), Dr. Akira Kato (National Museum of Nature and Science), Prof. Hiroaki Imai (Keio Univ.), Prof. Juan Manuel Garcia-Ruiz (Granada Univ.), Prof. Elias Vlieg (Radboud Univ. Nijimegen), Prof. Koji Ioku (Keio Univ.), Prof. Masanobu Kamitakahara (Tohoku Univ.), Dr. Jun Kawano (Hokkaido Univ.), Dr. Hiroki Nada (AIST), Prof. Yoshinori Furukawa (Hokkaido Univ.), Prof. Gen Sazaki (Hokkaido Univ.), Prof. Yoshihisa Suzuki (Tokushima Univ.), Prof. Tsubasa Ohtake (Hokkaido Univ.), Prof. Chao-Long Li (Zhejiang Sci. Tech. Univ.) and Dr. Jaime Gomez-Morales

(Granada Univ.) discussed me and gave many fruitful suggestions.

Dr. Masao Sorai (AIST) and Mr. Takao Maki (Olympus Co.) helped me for optical microscopy observation. Mr. Takahiro Goto, Mr. Natsuhiko Sugimura, Mr. Masaki Ito, Dr. Toshimichi Shibue, Mr. Daisuke Fukagawa, Ms. Chisato Izutani and all staffs at material characterization central laboratory (MCCL), Waseda University helped me for many technical supporting and fruitful suggestions.

Support and encouragement given by Mr. Yoshiaki Fukuda, Dr. Mana Yasui, Dr. Kan Tei, Dr. Yushin Yazaki, Dr. Masahiro Nagao and all staffs and students of Yamazaki’s laboratory.

Financial aided given by Japan Society of Promotion Science (JSPS) as fellowship for doctoral course student (DC2).

I would like to say thank you for my parents and grandmother, Mr. Fuminori Sugiura, Ms. Midoriko and Ms. Mieko Yamaki for their helpful support and kindful suggestion. I also say thank you for all my friends at Toho High school, Tohoku University and Waseda University.

Ｎｏ．１

早稲田大学　博士（理学）　学位申請　研究業績書

氏 名　杉浦　悠紀　　　印

（2015年　2月　現在）

種 類 別	題名、　発表・発行掲載誌名、　発表・発行年月、　連名者（申請者含む）
学術論文 （筆頭著者）	○The effects of immobilized carboxylic-functional groups on the dynamics of phase transformation from amorphous to octacalcium phosphate, Yuki Sugiura, Kazuo Onuma, Masahiro Nagao, Atsushi Yamazaki *American Mineralogist*, **Accepted** ○ Dissolution behavior of vaterite spherulites in solution containing phosphate ions, Yuki Sugiura, Kazuo Onuma, Masahiro Nagao, Koichi Momma, Yuki Kimura, Atsushi Yamazaki, *Journal of the Ceramic Society of Japan*, *122,* 679-684, **2014**. ○ Solution Chemical Synthesis of Hollow Vaterite Polycrystalline Particles for Advanced Biomaterial Applications, Yuki Sugiura, Kazuo Onuma and Atsushi Yamazaki *Chemistry Letters*, DOI: http://dx.doi.org/10.1246/cl.140823, **2014**. ○Acceleration and inhibition effects of phosphate on phase transformation of amorphous calcium carbonate into vaterite, Yuki Sugiura, Kazuo Onuma, Yuki Kimura, Katsuo Tsukamoto, Atsushi Yamazaki, *American Mineralogist*, *98*, 262-270, **2013**. Morphological evolution of precipitates during transformation of amorphous calcium phosphate into octacalcium phosphate in relation to role of intermediate phase, Yuki Sugiura, Kazuo Onuma, Yuki Kimura, Hitoshi Miura, Katsuo Tsukamoto, *Journal of Crystal Growth*, Elsevier, Amsterdam, *332*, 58-67, **2011**.

Ｎｏ.２

早稲田大学　博士（理学）　学位申請　研究業績書

種類別	題名、　発表・発行掲載誌名、　発表・発行年月、　連名者（申請者含む）
講演 （筆頭著者）	○　擬似人工タンパク質による水酸アパタイトの形成促進、 杉浦悠紀、小沼一雄、山崎淳司 2014年11月　第44回結晶成長国内会議 ○　ドラッグデリバリーシステム応用のためのナノ粒子集合体バテライト作製 杉浦悠紀、小沼一雄、山崎淳司 2014年9月　第27回秋季セラミックスシンポジウム ○　アモルファス炭酸カルシウム(ACC)相変化へのリン酸イオンの影響、 杉浦悠紀、小沼一雄、山崎淳司 2014年4月　第28回日本地球惑星科学連合合同大会 ○ Ca-CO3-PO4 3成分系におけるバテライトの安定性 杉浦悠紀、小沼一雄、山崎淳司 2013年11月 第8回バイオミネラリゼーションワークショップ ○ Vaterite intermediate phase: physicality and dynamics in presenting PO_4, Yuki Sugiura, Kazuo Onuma, Yuki Kimura, Koichi Momma, Atsushi Yamazaki, 2013年8月　The 17th International Conference on Crystal Growth ○　ACC-バテライト相転移時における中間体 杉浦悠紀、小沼一雄、木村勇気、門馬綱一、山崎淳司 2012年12月　第7回バイオミネラリゼーションワークショップ ○ バテライト形成過程における結晶質の前駆体、 杉浦悠紀、小沼一雄、木村勇気、門馬綱一、塚本勝男、山崎淳司 2012年11月　第42回結晶成長学会国内会議 ○ Crystalline Precursor of Vaterite during Mineralization via ACC, Yuki Sugiura, Kazuo Onuma, Yuki Kimura, Katsuo Tsukamoto, Atsushi Yamazaki, 2012年7月 International Crystal Growth in Sendai リン酸第8カルシウム(OCP)モルフォロジー形成時における中間相の役割 杉浦悠紀、小沼一雄、木村勇気、三浦均、塚本勝男、 2011年11月　第41回結晶成長学会国内会議

早稲田大学　博士（理学）　学位申請　研究業績書

種類別	題名、　発表・発行掲載誌名、　発表・発行年月、　連名者（申請者含む）
	The morphological relationship of octacalcium phosphate from precursor: the role of intermediate phase, Yuki Sugiura, Kazuo Onuma, Yuki Kimura, Hitoshi Miura, Katsuo Tsukamoto, 2011年5月　The 3rd International School of Biological Crystallization HAP Precursor, OCP Morphology Formation and Phase Transition to β-TCP, Yuki Sugiura, Yuki Kimura, Kazuo Onuma, Hitoshi Miura, Katuo Tsukamoto 2010年9月　8th Japan-China-Korea Workshop on Microgravity Sciences for Asian Microgravity Pre-Symposium Phase Transition of HAP Precursors with Maintaining Morphology, Yuki Sugiura, Yuki Kimura, Kazuo Onuma, Hitoshi Miura, Katuo Tsukamoto, 2010年8月　The 16th International Conference on Crystal Growth HAP Precursors, OCP Formation and Phase Transition to β-TCP, Yuki Sugiura, Yuki Kimura, Kazuo Onuma, Hitoshi Miura, Katsuo Tsukamoto 2010年8月　The 14th International Summer School on Crystal Growth
外部獲得資金	日本学術振興会特別研究員DC2 科研費奨励金「生体鉱物の中間相の構造・安定性について」 平成25-26年度　2400千円
受賞等	“International Mohri Poster Award, Excellent Poster Award” Yuki Sugiura, Yuki Kimura, Kazuo Onuma, Hitoshi Miura, Katuo Tsukamoto 2010年8月　8th Japan-China-Korea Workshop on Microgravity Sciences for Asian Microgravity Pre-Symposium, Akiu, Sendai, Japan